

# Aerodynamic characteristics of tall buildings with porous façades

---

Škvorc, Petar

Doctoral thesis / Doktorski rad

2024

*Degree Grantor / Ustanova koja je dodijelila akademski / stručni stupanj:* **University of Zagreb, Faculty of Mechanical Engineering and Naval Architecture / Sveučilište u Zagrebu, Fakultet strojarstva i brodogradnje**

*Permanent link / Trajna poveznica:* <https://urn.nsk.hr/urn:nbn:hr:235:576689>

*Rights / Prava:* [In copyright / Zaštićeno autorskim pravom.](#)

*Download date / Datum preuzimanja:* **2024-11-29**

*Repository / Repozitorij:*

[Repository of Faculty of Mechanical Engineering and Naval Architecture University of Zagreb](#)





University of Zagreb

Faculty of Mechanical Engineering and Naval Architecture

Petar Škvorc

**AERODYNAMIC CHARACTERISTICS OF  
TALL BUILDINGS WITH POROUS  
FAÇADES**

PhD thesis

Zagreb, 2024



University of Zagreb

Faculty of Mechanical Engineering and Naval Architecture

Petar Škvorc

AERODYNAMIC CHARACTERISTICS OF  
TALL BUILDINGS WITH POROUS  
FAÇADES

PhD thesis

Supervisor:

Prof. Hrvoje Kozmar, PhD

Zagreb, 2024



Sveučilište u Zagrebu

Fakultet strojarstva i brodogradnje

Petar Škvorc

# AERODINAMIČKA SVOJSTVA VISOKIH ZGRADA S POROZNIM PROČELJEM

Doktorski rad

Mentor:

Prof. dr. sc. Hrvoje Kozmar

Zagreb, 2024.

## BIBLIOGRAPHY DATA

Keywords: Tall building aerodynamics; porous double-skin façade systems; aerodynamic loads; wind-tunnel experiments.

Scientific area: Technical sciences

Scientific field: Mechanical Engineering

Institution: University of Zagreb, Faculty of Mechanical Engineering and Naval Architecture

Supervisor: Prof. Hrvoje Kozmar, PhD

Number of pages: 157

Number of figures: 71

Number of tables: 3

Number of references: 150

Date of oral examination:

Jury members: Prof. Milan Vrdoljak, PhD  
Prof. Gianni Bartoli, PhD  
Andrija Buljac, PhD

Archive: University of Zagreb,  
Faculty of Mechanical Engineering and Naval Architecture

## Preface

This thesis was developed at the Faculty of Mechanical Engineering and Naval Architecture, University of Zagreb, Croatia. The experiments were performed at the Inter-University Research Centre on Building Aerodynamics and Wind Engineering (CRIACIV), University of Florence, Italy.

The thesis is based on the following journal articles and conference contributions:

- 1) Škvorc P, Kozmar H (2021) Aerodynamic characteristics of tall buildings with porous double-skin façades: State of the art and future perspectives, *Wind and Structures* 33(3), 233-249.
- 2) Škvorc P, Kozmar H (2023) The effect of wind characteristics on tall buildings with porous double-skin façades, *Journal of Building Engineering* 69, 106135, 1-28.
- 3) Škvorc P, Melnjak P, Kozmar H, Giachetti A, Bartoli G (2022) Aerodynamic interference of tall buildings subjected to the atmospheric boundary layer flow, *Proceedings of the 10<sup>th</sup> International Congress of Croatian Society of Mechanics*, Pula, Croatia, 249-250.
- 4) Škvorc P, Giachetti A, Kozmar H, Bartoli G (2022) Aerodynamic loading of tall buildings with porous double-skin façade systems, *17<sup>th</sup> Conference of the Italian Association for Wind Engineering*, Milano, Italy, 157-158.
- 5) Škvorc P, Giachetti A, Kozmar H, Bartoli G (2022) Wind loads on tall buildings with double-skin façade systems: The effect of wind characteristics, *Proceedings of the 8<sup>th</sup> European-African Conference on Wind Engineering*, Bucharest, Romania, 191-194.
- 6) Škvorc P, Kozmar H (2023) Aerodynamic loading of tall buildings of a varying geometric aspect ratio equipped with PDSF systems, *16<sup>th</sup> International Conference on Wind Engineering*, Florence, Italy.

## Acknowledgements

The study was funded by the Croatian Science Foundation IP-2016-06-2017 and IP-2022-10-9434 grants and the Erasmus+ program Mobility for Traineeship, whose support is gratefully acknowledged. The work was supported by the “Young researchers’ career development project – training of doctoral students” of the Croatian Science Foundation.

My sincerest gratitude goes to my advisor, Professor Hrvoje Kozmar, for entrusting me with this work. Our discussions and travels have allowed me to grow both professionally and personally. His expertise and experience have been invaluable to me on this journey, and I hope our collaboration will continue in the years to come.

I would like to extend my sincere gratitude to Professor Gianni Bartoli and Dr. Andrea Giachetti for their support of my experimental work in the wind tunnel at the University of Florence, Italy. Many thanks to Professor Claudio Mannini for useful discussions and advice.

Sincere thanks to Tommaso, Petar, Michael and Niccolò for their help with the experiments, and for our daily breaks which made me addicted to coffee.

My gratitude goes to my friends and co-workers at the faculty, mainly Ivan, Vedrana and Mihael, as well as to the Department of Fluid Mechanics, who all substantially contributed to this work.

Special thanks to my family for their constant support during my education, and to my lifelong friends.

Finally, I wish to express my love and gratitude to my girlfriend Ines, for her unwavering support, patience and understanding. And to Hugo and Kira.

## Abstract

A porous double-skin façade system (PDSF) is a type of building cladding used on contemporary buildings. It is developed by attaching outer, porous skins to a solid façade. On tall buildings, the inner skin is usually made of glass and steel, while the outer, porous skin is made of perforated steel or aluminum plates. The purpose of the PDSF system is to enhance building energy efficiency, acoustic insulation, and visual appearance. For example, the outer skin may be used to tune the amount of sunlight on the building, thus cooling the building in the summer and heating it in the winter. This approach yields energy savings and leads to a decrease in the carbon footprint of buildings. The main goal of the present work is to experimentally determine the effect of PDSF systems on the aerodynamic characteristics of tall buildings, a topic that is currently underexplored.

The experimental work was performed in the boundary layer wind tunnel of the Inter-University Research Centre on Building Aerodynamics and Wind Engineering (CRIACIV) at the University of Florence, Italy. Two atmospheric boundary layer (ABL) simulations were created that correspond to suburban and rural terrains. To study the effects of PDSF porosity, a building model of a 1:1:5 geometric aspect ratio was manufactured. It corresponds to a 200 m tall building in the simulation length scale of 1:400. The material used for the building model was stainless steel. Three sets of outer skins were produced, with a porosity of 25%, 50% and 65%. The outer skins were perforated metal sheets with circular openings 10 mm in diameter. The porosity was achieved by altering the number of openings. This allowed for four different configurations, the three different PDSF systems, as well as a single-skin building model as a reference case. Additional building models of 1:1:3, 1:1:4, 1:2:5 and 1:3:5 aspect ratios were used in the single-skin configuration and with the 65% PDSF porosity only. To study the effects of the aerodynamic interference of tall buildings in an urban environment, eight 1:1:5 dummy building models were designed. They were placed in an in-line formation around the principal 1:1:5 building model in three configurations regarding the spacing between the building models. All the building models were studied at various flow incidence angles  $\beta$ .

Integral aerodynamic loads on the building models were assessed using high-frequency force balance (HFFB). An array of pressure sensors was used on four vertical surfaces of the 1:1:5 building model to observe aerodynamic pressure on the inner skin of the studied building model.

Several major findings emerged from this work. In particular, the application of a PDSF system generally yields a decrease in the standard deviation of the integral mean across-wind moment coefficient. The along-wind aerodynamic loads on the building models generally proved negligibly influenced by the PDSF system. The outer façade acts as a shelter to the inner façade, thus causing a large decrease in the aerodynamic pressure acting on the inner façade. This is highly dependent on the porosity of the outer façade, with higher porosity causing a



lower decrease of the surface pressure on the inner façade. High local pressures can occur on the inner façade depending on the openings situated on the outer façade. The aerodynamic characteristics of tall buildings with PDSF systems are rather complex. General findings do not necessarily apply to all cases due to highly complex, local phenomena caused by the porosity of the outer façade. Therefore, the design of engineering structures should be subject to laboratory tests or computational analysis to accurately resolve all the relevant aerodynamic phenomena.

Keywords:

Tall building aerodynamics; porous double-skin façade systems; aerodynamic loads; wind-tunnel experiments.

## Prošireni sažetak

Visoke zgrade se često izvode uz primjenu sustava poroznih dvostrukih pročelja. Glavna svrha poroznih dvostrukih pročelja je poboljšanje energetske učinkovitosti i izgleda zgrade. Poboljšanje energetske učinkovitosti se ostvaruje podešavanjem svjetla u unutrašnjosti zgrade, dok se odgovarajući arhitektonski oblik zgrade postiže otvorima na vanjskom pročelju.

Sustav poroznog dvostrukog pročelja se sastoji od unutarnjeg i vanjskog pročelja postavljenih na međusobnoj udaljenosti od 0.1 m do 2 m. Unutarnje pročelje se uobičajeno izvodi primjenom stakla i čelika, dok se vanjsko pročelje izrađuje od nehrđajućeg čelika ili aluminijske. Na vanjskom pročelju se nalaze otvori koji mogu biti različitih oblika i dimenzija, od kružnih ili četvrtastih otvora promjera nekoliko milimetara, sve do geometrijskih oblika dimenzija nekoliko metara. Na vanjsko pročelje se može postaviti rasvjeta koja dodatno doprinosi poboljšanju izgleda zgrade. Vanjsko pročelje doprinosi energetske učinkovitosti zgrade i štiti unutarnje pročelje od nepovoljnih atmosferskih uvjeta. S obzirom na činjenicu da je često tlocrt visokih zgrada kvadratnog oblika, pri čemu visina bitno nadmašuje širinu i duljinu zgrade, porozno vanjsko pročelje je jednostavan način isticanja arhitektonske izvedbe zgrade.

Trenutno na svijetu postoji mali broj visokih zgrada s poroznim dvostrukim pročeljima. Glavni razlog je nedovoljno poznavanje aerodinamičkih značajki takvih zgrada. Opterećenje vjetrom je važan čimbenik dinamičke stabilnosti visokih zgrada, jer vjetar može uzrokovati značajne vibracije na višim katovima, kao i izraženi površinski tlak na pročeljima zgrade. Unatoč činjenici da su vibracije očekivane i prihvatljive s obzirom na dinamička svojstva zgrade, one mogu uzrokovati nelagodu kod ljudi, i stoga ih je potrebno umanjiti.

Istraživanje aerodinamičkih značajki visokih zgrada s poroznim pročeljima je provedeno u zračnom tunelu CRIACIV (Inter-University Research Centre on Building Aerodynamics and Wind Engineering) Sveučilišta u Firenci, Italija. Provedene su ukupno četiri vrste eksperimenata:

- Aerodinamička opterećenja visoke zgrade opremljene dvostrukim poroznim pročeljima, pri čemu omjer duljine, širine i visine iznosi 1:1:5,
- Utjecaj atmosferskog graničnog sloja (AGS) na aerodinamička opterećenja visoke zgrade opremljene dvostrukim poroznim pročeljima, pri čemu omjer duljine, širine i visine iznosi 1:1:5,
- Aerodinamička opterećenja visoke zgrade opremljene dvostrukim poroznim pročeljima za različite omjere visine i tlocrtne površine zgrade,
- Aerodinamička opterećenja visoke zgrade opremljene dvostrukim poroznim pročeljima i smještene u urbanom okolišu.

Zračni tunel Sveučilišta u Firenci je Eiffelovog tipa i namijenjen eksperimentalnom modeliranju AGS-a uz primjenu barijere i podne hrapavosti. Na ulazu u ispitnu sekciju zračnog tunela jednolika struja zraka struji preko barijere, pri čemu nastaju vrtlozi s horizontalnom osi vrtnje. Elementi podne hrapavosti postavljeni nizvodno od barijere omogućavaju stvaranje i održavanje potrebne turbulencije u donjem dijelu modela AGS-a, koji je karakteriziran osrednjenom brzinom strujanja zraka, intenzitetom turbulencije, integralnom duljinskom mjerom turbulencije i spektralnom gustoćom snage pulzacija brzine strujanja zraka. Značajke modela AGS-a se određuju na temelju mjerenja brzine strujanja, tlaka i temperature zraka. Budući da su gradijenti osrednjene brzine i intenziteta turbulencije najveći neposredno iznad podloge mjerne sekcije zračnog tunela, mjerne točke su gusto raspoređene u tom području modela AGS-a. Primjenom elemenata podne hrapavosti i nazubljene barijere su razvijena dva modela AGS-a, koji su sukladni strujanju vjetra iznad prigradskog i ruralnog terena u mjerilu duljine 1:400.

Ispitivani model zgrade je oblika kvadra uz odnos duljine, širine i visine u iznosu 1:1:5. Model je visine 0.5 m, te u duljinskom mjerilu 1:400 predstavlja 200 m visoku zgradu. Donji dio modela zgrade je izrađen u skladu s dimenzijama visokofrekventne vage (HFFB) koja je korištena za određivanje integralnih aerodinamičkih opterećenja modela zgrade. Na vertikalnim površinama modela zgrade su postavljeni osjetnici tlaka. Model zgrade je izrađen od nehrđajućeg čelika da bi se postigla krutost modela zgrade i izbjegle aeroelastične pojave. Za model vanjskog, poroznog pročelja su korištene tanke ploče od nehrđajućeg čelika na koje su laserom izrezani kružni otvori 10 mm promjera u četvrtastom uzorku. Mijenjanjem broja otvora su izrađena tri modela pročelja poroznosti 25%, 50% i 65%.

Dvije eksperimentalne metode su korištene za određivanje aerodinamičkih opterećenja modela zgrade. Za mjerenje integralnih aerodinamičkih sila i momenata je model zgrade postavljen na HFFB, dok su osjetnici tlaka postavljeni na unutarnjem pročelju kako bi se odredio površinski tlak na unutarnjem pročelju.

Ispitivanje utjecaja omjera visine i tlocrtne površine modela zgrade opremljenog dvostrukim poroznim pročeljima na aerodinamička opterećenja modela zgrade je provedeno na modelima zgrada odnosa duljine, širine i visine 1:1:3, 1:1:4, 1:2:5 i 1:3:5. Modeli zgrada su izrađeni od aluminijske legure da bi se postigla njihova čvrstoća i krutost. Modeli zgrada su ispitani u izvedbi s klasičnim, jednostrukim pročeljem, i s dvostrukim poroznim pročeljem poroznosti 65%.

Model zgrade je uz samostojeći postav, tj. bez susjednih modela zgrada, također ispitan i uz prisustvo osam okolnih modela zgrade odnosa duljine, širine i visine 1:1:5. Na ovim dodatnim modelima zgrada nisu provedena mjerenja, već su oni poslužili isključivo za simulaciju strujanja vjetra u urbanom okruženju. Modeli dodatnih zgrada su postavljeni u kvadratnom obliku oko ispitivanog modela zgrade na kojem su provedena mjerenja s ciljem ispitivanja utjecaja urbanog okoliša. Ispitivanja su provedena za različite kuteve nastrojavanja zraka.

Na temelju provedenih eksperimenata su ostvarena sljedeća saznanja:

- Na modelu zgrade opremljenom sustavom poroznog dvostrukog pročelja je zabilježeno smanjenje standardne devijacije integralnog momenta u horizontalnom, poprečnom smjeru u odnosu na smjer strujanja zraka;
- Porozna dvostruka pročelja ne utječu na koeficijent integralnog momenta u smjeru strujanja;
- Iznos tlaka na unutarnjem pročelju modela zgrade opremljenog sustavom poroznog dvostrukog pročelja je bitno manji u odnosu na model zgrade s jednostrukim, klasičnim pročeljem, i ovisi o poroznosti vanjskog pročelja;
- Kod sustava poroznih dvostrukih pročelja je moguća pojava izraženog lokalnog tlaka na unutarnjem pročelju, ovisno o poziciji otvora na vanjskom pročelju modela zgrade.

Aerodinamičke značajke visokih zgrada s poroznim pročeljima su izrazito složene i opći zaključci ne vrijede nužno za sve slučajeve. Izvedba takvih konstrukcija treba prije izgradnje biti detaljno ispitana. U budućnosti je bitno istražiti učinak takvih konstrukcija na strujanje zraka u njihovoj blizini i moguće nepovoljne aerodinamičke pojave u urbanim okruženjima. Dodatno je potrebno istražiti pojavu izraženog lokalnog tlaka na površini unutarnjeg pročelja zgrade, utjecaj poroznih dvostrukih pročelja na površinski tlak na donjem dijelu zgrade, i aerodinamičke značajke zgrada složene arhitekture opremljenih dvostrukim poroznim pročeljima. Ovaj rad predstavlja temelj i polazišnu točku budućih računalnih simulacija strujanja zraka u blizini zgrade opremljene dvostrukim poroznim pročeljem.

# Contents

1	Introduction .....	1
1.1	Motivation .....	1
1.2	Literature survey.....	2
1.3	Objectives .....	4
2	Atmospheric winds.....	5
2.1	Driving forces .....	5
2.2	Synoptic winds .....	11
2.3	Non-synoptic winds.....	17
3	Bluff body aerodynamics .....	20
3.1	Boundary layer flows .....	22
3.2	Separated shear flows .....	23
4	Tall building aerodynamics.....	26
4.1	Aerodynamic loads on buildings .....	26
4.2	Building vibration mitigation .....	27
5	Porous materials .....	33
5.1	Fluid flow through porous structures .....	33
5.2	Porous elements in closed conduits.....	34
5.3	Porous structures in open flow .....	35
6	Experimental setup.....	37
6.1	Boundary layer wind tunnel .....	37
6.2	Building models.....	38
6.3	Flow simulation .....	45
6.4	Similarity criteria.....	47
6.5	Flow measurement.....	50
6.6	Aerodynamic load measurement .....	51
6.7	Surface pressure measurement .....	53
7	Results and discussion.....	54
7.1	Wind simulation .....	54
7.2	The aerodynamic effects of façade porosity.....	61

---

7.2.1	Integral aerodynamic load moments .....	62
7.2.2	Power spectral density of aerodynamic load fluctuations .....	64
7.2.3	Surface pressure .....	67
7.3	The effect of wind characteristics.....	78
7.3.1	Integral aerodynamic loads .....	78
7.3.2	Power spectral density of the aerodynamic load fluctuations .....	81
7.3.3	Surface pressure .....	84
7.4	The effect of the building aspect ratio .....	98
7.4.1	Square cross-section building model.....	98
7.4.2	Rectangular cross-section building model .....	103
7.5	Aerodynamic interference of tall buildings with porous façades .....	107
7.5.1	The effect of the flow incidence angle .....	108
7.5.2	The effect of the spacing between buildings .....	123
8	Conclusions .....	140

## List of Figures

Figure 1.	Balanced geostrophic flow in the southern hemisphere .....	7
Figure 2.	Force balance in the lower ABL .....	9
Figure 3.	Velocity profile in the ABL considering the Ekman spiral .....	10
Figure 4.	Schematic view of the energy cascade process .....	15
Figure 5.	Comparison of von Kármán design curves with the present experimental results of the power spectral density of longitudinal flow velocity fluctuations .....	16
Figure 6.	Shear stress in the ABL .....	17
Figure 7.	Airflow around streamlined and bluff bodies .....	20
Figure 8.	a) Wind axes and b) body axes .....	21
Figure 9.	Flow separation.....	23
Figure 10.	Flow around a flat plate perpendicular to the flow .....	24
Figure 11.	Schematic view of the cube surface pressure in the turbulent boundary layer flow .....	25
Figure 12.	Schematic view of the flow reattachment on a) cube and b) rectangular cylinder .....	26
Figure 13.	a) Burj Khalifa, b) 432 Park Avenue, c) Taipei 101, d) Beijing Olympic Tower, e) Petronas Towers, f) Shanghai World Financial Center, Photo courtesy of <a href="https://commons.wikimedia.org/">https://commons.wikimedia.org/</a> .....	31
Figure 14.	Porous materials.....	33
Figure 15.	Flow conditioners and turbulence generators .....	34
Figure 16.	Porous roadway wind barriers; photos courtesy of Zoran Lončarec .....	35
Figure 17.	CRIACIV boundary layer wind tunnel.....	38
Figure 18.	a) Tall building model, b) pressure taps tubing in the building model, c) arrangement of pressure taps on building façade models.....	39
Figure 19.	Schematic view of the studied building models with a single-skin façade and the PDSF systems of 25%, 50% and 65% porosity .....	40
Figure 20.	Building model with PDSF system: a) 25% porosity; b) 50% porosity and c) 65% porosity .....	41
Figure 21.	Arrangement of building models situated in the urban environment model ....	42
Figure 22.	Building models with the a) 1:3:5, b) 1:2:5, c) 1:1:4, d) 1:1:3 aspect ratios ....	43
Figure 23.	Connector for building models with various geometric aspect ratios .....	44
Figure 24.	a) 1:3:5 and b) 1:2:5 building models in the wind-tunnel test section.....	44
Figure 25.	Sawtooth barrier; left-hand side used for the ABL model of category I, right-hand side used for the ABL model of category III, all values are in cm. ....	46
Figure 26.	Arrangement of surface roughness elements for the ABL model of a) category I and b) category III .....	47
Figure 27.	ABL model category III setup in the wind-tunnel test section.....	47

Figure 28.	CTA measurement system, Jorgensen [142] .....	51
Figure 29.	High frequency force balance in the wind tunnel .....	52
Figure 30.	DTC pressure scanner .....	53
Figure 31.	Pressure system in the building model .....	54
Figure 32.	Mean flow velocity profiles in the rural and suburban ABL simulations and Eurocode [44] .....	55
Figure 33.	Turbulence intensity profiles in the rural and suburban ABL simulations and Eurocode [44] .....	56
Figure 34.	Integral turbulence length scale profiles in the rural and suburban ABL simulations and Eurocode [44] .....	57
Figure 35.	Power spectral density of longitudinal velocity fluctuations in the rural and suburban ABL simulations .....	58
Figure 36.	Comparison of the created suburban ABL simulation with the ABL profiles reported in Tamura [148]: a) mean flow velocity, b) longitudinal turbulence intensity.....	58
Figure 37.	Comparison of the mean pressure coefficient $C_p$ distribution on the building model of a) Tamura, [148] and b) present study .....	59
Figure 38.	Validation of the HFFB results: a) across-wind moment coefficient $C_{ML}$ , b) along-wind moment coefficient $C_{MD}$ .....	60
Figure 39.	Flow incidence angle $\beta$ and aerodynamic moments acting on the building model .....	61
Figure 40.	Power spectral density of force fluctuations exerted by an impulse load of the principal building model .....	62
Figure 41.	HFFB measurements of the building model with single-skin and three porous outer skin porosities, a) $\overline{C_{ML}}$ , b) $\overline{C_{MD}}$ , c) $\sigma_{CML}$ and d) $\sigma_{CMD}$ .....	63
Figure 42.	Integral across-wind moment power spectra for $0^\circ < \beta < 45^\circ$ with the $5^\circ$ increment .....	65
Figure 43.	Integral along-wind moment power spectra for $0^\circ < \beta < 45^\circ$ with the $5^\circ$ increment .....	67
Figure 44.	$\overline{C_p}$ distribution of on the principal building model with and without PDSF systems.....	72
Figure 45.	Distribution of $\sigma_{C_p}$ on all four surfaces of the building model with and without PDSF system.....	76
Figure 46.	Mean across-wind and along-wind moment coefficients ( $\overline{C_{ML}}, \overline{C_{MD}}$ ) and their respective standard deviations ( $\sigma_{CML}, \sigma_{CMD}$ ) for the single-skin building model (0%), 25% and 65% PDSF systems in the rural and suburban ABL simulations .....	80
Figure 47.	Integral across-wind moment power spectra for $\beta = 0^\circ, 15^\circ, 30^\circ$ and $45^\circ$ .....	82
Figure 48.	Integral along-wind moment power spectra for $\beta = 0^\circ, 15^\circ, 30^\circ$ and $45^\circ$ .....	83



Figure 49.	$\overline{C_p}$ distribution on the building model subjected at $\beta = 0^\circ, 15^\circ, 30^\circ$ and $45^\circ$ to the rural and suburban ABL simulations; building model is characterized by the smooth single-skin surface (0%), 25% and 65% PDSF systems.....	92
Figure 50.	$\sigma_{C_p}$ distribution on the building model subjected at $\beta = 0^\circ$ to the rural and suburban ABL simulations; building model is characterized by the smooth single-skin surface (0%), 25% and 65% PDSF systems.....	96
Figure 51.	Orientation of the 1:3:5 building model to the flow direction.....	98
Figure 52.	$\overline{C_{ML}}, \overline{C_{MD}}$ and $\sigma_{CML}, \sigma_{CMD}$ for the 1:1:3, 1:1:4 and 1:1:5 single-skin building models and 65% PDSF systems .....	99
Figure 53.	Integral across-wind moment power spectra for the 1:1:3 and 1:1:4 aspect ratio building models with the single-skin and the 65% PDSF system .....	101
Figure 54.	Integral along-wind moment power spectra for the 1:1:3 and 1:1:4 building models with the single-skin and the 65% PDSF system.....	102
Figure 55.	$\overline{C_{ML}}, \overline{C_{MD}}$ and $\sigma_{CML}, \sigma_{CMD}$ for the 1:2:5 and 1:3:5 single-skin building models and 65% PDSF systems.....	103
Figure 56.	Integral across-wind moment power spectra for the 1:2:5 and 1:3:5 building models with the single skin and the 65% PDSF system.....	105
Figure 57.	Integral along-wind moment power spectra for the 1:2:5 and 1:3:5 building models with the single-skin and the 65% PDSF system.....	107
Figure 58.	Urban environment model .....	108
Figure 59.	$\overline{C_{MD}}$ for the building model situated in the urban environment model at $D = 5d$ .....	108
Figure 60.	$\overline{C_{ML}}$ of the building model situated in the urban environment model at $D = 5d$ .....	109
Figure 61.	Integral along-wind moment power spectra for the principal building model situated in the urban environment model at $D = 5d$ .....	111
Figure 62.	Integral across-wind moment power spectra for the principal building model situated in the urban environment model at $D = 5d$ .....	112
Figure 63.	$\overline{C_p}$ distribution for various $\beta$ .....	117
Figure 64.	$\sigma_{C_p}$ for various $\beta$ .....	122
Figure 65.	Studied spacing between building models.....	124
Figure 66.	$\overline{C_{MD}}$ for the principal building model situated in the urban environment model at $D = d, D = 3d$ and $D = 5d$ .....	125
Figure 67.	$\overline{C_{ML}}$ for the principal building model situated in the urban environment model at $D = d, D = 3d$ and $D = 5d$ .....	126
Figure 68.	Integral along-wind moment power spectra for the principal building model situated in the urban environment model at $D = 3d$ and $D = 5d$ .....	127

Figure 69.	Integral across-wind moment power spectra for the principal building model situated in the urban environment model at $D = 3d$ and $D = 5d$ .....	129
Figure 70.	$\overline{C_p}$ distribution on the principal building model at $D = 3d$ and $D = 5d$ .....	133
Figure 71.	$\sigma_{C_p}$ on the principal building model at $D = 3d$ and $D = 5d$ .....	138

## List of Tables

Table 1.	Terrain types and aerodynamic surface roughness length, Holmes [22].....	13
Table 2.	Calibration results of the FT-Delta SI-165-15 HFFB.....	52
Table 3.	The major effects of the PDSF systems regarding mean surface pressure on the inner building model façade .....	74

## List of Symbols

<b>Symbol</b>	<b>Unit</b>	<b>Description</b>
$A$	$\text{m}^2$	Reference area
$C_F$	-	Force coefficient
$C_M$	-	Moment coefficient
$C_p$	-	Pressure coefficient
$c_w$	J	Heat capacity
$d_{\text{dis}}$	m	Displacement height
$f$	$\text{rad}^2/\text{s}$	Coriolis parameter
$F_a$	N/m	Aerodynamic force per unit length
$F_c$	N	Coriolis force
$F_L, F_D$	N	Across- and along-wind force, respectively
$F_p$	N/kg	Force per unit mass
$h$	m	Body height
$I_u, I_v, I_w$	-	Turbulence intensity in the $x$ -, $y$ -, and $z$ -direction, respectively
$I_w$	A	Current intensity
$Je$	-	Jensen number
$L$	m	Reference length
$L_{u,x}, L_{u,y}, L_{u,z}$	m	Integral length scales of turbulence
$m$	kg	Mass
$M$	Nm	Moment
$M_D$	Nm	Along-wind moment
$M_L$	Nm	Across-wind moment
$p$	Pa	Pressure
$r$	m	Radius of the curvature of the isobars
$Re$	-	Reynolds number
$R_w$	V	Current resistance
$S_M$	$\text{N}^2\text{m}^2\text{s}$	Integral moment power spectrum
$St$	-	Strouhal number
$S_u$	$\text{m}^2\text{s}$	Velocity power spectrum
$T$	s	Time record length

$t$	s	Time
$T_w, T_a$	K	Hot-wire temperature when operating and not operating, respectively
$u, v, w$	m/s	Flow velocity in the $x$ -, $y$ -, and $z$ -direction, respectively
$\overline{u}_{\text{ref}}$	m/s	Mean flow velocity at the reference height
$\overline{u}_z$	m/s	Mean flow velocity at height $z$
$\overline{u}_\tau$	m/s	Friction velocity
$\overline{u}, \overline{v}, \overline{w}$	m/s	Mean flow velocity in the $x$ -, $y$ -, and $z$ -direction, respectively
$u'(t), v'(t), w'(t)$	m/s	Fluctuating flow velocity in the $x$ -, $y$ -, and $z$ -direction, respectively
$U$	m/s	Wind velocity vector
$x, y, z$	-	Cartesian axes
$z_{\text{ref}}$	m	Reference height
$z^+$	-	Dimensionless height
$z_0$	m	Aerodynamic surface roughness length
$\beta$	°	Flow incidence angle
$\alpha$	-	Power-law exponent
$\Theta$	rad	Phase angle
$\Phi_{\text{conv}}(U)$	W/m <sup>2</sup>	Convection function
$\mu$	Pas	Dynamic viscosity
$\nu$	m <sup>2</sup> /s	Kinematic viscosity
$\rho_a$	kg/m <sup>3</sup>	Air density
$\sigma_{CMD}$	-	Standard deviation of integral along-wind moment coefficient
$\sigma_{CML}$	-	Standard deviation of integral across-wind moment coefficient
$\sigma_{Cp}$	-	Standard deviation of pressure coefficient
$\tau$	N/m <sup>2</sup>	Shear stress
$\varphi$	rad	Latitude
$\omega$	rad/s	Angular velocity
$\kappa$	-	von Kármán constant
$\lambda$	m	Eddy wavelength

# 1 Introduction

## 1.1 Motivation

Wind is one of the most destructive natural elements. At almost any given moment there is a severe windstorm somewhere on Earth, while some areas tend to be more affected by strong winds than others. For example, typhoons are characteristic of East Asia, while hurricanes occur in the Americas. The number of people affected by severe windstorms increases every year, while the number of fatalities decreases, a fact likely due to the advances in the design of high-rise buildings. Particularly affected by the windstorms are the rapidly growing countries of East Asia, such as China and the Pacific Rim, Zheng et al. [1].

Around 80% of all economic losses due to worldwide natural disasters are caused by wind and wind-related events, such as floods and tsunamis, Tamura and Cao [2]. Wind-induced economic losses encompass structural damage, but also adverse agricultural and traffic effects. Strong winds can destroy plants and stop the transport of goods and people, which affects the economy along with the related costs of structural repairs. According to the Insurance Information Institute [3], in the 2019 hurricane season in the US, there were 18 storms, six of which became hurricanes, with three of them becoming major events, Category 3 hurricanes with a wind speed exceeding 160 km/h. Hurricane Dorian hit the Caribbean in September 2019 and caused an estimated damage of nearly USD 2 billion. In 2018, hurricane Florence caused an estimated damage of USD 2-5.5 billion in the US, while in the same year, hurricane Michael caused about USD 8-13 billion of property damage.

One of the best-known wind-induced pieces of structural damage is the collapse of the Tacoma Narrows Bridge in November 1940, Olson et al. [4]. Strong wind caused torsional flutter of the bridge, which ultimately led to structural failure, Arioli and Gazzola [5]. There were no human casualties in the collapse. However, the property damage was immense, since the value of the bridge is estimated at USD 1 billion USD adjusted for inflation. Ultimately, this event led to advances in wind engineering and a deeper understanding of vortex-induced vibration and building aerodynamics, a topic relevant for the present work.

Given the loss of life and property damage caused by wind every year, the motivation of the present work is to increase understanding of the aerodynamic characteristics of tall buildings equipped with porous double-skin façade systems to increase occupant safety and comfort, and to raise the structural resilience of buildings with regard to wind loads.

## 1.2 Literature survey

Previous studies in the aerodynamics of buildings, particularly with respect to the application of porous facades, form an important base for the present study. Major issues of tall buildings subjected to wind include structural stability and human comfort. In particular, while wind-induced vibration can be catastrophic and cause property damage, even low wind loads may cause problems regarding human comfort in tall buildings.

Engineering structures tend to move when subjected to wind loads, and high-rise buildings are particularly susceptible to deformation. While deformation is indeed expected, it can cause discomfort for building occupants, especially on higher floors where the magnitude of building deformation reaches a maximum. Building motion can be addressed as a static component and an oscillatory component, Burton et al. [6]. The static component does not have a great impact on the building occupants, while the oscillatory component, caused mostly by vortex shedding on the building edges, can be noticed by the occupants. If the building oscillations become excessive, they can cause substantial discomfort to the occupants. This is mainly due to the building acceleration, while its deformation does not play a substantial role. It is difficult to assess the effect of building acceleration on occupant discomfort, Bernardini et al. [7], where the main challenge is the difference in the perception of motion from person to person. The perception of motion is further complicated by factors such as the posture of the body and human activity at that moment, Burton et al. [8], and the presence of visual cues, Isyumov [9].

High-rise buildings are common in business districts around the world, which means that many people work in offices located on the upper floors of tall buildings. Lamb et al. [10] surveyed 1,014 workers in the central business district in Wellington, New Zealand, and found that ~41% of these people felt wind-induced building motion. The loss of concentration was the most common effect of building motion, thus yielding lower productivity. While building acceleration is the cause of motion sickness, it is still unknown which of the building response parameters is most responsible for occupant discomfort. Some argue that this is the acceleration root mean square, others that it is the peak value, and others still that it is the acceleration derivative, McNamara et al. [11], while further work is required regarding the relevance of these parameters for tall buildings equipped with porous façades.

The reduction of building motion is therefore an important parameter in structural design. Advances in material science have resulted in high strength steel capable of sustaining stress of more than 450 MPa, high strength concrete and various composite materials, which in turn result in the reduction of building material, Johann [12]. A reduction in building material can be achieved using topological optimization, Beghini et al. [13], by optimizing material distribution on buildings.

Various materials and methods enable the design of slender buildings at reduced stiffness, which consequently increases building motion. One of the common ways of mitigating excessive building motion is the use of tuned mass dampers, Petrini et al. [14]. A tuned mass damper is essentially a large mass placed usually on the top floor of a high-rise building which can be controlled to move in the opposite direction of the building, therefore reducing the building motion. Their use is not limited to buildings, but can also be utilized in wind turbines, bridges, and other motion-sensitive structures.

Along with building occupant comfort, an important factor in building design is pedestrian comfort, regarding the low-level wind speeds which affect pedestrians and vehicles in the building vicinity. Numerous wind-tunnel experiments have been performed regarding low-level wind flow around typical buildings, e.g., Tamura et al. [15], Xu et al. [16], while further work is still needed in this regard. In this type of work, the use of computational fluid dynamics (CFD) can be demanding, and the results are inherently uncertain, Serteser and Karadag [17], while, on the other hand, wind-tunnel experiments are challenging because of the need to satisfy the similarity criteria and on account of the complex experimental techniques.

In recent times, double-skin façade (DSF) systems have been increasingly used on tall buildings. A double-skin façade system is designed as two façades placed at a small distance apart, usually 0.1 m to 2 m, so a cavity (gap) exists between the two façades, Lou et al. [18]. This cavity is used as an additional insulator and can also serve as a ventilation system by circulating air through it. If the outer façade is porous, this design is a porous double-skin façade (PDSF) system. While DSF systems on tall buildings are usually made so that both the inner and outer skins are combined of steel and glass, the outer skin of a PDSF system is usually made of perforated sheet metal, usually stainless steel, or aluminum, e.g., Pomaranzi et al. [19].

For a PDSF system, the cavity between the inner and outer skins allows for the airflow to enter and exit through the openings on the outer façade, which reduces its insulation properties, Kosiński et al. [20]. Consequently, a PDSF system does not have the air conditioning characteristics of a DSF system; however, since the outer skin of a PDSF system is made of metal, it provides some sun shading for the interior of the building. The amount of sun shading strongly depends on the porosity of the outer skin, Baldinelli [21].

An additional benefit of the PDSF system is its ability to protect the building from flying debris. A single broken glass panel can cause severe damage since the difference in internal and external pressure of the building in a windstorm can create damage by inducing low pressure inside the building. The outer, metal skin is more resistant to various impacts compared to the inner, glass skin. This is particularly important in regions of the world which experience strong local winds, such as hurricanes or tornadoes, Holmes [22]. Sheltering of the building is dependent on the porosity of the outer skin.



It is also important to note that PDSF systems can substantially enhance the visual appeal of buildings. The outer skin can be used for artistic expression, since it can be painted in any color, and the openings can be of various shapes and sizes. There are examples of various LED lights installed on the outer skin, which can be controlled to create attractive visual effects.

At the moment, PDSF systems are used predominantly on low-rise buildings since their impact on the aerodynamic characteristics of tall buildings is still unknown. However, there are still important previous works to be noted. Gerhardt and Janser [23] measured the net pressure coefficients on buildings with various aspect ratios, ABLs and façade porosities. The width of the gap between the inner and outer façade proved to be the most important parameter for the pressure coefficient difference between the inner and outer façade, with the smallest gap yielding the largest absolute value of the pressure coefficient. Kemper and Feldmann [24] proposed wind load recommendations for rectangularly shaped buildings with PDSF systems. Porous spires have proved to reduce vortex-induced excitations, diminish vortex shedding on building surfaces, and consequently reduce the dynamic response of buildings, Cammelli et al. [25], Belloli et al. [26], [27].

Porous windward screens have proved to reduce surface pressures on the inner façade but concurrently increase the vortex-shedding frequency, Hu et al. [28], [29]. A two-dimensional study of a rectangular cylinder with solid screens at various distances from the windward building surface was carried out by Giachetti [30] and Giachetti et al. [31]. Giachetti et al. [32], [33] observed that a solid, laterally open screen at a small distance from the windward surface of a tall building can reduce the gradient of the lateral force coefficient and pressure distributions on lateral surfaces. Jafari and Alipour [34] developed a design methodology for PDSF systems, an approach based on optimization techniques and computational modeling.

Given the current knowledge gap, the goal of the present work is to experimentally determine the effect of PDSF systems of various porosities on the aerodynamic characteristics of tall buildings in various wind conditions.

### **1.3 Objectives**

The present work focuses on the aerodynamic characteristics of tall buildings with PDSF systems for various flow conditions, outer skin porosities, building aspect ratios, and the aerodynamic interference of buildings.

Laboratory experiments were performed in a boundary layer wind tunnel in two ABL simulations. Integral wind loads on building models were determined using an HFFB. Surface pressure was recorded on the inner skin of the building model equipped with PDSF systems. This was performed using an array of pressure sensors mounted on four surfaces of the building

model. Four PDSF systems were employed with various outer skin porosities of the building model characterized by a 1:1:5 geometric aspect ratio. The porosities were 0% (single-skin building model), 25%, 50% and 65% for this building model. Five building models of 1:1:3, 1:1:4, 1:1:5, 1:2:5, 1:3:5 aspect ratios were studied with two outer skin porosities, i.e., the 0% (single-skin) and 65% porosity.

In addition to the single (lone standing) building model, the effects of surrounding building models were assessed as well. In this case, eight 1:1:5 single-skin dummy building models were used in an in-line array surrounding the principal 1:1:5 building model to study the aerodynamic interference of buildings. The building models were arranged at three spacings among the building models. All experiments were performed for a full range of flow incidence angles  $\beta$ .

The research hypotheses of the present work are:

- Aerodynamic forces and moments acting on a tall building with a PDSF system are greater than those acting on a tall building with a smooth, single-skin façade. This is caused by turbulent airflows in the cavity between the two façades, characteristic vortex-shedding frequencies, and the size of the separated airflow.
- Surface pressure on the inner skin of a tall building with a PDSF system is lower than that of a tall building with a smooth, single-skin façade due to the sheltering effect of the building surface.
- The vibration frequency of a tall building with a PDSF system is higher when the building is exposed to the urban ABL type compared to suburban and rural wind conditions.

This thesis provides insight into the previously unknown aerodynamic effects of PDSF systems on tall buildings, with particular emphasis on the effects of flow characteristics, façade porosity, building aspect ratio, and the aerodynamic interference of buildings.

## 2 Atmospheric winds

### 2.1 Driving forces

The motion of air in the atmosphere is primarily a consequence of the radiation heat transfer from the Sun to the Earth. However, as the Sun heats the ground and air to various degrees, it causes a pressure difference on a global scale. The pressure forces caused by the pressure difference and the forces generated by the Earth's rotation are the two main parameters influencing atmospheric flow, i.e., the wind, e.g., Stull [35], Garratt [36].

*Pressure force*

Considering a fluid point at a pressure gradient  $\partial p/\partial x$  in the  $x$ -direction, the force in the respective direction is:

$$F_p = -\left(\frac{1}{\rho_a}\right)\frac{\partial p}{\partial x}, \quad (2.1)$$

where  $\rho_a$  is the air density. The negative sign indicates that the pressure force acts from the high-pressure region towards the low-pressure region.

*Coriolis force*

The Coriolis force is an apparent force caused by the Earth's rotation. An observer on the Earth's surface can only measure the relative wind velocity, unlike an observer from space who can measure both the Earth's rotational velocity and the absolute wind velocity. For this reason, the ground observer measures an additional rotational component of the wind velocity. This is the Coriolis force:

$$F_c = m f_c U, \quad (2.2)$$

where  $m$ ,  $U$  and  $f_c$  are the mass of air, the air velocity vector and the Coriolis parameter, respectively. The Coriolis parameter is:

$$f_c = 2\omega \sin(\varphi), \quad (2.3)$$

where  $\omega$  is the Earth's angular velocity, and  $\varphi$  is the latitude angle.

The Coriolis parameter in the Coriolis force equation yields:

$$F_c = 2mU\omega \sin(\varphi). \quad (2.4)$$

Since the Earth rotates from the west towards the east, in the northern hemisphere it acts to the right of the direction of motion, whereas it acts to the left of the direction of motion in the southern hemisphere. At the equator there is no Coriolis force effect.

### *Geostrophic wind*

If a point in a fluid is under equal and opposite pressure gradients and Coriolis force, the flow is considered to be a balanced geostrophic flow, Figure 1. Equalizing the pressure gradient force per unit mass from Equation (2.1) and the Coriolis force from Equation (2.2) yields:

$$U_g = -\left(\frac{1}{\rho_{af}}\right)\frac{\partial p}{\partial x}, \quad (2.5)$$

where  $U_g$  is the geostrophic wind speed vector.

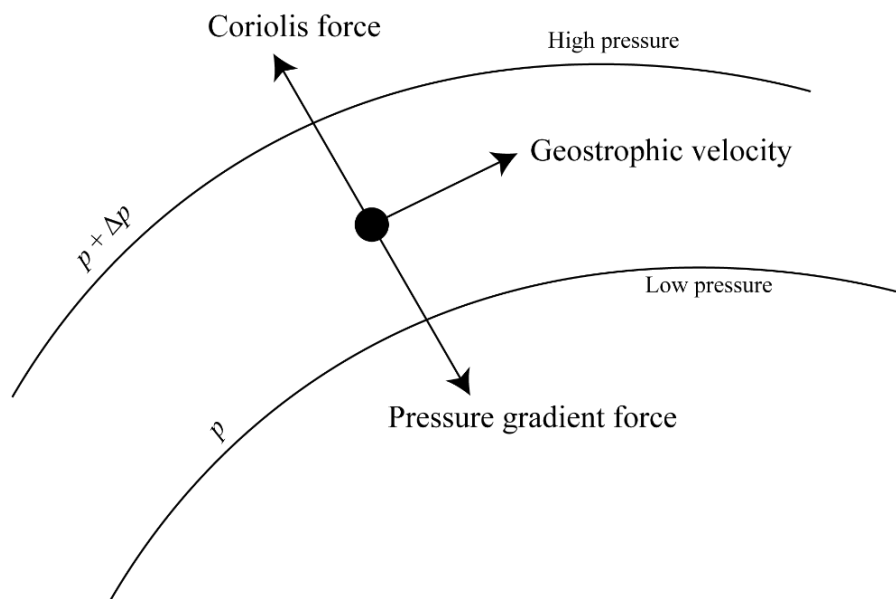


Figure 1. Balanced geostrophic flow in the southern hemisphere

In Figure 1, it can be noticed that the wind direction is parallel to the lines of the constant pressure (isobars). In the geostrophic flow, the Coriolis force and the pressure gradient force are equal in magnitude and opposite in direction. Since the direction of the Coriolis force depends on the hemisphere, the low- and high-pressure regions are oriented regarding the flow direction based on the direction of the Coriolis force. In Figure 1, the Coriolis force is to the left of the geostrophic wind direction, which indicates that the flow is in the southern hemisphere. If the flow was in the northern hemisphere, the Coriolis force would be oriented to the right of the flow direction, and the pressure gradient force would be in the opposite direction to the Coriolis force.

### *Gradient wind*

In the case where the isobars have a significant curvature, the centrifugal force cannot be neglected. The centrifugal force can be calculated as  $U^2/r$ , where  $v$  is the wind velocity and  $r$  is the radius of the curvature of the isobars.

The direction of the centrifugal force is radial and away from the center of the curvature of the isobars. If the airflow is around a high-pressure center, the centrifugal force acts in the same direction as the pressure gradient force and opposite the Coriolis force. This is an anti-cyclone. In contrast, if the airflow is around a low-pressure center, the centrifugal force acts in the direction opposite to the pressure gradient force and in the direction of the Coriolis force. This is a cyclone. The equation of motion of the gradient wind at the constant velocity vector  $U$  is:

$$\frac{U^2}{r} - |f|U + \frac{1}{p_a} \left| \frac{\partial p}{\partial r} \right| = 0, \quad (2.6)$$

$$\frac{U^2}{r} + |f|U - \frac{1}{p_a} \left| \frac{\partial p}{\partial r} \right| = 0, \quad (2.7)$$

where Equation (2.6) is valid for an anti-cyclone, and Equation (2.7) for a cyclone. Both equations apply for both hemispheres.

### *Friction effects*

Near the Earth's surface, friction forces occur between the ground surface and the airflows and are transferred due to the shear stress in the surface layer. These forces appear in the direction opposite to the flow direction, which in the lower regions of the atmosphere point towards the low-pressure region. The balance of the forces in the lower atmosphere is shown in Figure 2.

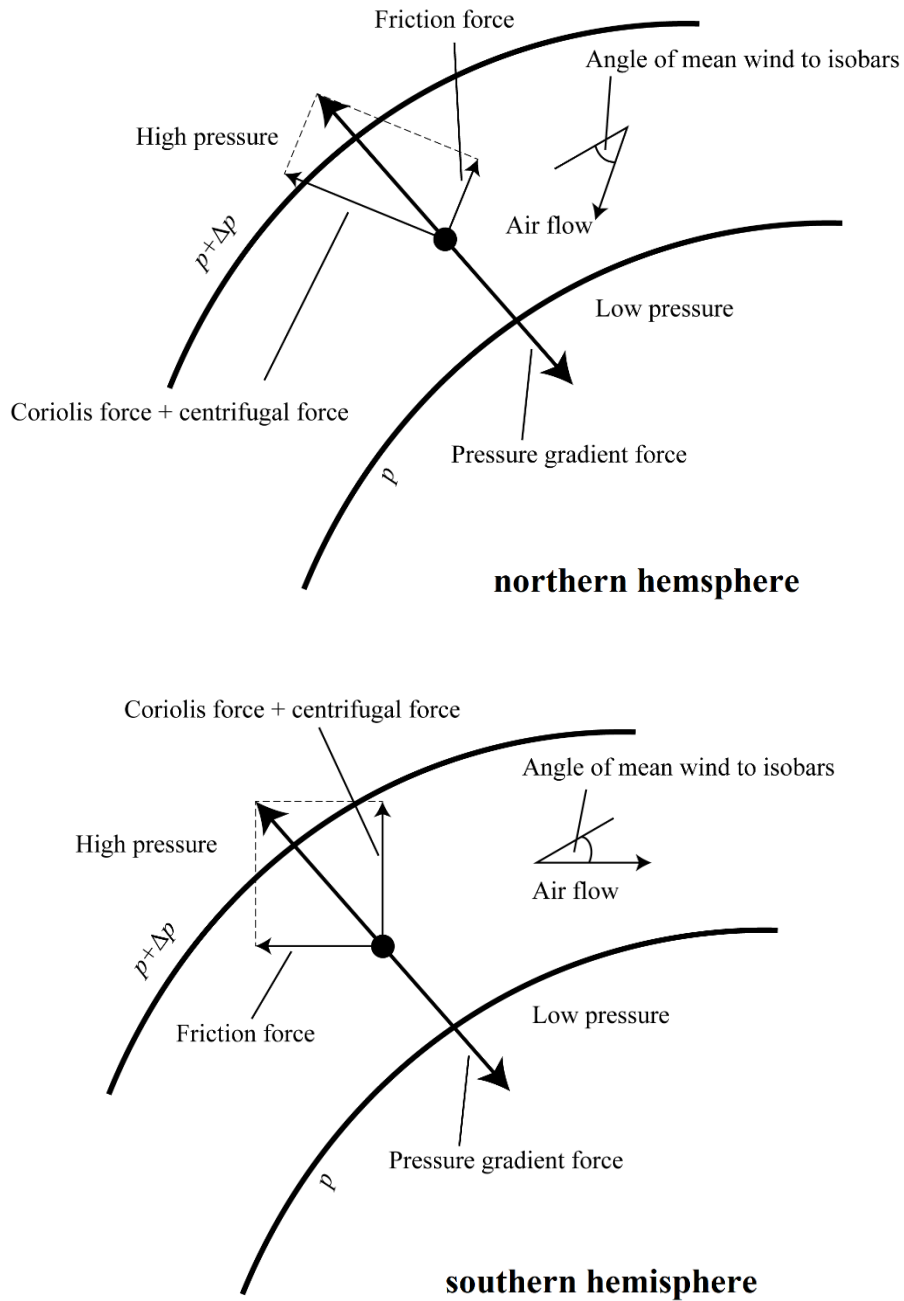


Figure 2. Force balance in the lower ABL

In the higher regions of the atmosphere, friction forces are negligible, and the geostrophic flow is parallel to the isobars. With a decrease in height, the friction force plays a larger role, gradually turning the direction of the flow towards the low-pressure region. This effect is the Ekman spiral, Figure 3. The total angular change of the wind direction may be as much as 30°, Stull [35].

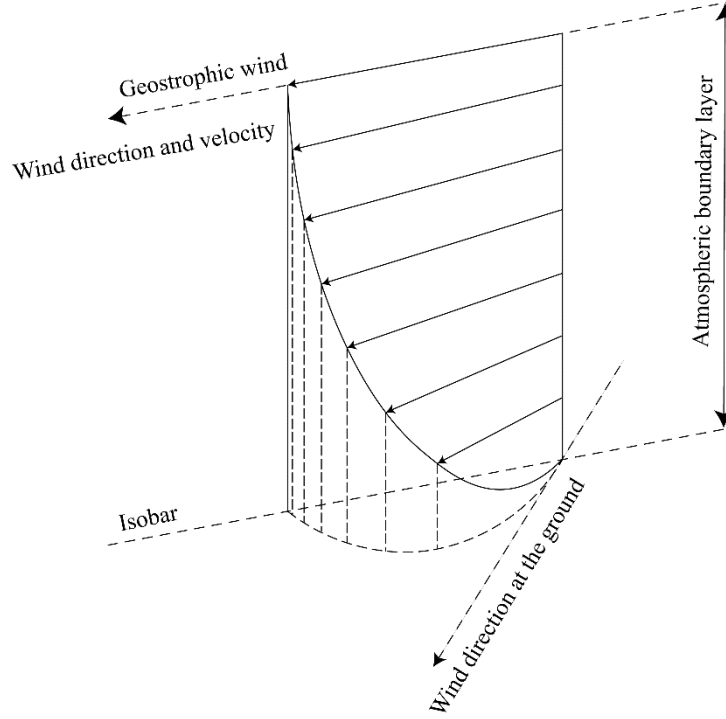


Figure 3. Velocity profile in the ABL considering the Ekman spiral

#### *Governing equations of motion*

Wind motion in the atmosphere is governed by mass conservation and momentum equations along with other equations of friction effects and the Coriolis force. The following set of equations describe the mean wind motion in the ABL:

$$u \frac{\partial u}{\partial x} + v \frac{\partial u}{\partial y} + w \frac{\partial u}{\partial z} + \frac{1}{\rho} \frac{\partial p}{\partial x} - f v - \frac{1}{\rho} \frac{\partial \tau_u}{\partial z} = 0, \quad (2.8)$$

$$u \frac{\partial v}{\partial x} + v \frac{\partial v}{\partial y} + w \frac{\partial v}{\partial z} + \frac{1}{\rho} \frac{\partial p}{\partial y} - f u - \frac{1}{\rho} \frac{\partial \tau_v}{\partial z} = 0, \quad (2.9)$$

$$\frac{1}{\rho} \frac{\partial p}{\partial z} + g = 0, \quad (2.10)$$

$$\frac{\partial u}{\partial x} + \frac{\partial v}{\partial y} + \frac{\partial w}{\partial z} = 0, \quad (2.11)$$

where  $u$ ,  $v$  and  $w$  are the mean velocity components in the  $x$ -,  $y$ -, and  $z$ -direction,  $p$ ,  $\rho$ ,  $f$  and  $g$  are pressure, air density, the Coriolis parameter and the acceleration of gravity, respectively, and  $\tau_u$  and  $\tau_v$  are the shear stress in the  $x$ - and  $y$ -directions, respectively.

## 2.2 Synoptic winds

Aerodynamic loads on tall buildings with porous façades are exerted by atmospheric winds that commonly occur in the lower atmosphere. It is therefore necessary to know these winds in detail. The synoptic ABL wind is balanced by three forces, i.e., the pressure gradient force and the Coriolis force as driving forces, and turbulence stress due to the friction between the airflow and a rough ground surface as the retarding force, e.g., Garratt [36], Cindori et al. [37]. Thermal stratification of the atmosphere commonly plays an important role in air pollution and dispersion in the lower atmosphere at wind speeds lower than 5 m/s. However, this aspect of synoptic winds has not been commonly considered relevant to wind loads on structures, so it is therefore not further addressed in the present study.

The basic parameters of synoptic winds considered relevant for aerodynamic loads on tall buildings are the mean wind velocity, turbulence intensity, integral turbulence length scales representing the mean turbulent eddy size, and the power spectra of wind velocity fluctuations.

### *Mean wind velocity*

Turbulent flow in the atmosphere is characterized by velocity fluctuations. In the Cartesian coordinate system, all three wind velocities can be presented using the Reynolds averaging procedure as the sum of the mean velocity component and the fluctuating velocity component:

$$\begin{aligned} u(t) &= \bar{u} + u'(t), \\ v(t) &= \bar{v} + v'(t), \\ w(t) &= \bar{w} + w'(t), \end{aligned} \tag{2.12}$$

where  $\bar{u}$ ,  $\bar{v}$  and  $\bar{w}$  are the mean velocity components, and  $u'(t)$ ,  $v'(t)$  and  $w'(t)$  are the fluctuating velocity components in the  $x$ -,  $y$ -, and  $z$ -directions, respectively.

The mean velocity component

$$\bar{u} = \frac{1}{T} \int_0^T u(t) dt \tag{2.13}$$

is for the wind velocity in the  $x$ -direction, while the same approach is also valid for the  $\bar{v}$  and  $\bar{w}$  velocity components.



In the surface layer, thus in the lower 10-15% of the ABL, also known as the constant-flux Prandtl layer, the logarithmic law has been commonly used to represent the mean wind velocity profile. It is given as:

$$\frac{\overline{u}_z}{\overline{u}_\tau} = \frac{1}{\kappa} \ln \frac{z - d_{\text{dis}}}{z_0}, \quad (2.14)$$

where  $\overline{u}_z$  is the mean wind velocity at the height  $z$ ,  $\overline{u}_\tau$  is the friction velocity,  $\kappa = 0.4$  is the von Kármán constant,  $z$  is the height from the ground,  $d_{\text{dis}}$  is the displacement height, and  $z_0$  is the aerodynamic surface roughness length.

Friction velocity is given as:

$$\overline{u}_\tau = \sqrt{\frac{\tau}{\rho}}, \quad (2.15)$$

where  $\tau$  is shear stress, and  $\rho$  is air density.

For the boundary layer on a flat plate, Oertel [38] suggested the logarithmic law for the  $z^+ = \frac{z u_\tau}{\nu} > 50$  range, where  $z^+$  is the dimensionless height, and  $\nu$  is the kinematic viscosity. Thuillier and Lappe [39] indicated that the logarithmic law is applicable in the inertial sublayer of the ABL, which extends to a height of  $\sim 100$  m, Garratt [36]. The logarithmic law cannot be considered for heights  $z$  below the displacement height  $d_{\text{dis}}$ .

The empirical power law can be used to represent the mean wind velocity profile throughout the entire ABL, Hellman [40]:

$$\frac{\overline{u}_z}{\overline{u}_{\text{ref}}} = \left( \frac{z - d_{\text{dis}}}{z_{\text{ref}} - d_{\text{dis}}} \right)^\alpha, \quad (2.16)$$

where  $\overline{u}_z$  and  $\overline{u}_{\text{ref}}$  are the mean wind velocity and the mean reference velocity at the reference height  $z_{\text{ref}}$ , respectively. The displacement height  $d_{\text{dis}}$  is used to account for the effect of buildings and other engineering structures on the ground surface. If the displacement height is larger than zero, the velocity profile starts above the height  $d_{\text{dis}}$ . Since the displacement height cannot be determined precisely, it is commonly taken as 75% or 100% of the height of the engineering structures or natural formations (forests, rocks, etc.) situated on the ground surface, Holmes [22].  $\alpha$  is the power-law exponent that depends on the aerodynamic surface roughness length  $z_0$ . The common values of  $z_0$  are presented in Table 1.

Table 1. Terrain types and aerodynamic surface roughness length, Holmes [22]

Terrain type	Aerodynamic surface roughness length, m
Very flat terrain (snow, desert)	0.001 - 0.005
Open terrain (grassland, few trees)	0.01 - 0.05
Suburban terrain (3 - 5 m high buildings)	0.1 - 0.5
Dense urban terrain (10 - 30 m high buildings)	1 - 5

### *Turbulence intensity*

Turbulence intensity is an integral parameter used to account for the turbulence in the atmosphere:

$$I_u(z) = \frac{\sqrt{u'^2(z)}}{u_{\text{ref}}}, \quad I_v(z) = \frac{\sqrt{v'^2(z)}}{u_{\text{ref}}}, \quad I_w(z) = \frac{\sqrt{w'^2(z)}}{u_{\text{ref}}}, \quad (1.17)$$

where  $I_u$ ,  $I_v$  and  $I_z$  are the turbulence intensity in the  $x$ -,  $y$ -, and  $z$ -direction, respectively.  $u_{\text{ref}}$  is the wind velocity in the  $x$ -direction at the reference height  $z_{\text{ref}}$ .

The turbulence intensity in the main flow direction is greater than in the lateral and vertical directions, e.g., Counihan [41]:

$$\frac{I_v}{I_u} = 0.75, \quad \frac{I_w}{I_u} = 0.50. \quad (2.18)$$

Another equation for  $I_u$  was suggested by Holmes [22]:

$$I_u = \frac{2.5u_\tau}{0.4 \ln\left(\frac{z}{z_0}\right)} = \frac{1}{\ln\left(\frac{z}{z_0}\right)}, \quad (2.19)$$

where

$$I_v \approx \frac{0.88}{\ln\left(\frac{z}{z_0}\right)}, \quad I_w \approx \frac{0.55}{\ln\left(\frac{z}{z_0}\right)}. \quad (2.20)$$

### *Integral turbulence length scale*

Turbulence can be accounted for as a group of eddies moving at the mean velocity of the flow, Taylor [42]. Each eddy at a given point causes a periodic pulsation of an angular frequency of  $\omega = 2\pi f$ , where  $f$  is the frequency. Therefore, the wavelength of an eddy can be described as  $\lambda = \bar{u}/f$ , and it represents the eddy size. The measure of an average eddy size is the integral length scale of turbulence.

Considering that there are three turbulent velocities and three eddy dimensions in turbulent flow, there are nine integral length scales of turbulence. For example,  $L_{u,x}$ ,  $L_{u,y}$  and  $L_{u,z}$  represent the average eddy size in the longitudinal, transversal, and vertical direction ( $x$ ,  $y$ , and  $z$ ) caused by the velocity fluctuations in the longitudinal direction ( $u'$ ).

The integral length scale of turbulence is:

$$L_{u,x} = \int_0^{\infty} R_{u,x}(\Delta x) d\Delta x, \quad (2.21)$$

with

$$R_{u,x}(\Delta x) = \frac{\overline{u'_1(t) \cdot u'_2(t)}}{\sqrt{\overline{u'^2_1}} \cdot \sqrt{\overline{u'^2_2}}}, \quad (2.22)$$

where the indices 1 and 2 represent two points in space. Equation (2.21) is for the integral length scale of turbulence caused by the longitudinal turbulence for the eddy size in the longitudinal direction.

Equations (2.21) and (2.22) can be transformed into the time domain using the Taylor hypothesis of frozen turbulence, Taylor [42], which indicates that all pulsations of velocity move with the mean velocity of the main fluid stream, i.e., all eddies have the mean velocity of the main fluid flow:

$$L_{u,x} = \int_0^{\infty} R_{u,x}(\Delta t) d\Delta t, \quad (2.23)$$

$$R_{u,x}(\Delta t) = \frac{\overline{u_1'(t) \cdot u_1'(t - \Delta t)}}{\overline{u_1'^2}}, \quad (2.24)$$

where  $\Delta t = \Delta x / \bar{u}$ .

#### *Power spectral density of wind velocity fluctuations*

The turbulent pulsations of a fluid flow are created by the superposition of eddies of various sizes. Therefore, the total kinetic energy of the turbulent flow is the result of the summation of the turbulence kinetic energy of all eddies. Consequently, the power spectral density of turbulence kinetic energy exhibits its distribution across the wavelengths of eddies. The power spectral density of longitudinal velocity fluctuations is

$$\overline{u'^2} = \int_0^{\infty} S_u(f) df, \quad (2.25)$$

where  $S_u(f)$  is the power spectral density of the longitudinal velocity fluctuations. In a fluid flow near the surface, large eddies develop. The large eddies then dissolve into smaller ones, with energy transported from the large to the smaller eddies. The process continues until the eddies are small enough for their kinetic energy to be dissipated into heat. This process is called the energy cascade, Figure 4.

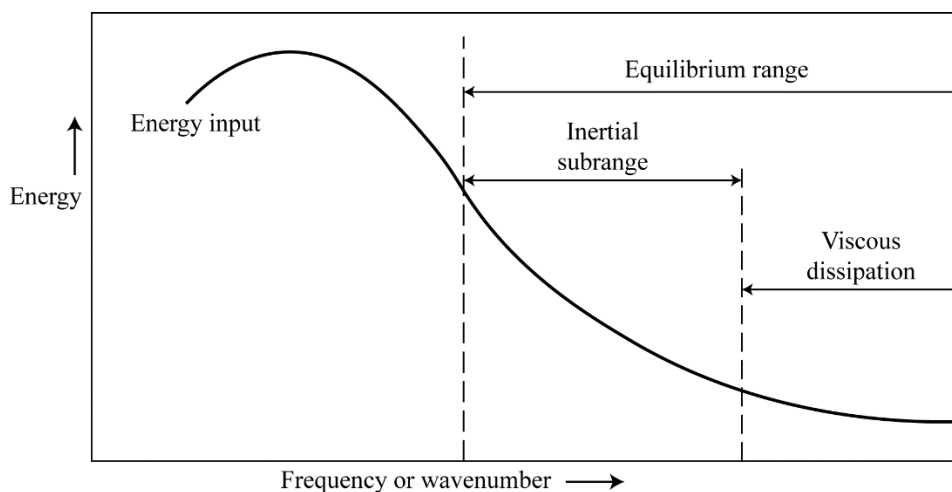


Figure 4. Schematic view of the energy cascade process

The highest energy is not contained in the largest eddies, but in slightly smaller ones, Figure 4. There are two distinct ranges in the energy cascade, i.e., the inertial subrange and the viscous dissipation range. In the inertial subrange, inertial forces dominate the flow. Plotting the energy cascade in the logarithmic scale yields a straight line with a  $-2/3$  slope. A comparison of two ABL simulations (rural and suburban) created in the present experiments with von Kármán design curves [43] in the rural (Cat. I) and suburban (Cat. III) Eurocode [44] terrains are shown in Figure 5.

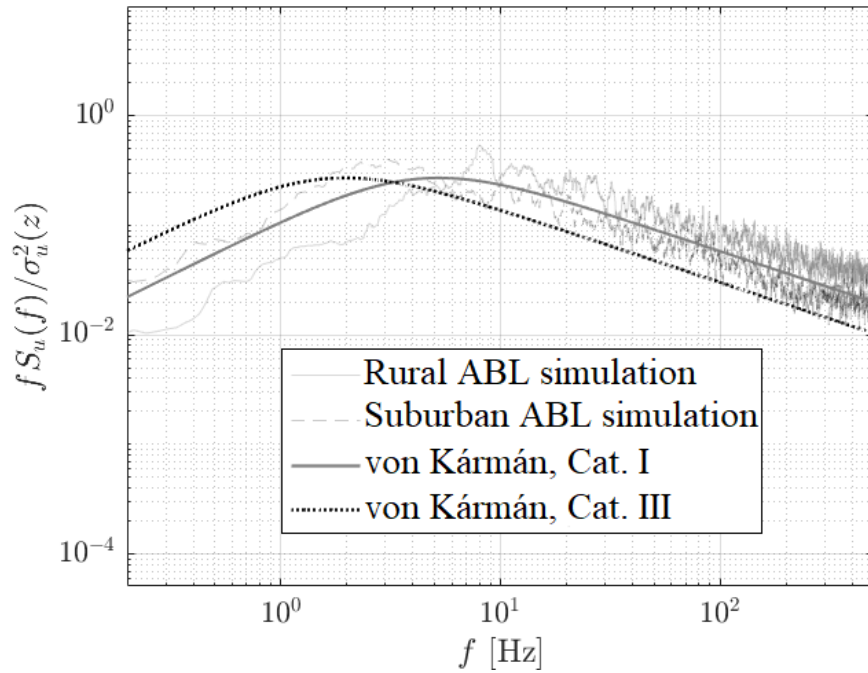


Figure 5. Comparison of von Kármán design curves with the present experimental results of the power spectral density of longitudinal flow velocity fluctuations

The slope is in agreement with the Kolmogorov [45] model:

$$S_u(f) \approx k_w^{-2/3}, \quad (2.26)$$

where  $k_w$  is the wave number.

### *Reynolds shear stress*

The friction force between the ground surface and the air is driven by shear stress. Shear stress is comprised of viscous and turbulent stress, e.g., Nakayama [46]:

$$\tau = \mu \frac{\partial \bar{u}}{\partial z} - \overline{\rho u' w'}. \quad (2.27)$$

Viscous stress  $\mu \frac{\partial \bar{u}}{\partial z}$  reaches a maximum on the surface and decreases rapidly with the increase in height. In the inertial sublayer, viscous forces are negligibly small, Figure 6.

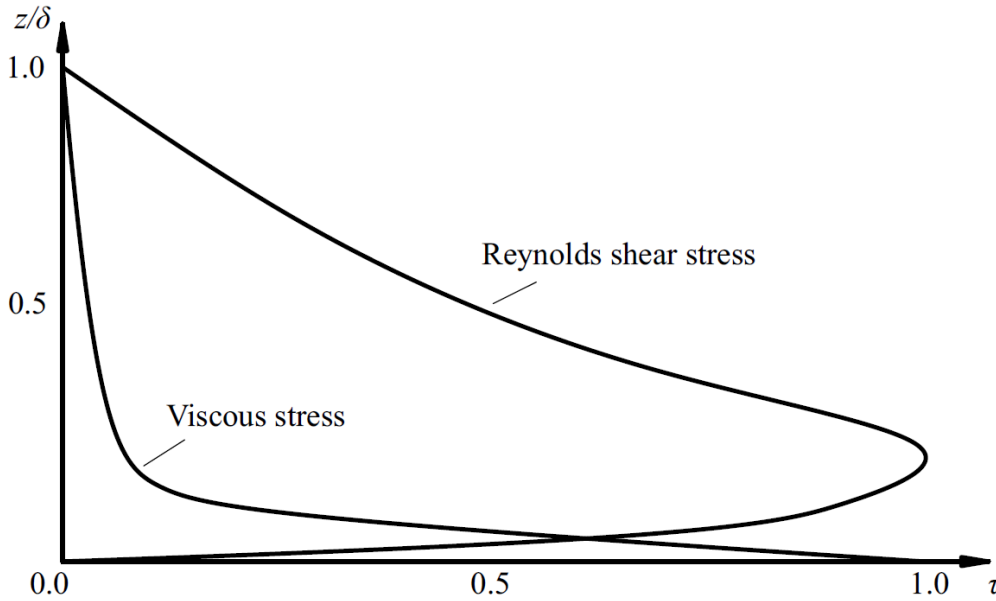


Figure 6. Shear stress in the ABL

Reynolds shear stress  $\overline{\rho u'w'}$  is zero on the ground surface. It increases strongly and remains nearly constant throughout the inertial (constant-flux) sublayer, i.e., surface layer. With a further increase in height, Reynolds shear stress decreases to zero. Reynolds shear stress components  $\overline{\rho u'v'}$ , and  $\overline{\rho v'w'}$  are substantially smaller than  $\overline{\rho u'w'}$ , so they are commonly neglected. Turbulent shear stress is defined as:

$$\tau = -\overline{\rho u'w'} = \rho u_\tau^2 (1 - z/z_{\text{ref}})^2, \quad (2.28)$$

where  $u_\tau$  is friction velocity, and  $z/z_{\text{ref}}$  is the reduced height from the ground.

## 2.3 Non-synoptic winds

ABL recommendations for tall buildings are provided in major international wind engineering standards and codes. However, these characteristics are provided only in the context of tall buildings with smooth façades, while aerodynamic loads acting on tall buildings with porous façades, not to mention tall buildings subjected to strong local winds, have still not been properly addressed. The precise characteristics of some local and unique winds are still unknown, so further work is required to entirely elucidate the characteristics of such winds and to make them available in a form suitable for engineering applications, also with respect to tall buildings with porous façades. Some of these winds are hurricanes and tornadoes and are

surveyed here because of their disastrous effects on engineering infrastructure. The origins and characteristics of downslope windstorms and downbursts are also briefly outlined.

A hurricane is a large rotating mass of air that forms over the Atlantic Ocean in areas where the sea surface temperature exceeds  $26.5^{\circ}\text{C}$ , Ho et al. [47]. It is of a spiral shape, rotating counterclockwise in the northern hemisphere and clockwise in the southern hemisphere. The center of hurricanes is characterized by calm air and is usually known as the eye of the hurricane, with the highest wind velocity close to the eyewall, Montgomery and Smith [48]. The size of the hurricane can vary in an order of magnitude between 100 km and 1000 km, without a clear link between the hurricane size and its maximum wind velocity, Emanuel [49]. Hurricanes are classified in five categories based on their mean wind velocities, i.e., the Saffir-Simpson hurricane wind scale, Simiu et al. [50]. In addition to strong winds, another important hurricane issue is the surge that causes massive infrastructural damage and loss of life. For example, in one hurricane season alone, from August to October 2004, the US reported insured hurricane losses of ~ USD 20 billion, while hurricane Andrew alone caused USD 30 billion in infrastructural damage, Leatherman [51]. Tropical storms similar to hurricanes occur both in the Northern Indian Ocean – cyclones, and in the Western Pacific Ocean – typhoons, Chan [52].

A tornado is another rapidly rotating mass of air, occurring as waterspouts or landspouts. Its size, however, is much smaller than that of a hurricane, usually less than 100 m in diameter. The maximum wind velocity for most tornadoes is ~150 km/h, Fujita [53]. Depending on the temperature and air moisture, a tornado can last from a few minutes to over an hour. It usually appears in the US (Tornado Alley) causing substantial structural damage. However, due to its relatively small size, it causes less damage than a hurricane, Changnon [54], Kikitsu and Sarkar [55].

A downburst is created by a column of sinking air that spreads radially in all directions upon impinging on the ground. It may develop as a microburst, where the wind extends radially for less than 4 km, and a macroburst, where the wind exceeds 4 km in a horizontal direction, Fujita [56]. A downburst can create a hazard for aircraft, with gusts reaching velocities of more than ~20 m/s, Holmes and Oliver [57]. The pressure increases near the center of the downburst due to the downdraft, while alternating high- and low-pressure rings develop around the high-pressure center.

Santa Ana is a dry downslope wind in Southern California and in the Northern Baja California region, Hughes and Hall [58]. It is driven by the pressure gradient between the high-pressure area of Inland California and the low-pressure area over the Pacific Ocean. This pressure gradient drives the synoptic wind towards the coast, where the wind blows through the mountain passes of Southern California, Sommers [59]. The wind ultimately reaches Los Angeles, CA, causing substantial wind loads on tall buildings. Santa Ana usually occurs

between September and April, fanning wildfires in that period, Fovell and Cao [60]. The Santa Ana wind speed can exceed 14 m/s, Guzman-Morales et al. [61].

The Bora is a downslope wind on the eastern Adriatic Coast and many other climatologically similar regions around the world, e.g., Lepri et al. [62], [63], [64]. It usually originates in the mountainous regions of Croatia, with cold air rolling towards the coast. It is common in winter when it may last from a few hours to several days. One of its main characteristics is its gustiness, with mean velocities rarely exceeding 20 m/s, while wind gusts may reach hurricane speeds of  $\sim 70$  m/s, Grisogono and Belušić [65]. This causes substantial difficulties in traffic, Kozmar et al. [66], complex wind flow, and turbulence on wind farms, Kozmar et al. [67], the collapse of electricity poles, and other structural damage. Building failures rarely occur because the buildings in coastal Croatia are designed to withstand Bora gusts with their low roof height and concrete structure.

The Zonda is a strong, warm, and dry downslope wind that occurs in subtropical latitudes of South America, Loredou-Souza et al. [68]. The Andes, rising to 4000 m, block the cold and wet air blowing from the Pacific Ocean. However, occasionally the air can rise and cross the mountains and descend onto the Eastern Andes, developing as the Zonda wind, Antico et al. [69]. Like the Bora, the Zonda is known to cause damage to power lines, topple trees, and overturn vehicles. The velocity of Zonda gusts may exceed 25 m/s, Puliafito et al. [70], Loredou-Souza et al. [68].

The Foehn is a warm and dry wind that descends in the lee of the European Alps. Although its name originates in the Alps, the term Foehn is used as a generic name for any warm and dry downslope wind, such as the Zonda in the Andes, the Chinook in the Rocky Mountains, and the South and North Foehn in the Alps. It is caused by warm air crossing mountain ranges, increasing in velocity during its descent, with gusts reaching 50 m/s, Hoinka [71]. The velocity of the Foehn may be further amplified in mountain valleys, Burlando et al. [72]. Along with severe gusts that can damage infrastructure, the Foehn causes a rise in temperature, thus enhancing the melting of snow. In the context of climate change, the Foehn is particularly critical in Antarctica because its higher-than-normal temperature leads to the melting of polar ice, Speirs et al. [73], Cape et al. [74].

Based on this overview of various wind types, two major wind characteristics are considered relevant to the aerodynamic characteristics of tall buildings – wind gustiness and turbulence, and its mean velocity. Strong wind gusts may cause extreme bending of buildings, while high mean wind velocity may enhance vortex shedding, thus potentially matching the resonance frequency of the building which can cause the swaying of the building in the lateral direction, i.e., perpendicularly to the main wind direction. Both these phenomena may substantially lessen the aerodynamic performance of tall buildings. Given that most tall



buildings are in cities where complex urban flows occur, a survey of characteristic aerodynamic loads is necessary for the successful design of tall buildings.

### 3 Bluff body aerodynamics

Structures can be bluff or streamlined depending on their shape and the fluid flow in their vicinity. Streamlined bodies are usually structures such as aircraft wings or propeller blades. The airflow around them is characterized by streamlines which follow the contours of the body, Figure 7. The freestream flow is separated on the leading edge of the airfoil in two pathways around the airfoil, with the characteristic boundary layer near the surface that develops due to viscous forces.

In contrast, flow separation on sharp leading edges dominates the flow on bluff bodies. In the height range between the separated flow and the freestream flow there is a free shear layer, which is a thin region of high shear and vorticity. Eddies are shed intermittently from both lateral surfaces of the bluff body, which may lead to excessive vibration of the body in the direction perpendicular to the freestream flow.

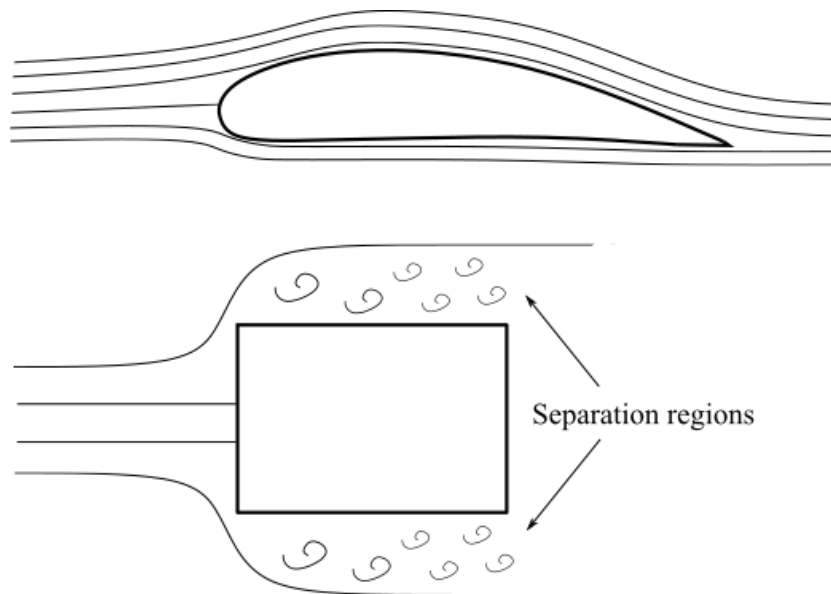


Figure 7. Airflow around streamlined and bluff bodies

The non-dimensional pressure coefficient on the surface of the body is:

$$C_p = \frac{p - p_0}{\frac{1}{2}\rho u_0^2}. \quad (3.1)$$

The maximum  $C_p = 1.0$  is achieved in the stagnation point where  $u = 0$ . For every other case,  $C_p < 1.0$ , while  $C_p$  can also be negative (suction) with an absolute magnitude greater than 1.0.

Force coefficients are defined in a reduced form:

$$C_F = \frac{F_a}{\frac{1}{2} \rho u_0^2 A}, \quad (3.2)$$

where  $F_a$  is the aerodynamic force per unit length, and  $A$  is the reference area.

Aerodynamic forces are commonly addressed as the across-wind component and the along-wind component with respect to the main flow direction. In aeronautics, the terms “lift” and “drag” are commonly used, which correspond to the “across-wind force” and “along-wind force” in wind engineering. The across- and along-wind coordinate axes are aligned relative to the flow direction, while the body axes  $F_x$  and  $F_y$  are aligned relative to the main axes of the body, usually width and length. The wind-direction axes and body axes can be at an angle, which is the angle of attack in aeronautics, and flow incidence angle in wind engineering, Figure 8.

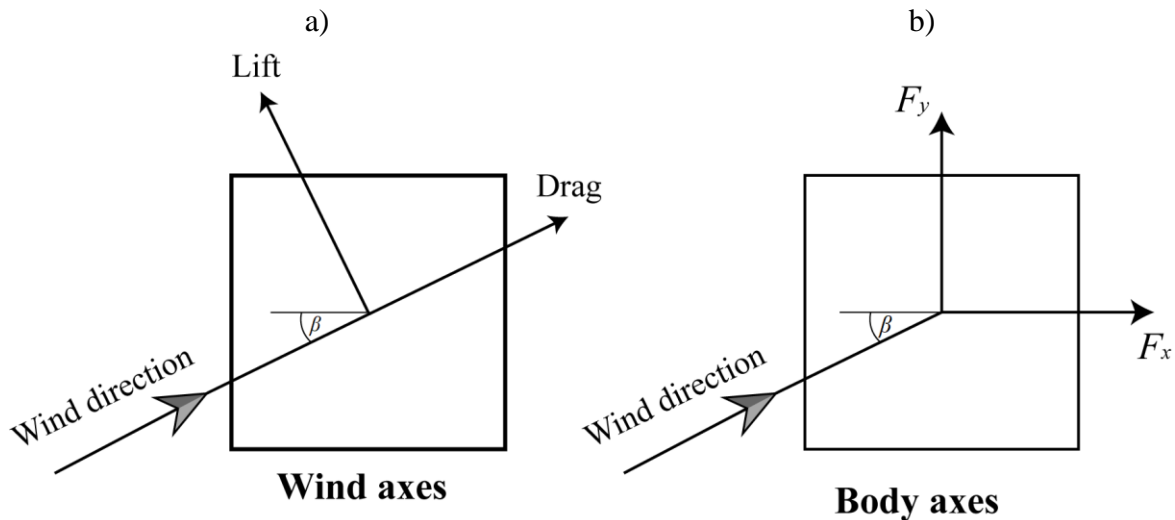


Figure 8. a) Wind axes and b) body axes

Regarding the aerodynamic characteristics of tall buildings, an important parameter is the aerodynamic moment coefficient, which primarily acts on the base of the building. It is defined similarly to the force coefficient. The difference is only that the force coefficient is calculated using the characteristic area, while the moment coefficient is calculated using the characteristic area multiplied by the height of the body  $h$ :

$$C_M = \frac{F_a}{\frac{1}{2}\rho u_0^2 Ah}. \quad (3.3)$$

Substituting the aerodynamic force  $F_a$  with the across-wind force  $F_L$  and along-wind force  $F_D$ , the across-wind moment  $C_{ML}$  and along-wind moment  $C_{MD}$  are:

$$C_{ML} = \frac{F_L}{\frac{1}{2}\rho u_0^2 Ah}, \quad C_{MD} = \frac{F_D}{\frac{1}{2}\rho u_0^2 Ah}. \quad (3.4)$$

### 3.1 Boundary layer flows

Although the air has relatively small viscosity compared to some other fluids, its viscosity nevertheless plays an important role in the boundary layer. It is proven experimentally that the air adheres to solid surfaces, the “no slip condition”. This causes the velocity of air on the surface to be zero. The viscosity of the air yields a decrease of the velocity from the maximum in the freestream to zero on the surface. This thin region near the surface is the boundary layer.

The airflow inherently exhibits both inertial and viscous effects. The ratio of inertial to viscous forces is expressed by the dimensionless Reynolds number:

$$Re = \frac{\rho u L}{\mu} = \frac{u L}{\nu}, \quad (3.5)$$

where  $\rho$  is the fluid density,  $u$  is the fluid velocity,  $L$  is the surface dimension, and  $\mu$  and  $\nu$  are the dynamic and kinematic viscosity, respectively.

Considering Equation (3.5), a large  $Re$  corresponds to large inertial forces, while a smaller  $Re$  corresponds to large viscous forces. It should be noted that the calculation of  $Re$  is in some ways arbitrary, since  $L$  is selected depending on the focus of the experiment or simulation. In the case of bluff body aerodynamics, the length  $L$  is commonly selected as the representative dimension of the body (width, length or height).

If the fluid particles in the boundary layer are decelerated so much that the flow near the surface becomes reversed, a boundary layer separation occurs, Figure 9. Such deceleration is caused by adverse pressure gradients, which are the effect, for example, of flow over the corners of a bluff body or over highly curved surfaces. The shed vortices can cause large suction near the separation point.

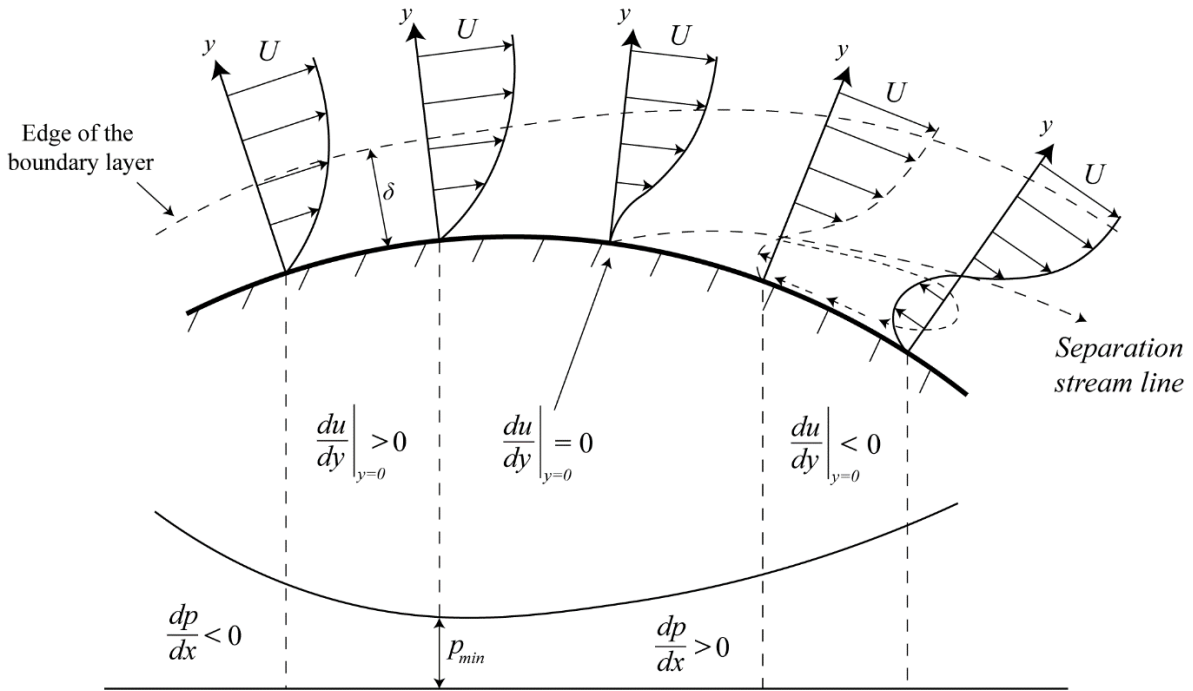


Figure 9. Flow separation

The  $Re$  can vary greatly, ranging from  $\sim 0$  to as high as  $10^8$  and  $10^9$ . The increase in the  $Re$  causes various flow phenomena. One of the most notable  $Re$  effects is the transition from laminar to turbulent flow. When the  $Re$  is small, the momentum transfer occurs at the molecular level through fluid viscosity rather than on the macroscopic scale. In this case, the boundary layer is considered laminar. However, for a large  $Re$ , the dominant momentum transfer is through the turbulent motion between the adjacent layers of fluid. This type of turbulent flow is common on tall buildings subjected to the ABL.

### 3.2 Separated shear flows

Considering a flat plate of length  $L$  perpendicular to a two-dimensional flow, at a very low  $Re < 1$ , the flow turns sharply around the edges of the plate and follows the contours of the plate. As the  $Re$  increases, the flow is not capable of following the contours of the plate, and consequently two symmetric vortices form in the lee of the plate and remain attached to the plate. Increasing the  $Re$  further, the symmetrical vortices shed from the plate in an alternating fashion, forming the von Kármán vortex street. The alternating vortex shedding can cause large suction on both surfaces of the body which can be detrimental to the stability of large engineering structures, including tall buildings, if the vortex shedding occurs at the natural frequency of structures. For an even larger  $Re$ , the inertial forces become dominant, and a turbulent wake

shapes up with a “shear layer” of small eddies in the space between the wake and the freestream flow.

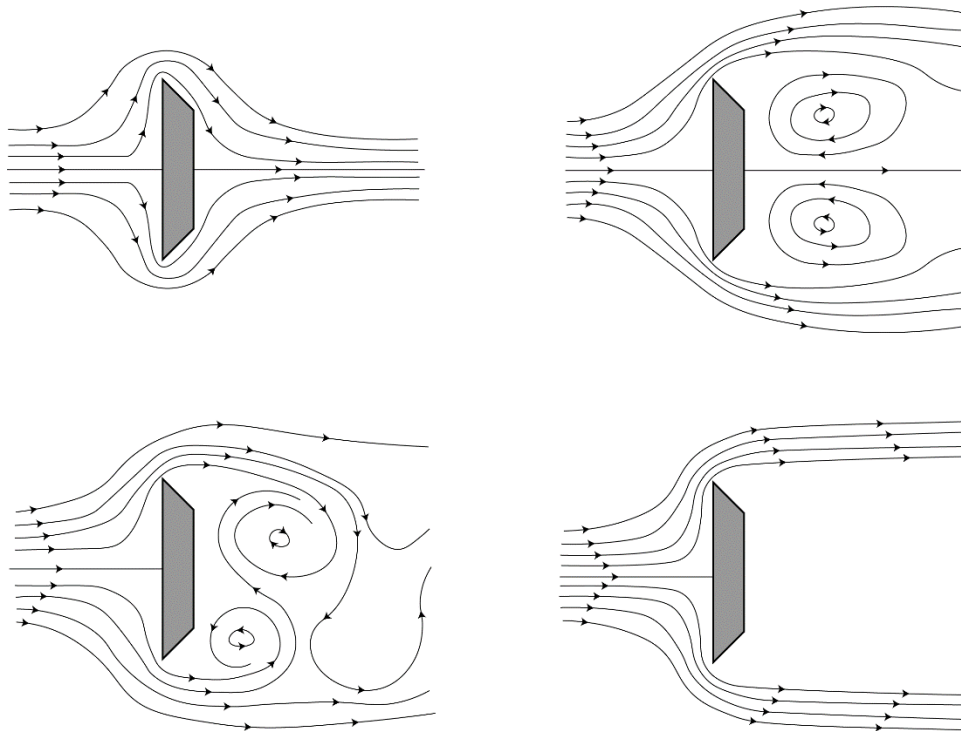


Figure 10. Flow around a flat plate perpendicular to the flow

Although the flow regime is dependent on the  $Re$ , it is important to note that in the flow around bluff bodies, like the flat plate, the vortices always shed at the sharp edges. However, around streamlined bodies, such as a circular cylinder, the location of vortex shedding changes with the  $Re$ . This creates challenges in wind-tunnel experiments, since the  $Re$  cannot be completely scaled from the prototype to the model due to the large size differences.

Considering a wall-mounted cube in a turbulent boundary layer, as an underlying case preceding a tall building in the ABL, the flow behavior is influenced by several factors, including the size and orientation of the cube and the characteristics of the boundary layer. For example, at  $\beta = 0^\circ$ , the flow impinges on the cube windward surface exhibited with a characteristic stagnation zone. This is the point with the highest positive pressure on the cube surface. The flow is stopped, converting the most energy into surface pressure, and the rest of the flow is diverted around the cube, Figure 10.

Separation bubbles occur downstream of the leading body edges. There are recirculation zones of the separated flow on the top and lateral body surfaces accompanied by the suction on the top, lateral, and leeward cube surfaces. Further downstream of the flow separation point, the flow may eventually reattach to the cube surfaces if the body is long enough in the flow direction. The reattachment is dependent on the  $Re$  and the size of the cube, i.e., if the  $Re$  and

the cube are small, it is possible for no reattachment to occur since the separation bubble is in this case larger than the cube. Rectangular cylinders with a longer dimension in the direction of the flow are a good example of flow separation and reattachment phenomena, Figure 11.

The leeward surface is entirely in the wake which causes relatively uniform suction across the entire leeward cube surface. The von Kármán vortex street [26] appears further downstream, caused by oscillations in the pressure field of the flow around the cube.

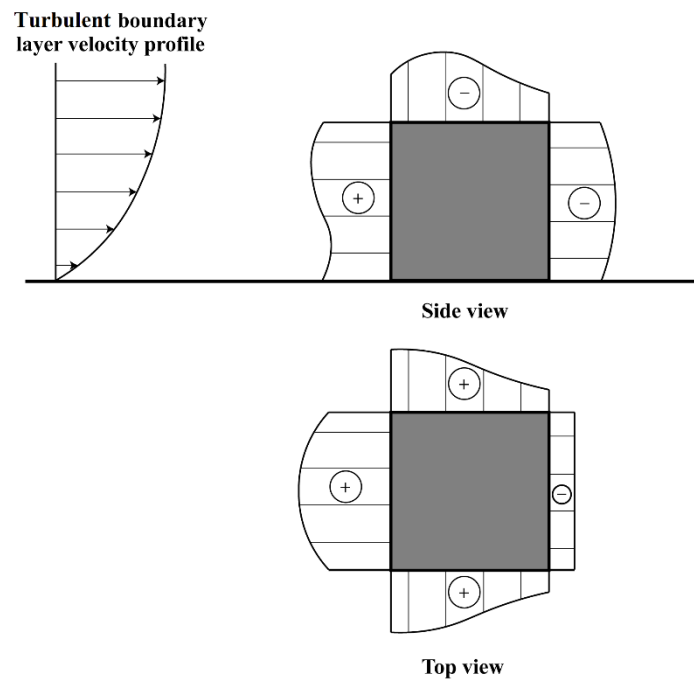


Figure 11. Schematic view of the cube surface pressure in the turbulent boundary layer flow

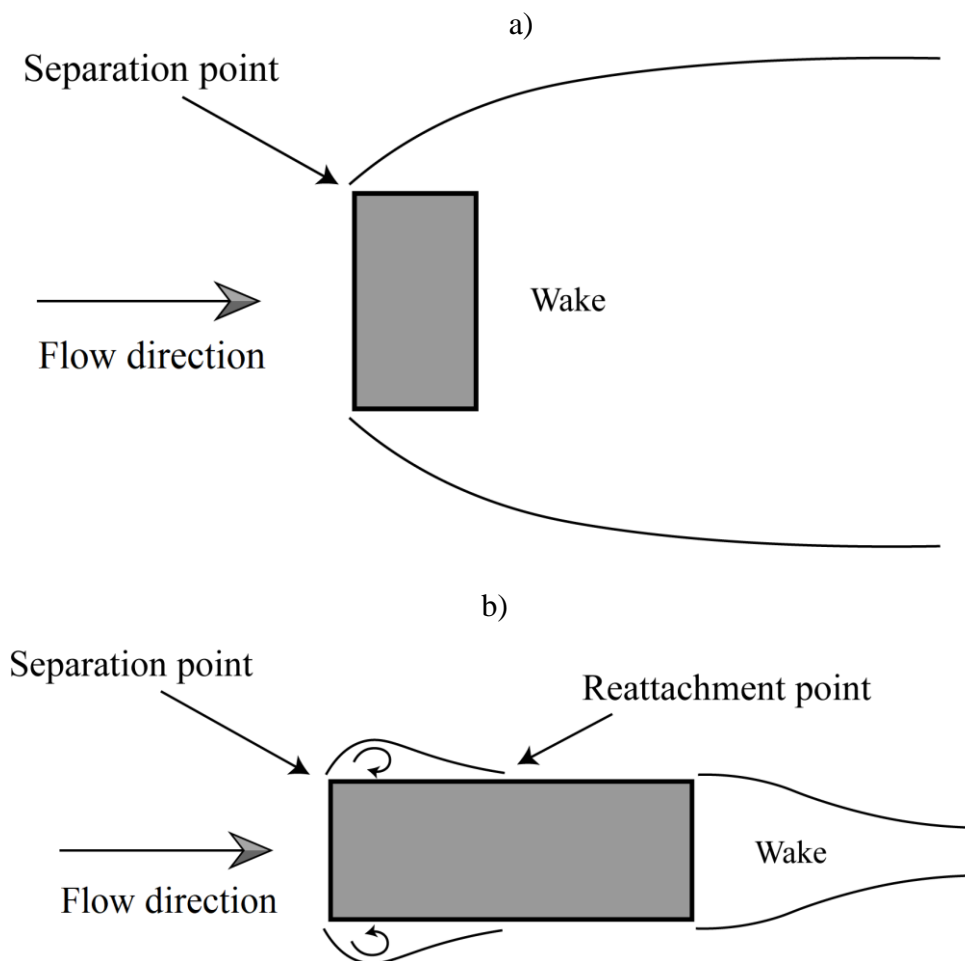


Figure 12. Schematic view of the flow reattachment on a) a cube and b) a rectangular cylinder

## 4 Tall building aerodynamics

### 4.1 Aerodynamic loads on buildings

Tall buildings with PDSF systems are essentially tall buildings with increased aerodynamic complexity. It can be expected that such buildings with PDSF systems will experience similar aerodynamic effects to those on tall buildings with smooth surfaces, i.e., excessive motion or vibration, so it is important to be aware of various vibration mitigation techniques utilized in current tall buildings. For this reason, an overview of the aerodynamic characteristics of tall buildings with smooth surfaces is presented along with some commonly used vibration mitigation techniques using examples of some of the tallest and most slender buildings in the world.

From the aerodynamics point of view, high-rise buildings are essentially bluff bodies, sharp or round cornered, with their height much greater than their width and length. With an increase in the height to base ratio, i.e., slenderness, a building becomes more susceptible to wind loads.

Two main challenges were identified when considering wind loads on tall buildings. The first is the serviceability problem regarding excessive motion of the top of the buildings because of the wind-induced vibration. Another important issue is damage due to cladding because of wind pressure and flying debris, Holmes [22]. These aspects previously observed on tall buildings with smooth façades are expected to additionally gain in complexity in tall buildings with porous façades.

Tall buildings are aerodynamically affected by atmospheric winds characterized by changing wind properties at various heights of the buildings. For a building subjected to the ABL, the stagnation point on the windward building surface with a rectangular base is located at ~70 to 80% of the building height, Baines [75]. Strong downward wind motion occurs below the stagnation point, which is detrimental to pedestrian wind comfort.

As is commonly the case with all bluff bodies, flow separates at the leading building corners, generating strong vortices and a pressure drop on the building surface parallel to the main wind direction. There is nearly uniform suction on the leeward building surface with usually ~50% of the pressure magnitude observed on the windward building surface. Unlike the mean surface pressure, peak pressures may occur on various building surface sections lasting only for short periods of time and they are difficult to predict. The peak minimum and maximum pressure fluctuations may be four times greater than the pressure standard deviation, Davenport [76], often indicating the non-Gaussian probability density of pressure fluctuations, Dalgleish [77], Peterka and Cermak [78].

## 4.2 Building vibration mitigation

Various vibration mitigation techniques have been implemented in contemporary high-rise buildings to reduce building motion and aerodynamic loads, Kareem [79]. The findings observed on smooth building surfaces are likely to be relevant for buildings with PDSF systems as well. By rounding the corners, the effect of drag force reduction at a critical  $Re$  can be achieved. Although there are several approaches to the corner design of buildings, such as chamfering or recessing, rounding the corners has proved to be an effective method to reduce the vibration amplitude with an increase in the corner radius, Kawai [80].

Another possibility is to increase the number of building surfaces, i.e., designing a building with a circular-shaped base without curved outer surfaces, Kim et al. [81]. The overturning and torsional moment coefficients decrease with the increase in the number of building surfaces. However, this trend is less exhibited in buildings with more than five building surfaces.



Buildings with a helical-shaped base have proved not to have a great impact on the overturning and torsional moments compared to buildings with straight-side surfaces. Nevertheless, the building shape influences the power spectra of across-wind forces in such a way that a greater aspect ratio yields higher peak frequency and magnitude. A small base aspect ratio, e.g., 1/3 to 2/3, tends to narrow the spectral peak with the peak frequencies remaining approximately the same, while the peak magnitude increases with the increase in the base aspect ratio. The secondary peak at higher frequencies may appear because of the flow re-attachment. Corner modifications in the form of chamfering, rounding, or recessing generally tend to have a favorable effect by causing a decrease in the peak magnitude of the across-wind force spectra, Gu and Quan [82].

Tapered and setback buildings are characterized by a significant decrease in the across-wind load compared to rectangular buildings. The reason is the altered frequency of vortex shedding, which occurs at nearly the same frequency along the entire height of a rectangular building, while in tapered and setback buildings, the vortices are shed at various frequencies along the building height, Tanaka et al. [73].

Kwok [84], Kwok et al. [85], Tamura et al. [86] showed that chamfering the building edges reduces wind-induced motion. Hayashida and Iwasa [87] concluded that building damping is likely due to the cross-section shape. Zhang et al. [88] proved that double and single recessions reduce wind loads, where a 7.5% recession ratio proved to be the most effective. Tse et al. [89] indicated that a recessed corner is more effective at small modification lengths. Tapered buildings proved to have smaller overturning moments, drag, and lift forces, e.g., Kim and You [90], Kim et al. [91], [92], Kim and Kanda [93]. In cases where the slenderness of the building is too great, aerodynamic modifications are not sufficient to reduce the building response to an acceptable level. In this case, tuned mass dampers are used, usually at the top of the building, to decrease its motion by shifting its mass distribution, e.g., Wang et al. [94].

These comprehensive findings on mitigating the motion of tall buildings have over the years been applied in the design of currently the tallest buildings in the world. These case studies are briefly reviewed here because their aerodynamic performance will be relevant when studying tall buildings equipped with porous façades.

Burj Khalifa, currently the tallest building in the world at a height of 829.8 m, utilizes a setback design to minimize wind-induced vibration, Figure 13a. The building has a star-shaped cross section and many setbacks, which causes changes in the characteristic frequency of vortex shedding at various building heights, thus improving its aerodynamic stability. Along with setbacks, a spiral pattern was used to make the building cross-section non uniform, Irwin [95]. Vortex shedding therefore cannot occur concurrently along the entire building height, thus yielding reduced adverse periodic building oscillations. With these passive damping

techniques, the building motion was successfully reduced, thus making active damping systems unnecessary on Burj Khalifa.

The 432 Park Avenue building in New York City is an example of a different design approach, Figure 13b. The building is shaped as a rectangular prism, at a height of 426 m, and where the side length of the square base is 28.5 m. These dimensions result in an aspect ratio of almost 1:15, thus making this building one of the slenderest in the world. This building is designed to be maximally stiff, with a concrete cylindrical tube of 9 m in diameter as its core. The wall thickness of the core varies from 760 mm at the base to 300 mm at the top. The only passive modification made to reduce wind-induced vibrations is partial openings created in the building frame by removing the windows by the height of two floors every 12<sup>th</sup> floor, thereby causing vortex shedding to occur at different frequencies at various heights, which is favorable for the dynamic stability of the building. However, these modifications were not sufficient to reduce the building motion below the acceptable limit, so two tuned mass dampers, weighing 1300 tons each, were placed on the 84<sup>th</sup> floor. They are suspended on cables and controlled by hydraulic cylinders, thus achieving optimal building damping.

Another example of a tall building designed by utilizing both corner modifications and a tuned mass damper is Taipei 101, Figure 13c. Its corners are recessed, the shape consists of several inverted pyramids, and it has a 740-ton tuned mass damper near the top. The corner modifications reduce the wind-induced base bending moments by ~25%, Irwin [95]. Taipei 101 is built at a location where there is no building of comparable size in its vicinity, which yields a relatively low turbulence intensity of the incoming wind at the top of Taipei 101. For this reason, vortex shedding tends to be accentuated because a larger inflow turbulence generally yields weaker vortex shedding, Li et al. [96].

The Beijing Olympic Tower consists of five cylindrical towers, each with a large mass on top, Figure 13d. Due to its unique design, the space available for vibration mitigation was limited to a room of 4.80 x 4.20 x 5.80 m. A double-stage pendulum tuned mass damper, which uses a fire water tank as the mass element, is suspended using a double-stage suspension system. With a damper mass of 0.058% of the total structural mass, the maximum acceleration reduction of each floor is ~30%, Chen et al. [97].

Modifications in the design of Petronas Towers were originally sufficient to reduce building motion to an acceptable level, Figure 13e. Similar to Burj Khalifa, these towers are set-back at various heights, and have a large number of corners. However, the cylindrical struts that support the sky-bridge connecting the two towers and the cylindrical spire on top experienced severe vortex-induced vibration. Consequently, tuned mass dampers were subsequently used in the cylindrical struts and spires, Irwin [95].

Creating openings on buildings is another way of improving their aerodynamic properties by reducing the aerodynamic drag and lift forces, Li et al. [98]. An opening allows for the air

to pass through the structure, thus weakening and disrupting vortex formation. Furthermore, the suction maximum on the leeward building surface is reduced, which has a favorable effect on the overall building drag force. The most notable building that utilizes a large opening near the top of the building is Shanghai World Financial Center, Figure 13f.



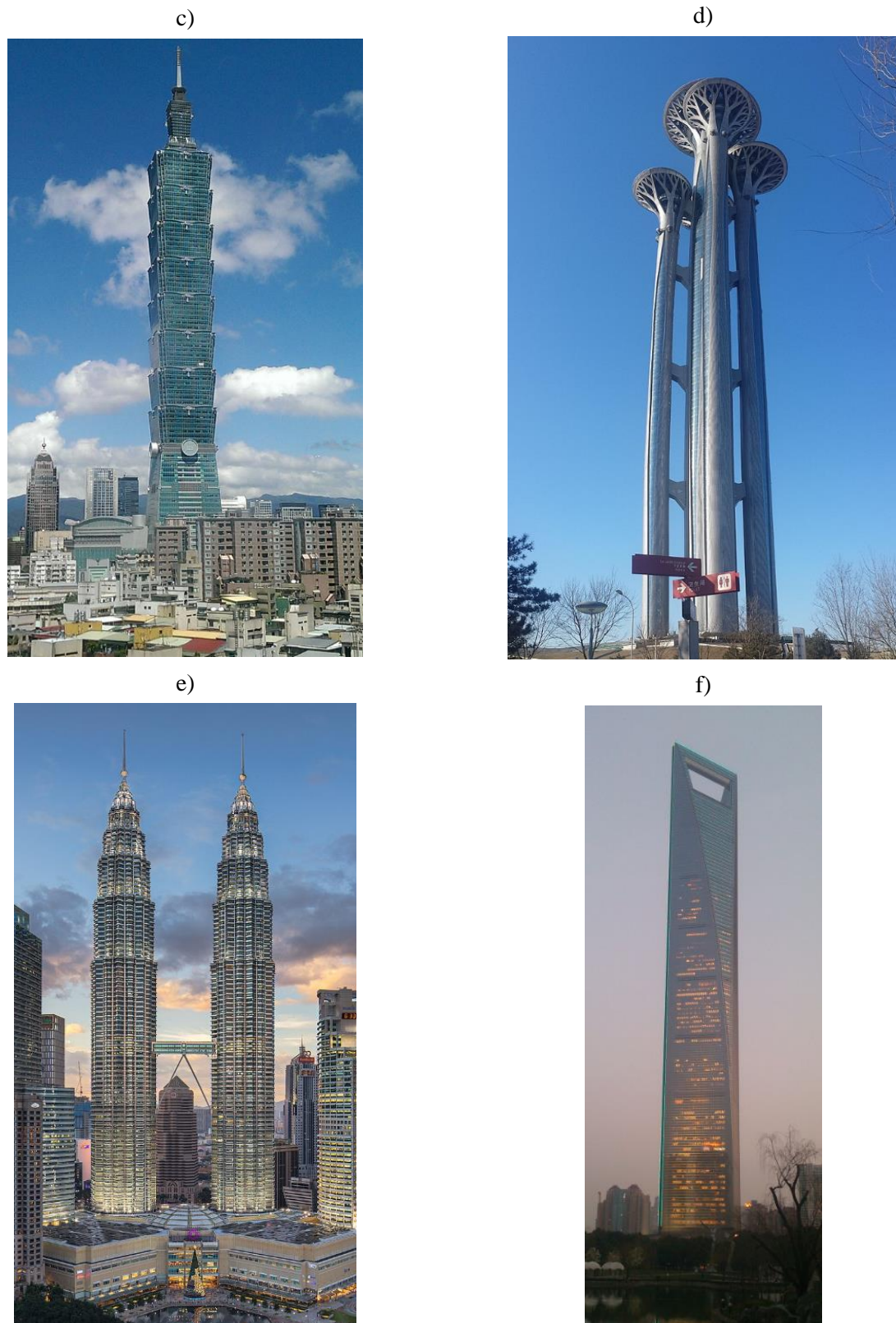


Figure 13. a) Burj Khalifa, b) 432 Park Avenue, c) Taipei 101, d) Beijing Olympic Tower, e) Petronas Towers, f) Shanghai World Financial Center, Photo courtesy of <https://commons.wikimedia.org/>

Along-wind openings are more effective in reducing building motion than across-wind openings, while the optimal solution is the application of both along- and across-wind openings. The optimal gap width is 4-5% of the building width, Dutton and Isyumov [99]. The application of through openings near the top of a building enables a further reduction of aerodynamic response, with through openings on all four surfaces of the building providing the maximum reduction, Miyashita et al. [100], Okada and Kong [101]. A pyramidal top of a building favorably affects, i.e., diminishes, both the along- and across-wind responses, Isyumov et al. [102].

It is important to note that tall buildings may alter the flow around other buildings in their proximity and can have an adverse effect on their serviceability, Li and Li [103], Quan et al. [104]. For this reason, a study of flow in the vicinity of tall buildings should be conducted before their erection to avoid adverse effects on their immediate surroundings.

While tall buildings are characterized by quite complex aerodynamic features, it is necessary to investigate local aerodynamic forces acting on the selected parts of building façades to mitigate adverse effects on various building portions. This has been commonly studied based on the surface pressure coefficient distribution  $\bar{C}_p$  and the  $\bar{C}_p$  fluctuations on the surface of tall buildings.

The pressure distribution on a setback building is similar to a square-base building, while the pressure distribution on a helical-base building is rather complex, with the suction on the leeward surface smaller than on other building shapes. For a building with an unconventional cross section, a study of aerodynamic pressure distribution is needed, Nagar et al. [105].

The pressure distribution on tall buildings equipped with PDSF systems is expected to have trends similar to those observed on smooth building façades, e.g., the stagnation point at ~80% of the building height. The pressure distribution on the inner façade is expected to be lower than that on a smooth façade due to the sheltering effect of the outer façade. However, this assumption is still to be investigated.

Various flow control measures may be used in extreme winds, e.g., Xie and Yang [106]. However, at this moment it is still unclear how the aerodynamic modifications of a building design would affect tall buildings with PDSF systems. The use of tuned mass dampers is nevertheless expected to be effective regardless of the façade system.

## 5 Porous materials

### 5.1 Fluid flow through porous structures

It is necessary to understand all the relevant flow and turbulence phenomena on various scales of time and space for fluid flow through porous materials to be able to successfully comprehend complex fluid-structure interactions that occur on tall buildings equipped with porous façades. In general, from a fluid mechanics point of view, any material that allows fluid to flow through it is considered porous. There are many examples and applications of porous materials, e.g., from meshes and plates commonly used in engineering to human and animal bones, underwater organisms, and sponges in the organic world, Figure 14.



Figure 14. Porous materials

Nevertheless, for the purposes of the present study, which focuses on tall buildings with porous façades, the main interest is in perforated plates, which are commonly manufactured by drilling openings in a sheet of metal, usually stainless steel or aluminum of various sizes and thickness. Openings can be of any shape, but are usually circular, while their porosity can be modified by changing the size, shape, and number of openings.

In the past, two lines of work have developed regarding the application of porous materials and surfaces in various branches of science and engineering, i.e., in closed conduits and open flows.

## 5.2 Porous elements in closed conduits

In closed conduits such as pipes, depending on the flow characteristics, perforated plates have been used both as flow conditioners, e.g., Erdal [107], Ouazzane and Benhadj [108], or turbulence generators, e.g., Liu and Ting [109], Mazzeliet al. [110], Figure 15.

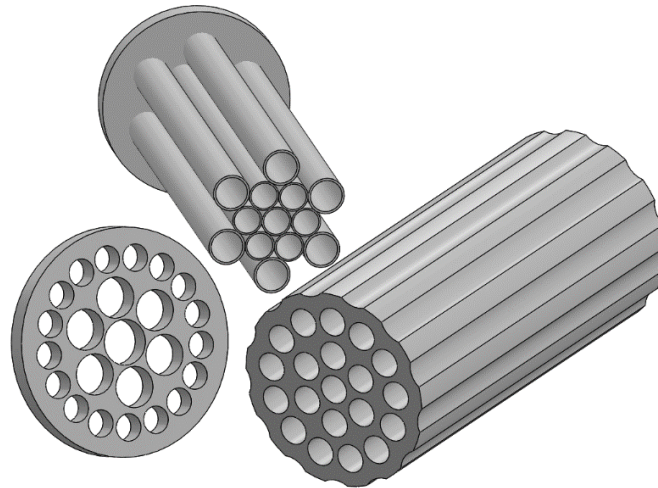


Figure 15. Flow conditioners and turbulence generators

Flow conditioners are devices installed in a fluid flow for the purpose of removing swirl and correcting a distorted flow profile, while turbulence generators are used to enhance turbulence in the flow. Flow conditioners have been commonly used to reduce turbulence behind pipe bends and to shorten the length of the straight pipe upstream of flow measurement devices, e.g., Spearman et al. [111], but also to condition the flow through diffusers to mitigate flow separation, e.g., Şahin and Ward-Smith [112]. Şahin [113] indicated that a single perforated plate of high porosity provides a more uniform velocity field in a diffuser compared to a flow without a plate, while a plate of low porosity can instead increase turbulence intensity because of the local increase in velocity through a limited number of openings. For this reason, it is not recommended to use multiple screens of low porosity near one another.

Concerning the effect of perforated plates on pressure and velocity distribution in a pipe flow, Castro [114], Gan and Riffat [115], Liu et al. [116], and Özahi [117] proved that a perforated plate in a pipe flow causes a decrease in the turbulence kinetic energy of the fluid, which has been commonly exhibited as a pressure drop. Plate characteristics that affect the pressure drop are the porosity, thickness, number, and distribution pattern of the openings, Malavasi et al. [118].

Porous materials have been commonly used as air filters in air conditioning and ventilation, healthcare, and in the automotive and aircraft industry, mostly in the form of cartridges to increase the contact area of air per filter volume. To collect particles, openings in an air filter must be extremely small, which can cause a substantial pressure drop, Jeon et al. [119].

### 5.3 Porous structures in open flow

As for the application of porous materials and elements in open flows, they have been extensively used as windbreaks, wind barriers and fences in civil engineering and agriculture, e.g., Figure 16.



Figure 16. Porous roadway wind barriers; photos courtesy of Zoran Lončarec

For two-dimensional solid and perforated fences with varying opening shapes and porosities, Perera [120] showed that a fence of low porosity caused the formation of a separation bubble behind the fence at a porosity level lower than 30%, where porosity is the ratio of the area open to the flow relative to the total fence area. The drag force acting on a porous windbreak decreases with the increase in the windbreak porosity, Seginer and Sagi [121], Ranga Raju et al. [122], Yaragal et al. [123], and Kozmar et al. [124], [125]. As for pressure fluctuations, a windbreak with 60% porosity caused a decrease in pressure fluctuations by ~50% compared to a solid windbreak. Telenta et al. [126] proved that the turbulence intensity decreases with an increase of the bleed flow at larger flow incidence angles.

Raine and Stevenson [127] showed that a windbreak with low to medium porosity caused a larger decrease in the mean flow velocity compared to a more porous windbreak. Windbreaks, i.e., wind barriers, also make wide, long-span cable-supported bridges more susceptible to torsional flutter, Buljac et al. [128], [129], Buljac [130], while bridges with wind barriers characterized by higher porosity are less sensitive to flutter. The reason for this is the change



of the aerodynamic drag force, lift force and pitch moment coefficients of the bridge deck due to the effect of porous wind barriers. On the other hand, low-porosity, i.e., more solid, wind barriers provide better shelter for vehicles on bridges while increasing the overall aerodynamic load on the bridge.

Allori [131] provided a risk analysis of the probability of vehicles overturning as a function of windbreak porosity, thus indicating the possibility to determine vehicle safety. Given that most studies on porous materials have commonly been performed in wind tunnels, Allori et al. [132] developed a downscaling prototype-to-model procedure for relevant physical parameters by considering material porosity, the ratio of the plate thickness to the hydraulic diameter, and the  $Re$ .

There are several flow types in the flow through porous obstacles, i.e., the bleed flow through the porous obstacle, the wall boundary layer, the freestream flow above the obstacle, the separated shear layer, the flow recirculation behind the obstacle, e.g., Lee and Kim [133]. The separated shear layer is the area between the undisturbed, freestream flow away from the body and the separated bubble close to the body.

Important trends were previously observed concerning fluid flow and turbulence through porous materials and elements depending on the flow regime due to the balancing of inertial and viscous forces, i.e.,  $Re$ , thus laminar and turbulent flows.

The decrease of pressure in the laminar flow has proved to be inversely proportional to the freestream velocity, Bayazit et al. [134]. Increasing the plate thickness causes a greater pressure decrease of ~50% when compared to the relative thickness of 0.5 to 1.0. Thicker plate is more sensitive to the distribution of openings with a ~21% greater pressure decrease in the staggered array than in the in-line array of the openings. This discrepancy is ~17% on the thinner plate. In turbulent flow, the pressure decrease remains almost constant regardless of the  $Re$  and it is highly sensitive to the plate porosity, whereas a thinner plate yields a greater pressure decrease. The pattern of the openings' distribution in both laminar and turbulent flows has proved to have a minor effect on the pressure drop.

Regarding the application of porous materials on building façades, the most common shapes are louvres, i.e., horizontal metal plates, which have been commonly used to control the natural lighting in buildings. Louvres represent a DSF system characterized by high porosity and a relatively small gap width between the inner and outer façades. In most cases, they are fixed, but a rotating system can be used to allow for rotation of each plate about the horizontal axis, thus allowing enhanced sunlight control. An alternative option for the DSF system is the use of perforated metal plates as the outer skin, which allow for various patterns on the façade,

thus enhancing the visual appeal of the building and its sunlight control. This type of porous DSF may be used for a wide range of porosities, in contrast to the fixed louvre system.

Given this literature survey to outline the fundamental aspects of fluid flow and turbulence through porous elements, and also intended to lay the groundwork for work on the aerodynamic characteristics of tall buildings equipped with porous DSFs, several important aspects may be relevant:

- Porosity is the dominant factor influencing the pressure drop in fluid flow through porous surfaces;
- Lower relative thickness of the porous surface yields a greater pressure drop at the same porosity and distribution pattern of the openings;
- In the laminar flow, the pressure drop coefficient decreases as the  $Re$  increases;
- In the turbulent flow, the pressure drop coefficient remains nearly constant regardless of the changes in the  $Re$ ;
- The distribution pattern of the openings on a porous surface has a minor effect on the pressure drop in the fluid flow through porous surfaces.

## 6 Experimental setup

### 6.1 Boundary layer wind tunnel

The experiments were conducted in the boundary layer wind tunnel (BLWT) of the Inter-University Research Centre on Building Aerodynamics and Wind Engineering (CRIACIV) at the University of Florence, Italy. This is an open-circuit wind tunnel situated in a laboratory, where the inlet and outlets are not connected to the external environment. The wind tunnel has a rectangular 2.2 m wide and 1.6 m high cross-section at the inlet, which gradually increases to a width of 2.4 m at the same height at the turntable. This is because of the lateral surfaces of the wind-tunnel test section that are divergent for the purpose of achieving a nearly zero pressure gradient from the inlet to the test section to the turntable. The overall length of the wind tunnel from the inlet to the outlets is 22 m. The inlet nozzle is equipped with a honeycomb. The support structure of the wind tunnel is made of structural steel, while the floor and the ceiling are made of wood. The lateral vertical walls of the wind-tunnel test section are made of transparent glazed panels which permit observation of the test section during the experiments.

Approximately 3 m after the test section, there is a fan powered by 156 kW electric motor which sucks the air into the wind tunnel and ejects it into a T-shaped diffuser. Upstream of the fan is a fine steel mesh used for protection of the fan from flying debris. A similar mesh is located at each of the outlets. The flow velocity is controlled by means of two parameters, i.e., the rotational velocity of the fan and the pitch of its ten blades. The maximum mean flow velocity in the wind tunnel is  $\sim 30$  m/s with a freestream turbulence intensity of  $\sim 0.7\%$  when no turbulence-generating devices are installed downstream of the inlet.

There are two main parts of the wind tunnel. The first part is immediately downstream of the inlet for the purpose of creating the ABL model. This is achieved by a combination of surface roughness elements and a sawtooth barrier and/or vortex generators. The second part is the test section, equipped with a circular turntable 2.2 m in diameter, which can be rotated remotely by an electric motor. A photograph of the wind tunnel is shown in Figure 17.



Figure 17. CRIACIV boundary layer wind tunnel

## 6.2 Building models

The principal building model was made of aluminum to limit its weight while maintaining stiffness. The overall dimensions are such that the model is 100 mm wide, 100 mm long and 500 mm high. The main structural element of this building model is a circular pipe that spans from the bottom to the top of the model. Thin, rectangular-shaped plates with a circular opening

in the middle are mounted onto the central pipe at equal distances to support the façades. Smaller openings were made in several locations on each plate to allow for the pressure tubing to be wired through the model. The façade models are 1 mm thick rectangular aluminum plates that are 100 mm wide and 500 mm high. Diameter openings of 0.8 mm were made in each façade at strategic locations to connect the pressure taps. There is a total of 40 openings on each of the façade models, which are arranged in an 8 x 5 grid. Figure 18a and Figure 18b show photographs of the building model, while Figure 18c shows a schematic view of the pressure tap locations on each façade.

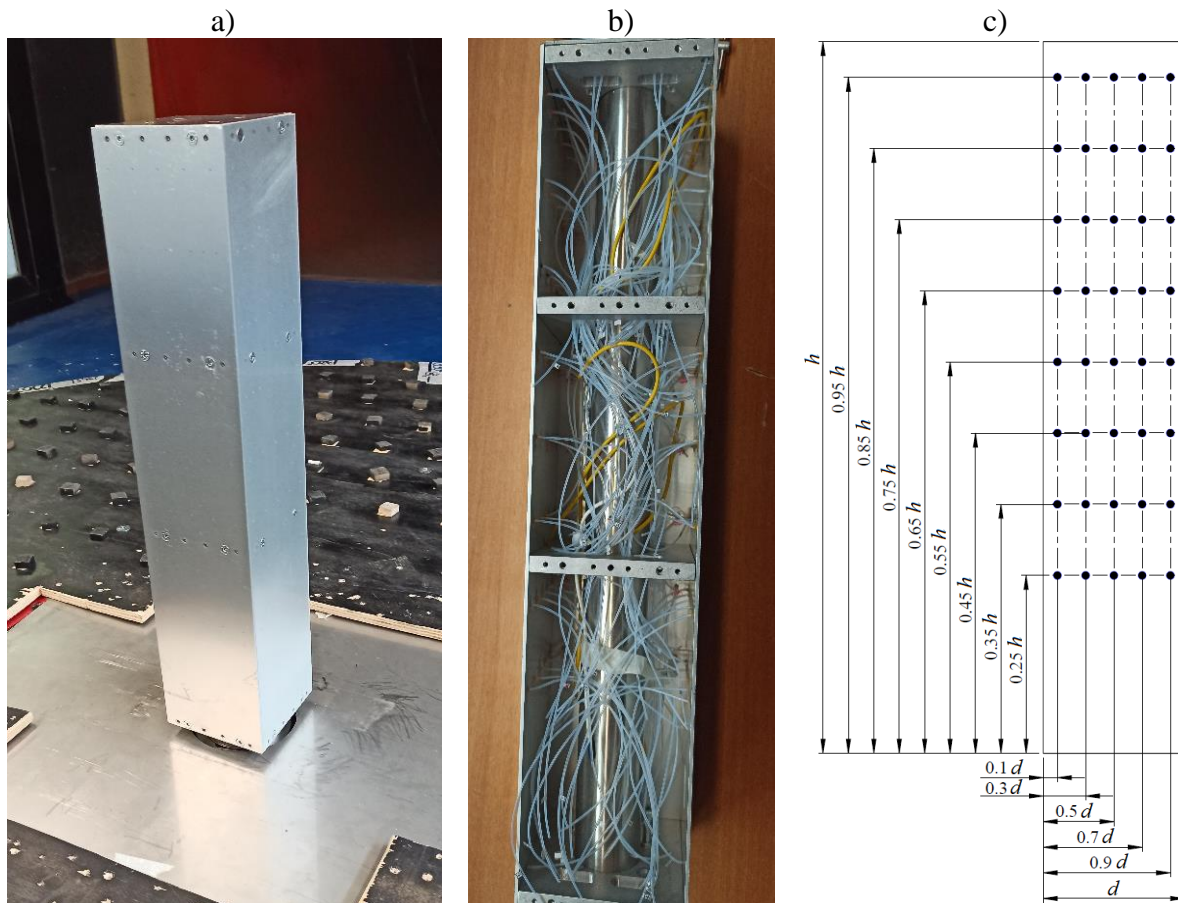


Figure 18. a) Tall building model, b) pressure tap tubing in the building model, c) arrangement of pressure taps on the building façade models

The porous outer façades were made of 1 mm thick and 500 mm high aluminum plates. A total of four plates were needed to completely equip the building model with a PDSF system. To ensure tightly closed corners between the façades, two plates are 108 mm wide, while the other two have a width of 110 mm. In this way the plates interlock at the corners to create an airtight fit. Diameter openings of 10 mm were laser-cut in the aluminum plates to achieve the desired porosity. The porosity of the façades is determined by the ratio between the summed area of the openings and the total area of the façade. Three porosities were selected, i.e., 25%, 50% and 65%. A porosity of more than 65% is not feasible with 10 mm diameter openings

since the material between the openings is too thin. The outer dimensions of the building model equipped with porous outer skins are 110 mm by 110 mm with a height of 500 mm. The gap between the inner and outer façade is 4 mm. The largest blockage of  $\sim 3\%$  appears when the flow incidence angle between the windward surface of the model and the freestream flow direction is  $\beta = 45^\circ$ , which is lower than the 5% suggested by Holmes [22], so no corrections of the data were necessary, and thus were not performed, in this regard. Figure 19 shows the schematic view of the models, while Figure 20 shows the photographs of the building models in the wind-tunnel test section.

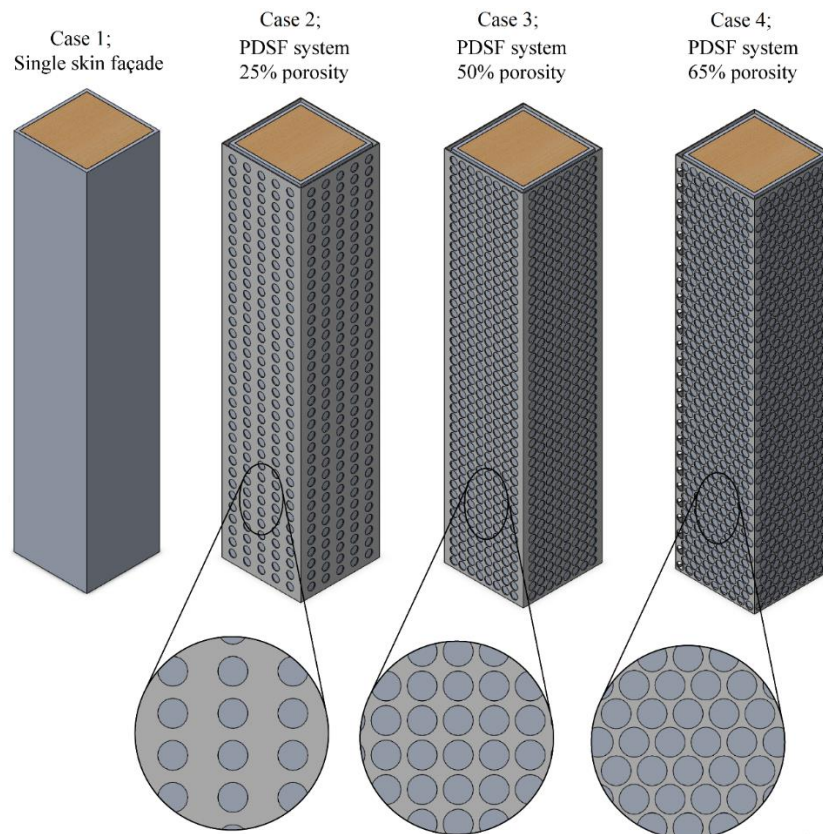


Figure 19. Schematic view of the studied building models with a single-skin façade and PDSF systems of 25%, 50% and 65% porosity

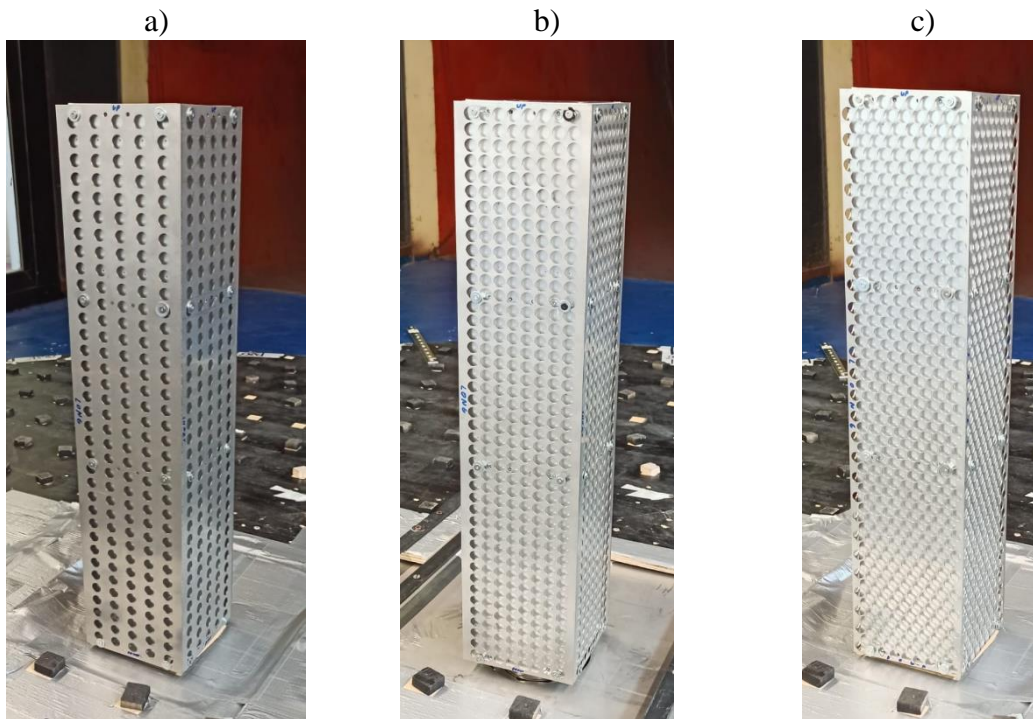


Figure 20. Building model with PDSF systems: a) 25% porosity; b) 50% porosity, and c) 65% porosity

To study the effect of the aerodynamic interference between tall buildings, eight dummy building models were designed to be placed around the principal building model equipped with a PDSF system. The dummy building models were made of square-section aluminum tubes which ensures that the edges are sharp, and they are not equipped with a PDSF system. The dimensions of the dummy building models are 100 mm wide 100 mm long and 500 mm high, which yields the 1:1:5 aspect ratio, i.e., identical to the principal building model. They were arranged in a 3x3 in-line pattern to simulate an urban environment. The interference effects were studied by changing the distances between the building models. Figure 21 shows one of the arrangements of the building models situated in the urban environment model.



Figure 21. Arrangement of building models situated in the urban environment model

To study the effect of the building model geometric aspect ratio, additional building models were made characterized by the 1:1:4, 1:1:3, 1:2:5 and 1:3:5 aspect ratios. They were all manufactured from aluminum tubes used to make dummy building models. The 1:1:4 and 1:1:3 models are 100 mm wide and 100 mm long, with heights of 400 mm and 300 mm, respectively. The 1:2:5 model was made by connecting two aluminum tubes together using multiple screws. Likewise, the 1:3:5 model was made by connecting three tubes. All four building models were connected to the HFFB by a steel connector designed to fit all the different aspect ratio models. The measurements on these models were performed using an HFFB. Figure 22 shows a schematic view of the building models with various geometric aspect ratios. The steel connector for the building models and the HFFB is shown in Figure 23.

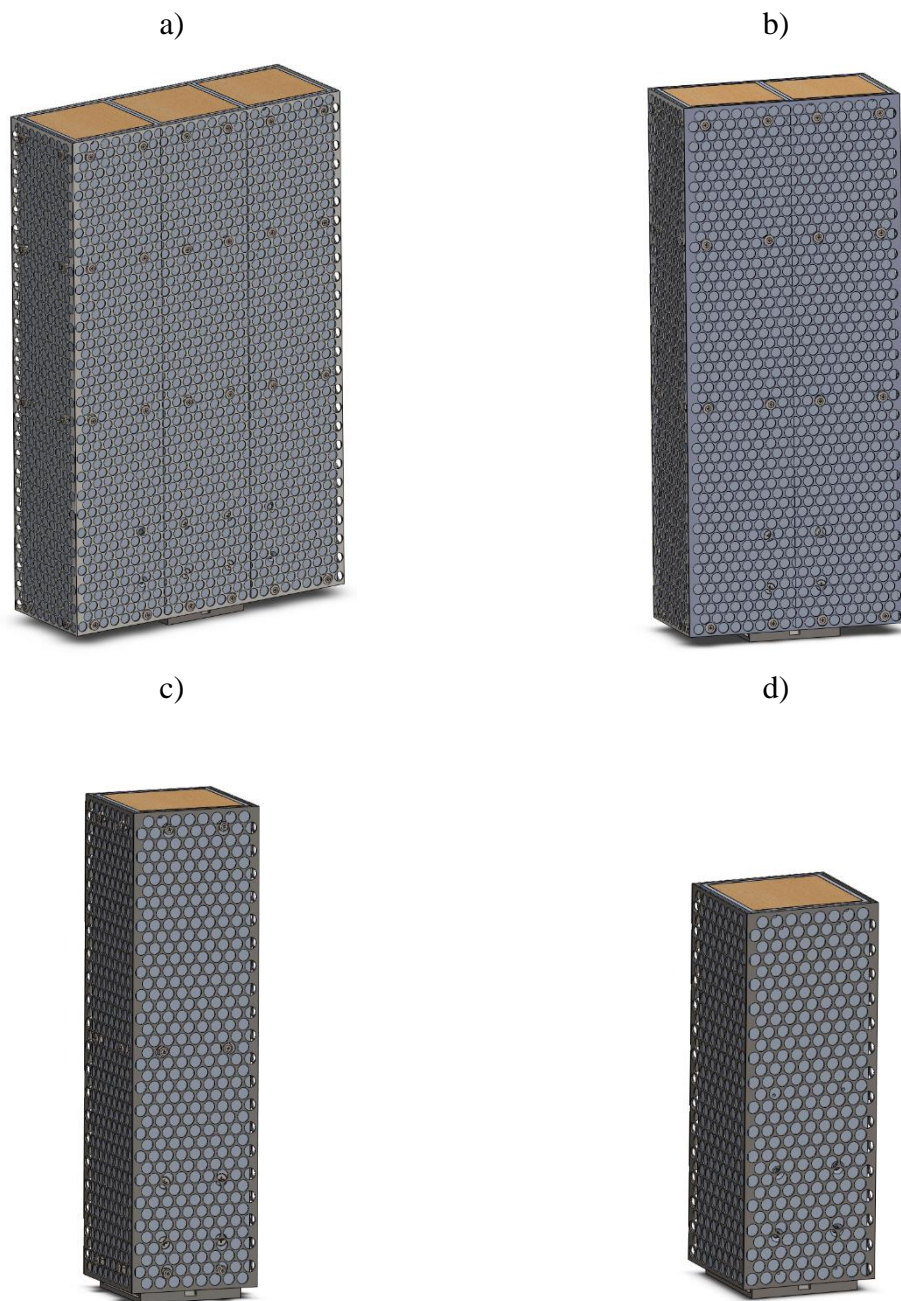


Figure 22. Building models with the a) 1:3:5, b) 1:2:5, c) 1:1:4, d) 1:1:3 aspect ratios



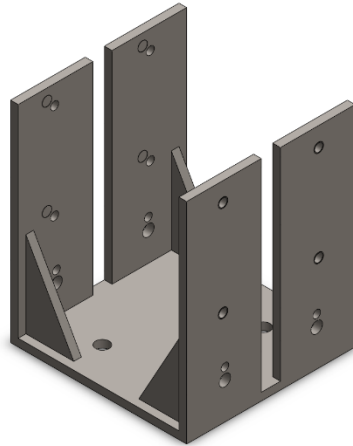


Figure 23. Connector for the building models with various geometric aspect ratios

Photographs of the 1:3:5 and 1:2:5 building models in the wind tunnel are shown in Figure 24.

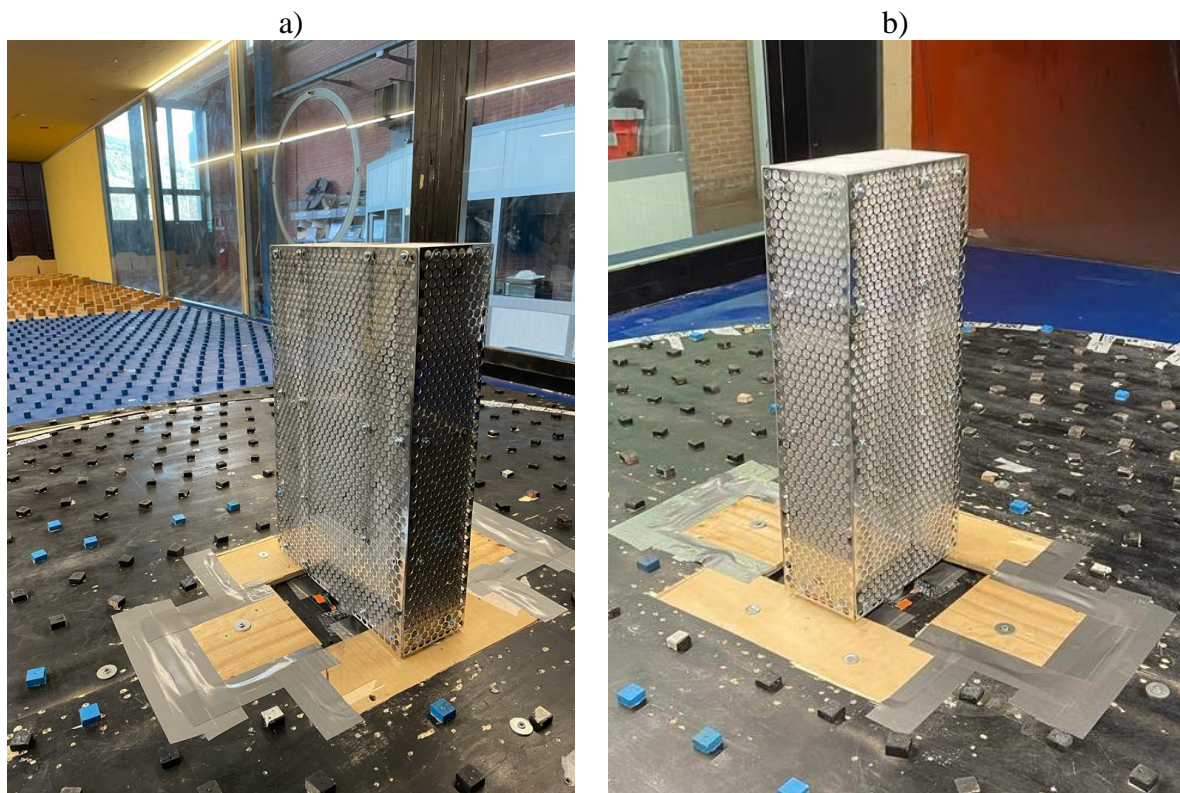


Figure 24. a) 1:3:5 and b) 1:2:5 building models in the wind-tunnel test section

### 6.3 Flow simulation

The Eurocode [44] guidelines were used to validate the ABL models created in the wind tunnel. Eurocode [44] classifies the ABL in five categories, from category 0 to category IV, where each of the categories represents the flow characteristics over a certain type of terrain. Category 0 represents an ABL which generally develops over large areas such as open seas or plains, thereby characterized by large gradients in the mean velocity profile in the lower area, and very low turbulence intensity. In contrast, category IV represents highly urban areas, with the lowest mean wind velocity, but the highest turbulence intensity. Categories I, II and III represent ABLs between the low-turbulent category 0 and highly turbulent category IV. For the present work, three characteristic ABL parameters were assessed, i.e., mean wind velocity, turbulence intensity, and integral turbulence length scale. It was not feasible to simulate categories 0 and IV in the wind tunnel, so categories I and III were selected to ensure a good representation of two clearly different ABLs.

To simulate the ABL, a sawtooth barrier was used together with surface roughness elements. The sawtooth barrier spans the width of the wind tunnel at the inlet and influences the flow near the surface. A larger barrier was used to create a category III (more turbulent) ABL, while a smaller barrier was used for category I. Furthermore, for category I, two barriers of the same dimensions were used, i.e., one barrier at the ground level, and another barrier rather unconventionally attached upside down to the ceiling of the wind-tunnel test section. Surface roughness elements were designed by attaching wooden cubes of various sizes to cardboard panels that were 1.6 m wide, 1 m long, and 0.01 m thick. These panels were then mounted to the floor of the wind-tunnel test section. Multiple panels with cubes of various dimensions were used to contribute to creating the desired ABL models.

The configuration of both the sawtooth barriers and surface roughness elements was determined after trial-and-error experiments performed until the ABL profiles reasonably matched the Eurocode [44] profiles. The simulation length scale of the experiments was  $S = 1:400$ . In particular, building models were selected to be 0.5 m high to allow for these models to be placed in the 1.6 m high test section of the CRIACIV boundary layer wind tunnel. The appropriate length scale of these models, so they can represent tall buildings, is 1:400, because at this length scale, the prototype buildings are 200 m high. The next step in this scaling procedure was to create the ABL simulations at this same 1:400 simulation length scale, so the length scales of the building models and the ABL simulations are the same to satisfy the Jensen [135] similarity. The characteristic profiles of the mean flow velocity, turbulence intensity and integral turbulence length scales for the intended rural and suburban ABL simulations at the 1:400 length scale were accordingly calculated from Eurocode [44] using the 1:400 simulation length scale, the ABL type and the height of the wind-tunnel test section as the input data. The setup of the experimental hardware in the wind-tunnel test section was subsequently tested in

the trial-and-error procedures until the created ABL simulations complied with the Eurocode [44] recommendations for the rural and suburban terrain types.

Figure 25 shows a schematic view of the small and large sawtooth barriers. Since the barriers are symmetric, the left-hand side shows the smaller barrier used for the ABL category I simulation, while the right-hand side shows the barrier used for the ABL category III simulation.

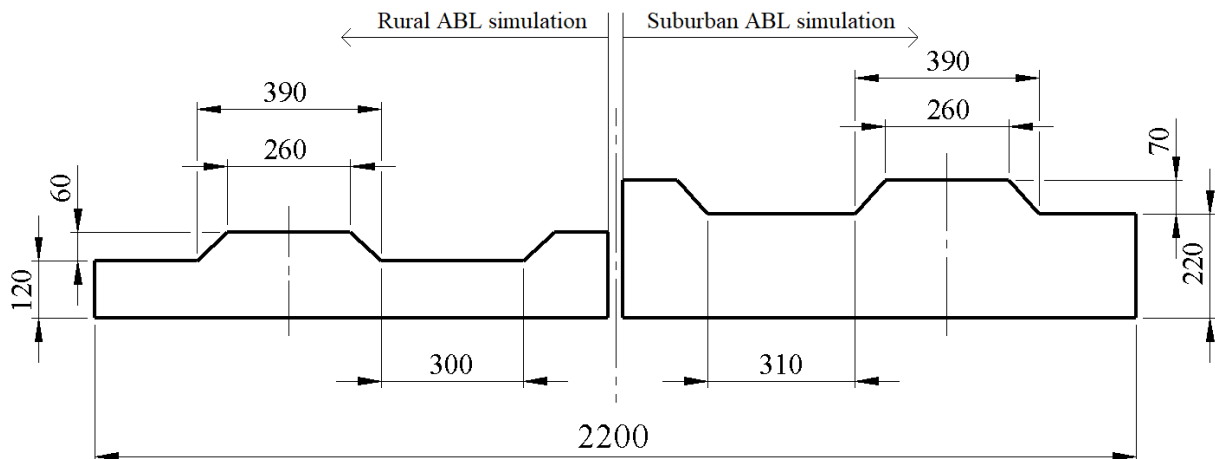
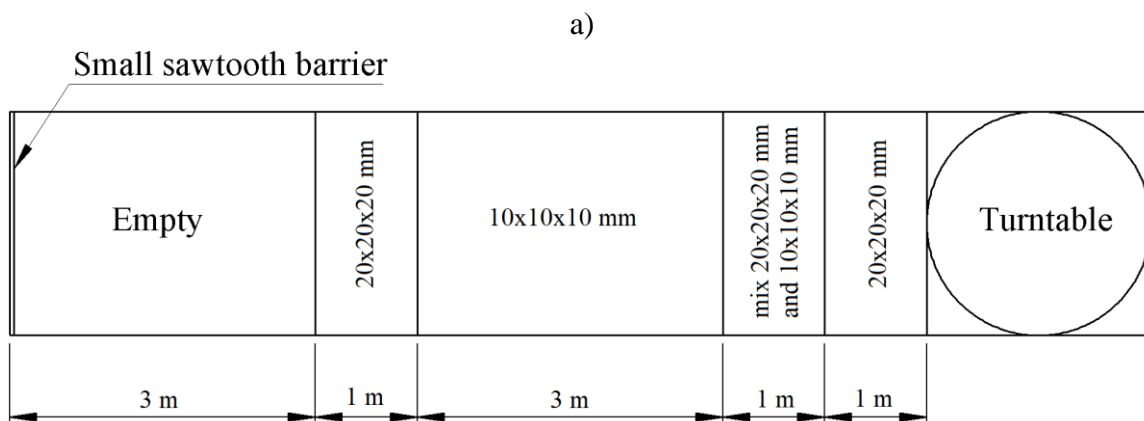


Figure 25. Sawtooth barrier; left-hand side used for the ABL model of category I, right-hand side used for the ABL model of category III. All values are in cm.

The wind-tunnel test section has a 9 m long fetch used for surface roughness elements. To achieve two different ABL models, surface roughness elements were arranged as shown in Figure 26a for ABL model category I and Figure 26b for ABL category III. The turntable was in both cases covered by 1 cm x 1 cm x 1 cm cubes.



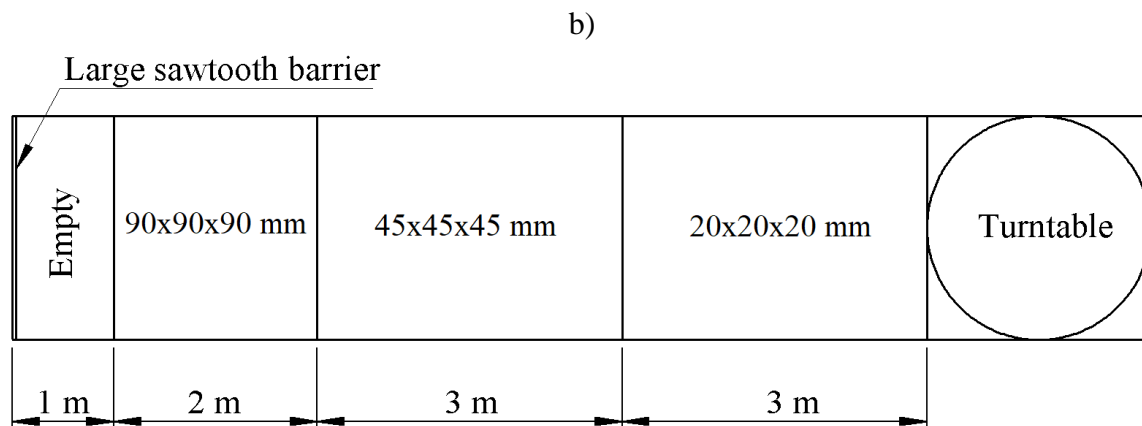


Figure 26. Arrangement of surface roughness elements for the ABL model of a) category I and b) category III

A photograph of the principal building model in the wind-tunnel test section with the ABL model category III sawtooth barrier and surface roughness configuration is shown in Figure 27.

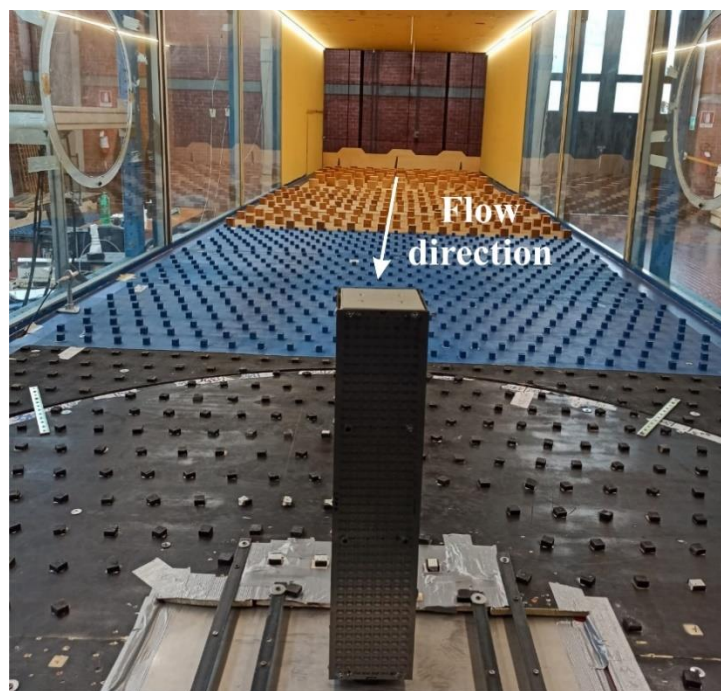


Figure 27. ABL model category III setup in the wind-tunnel test section

## 6.4 Similarity criteria

To accurately reproduce physical phenomena in the wind tunnel, a proper scaling procedure must be performed. The need for scaling arises from the fact that the prototype engineering structures are much larger than their wind-tunnel models. Particularly for civil engineering

structures, the reference length of the structure can be scaled down several hundred times from the prototype to the model scale. Since the size of the structure is largely reduced, it is necessary to perform proper scaling of other relevant dimensions as well. A set of governing dimensionless parameters was selected for the present work based on a dimensional analysis.

### *Reynolds number*

The Reynolds number defines the ratio of the inertial and viscous forces in the fluid flow, as provided in Equation (3.5). Consider a case with a ratio of prototype to model length 1:400, which is not an unusual scale for wind-tunnel models of civil engineering structures. Since the  $Re$  should be equal in the prototype and model to maintain the ratio of inertial to viscous forces, the flow velocity in the wind tunnel should be 400 times larger than in the prototype scale. If an arbitrary value of 10 m/s wind velocity in the prototype scale (which is reasonably low) is assumed, the  $Re$  similarity would mean that the flow velocity in the wind tunnel should be 4000 m/s. While this is not feasible, the  $Re$  similarity cannot be satisfied, a well-known issue in the wind engineering community.

However, the effect of the  $Re$  on bluff bodies is, for the most part, exhibited by changing the locations of the flow separation and the respective drag coefficient. As the flow velocity increases, the flow regime changes from subcritical, critical, supercritical and transcritical, depending on the  $Re$ . The critical  $Re$  is associated with the large drag reduction, when the drag coefficient stabilizes and remains approximately constant at a higher  $Re$ . Furthermore, the separation points are located at the sharp corners of the bluff bodies, regardless of the  $Re$ . The critical  $Re$  commonly considered in the aerodynamics of smooth bluff bodies is 50,000, Költzsch et al. [136], Tieleman et al. [137]. For this reason, it is not necessary to achieve the  $Re$  similarity in bluff body aerodynamics, but rather to ensure that the  $Re$  is larger than the critical  $Re$ .

### *Strouhal number*

The Strouhal number is relevant in transient phenomena including flow fluctuations or structure vibration:

$$St = \frac{fL}{u}, \quad (4.16)$$

where  $f$  is the vortex-shedding frequency,  $L$  is the characteristic body length, and  $u$  is the mean freestream flow velocity. In the subcritical range, the  $St$  for circular cylinders is almost constant, i.e.,  $St \sim 0.20$ . When the  $Re$  becomes critical (the flow separation point changes location and the drag coefficient decreases), the  $St$  increases to 0.48. Moreover, it subsequently

decreases to 0.40, until  $Re = 2 \cdot 10^6$ , where the  $St$  further decreases to 0.2, Holmes [22], Bearman [138]. It is useful to point out that in the subcritical regime, when the  $St$  is nearly constant, the vortex-shedding frequency concurrently increases with the increasing flow velocity.

As the vortex-shedding frequency increases, it can become equal to the natural frequency of the body. The body then oscillates with the maximal amplitude, which in turn affects the vortex-shedding frequency in the “lock-in” phenomenon. To describe lock-in, first the equation of motion for vortex-induced-vibration must be introduced. The equation of motion is generally used to represent the vibrations of a cylinder oscillating in the lateral direction to the main flow:

$$m \frac{\partial^2 y}{\partial t^2} + c \frac{\partial y}{\partial t} + ky = F(t), \quad (4.17)$$

where  $m$  is the mass of the body,  $c$  is the structural damping of the body,  $k$  is the elastic constant and  $F$  is the aerodynamic force in the transverse direction, e.g., Williamson and Govardhan [139]. The oscillating aerodynamic force can be expressed as a periodic function:

$$F(t) = F_0 \sin(\omega t + \theta), \quad (4.18)$$

with  $\omega = 2\pi f$ , where  $f$  is the oscillating frequency of the body, and  $\theta$  is the phase angle of the periodic function. When the frequency of the vortex-induced vibration reaches the natural frequency of the body, a change in amplitude occurs. At this point, the  $St$  is no longer constant, and the vortex-shedding frequency tends to remain constant, thus further increasing the amplitude. Feng [140] found that the change in amplitude is accompanied by a change in phase angle  $\theta$ . The jump in the phase angle is exhibited in the vortex-shedding characteristics, Zdravkovich [141].

### *Jensen number*

The Jensen number is based on the fact that the ABL must be accurately represented in the model scale, Jensen [135]:

$$Je = \frac{h}{z_0}, \quad (4.19)$$

where  $h$  is the height of the structure, and  $z_0$  is the aerodynamic surface roughness length. The surface roughness length can be modelled in the wind tunnel by the arrangement of the surface roughness elements along the wind-tunnel test section. While the Jensen model law should be satisfied in wind-tunnel testing, it is necessary to gather data on the mean wind velocity, the turbulence intensity and the integral turbulence length scale in the prototype to be

able to accurately reproduce these profiles in the wind tunnel. Alternatively, if prototype data are unavailable, international standards provide recommendations on the ABL characteristics for various climates and topographies.

## 6.5 Flow measurement

Velocity measurements in the wind tunnel were carried out using the Prandtl-Pitot tube and hot-wire anemometry system. Both transducers are small enough not to cause a significant pressure drop or flow disturbance. The Prandtl-Pitot tube was used to determine the flow velocity based on the difference between the total and static pressure in the flow. It was used to determine the mean flow velocity, while it is considered inadequate for the measurement of flow velocity fluctuations.

A hot-wire anemometer was used to measure both the mean flow velocity and the flow fluctuations. Heat transmission between the heated hot-wire and the airflow is the basic principle of this method. The anemometer probe is generally designed as a tiny cylinder wire or a stretched thin film. Each wire or film is used to measure a single flow velocity component. However, to measure two or three flow velocity components at the same time, the probes may be fitted with extra wires.

Sensors are generally classified into four groups, i.e., gold-plated wires, miniature wires, fiber-film sensors, and film sensors. Gold-plated wires are appropriate for one-dimensional high-turbulence flows. Miniature wires are suitable for low-turbulence flows due to their small diameters, but they are also sturdy and suited for high-velocity measurements. Quartz fibers are wrapped in a thin nickel film to form film sensors. These sensors are mostly employed in liquids, where more robust sensors are required.

A current passing through the wire generates heat (Joule heating), and a part of the generated heat is dissipated by the forced convection from the airflow. The basic heat balance for the steady flow is defined as:

$$R_W I_W^2 = (T_W - T_a) \Phi_{\text{conv}}(U). \quad (6.1)$$

The left-hand side of the equation represents the heat generated using the current intensity  $I_W$  through the sensor with resistance  $R_W$ . The right-hand side of the equation represents the heat transferred by the convection.  $T_W$  represents the wire temperature while operating,  $T_a$  is the wire temperature while it is not operating, and  $\Phi_{\text{conv}}(U)$  is the convection function, which depends on the velocity in the direction normal to the wire.

In the turbulent flow, some heat remains in the sensor, and the heat balance is expressed as:

$$m_W c_W = R_W I_W^2 - (T_W - T_a) \Phi_{\text{conv}}(U). \quad (6.2)$$

The first term on the right-hand side is the heat stored in the sensor, where  $m_W$  is the sensor mass, and  $c_W$  is the specific heat coefficient of the sensor.

Hot-wire anemometers may be the Constant Voltage Anemometer (CVA), Constant Temperature Anemometer (CTA), and Constant Current Anemometer (CCA). For each of these anemometer types, one variable in the term  $R_W I_W^2$  of the Equation (6.2) is constant to measure only one physical quantity. Since  $R_W I_W$  is the voltage, in the case of a CVA system, this term is constant while the current intensity  $I_W$  is measured. In the CTA system, the temperature of the wire is constant, which implies that the resistance of the wire is constant as well. The only variable that can be measured in that case is the current intensity  $I_W$ . The CCA system keeps the current intensity constant while the change of resistance  $R_W$  is measured. In the present study, a CTA system was used, Figure 28.

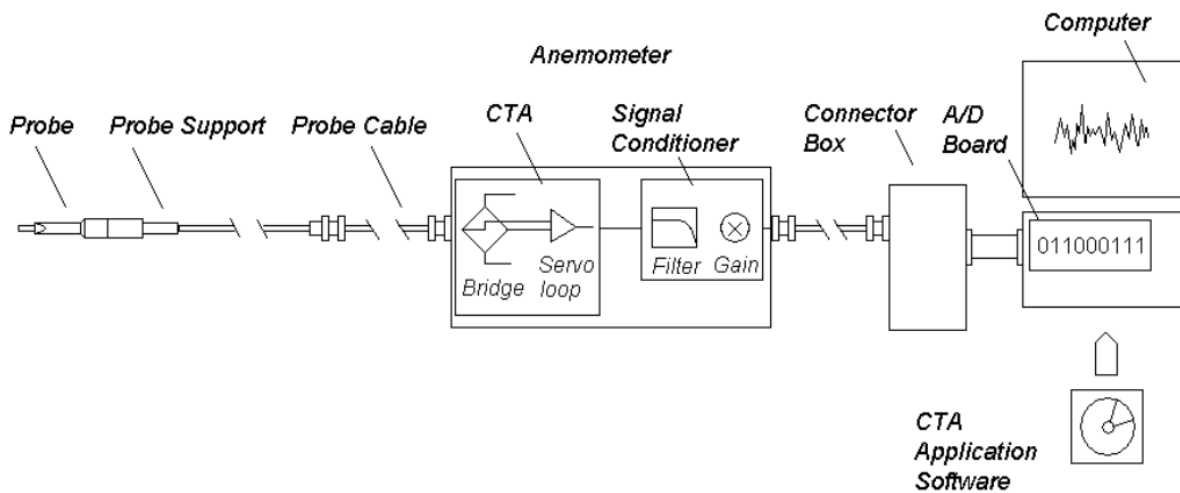


Figure 28. CTA measurement system, Jorgensen [142]

This system consists of a probe on a support, a probe cable that connects the anemometer with the probe sensor, an anemometer with a Wheatstone bridge and a conditioner for high- and low-pass filtering, an A/D board for analog-to-digital signal conversion, and a personal computer for signal control, postprocessing, and analysis.

## 6.6 Aerodynamic load measurement

HFFB is used to measure integral aerodynamic loads in three directions on the studied building model. Measurements were performed using the FT-Delta SI-165-15 system by ATI Industrial Automation, Figure 29, a strain-gauge multi-axis force and torque system that is used



to concurrently measure forces and moments in three directions. The accuracy of the measured moments is higher than for the corresponding shear forces (Table 2), so the emphasis of this work is on integral moments.

Table 2. Calibration results of the FT-Delta SI-165-15 HFFB

Calibration	$F_x, F_y$	$F_z$	$M_x, M_y$	$M_z$
Range	165 N	495 N	15 Nm	15 Nm
Resolution	1/32 N	1/16 N	1/528 Nm	1/528 Nm
Accuracy	$\pm 0.06\%$	$\pm 0.06\%$	$\pm 0.01\%$	$\pm 0.01\%$



Figure 29. High frequency force balance in the wind tunnel

The integral aerodynamic moment coefficients were calculated as:

$$C_M = \frac{M}{0.5\rho u^2 dh^2}, \quad (6.3)$$

where  $C_M$  is the aerodynamic moment coefficient,  $M$  is the moment,  $\rho$  is the air density,  $u$  is the mean freestream flow velocity at the building model height, and  $d$  and  $h$  are the width and height of the building model, respectively. The across-wind and along-wind moment coefficients were addressed. For the building model equipped with porous façades,  $d$  is 10%

larger than for the smooth building model, i.e.,  $d_{\text{PDSF}} = 1.1D_{\text{PDSF}} = 1.1Dd$ . Since the  $d$  is in the denominator, its increase accordingly yields a decrease in the  $C_M$  of the building model with PDSF systems relative to the single-skin building model. This is accounted for in the data analysis, i.e.,  $d = 1$  for the single-skin building model, and  $d = 1.1$  for the building model with a PDSF system.

## 6.7 Surface pressure measurement

Surface pressure measurements on the inner façade of the building model were carried out using a PSI-DTC Initium pressure measurement system together with four miniature 32 port DTC scanners. DTC Initium is a data acquisition system that supports eight miniature 32 or 64 port DTC scanners for measurements in 512 pressure points. DTC pressure scanners are differential pressure measurement units. Each of the 32 or 64 ports consists of a silicon piezoresistive pressure sensor that transfers the analog signal to the A/D converter. Polytetrafluoroethylene (PTFE) tubes of 100 mm and 200 mm length were used as pressure tubing. 100 mm long tubes are connected to the pressure scanners, which are connected to 200 mm long tubes by a pneumatic damper. The pneumatic damper is made of 110 mm long tube with a 0.3 mm inner diameter. The outer and inner tube diameters are 1.3 and 0.8 mm, respectively. The DTC pressure scanner is shown in Figure 30.



Figure 30. DTC pressure scanner

The surface pressure coefficient was calculated as:

$$C_p = \frac{p_{\text{tap}}}{p_{\infty}}, \quad (6.4)$$

where  $p_{\text{tap}}$  is the dynamic pressure measured at the pressure tap, and  $p_{\infty}$  is the dynamic pressure of the freestream flow at the top of the building model. All pressure measurements were performed at the sampling rate of 500 Hz and a time record length of 100 s.

The pressure tubing in the building model is shown in Figure 31.

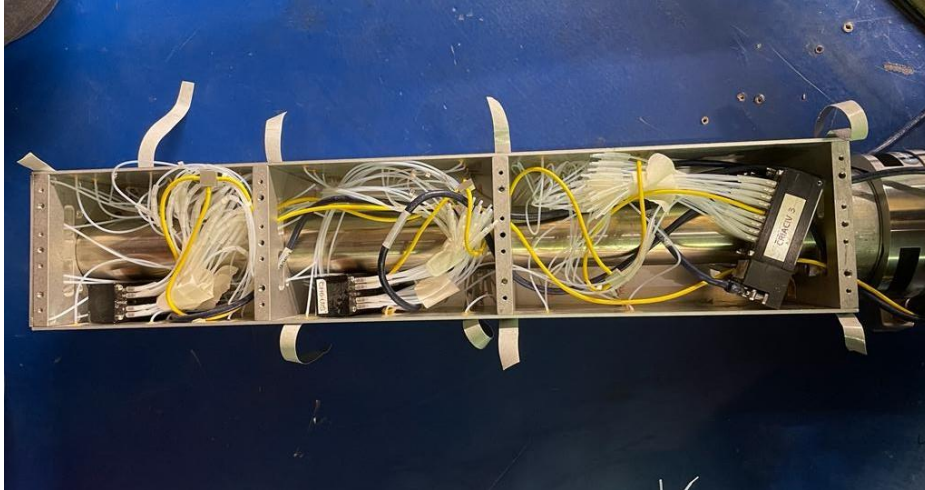


Figure 31. Pressure system in the building model

## 7 Results and discussion

### 7.1 Wind simulation

Two created ABL models are compared with Eurocode [44] categories I and III, thus rural and suburban ABL simulations, respectively. A comparison of the measured flow velocity profiles and the respective Eurocode [44] data is shown in Figure 32. Height  $h$  and velocity  $u_{\text{ref}}$  are the building model height and the mean freestream velocity at  $h$ , respectively.

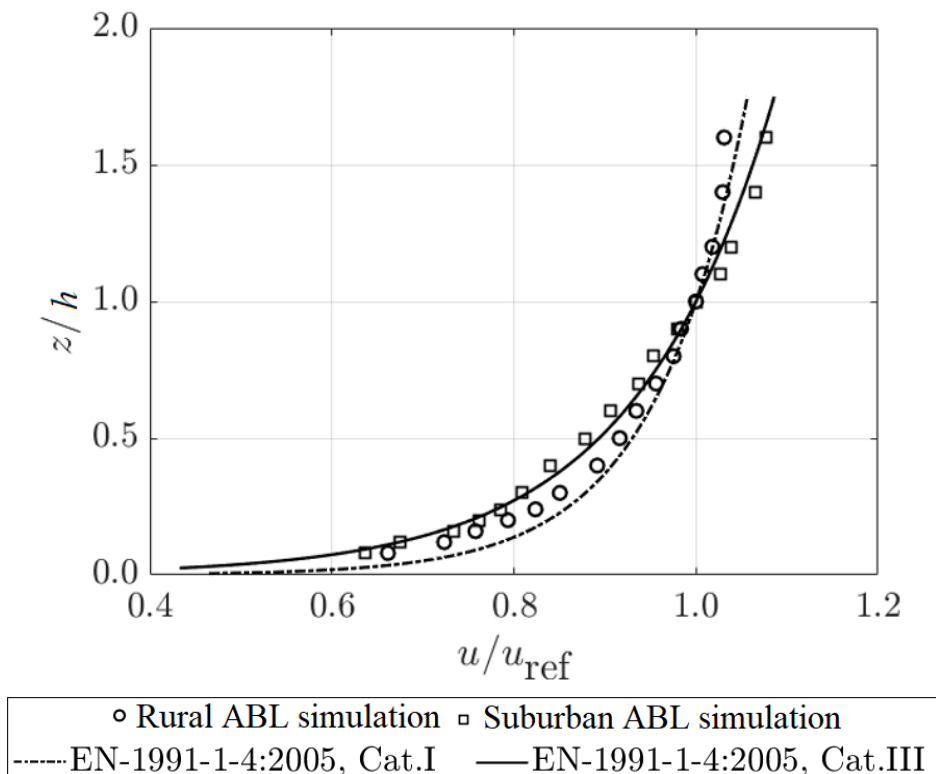


Figure 32. Mean flow velocity profiles in the rural and suburban ABL simulations and Eurocode [44]

The mean flow velocity profiles show the characteristic high gradient in the lower portion of the ABL ( $z < h$ ) due to the effects of surface roughness. The slope of the profiles straightens with the increase in height, particularly above the reference height. The mean flow velocity is low near the ground and increases substantially with the increasing height. This is in accordance with Holmes [22], Simiu and Scanlan [143]. In general, the created rural ABL and suburban ABL simulations both correspond well to the Eurocode [44] recommendations.

Figure 33 shows the created turbulence intensity profiles in comparison with Eurocode [44].

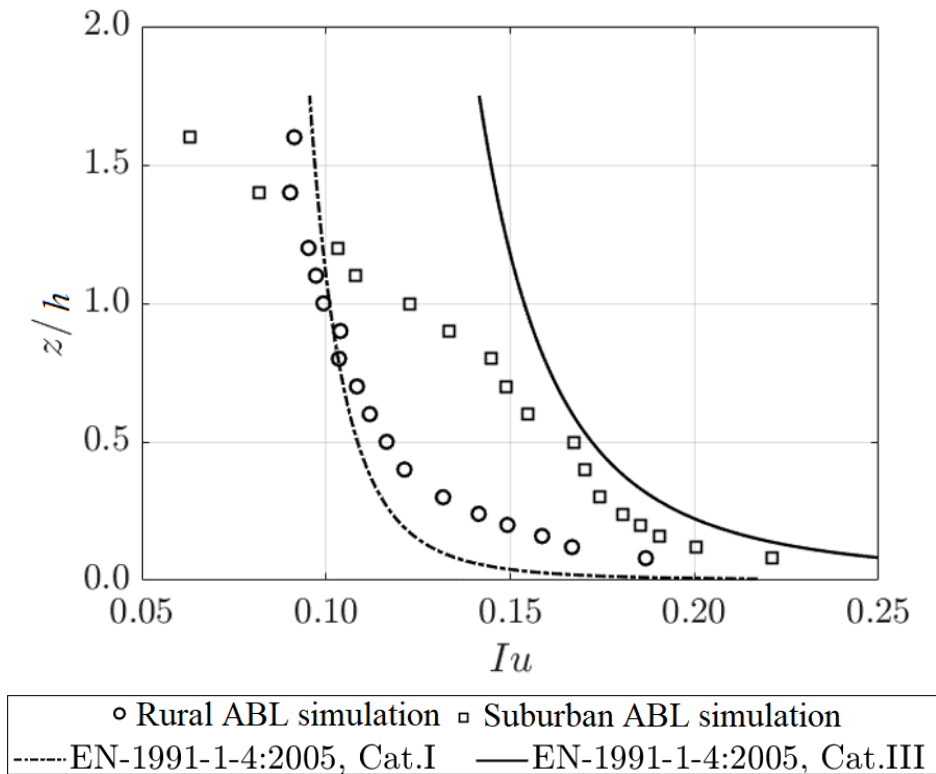


Figure 33. Turbulence intensity profiles in the rural and suburban ABL simulations and Eurocode [44]

There is an almost constant offset of 0.05 in the turbulence intensity profiles. A large gradient is present in the lower part of both Eurocode [44] profiles, particularly exhibited below  $0.5 h$  in the rural ABL simulation. Apart from the trends observed near the ground surface, the rural ABL simulation corresponds well with Eurocode [44] category I. There is a considerable discrepancy between the turbulence intensity in the wind tunnel and Eurocode [44] category III ABL. Nevertheless, this discrepancy is present higher in the ABL simulation, so this trend is generally not considered to have a major effect on the aerodynamic loads on the building model. Moreover, it can be observed that the turbulence intensity at  $z > 1.50 h$  is rather low in both ABL simulations, a known issue indicating the difficulty in creating large turbulence intensity high up from the ground surface.

The profiles of the integral turbulence length scale are shown in Figure 34.

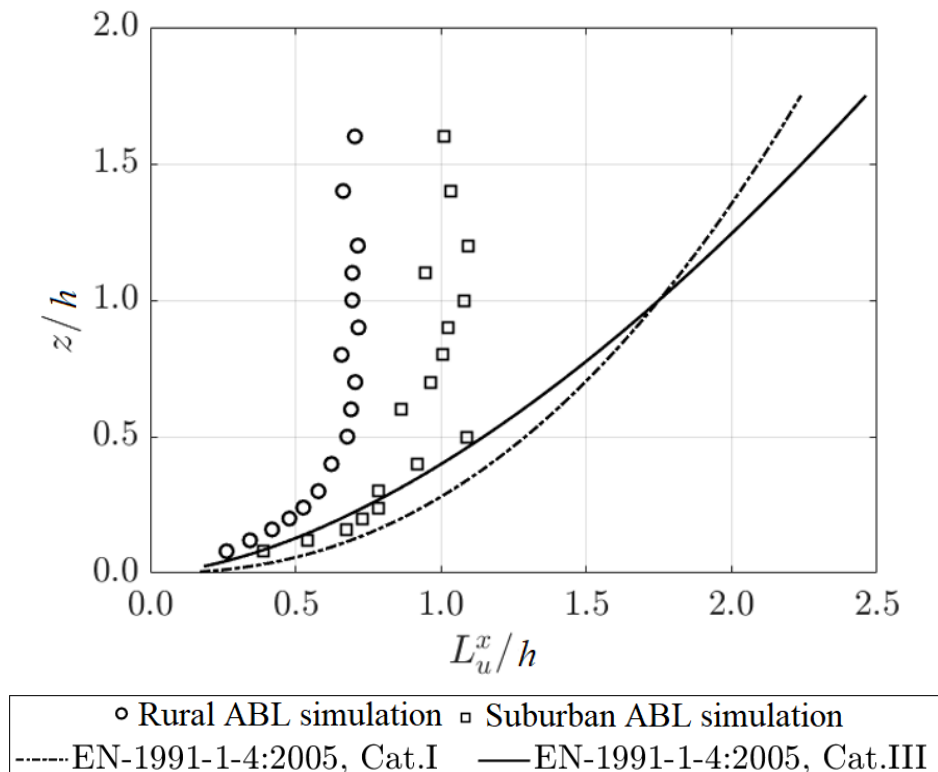


Figure 34. Integral turbulence length scale profiles in the rural and suburban ABL simulations and Eurocode [44]

The integral turbulence length scale in the wind tunnel corresponds reasonably well to the Eurocode [44] profiles only close to the ground, i.e., for  $z < 0.25 h$ . With an increase in height, the profiles remain almost constant. This is because the enclosed wind-tunnel test section does not allow for large eddies to develop fully, in agreement with Kozmar [144], Golubić et al. [145].

Figure 35 shows a comparison of the normalized power spectral density  $S_u$  of the streamwise fluctuating velocity component  $u'$  observed at  $h$  in both ABL models. The spectra of both ABL models correspond well with the von Kármán [146] spectrum for all frequency ranges. The characteristic  $-2/3$  slope is evident, i.e., the Kolmogorov [147] inertial subrange. The spectra evaluated at other heights exhibit similar trends, and are thus not reported.

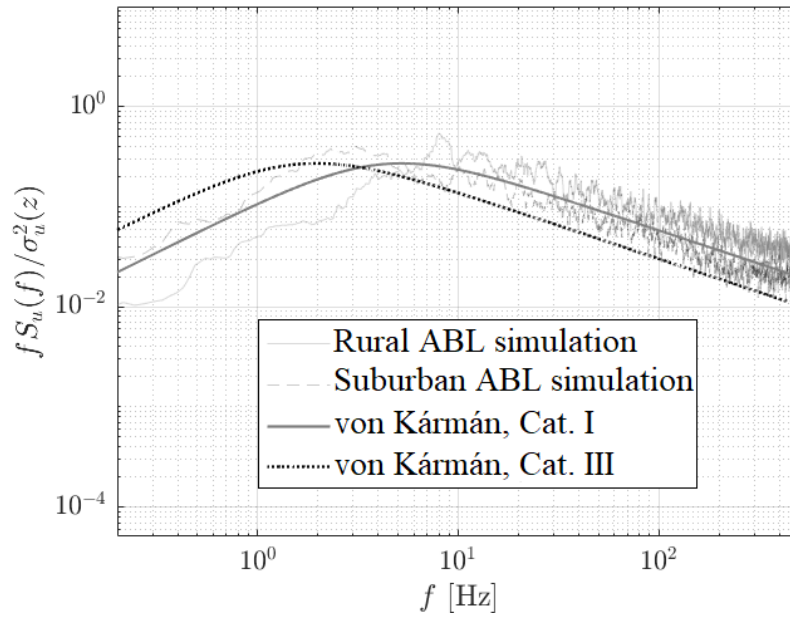


Figure 35. Power spectral density of longitudinal velocity fluctuations in the rural and suburban ABL simulations

To test the experimental setup, pressure measurements were performed on the single-skin building model at  $\beta = 0^\circ$ . The results were compared with Tamura [148]. The ABL profiles are first compared for the suburban ABL category III model, Figure 36.

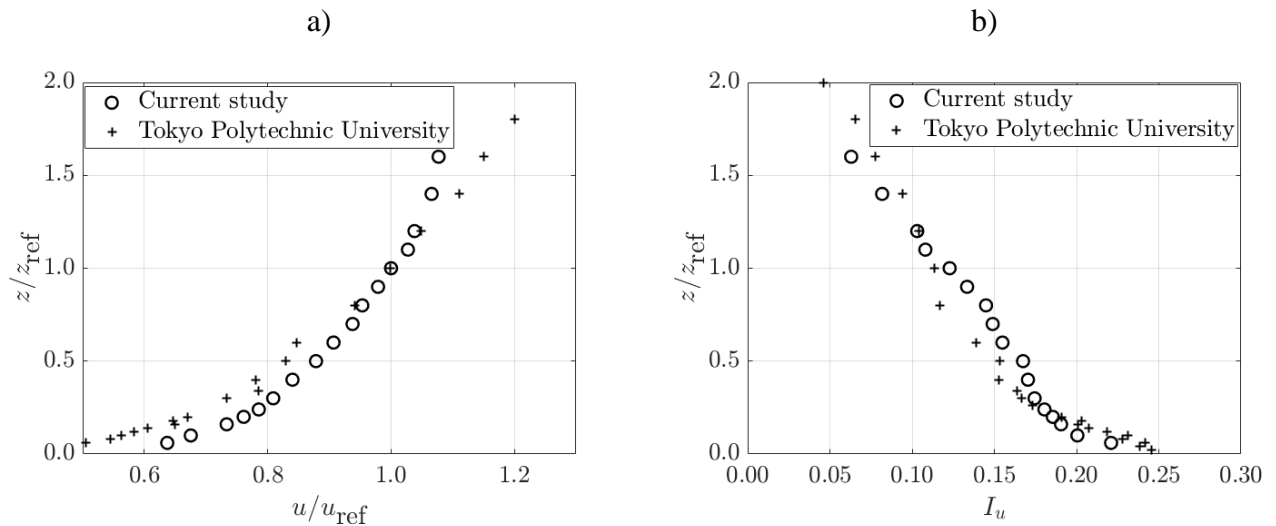


Figure 36. Comparison of the created suburban ABL simulation with the ABL profiles reported in Tamura [148]: a) mean flow velocity, b) longitudinal turbulence intensity

Although there are some differences between the two ABL profiles, most likely caused by the different experimental hardware, they are small enough to enable a good comparison to be

made between the mean pressure coefficients from Tamura [148] and the present study, Figure 37.

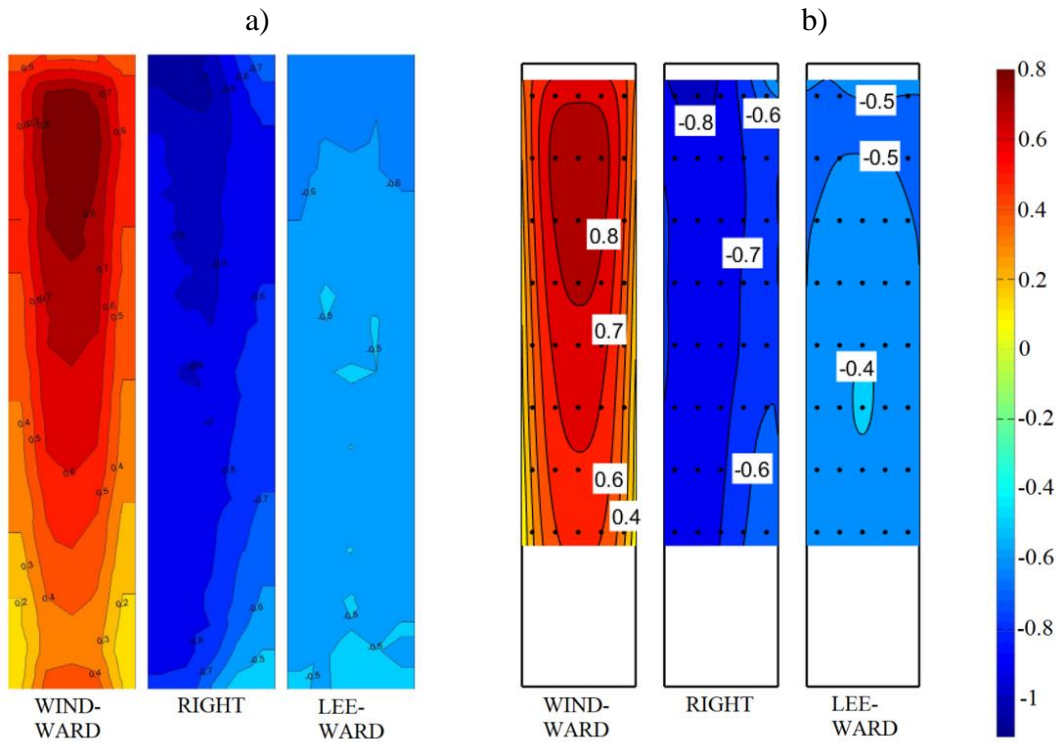


Figure 37. Comparison of the mean pressure coefficient  $\overline{C_p}$  distribution on the building model of a) Tamura, [148] and b) the present study

The pressure distribution in the present study is shown only for the area where the pressure sensors were located, as indicated by the black dots in Figure 37b. No extrapolation was performed, which is exhibited by the lack of data (white area) near the top and bottom of the building model. Since the building model is symmetric according to the main flow direction at  $\beta = 0^\circ$ , the pressure distribution is shown only on one lateral surface. The  $C_p$  distribution in Tamura [148] and the present study have the same trend on all surfaces, as well as similar values of mean  $C_p$ . On the windward surface, the stagnation point is clearly shown at  $\sim 0.75h$ , in agreement with Baines [75]. The maximum mean  $C_p$  of  $\sim 0.8$  is in both cases on the windward surface.  $C_p$  gradually decreases towards the ground as the mean flow velocity is impacted by the surface roughness. On the right-hand lateral surface, Tamura [148] reports the minimum mean  $C_p$  of  $\sim -1$ , while in the present study  $C_p$  is  $\sim -0.9$  at this same location (top left corner in Figure 37). This is most likely due to the slight differences in the ABL profiles impinging on the building model. The absolute  $C_p$  decreases in the main flow direction in both cases. The pressure distribution on the leeward surface is similar in Tamura [148] and in the present study, while the mean  $C_p \sim -0.5$  is nearly constant on the entire leeward surface.



A comparison of the mean across-wind moment coefficient  $\overline{C_{ML}}$  and along-wind moment coefficient  $\overline{C_{MD}}$  determined using the HFFB on the single-skin building model in the present study with the moment coefficients calculated using the Tamura [148] data is shown in Figure 38.

$\overline{C_{ML}} = 0$  at  $\beta = 0^\circ$  and  $45^\circ$  due to the symmetry of the building model relative to the flow direction. This is due to the vortices that shed concurrently on the building model, which means that the average  $\overline{C_{ML}}$  is zero. The maximum  $C_{ML}$  is at  $10^\circ < \beta < 15^\circ$ . This is likely due to the orientation of the building model, where one of the surfaces is at a low angle to the main flow direction, thus exerting the most wind load in the across-wind direction.  $\overline{C_{MD}}$  has a maximum at  $\beta = 45$ , likely due to the largest blockage in this case as the building's base diagonal is perpendicular to the flow. The lowest along-wind load appears at  $\beta = 15^\circ$ , which corresponds to the maximum across-wind load.

The same trend is observed in both sets of results, while the HFFB results are offset by  $\sim 10\%$ , likely due to: a) the difference in the ABL profiles reported in Figure 36; and b) the integration of surface pressure over the building model surface. Even though the building model in Tamura [148] was equipped with 125 pressure taps on each building model surface, the discretization inevitably introduces errors in pressure integration over the surface. Since the trends in both moment coefficients are similar and the differences are constant (clear offset), these results may be adopted to validate the experimental setup of the present study.

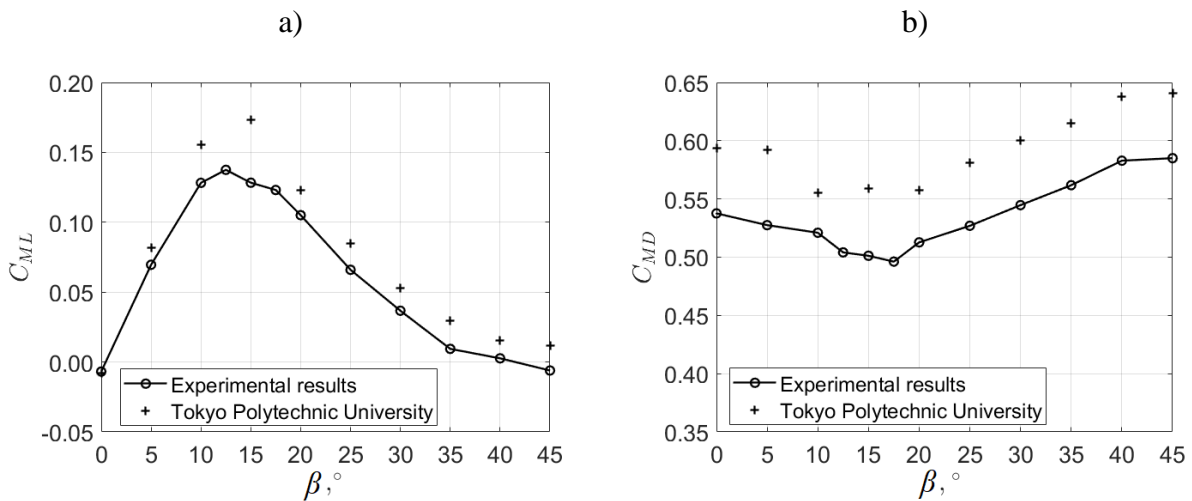


Figure 38. Validation of the HFFB results: a) across-wind moment coefficient  $C_{ML}$ , b) along-wind moment coefficient  $C_{MD}$

## 7.2 The aerodynamic effects of façade porosity

The first set of experiments was performed on the 1:1:5 tall building model. Aerodynamic loads were exerted by the ABL simulation created to correspond to Eurocode [44] ABL category III. The reference case is the single-skin building model. After the measurements of the reference case, three PDSF systems of the 25%, 50% and 65% porosities were tested. Measurements were performed using an HFFB and a surface pressure measurement system. The experiments were performed for  $0^\circ < \beta < 45^\circ$  with a  $5^\circ$  increment, Figure 39. This is considered sufficient for the present experimental campaign due to the symmetry of the principal building model. Measurements were also carried out for  $\beta = 12.5^\circ$  and  $\beta = 17.5^\circ$  to gain further evidence in support of the prospective conclusions.

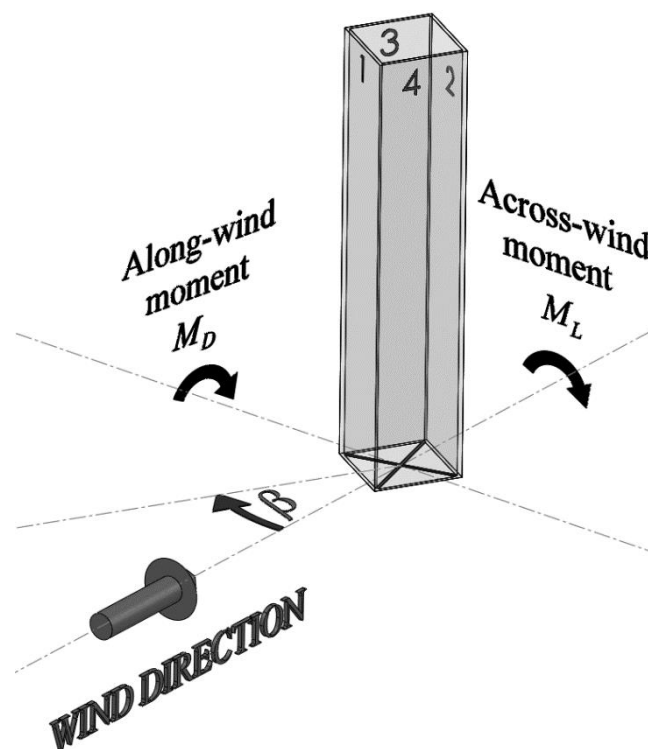


Figure 39. Flow incidence angle  $\beta$  and the aerodynamic moments acting on the building model

The loads recorded on the principal building model also took into account the natural frequency of the model-HFFB system as well as the aerodynamic loads. Therefore, the loads recorded at the base of the building model had to be corrected, and the effects of amplification had to be discarded, in order to accurately evaluate the aerodynamic forces and moments on the building model. To determine the natural frequency of the experimental system, an impulse loading test was performed. This was done by exciting the system with a rubber hammer and recording its response with the HFFB. The analysis of the Fourier transform of the signal indicated two natural frequencies at 28 Hz and 37 Hz, Figure 40. These frequencies were

accordingly filtered out using a low-pass filter to ensure that the natural frequencies of the building model do not affect the aerodynamic loads on the principal building model.

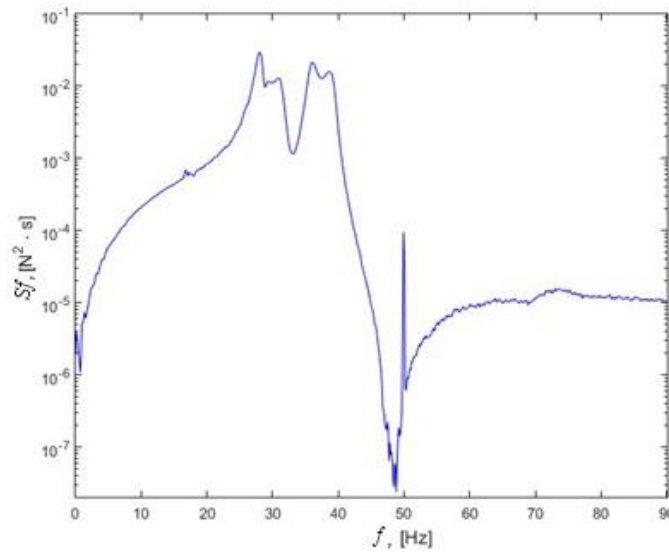
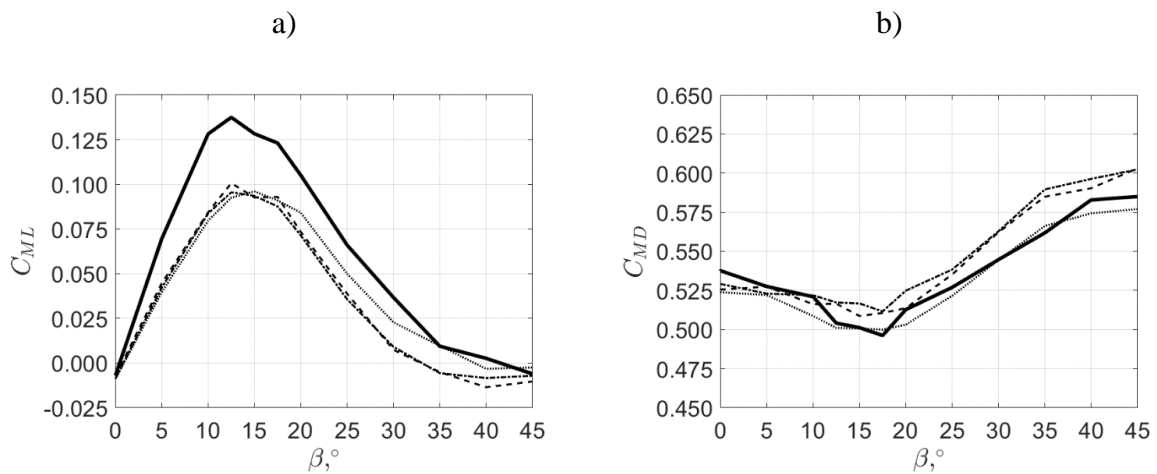


Figure 40. Power spectral density of force fluctuations exerted by an impulse load of the principal building model

### 7.2.1 Integral aerodynamic load moments

All the HFFB experiments were performed at the sampling rate of 2 kHz and a time record length of 100 s.  $\overline{C_{ML}}$  and  $\overline{C_{MD}}$  and their respective standard deviations,  $\sigma_{CML}$  and  $\sigma_{CMD}$ , are shown in Figure 41.



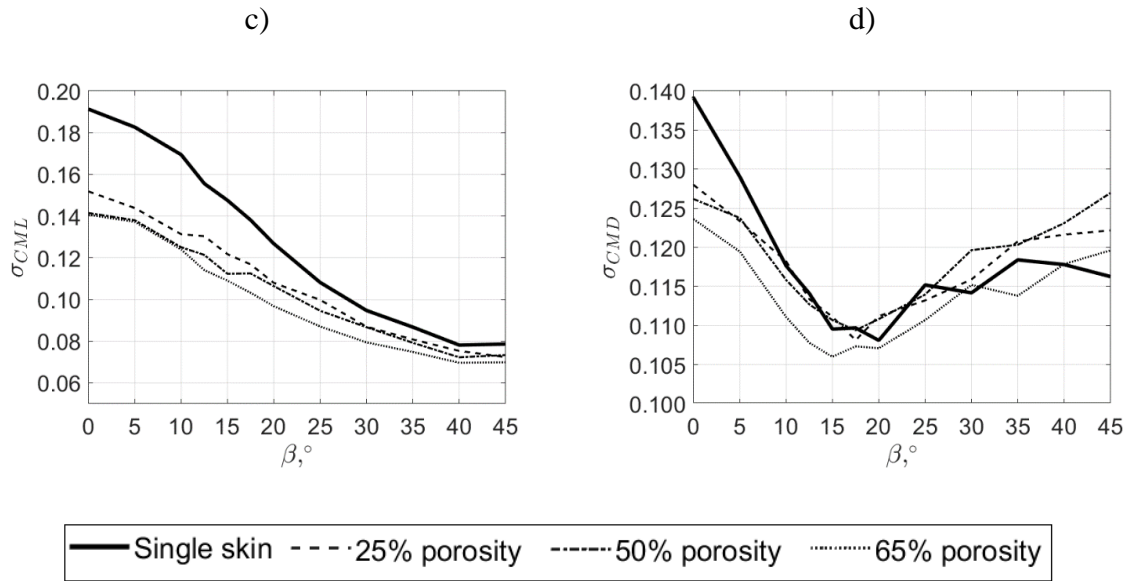


Figure 41. HFFB measurements of the building model with single-skin and three porous outer skin porosities, a)  $\overline{C_{ML}}$ , b)  $\overline{C_{MD}}$ , c)  $\sigma_{CML}$  and d)  $\sigma_{CMD}$

Figure 41a shows  $\overline{C_{ML}}$  on the principal building model for various  $\beta$ . At both  $\beta = 0^\circ$  and  $\beta = 45^\circ$  the building orientation is symmetric to the flow direction. As the flow separates on the leading edges of the building model,  $\overline{C_{ML}}$  at  $\beta = 0^\circ$  and  $\beta = 45^\circ$  was supposed to be zero. However, even a very minor misalignment in the building model orientation may cause a slightly asymmetrical mean flow around the building model, and thus a slight discrepancy of the across-wind moment from zero, e.g., Figure 41a.

The largest difference in the  $\overline{C_{ML}}$  between the reference (single-skin) building model and the building model equipped with various PDSF systems is at  $\beta = 12.5^\circ$ , where the maximum  $\overline{C_{MD}}$  appears. The peak  $\overline{C_{ML}}$  for all studied PDSF porosities is  $\sim 13\%$  lower than the respective peak on the single-skin building model, thus indicating that the effect of the PDSF regarding the maximum  $\overline{C_{ML}}$  is similar for all PDSF porosities. A decrease in the peak  $\overline{C_{ML}}$  of the principal building model equipped with PDSF systems is likely due to a more exhibited surface roughness of the building model because of the openings on its outer façade. This characteristic of the PDSF building models causes modifications in the vortices shed from the building model lateral surfaces, the vortices considered to be a major source of across-wind building model vibration.

Figure 41c shows  $\sigma_{CML}$ , where the maximum  $\sigma_{CML}$  is at  $\beta = 0^\circ$  due to the most pronounced vortex-induced vibration at this  $\beta$  and it monotonically decreases to its minimum at  $\beta = 45^\circ$ , where the diagonal of the cross-section is aligned with the flow. The  $\beta = 45^\circ$  is the most streamlined configuration, where the effect of vortex-induced vibration is less exhibited. The large difference of  $\sim 27\%$  between the  $\sigma_{CML}$  for the single-skin building model and the PDSF building models of any porosity is at  $\beta = 0^\circ$ . The difference in  $\sigma_{CML}$  between the building models with

and without PDSF systems gradually decreases to  $\sim 10\%$  at  $\beta = 45^\circ$ . The PDSF system generally yields a substantial decrease in  $\sigma_{\text{CML}}$ . Since the main cause of  $\sigma_{\text{CML}}$  is vortex-induced vibration, the porosity of the outer façades yields lower peak pressure fluctuations on the lateral building model surfaces caused by shed vortices. It is thus proven that a PDSF system is characterized by more favorable aerodynamic behavior (less across-wind vibration) compared to a single-skin façade system, which may in turn enhance the serviceability of tall buildings.

There is a very minor effect of PDSF systems regarding the  $\overline{C_{MD}}$  of the studied building models, Figure 41b. For  $0^\circ < \beta < 25^\circ$ ,  $\overline{C_{MD}}$  is nearly the same in all test cases with a discrepancy in the range of  $\pm 5\%$  without a clear trend. For  $25^\circ < \beta < 45^\circ$ , the results for the single-skin building model and the building model equipped with a 65% PDSF system are very similar, while the results for the 25% and 50% PDSF systems are both  $\sim 8\%$  larger. These results indicate that the very porous PDSF system (65%) exhibits quite the same behavior regarding  $\overline{C_{MD}}$ , while the 25% and 50% PDSF systems tend to vibrate more intensely in the main flow direction at  $\beta > 30^\circ$ .

In terms of  $\sigma_{\text{CMD}}$ , Figure 41d, the largest difference of  $\sim 10\%$  is at  $\beta = 0^\circ$  for the single-skin and PDSF building, similarly to  $\sigma_{\text{CML}}$ . For  $0^\circ < \beta < 20^\circ$ ,  $\sigma_{\text{CMD}}$  monotonically decreases, and it is lower for all PDSF building models compared to the single-skin building model, particularly for the more porous PDSF systems. At  $\beta > 45^\circ$ , there is no clear trend in the results.

These results indicate that the application of PDSF systems on tall buildings may yield some advantages, while no clear drawback regarding integral aerodynamic loads was observed.

## 7.2.2 Power spectral density of aerodynamic load fluctuations

The power spectra of integral across-wind moments are shown in Figure 42, where the  $x$ -axis is the dimensionless frequency  $f \cdot d/v_\infty$ , the  $y$ -axis is the dimensionless moment power spectra  $S_M \cdot f/\sigma^2$ ,  $f$  is the frequency in Hz,  $d$  is the width of the building model in m,  $v_\infty$  is the freestream velocity at the location of the building model in m/s,  $S_M$  is the integral moment power spectrum in  $\text{N}^2\text{m}^2\text{s}$ , and  $\sigma^2$  is the integral moment variance in  $\text{N}^2\text{m}^2$ .

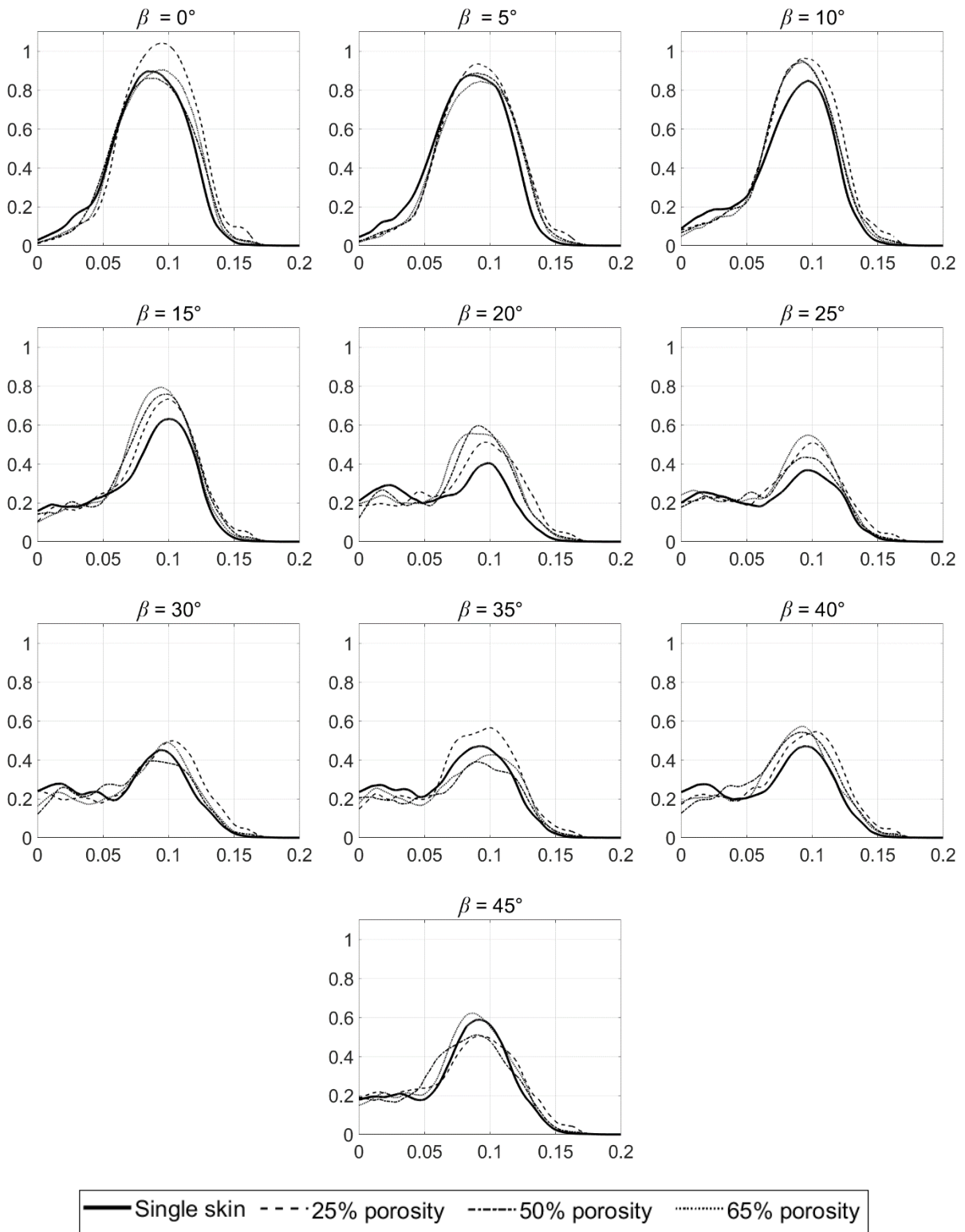
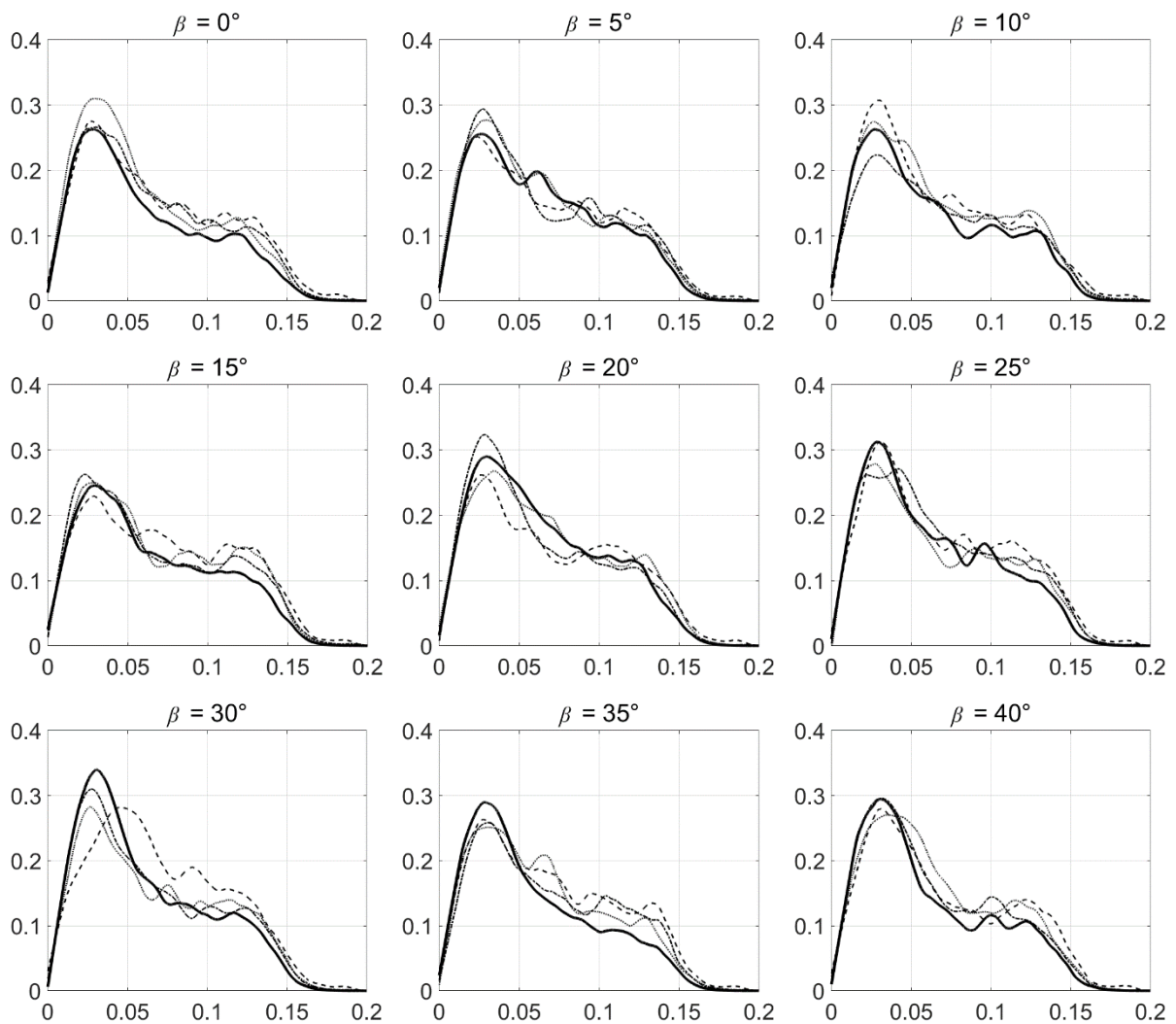


Figure 42. Integral across-wind moment power spectra for  $0^\circ < \beta < 45^\circ$  with the  $5^\circ$  increment

There is a characteristic peak which corresponds to the frequency of vortex-induced vibration. The largest peak magnitude is observed at the low flow incidence angles  $0^\circ < \beta < 15^\circ$ . This was expected since in this orientation the vortex-induced vibration of the building

model is indeed exhibited the most. At  $\beta = 0^\circ$ , the flow is perpendicular to the windward building model surface where the stagnation zone occurs near the top of the windward building model surface. The flow separates intermittently on the leading edges of the lateral surfaces, and it is further transferred by the freestream flow. There is strong suction on the leeward surface. The shed vortices cause the building model to periodically move (vibrate) from one lateral side to the other. As  $\beta$  increases, the effect of this across-wind building model vibration decreases in magnitude due to the less exhibited vortex-shedding magnitude.

There is an increase in the Strouhal frequency at  $\beta = 0^\circ$  for the PDSF with 50% porosity, while the peak frequency decreases at  $\beta > 15^\circ$  for all tested porosities. However, it is rather ambiguous whether the PDSF significantly alters the peak frequency of the across-wind moment variations.



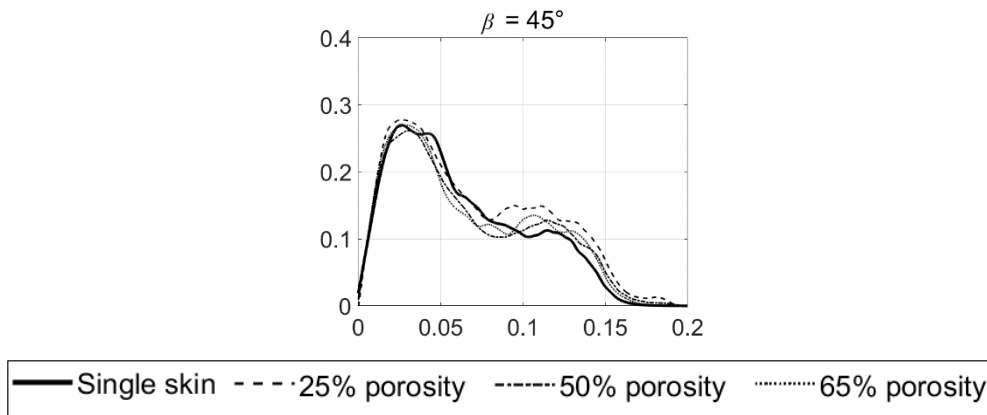


Figure 43. Integral along-wind moment power spectra for  $0^\circ < \beta < 45^\circ$  with a  $5^\circ$  increment

There is generally a good agreement of the spectra, more exhibited at a lower  $\beta$ . For  $15^\circ < \beta < 25^\circ$ , the peak magnitude in the PDSF cases of all porosities is larger than the single-skin configuration, a phenomenon which may be relevant for practical applications. There is no clear effect of the PDSF system porosity at  $\beta > 30^\circ$ .

The power spectra of integral along-wind moments are shown in Figure 43, where the  $x$ -axis is the dimensionless frequency  $f \cdot d / v_\infty$ , the  $y$ -axis is the dimensionless moment power spectra  $S_M \cdot f / \sigma^2$ ,  $f$  is the frequency in Hz,  $d$  is the width of the building model in m,  $v_\infty$  is the freestream velocity at the location of the building model in m/s,  $S_M$  is the integral moment power spectrum in  $N^2 m^2 s$ , and  $\sigma^2$  is the integral moment variance in  $N^2 m^2$ .

The along-wind moment power spectra are not as strong as the across-wind spectra, Figure 43, a phenomenon exhibited in lower peak magnitudes. The spectra are characterized by a similar shape of the curves in all experiments and all  $\beta$ , both for the single-skin and PDSF building models. The major spectral peak at  $\sim 0.04$  is a consequence of the incident flow characteristics, while another minor peak may be observed at  $\sim 0.15$  as the spectral curve monotonically decreases with the increasing frequency.

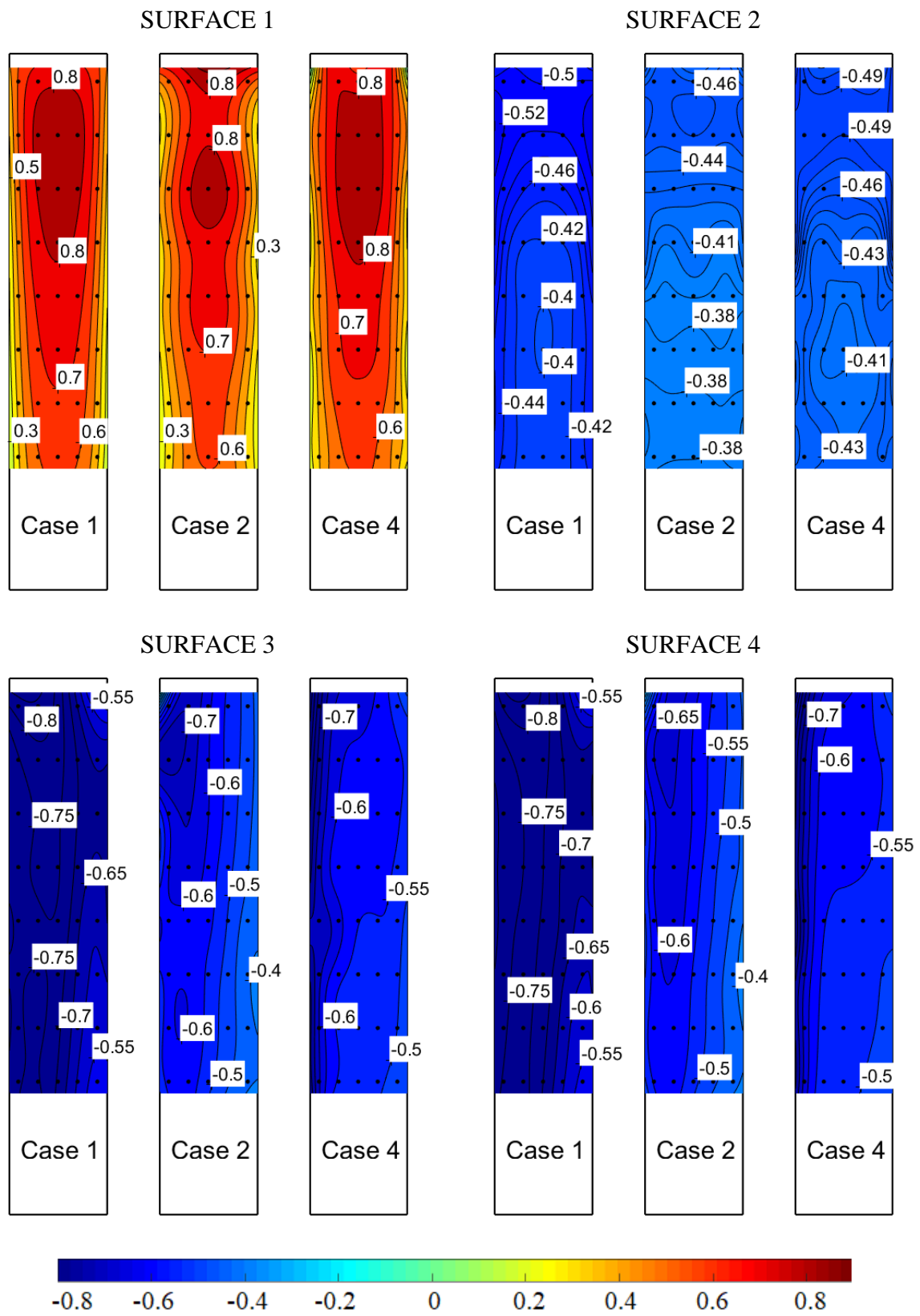
### 7.2.3 Surface pressure

The mean surface pressure distribution on the building model surfaces with and without the PDSF systems is shown in Figure 44. Contour maps of  $\overline{C_p}$  were generated by a two-dimensional linear interpolation of the data recorded using pressure taps. The interpolation was performed by expanding the 8 by 5 matrix of the pressure tap data into a refined mesh of 375 by 100 to enhance the presentation. The results of the interpolated  $\overline{C_p}$  function contain the exact  $\overline{C_p}$  measured in each pressure tap at the respective position. The pressure taps are presented as black dots. Since the interpolation inevitably introduces errors, the interpolated  $\overline{C_p}$  distribution

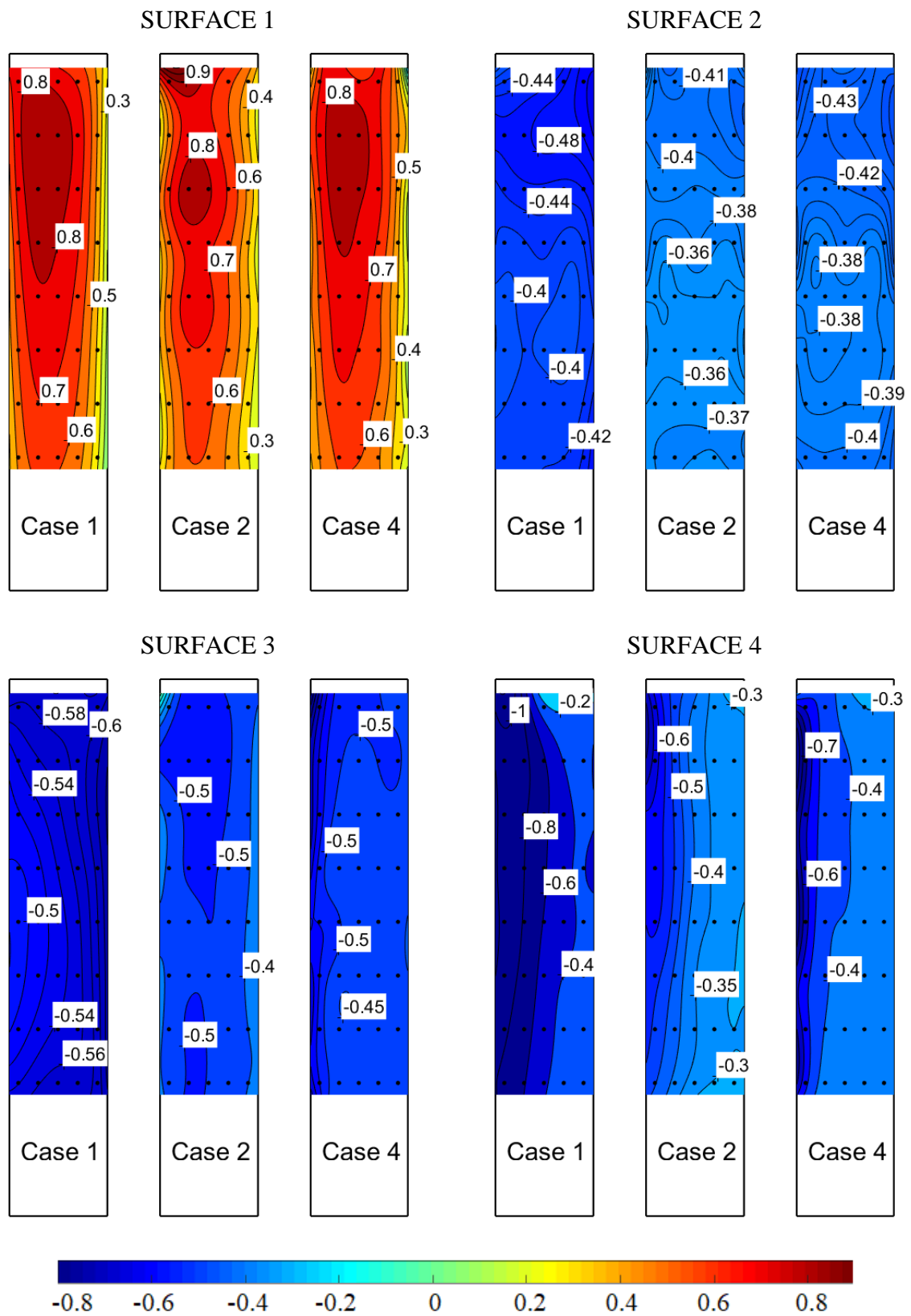


was limited to a vertical distance of  $0.025h$  ( $h$  being the model height) from the top to the bottom row of the pressure taps. This indicates that the  $\overline{C_p}$  distribution at the very top of the building model and near to its bottom at  $0.225h$  is not known because there were no pressure taps at these locations. These areas are exhibited as white areas in Figure 44 and in other figures of this type. In all panels, the left vertical boundary is the leading edge relative to the main flow. The necessary exception to this rule is the windward and leeward surface at  $\beta = 0^\circ$  because in this case both surfaces are perpendicular to the flow, i.e., both vertical edges are at an equal distance to the inlet. However, on those surfaces, at  $\beta = 0^\circ$ , the pressure distribution is vertically symmetric, so the orientation is basically irrelevant. The surfaces depicted in Figure 44 are numbered from 1 to 4, the same approach as in Figure 39. Cases 1 through 4 refer to the PDSF system, where Case 1 is the reference case (single-skin) building model, Case 2 is the 25% porosity PDSF system, and Case 4 is the 65% porosity PDSF system, Figure 19.

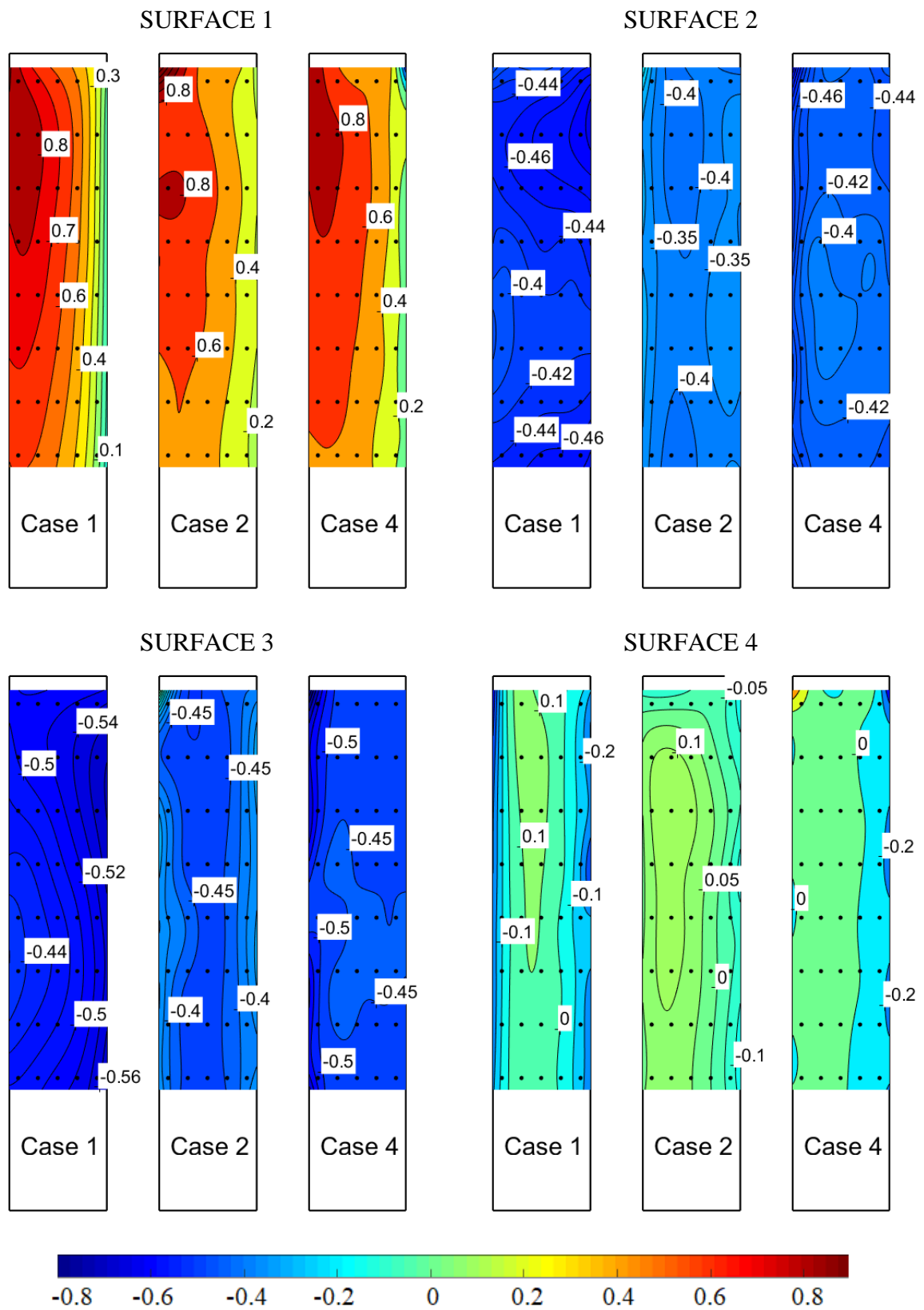
$\overline{C_p}$  for  $\beta = 0^\circ$



$\overline{C_p}$  for  $\beta = 15^\circ$



$\overline{C_p}$  for  $\beta = 30^\circ$



$\overline{C_p}$  for  $\beta = 45^\circ$

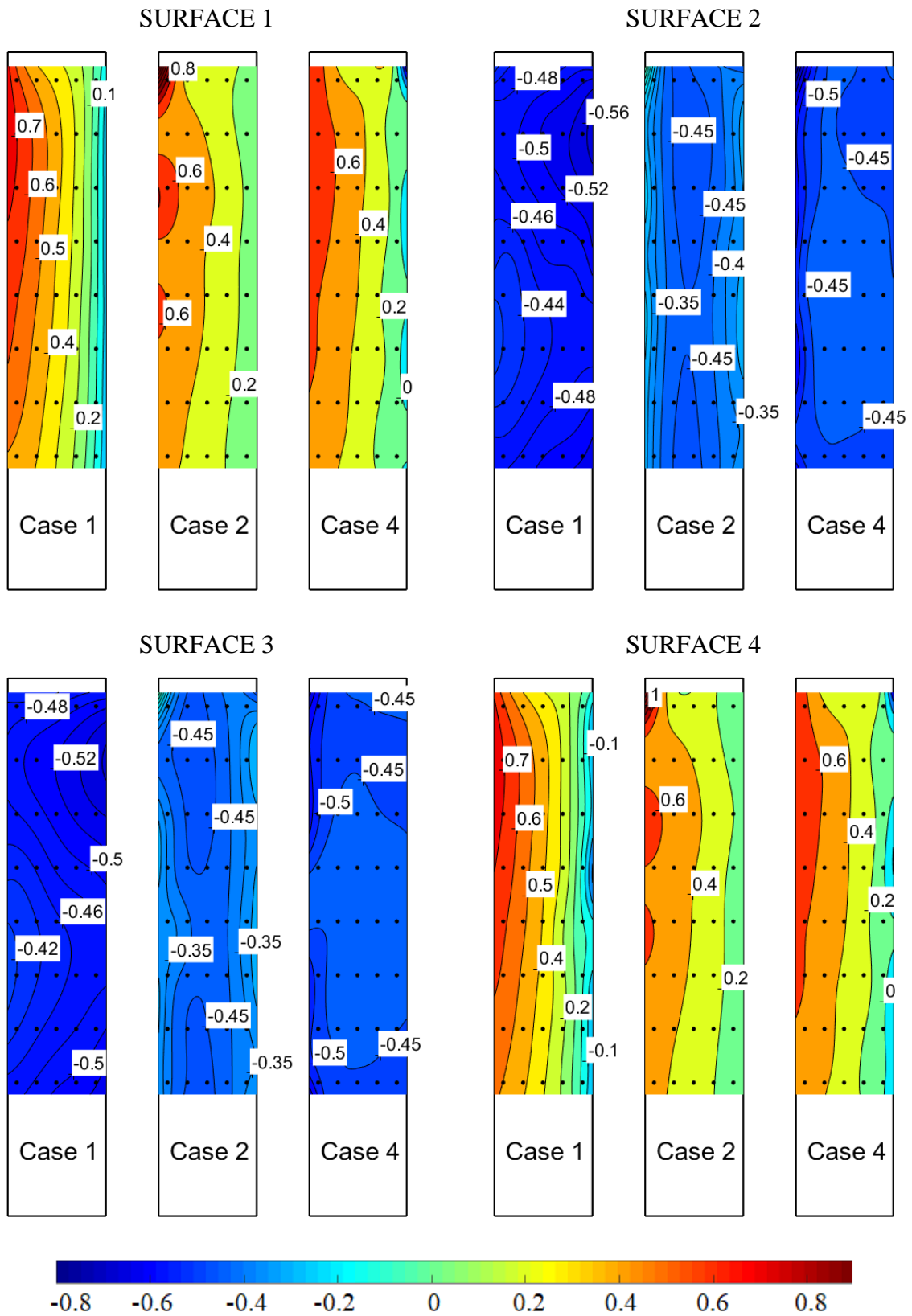


Figure 44.  $\overline{C_p}$  distribution on the principal building model with and without PDSF systems

The  $\overline{C_p}$  distribution on the single-skin building model (Case 1) is in agreement with Tamura [148], with all the  $\overline{C_p}$  obtained in the present study slightly lower because of the differences in the ABL simulations. The stagnation point on the windward surface is at  $\sim 0.75h$ , in agreement with Baines [75]. At  $\beta = 0^\circ$ , a substantial difference for Surface 1 (windward surface) in the  $\overline{C_p}$  distribution in Cases 1 and 2 is particularly exhibited in the size of the stagnation zone, a phenomenon caused by the low porosity (greater solidity) of the outer façade in Case 2 compared to the single-skin building model (Case 1). There is a correlation between the larger surface pressure situated directly downstream of the openings on the outer façade, thus indicating a sheltering of the inner façade downstream of the solid portions of the porous outer façade surface. The outer, low-porous façade yields a decrease in  $\overline{C_p}$  of  $\sim 0.1$  on the entire inner surface. One exception is the pressure tap situated in the stagnation zone, which is the tap directly downstream of the opening on the outer façade, thereby recording almost undisturbed freestream dynamic pressure. This is an important finding which supports the fact that relatively large openings on the outer façade can still yield local regions of high pressure on the inner façade. The  $\overline{C_p}$  distribution in Case 1 (single skin) and Case 4 (65% porosity façade) is similar, thus indicating that the  $\overline{C_p}$  distribution on the inner façade downstream of a very porous outer façade is basically the same as on the single-skin façade without a PDSF system.

The effect of the PDSF system on  $\overline{C_p}$  on the (leeward) Surface 2 at  $\beta = 0^\circ$  is negligible because of the wake flow which exerts evenly distributed suction on the leeward surface which here proves not to be influenced by the characteristics of the PDSF systems. On the other hand, there is a noticeable difference in the  $\overline{C_p}$  distribution pattern, changing from ellipses in Case 1 to horizontal curved lines in Case 2 and back to ellipses in Case 4. This is because of the altered characteristics in the flow separated from the vertical lateral surfaces and the top surface in various PDSF configurations, where the single-skin and less porous PDSF system are characterized by the same trend in the results.

The  $\overline{C_p}$  distribution on Surfaces 3 and 4 is similar since these surfaces are symmetric relative to the main flow direction. In Case 1, there is suction near the leading edge due to flow separation. The suction decreases towards the trailing edge as the flow tends to reattach on the lateral surfaces (still to be confirmed by flow visualization), thus resulting in  $\overline{C_p}$  increasing from  $-0.8$  near the leading edge to  $-0.55$  near the leeward edge. In the 25% porosity PDSF experiment (Case 2), the suction is lower ( $-0.65$  compared to  $-0.8$ ) than on the single-skin building model (Case 1). It is clear that there are substantial modifications in the gap flow characteristics near the vertical lateral building model surfaces for various PDSF systems, modifications which in turn dictate the pressure distribution features on the inner building model façade.

The effect of the PDSF system on  $\overline{C_p}$  observed at  $\beta = 0^\circ$  is similar at other studied  $\beta$ , i.e.,  $\beta = 15^\circ, 30^\circ$ , and  $45^\circ$ . For surfaces more directly subjected to the incident flow, a less porous

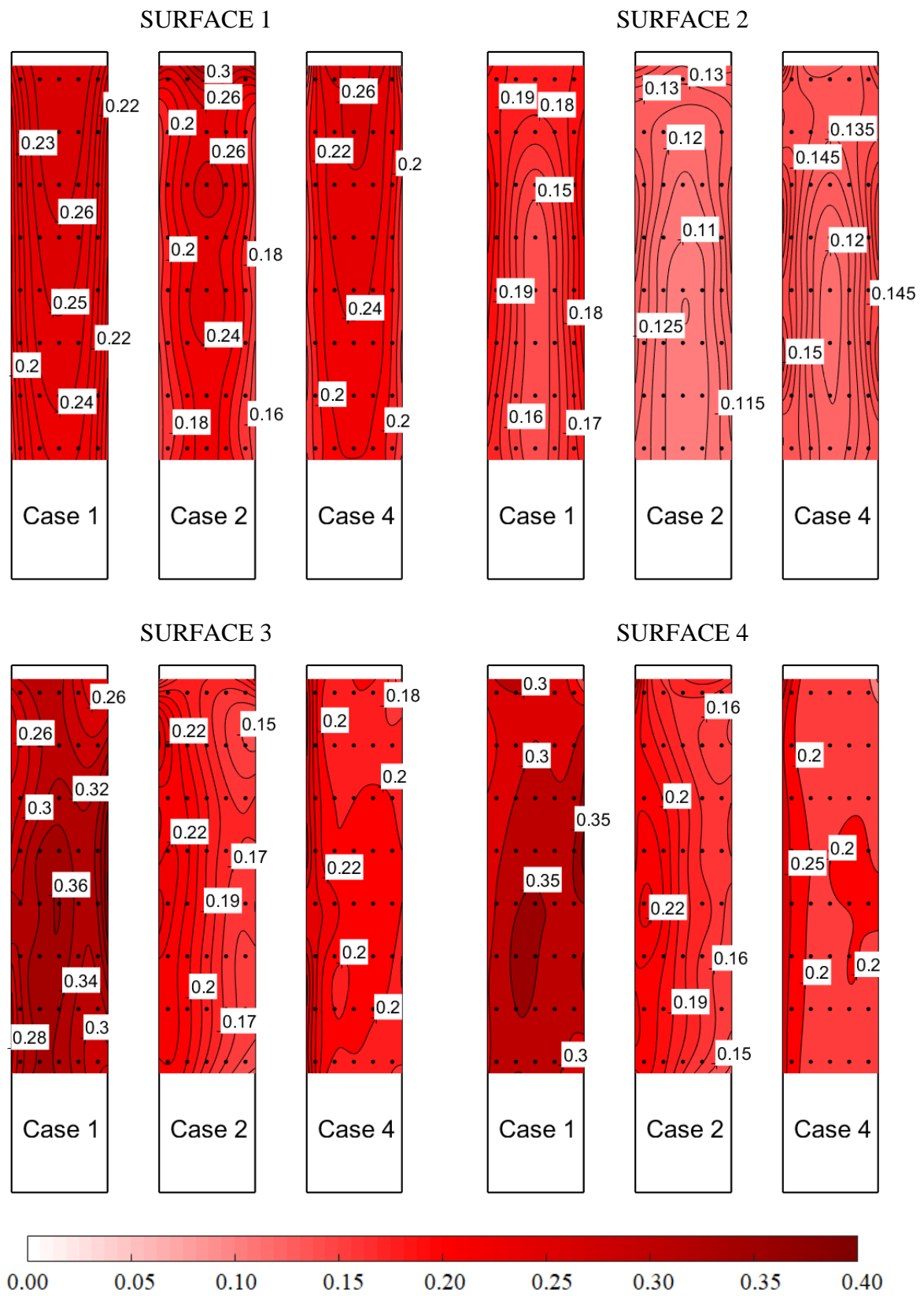
(more solid) outer façade causes a decrease in  $\overline{C_p}$ , while the trends observed on a more porous (less solid) façade are similar to the results on the single-skin façade (without a PDSF system). For the sake of clarity, the major findings in this regard are outlined in Table 3.

Table 3. The major effects of PDSF systems regarding the mean surface pressure on the inner building model façade

25% porosity PDSF system
<ul style="list-style-type: none"> <li>• A decrease in the peak <math>\overline{C_p}</math> by ~10% to ~20% depending on <math>\beta</math>;</li> <li>• A substantial change in the <math>\overline{C_p}</math> distribution pattern respective to openings on the outer building façade model, particularly exhibited on surfaces at a low <math>\beta</math>;</li> <li>• A possible occurrence of local high-pressure zones on surfaces at a low <math>\beta</math>;</li> <li>• Nonexistence of flow separation on the leading edge of the vertical lateral inner façade.</li> </ul>
65% porosity PDSF system
<ul style="list-style-type: none"> <li>• Peak <math>\overline{C_p}</math> and <math>\overline{C_p}</math> at a low <math>\beta</math> similar to those on the single-skin building model;</li> <li>• <math>\overline{C_p}</math> gradient on surfaces at a high <math>\beta</math> substantially smaller than on the single-skin building model.</li> </ul>

The standard deviation of  $C_p$  ( $\sigma_{Cp}$ ) is shown at  $\beta = 0^\circ$  and  $\beta = 45^\circ$  in Figure 45.

$\sigma_{Cp}$  for  $\beta = 0^\circ$





$\sigma_{Cp}$  for  $\beta = 45^\circ$

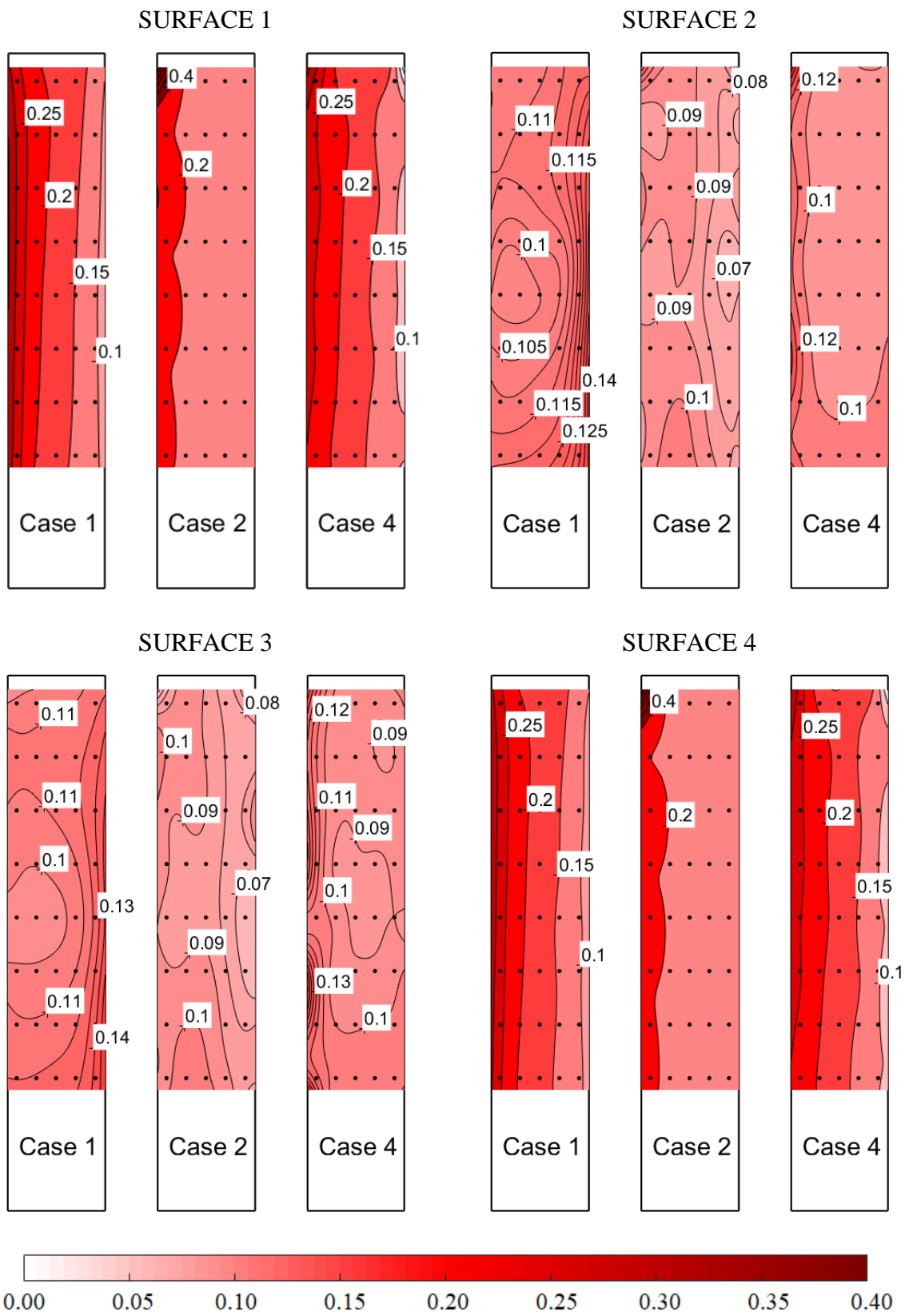


Figure 45. Distribution of  $\sigma_{Cp}$  on all four surfaces of the building model with and without a PDSF system

At  $\beta = 0^\circ$  on Surface 1 in Case 1 (single-skin building model),  $\sigma_{C_p}$  is generally constant over the entire windward surface of the building model ( $0.24 < \sigma_{C_p} < 0.26$ ). The 25% PDSF system (Case 2) yields a slightly lower  $\sigma_{C_p}$  on the entire surface, with the exception of the pressure taps directly downstream of the outer façade openings. This indicates a decrease in turbulence in the gap flow between the inner and outer façades and is the result of the sheltering effect of the outer, low porous façade. A large increase in  $\sigma_{C_p}$  is observed at the top of the building model, indicating the increased turbulence of the gap flow. The 65% PDSF system in Case 4 does not provide a substantial decrease in the gap flow turbulence due to less sheltering. A reduction of  $\sigma_{C_p}$  is found on the vertical edges, which is a consequence of the closed corners of the outer façade, which effectively separate the gap flow from the freestream flow at the building edges.

Surface 2 of Case 1 at  $\beta = 0^\circ$  shows large  $\sigma_{C_p}$  at the vertical edges, indicating the vortex-shedding phenomenon. The 25% PDSF system yields a significantly lower  $\sigma_{C_p}$  on the entire surface. The greatest reduction of  $\sim 50\%$  is recorded in the center of the surface, thus indicating the greatest sheltering effect in this surface area. It is important to emphasize that the decrease of  $\sigma_{C_p}$  does not necessarily yield a decrease in  $\overline{C_p}$ , Figure 44.

Surface 3 of Case 1 shows an increase in  $\sigma_{C_p}$  towards the leeward edge, which is likely due to a partial flow reattachment. This is further confirmed by a decrease in suction, Figure 44. The 25% PDSF yields a  $\sim 40\%$  lower  $\sigma_{C_p}$  over the entire surface, which is rather significant, with the greatest decrease observed at the leeward edges. The outer façade prevents the occurrence of flow reattachment on the inner façade, thus significantly diminishing the turbulent inflow at the inner corners of the building model. The 65% PDSF system in Case 4 also yields a significantly lower  $\sigma_{C_p}$ ; however, the effect is not as pronounced as at the corners. This means that the high porosity of the outer façade allows for flow into the gap between the inner and outer façades. Surface 4 is symmetric to Surface 3 for  $\beta = 0^\circ$ .

A very large  $\sigma_{C_p} \sim 0.3$  is recorded at  $\beta = 45^\circ$  on the windward corner of the single-skin building model. This indicates the increased turbulence as the flow splits into two symmetrical streams along Surfaces 1 and 4.  $\sigma_{C_p}$  decreases towards the right-hand edges of Surfaces 1 and 4, Figure 45, to  $\sim 0.1$ , thus indicating a decrease in the pressure fluctuations as the flow tends to reattach on the surfaces. While the  $\sigma_{C_p}$  of the single-skin building façade decreases almost linearly from  $\sim 0.3$  at the left edge to  $\sim 0.1$  at the right edge, the 25% PDSF system yields a decrease in the peak  $\sigma_{C_p}$  at the left edge to  $\sim 0.2$ , and further to  $\sim 0.1$ . This is an indication of the less turbulent flow in the gap between the inner and outer façades. The 65% PDSF system in Case 4 does not alter the  $\sigma_{C_p}$  on Surfaces 1 and 4 compared to Case 1, which indicates that the high porosity of the outer façade does not yield a lower turbulence in the gap flow as it interacts with the freestream.

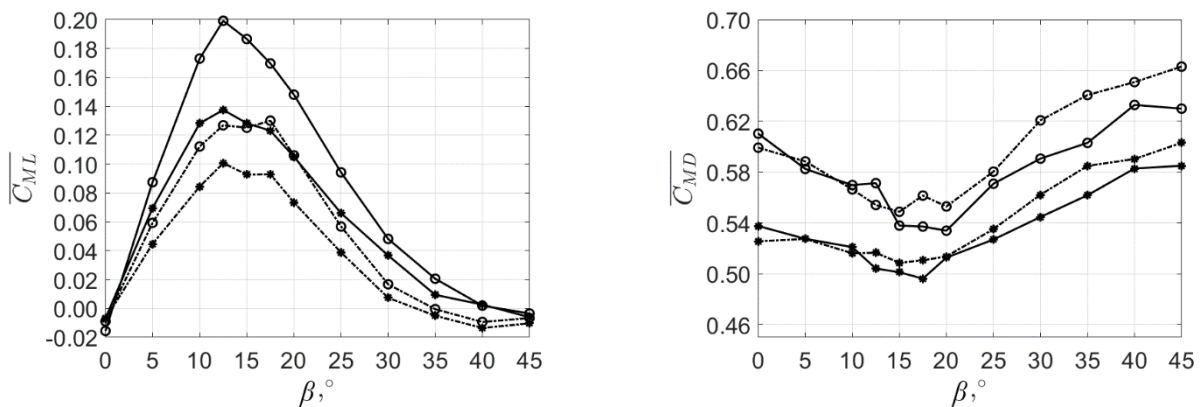
The  $\sigma_{C_p}$  on Surfaces 2 and 3 of the single-skin building model is rather uniform, except for a slight increase from  $\sim 0.10$  to  $\sim 0.12$  towards the right-hand vertical edge, which is an indication of the likely flow reattachment. The 25% PDSF system yields only a slight decrease in  $\sigma_{C_p}$  on those surfaces, with the greatest decrease at the leeward edge sheltered from the freestream flow. The effect of the 65% PDSF system is negligible in terms of the peak  $\sigma_{C_p}$ , with a slightly lower  $\sigma_{C_p}$  gradient.

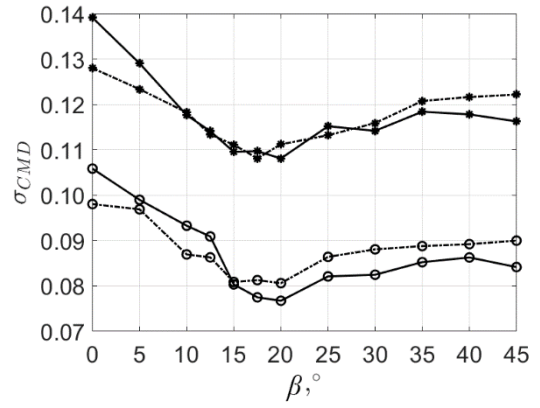
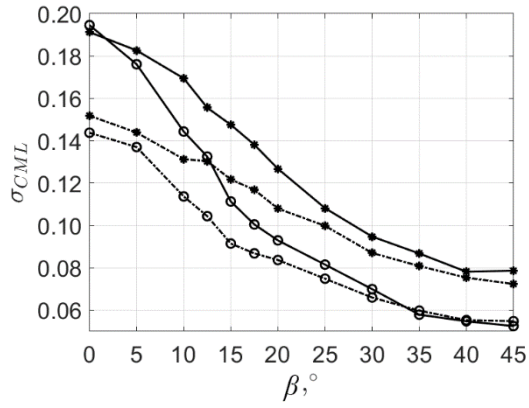
### 7.3 The effect of wind characteristics

Using the 1:1:5 tall building model, experiments were further performed to determine the effect of various inflow characteristics on the aerodynamic loads of the principal building model. Two ABL models were created to match Eurocode [44] category I (rural ABL model) and category III (suburban ABL model). The reference case was the single-skin building model. Four different porosities of the PDSF system were studied, i.e., 25%, 50% and 65%. The experiments were performed for  $0^\circ < \beta < 45^\circ$  with a  $5^\circ$  increment. Integral aerodynamic loads were measured using an HFFB, while the surface pressure distribution was assessed using a pressure measurement system.

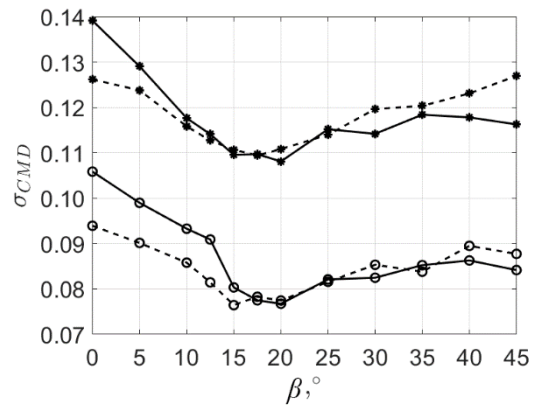
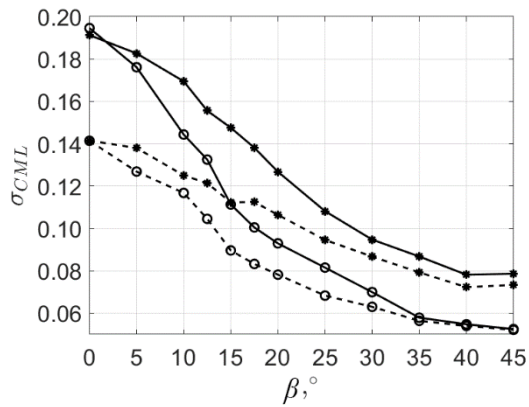
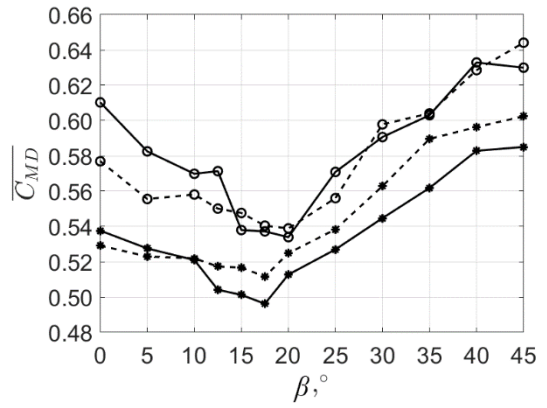
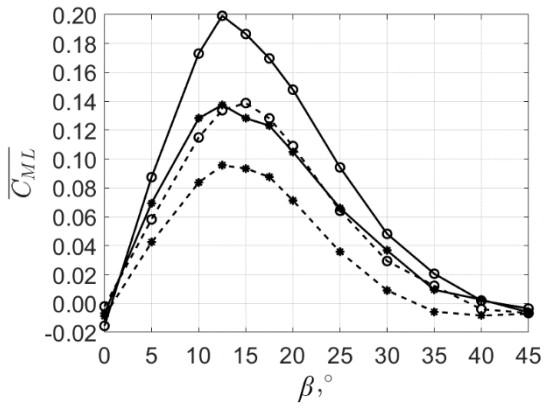
#### 7.3.1 Integral aerodynamic loads

$\overline{C_{ML}}$  and  $\overline{C_{MD}}$  and their respective standard deviations, analyzed on the principal building model equipped with various PDSF systems subjected to rural and suburban ABL simulations, are shown in Figure 46. The figure is arranged in three groups where each group consists of four panels. Each figure contains four lines, showing a comparison between the respective physical quantity on the single-skin building and one PDSF system in two ABL models.





—○— 0% porosity, rural ABL    - -○- - 25% porosity, rural ABL  
 —●— 0% porosity, suburban ABL    - -●- - 25% porosity, suburban ABL



—○— 0% porosity, rural ABL    - -○- - 50% porosity, rural ABL  
 —●— 0% porosity, suburban ABL    - -●- - 50% porosity, suburban ABL

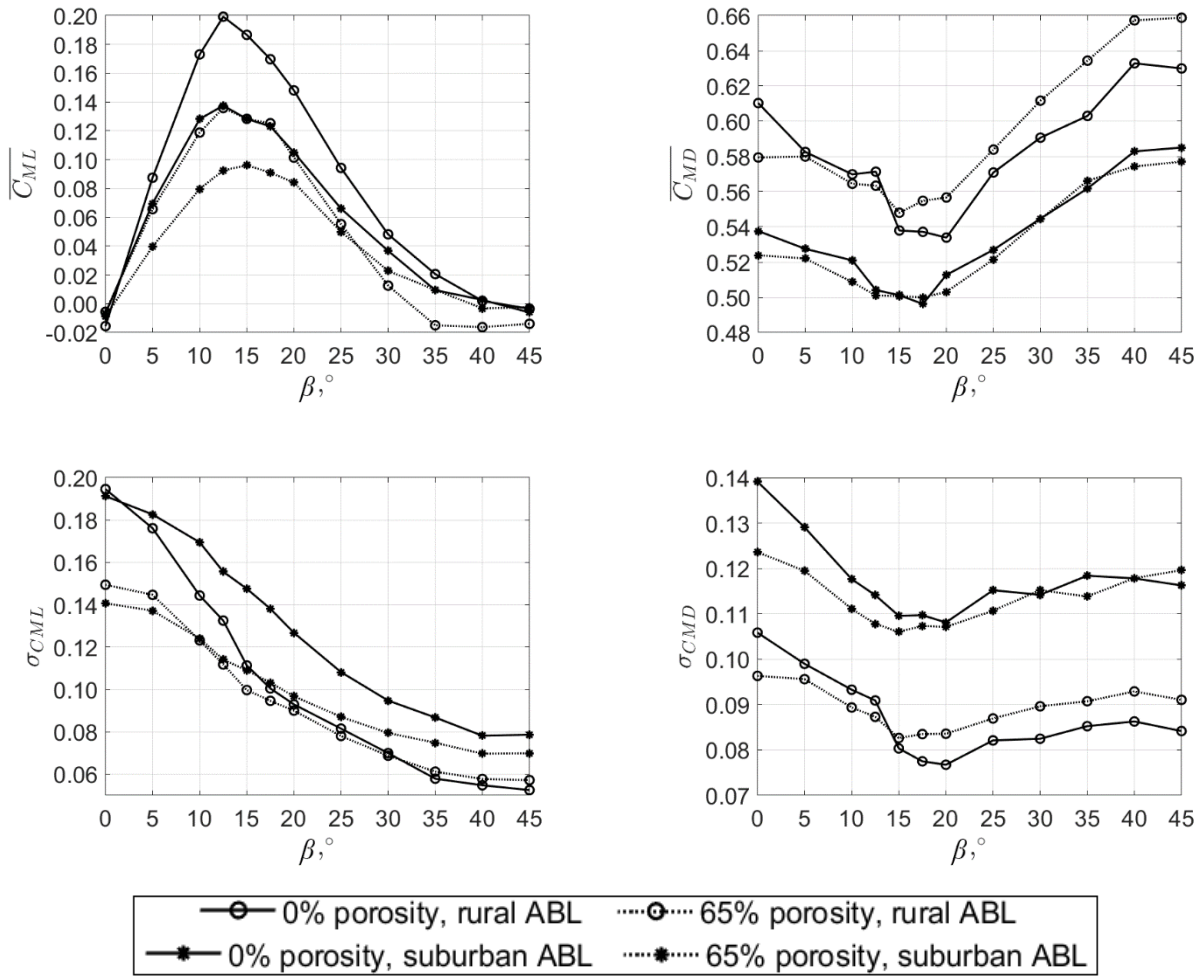


Figure 46. Mean across-wind and along-wind moment coefficients ( $\overline{C_{ML}}$ ,  $\overline{C_{MD}}$ ) and their respective standard deviations ( $\sigma_{CML}$ ,  $\sigma_{CMD}$ ) for the single-skin building model (0%), 25% and 65% PDSF systems in the rural and suburban ABL simulations

The  $\overline{C_{ML}}$  for all PDSF systems is nearly zero at  $\beta = 0^\circ$ , which was indeed expected due to the symmetric orientation of the building model relative to the main flow direction. The maximum  $\overline{C_{ML}}$  is at  $\beta = 12.5^\circ$ , most likely due to the low  $\beta$  of the windward building model surface, which yields consistently large across-wind loads. The  $\overline{C_{ML}}$  slowly decreases to zero as  $\beta$  increases to  $45^\circ$ . The maximum  $\overline{C_{ML}}$  (at  $\beta = 12.5^\circ$ ) is substantially greater (~30%) for the building model subjected to the rural ABL simulation. The reason for this is most probably the flow velocity that increases with the increasing height from the ground surface, i.e., although the mean flow velocity at the top of the building model is equal in both ABL simulations, the rural ABL simulation is characterized by higher velocity at lower heights compared to the suburban ABL simulation. The PDSF system of any porosity in the rural ABL simulation yields a lower  $\overline{C_{ML}}$  peak than the single-skin building model in the suburban ABL case. This is considered beneficial to the aerodynamic loads on the building model. The porosity of the PDSF system has a negligible effect on  $\overline{C_{ML}}$ .

The  $\sigma_{CML}$  reaches a maximum at  $\beta = 0^\circ$ , which was expected since vortex shedding is the most exhibited at this  $\beta$ . There is no substantial difference in the  $\sigma_{CML}$  in the two ABL simulations, which indicates that the difference in turbulence intensity of the airflow has little effect on the  $\sigma_{CML}$  at  $\beta = 0^\circ$ . The  $\sigma_{CML}$  in the rural ABL case decreases compared to the suburban ABL experiment, which is likely due to the increased effect of the turbulence intensity on the across-wind loads on the building model. The difference in  $\sigma_{CML}$  is greatest at  $\beta = 45^\circ$ , with the  $\sigma_{CML}$  in the rural ABL model  $\sim 20\%$  lower than the suburban ABL case. The PDSF system has the greatest effect on  $\sigma_{CML}$  at  $\beta = 0^\circ$ , most likely due to the complex interaction of the flow with the lateral surfaces of the building model. At  $\beta = 45^\circ$ , the difference in the  $\sigma_{CML}$  for the single-skin building model and the building model with the PDSF system of any porosity is  $\sim 10\%$ .

Regarding  $\overline{C_{MD}}$ , the difference relative to the ABL simulations is clear, with an offset in the  $\overline{C_{MD}}$  present at all  $\beta$ . The suburban ABL case yields lower aerodynamic loads on the building model in the along-wind direction, which was expected due to the lower flow velocity relative to the height in this experiment. There is a slight decrease in the effect of the ABL on the building model with the PDSF system of 50% porosity, as the  $\overline{C_{MD}}$  in this case is very similar at  $20^\circ < \beta < 30^\circ$ .

The  $\sigma_{CMD}$  is consistently larger for any building model in the suburban ABL simulation, as was envisaged due to the higher turbulence intensity of this ABL case. For different PDSF systems, the  $\sigma_{CMD}$  is  $\sim 10\%$  smaller for the building model with the PDSF system at  $\beta < 20^\circ$ .

### 7.3.2 Power spectral density of aerodynamic load fluctuations

The non-dimensional power spectra of the integral across-wind moment of the building model are shown in Figure 47. Experiments were performed at  $0^\circ < \beta < 45^\circ$  with a  $5^\circ$  increment; however, for the sake of brevity, the spectra are presented only for  $\beta = 0^\circ, 15^\circ, 30^\circ$  and  $45^\circ$ . The  $x$ -axis is the dimensionless frequency  $f \cdot d/v_\infty$ , the  $y$ -axis is the dimensionless moment power spectra  $S_M \cdot f/\sigma^2$ , where  $f$  is the frequency in Hz,  $d$  is the width of the building model in m,  $v_\infty$  is the freestream velocity at the location of the building model in m/s,  $S_M$  is the integral moment power spectrum in  $N^2m^2s$ , and  $\sigma^2$  is the integral moment variance in  $N^2m^2$ .

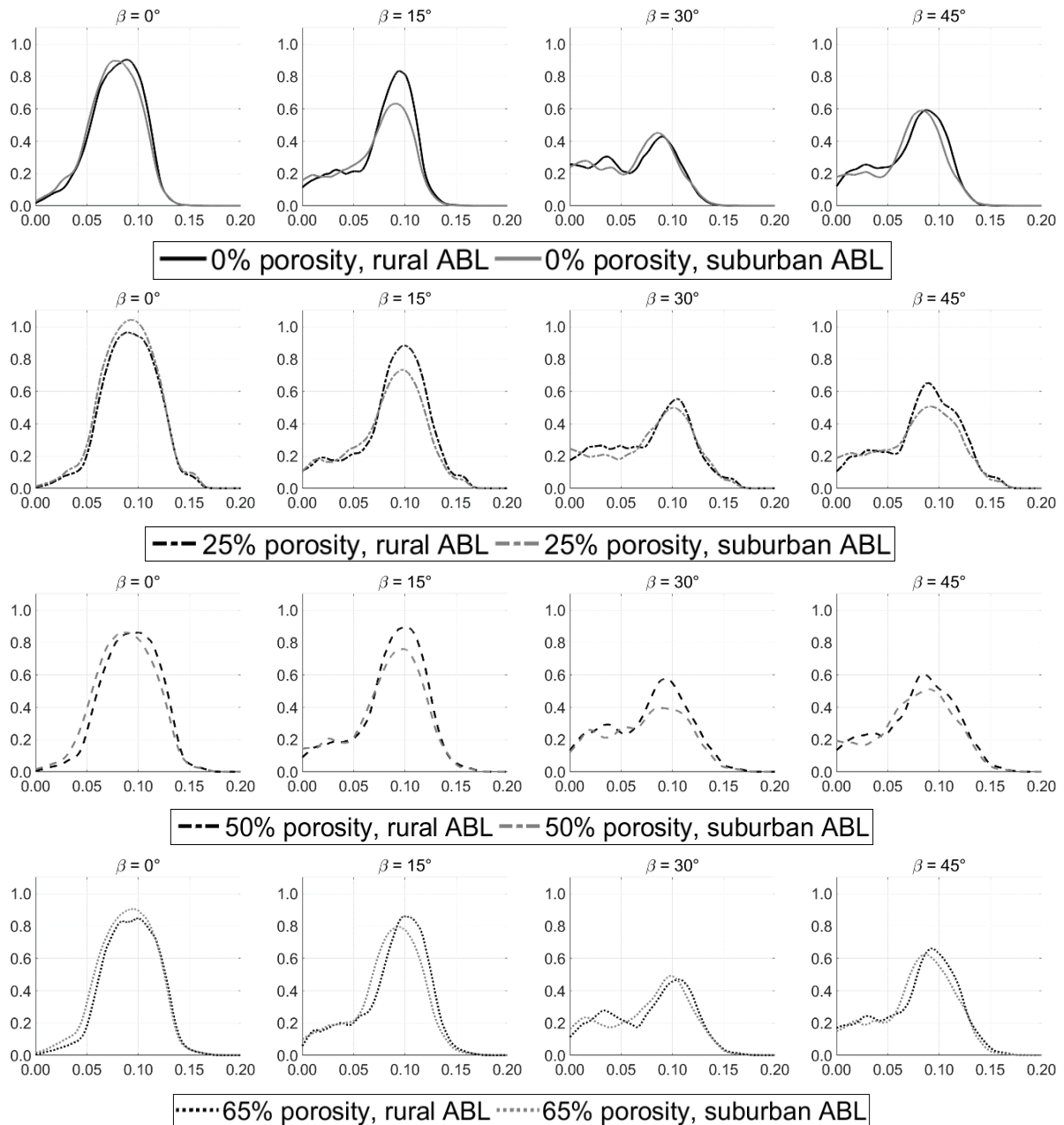


Figure 47. Integral cross-wind moment power spectra for  $\beta = 0^\circ, 15^\circ, 30^\circ$  and  $45^\circ$

A distinct peak is present in all spectra at  $\sim 0.1$ , which corresponds to the vortex-shedding (Strouhal) frequency. With the increase in  $\beta$ , the peak decreases from  $\sim 0.9$  to  $\sim 0.5$  at  $\beta = 30^\circ$ , then slightly increases to  $\sim 0.6$  at  $\beta = 45^\circ$ . The difference in inflow characteristics has a noticeable effect only at  $\beta = 15^\circ$ , where the peak is consistently lower for the building model in the suburban ABL simulation. Various PDSF systems do not influence the across-wind moment power spectra. The vortex-shedding frequency is slightly lower in the suburban ABL simulation, which can be particularly observed for the building model with the PDSF system of 65% porosity.

The power spectra of the integral along-wind moment are shown in Figure 48. The  $x$ -axis is the dimensionless frequency  $f \cdot d/v_\infty$ , the  $y$ -axis is the dimensionless moment power spectra  $S_M \cdot f/\sigma^2$ , where  $f$  is the frequency in Hz,  $d$  is the width of the building model in m,  $v_\infty$  is the freestream velocity at the location of the building model in m/s,  $S_M$  is the integral moment power spectrum in  $N^2m^2s$ , and  $\sigma^2$  is the integral moment variance in  $N^2m^2$ .

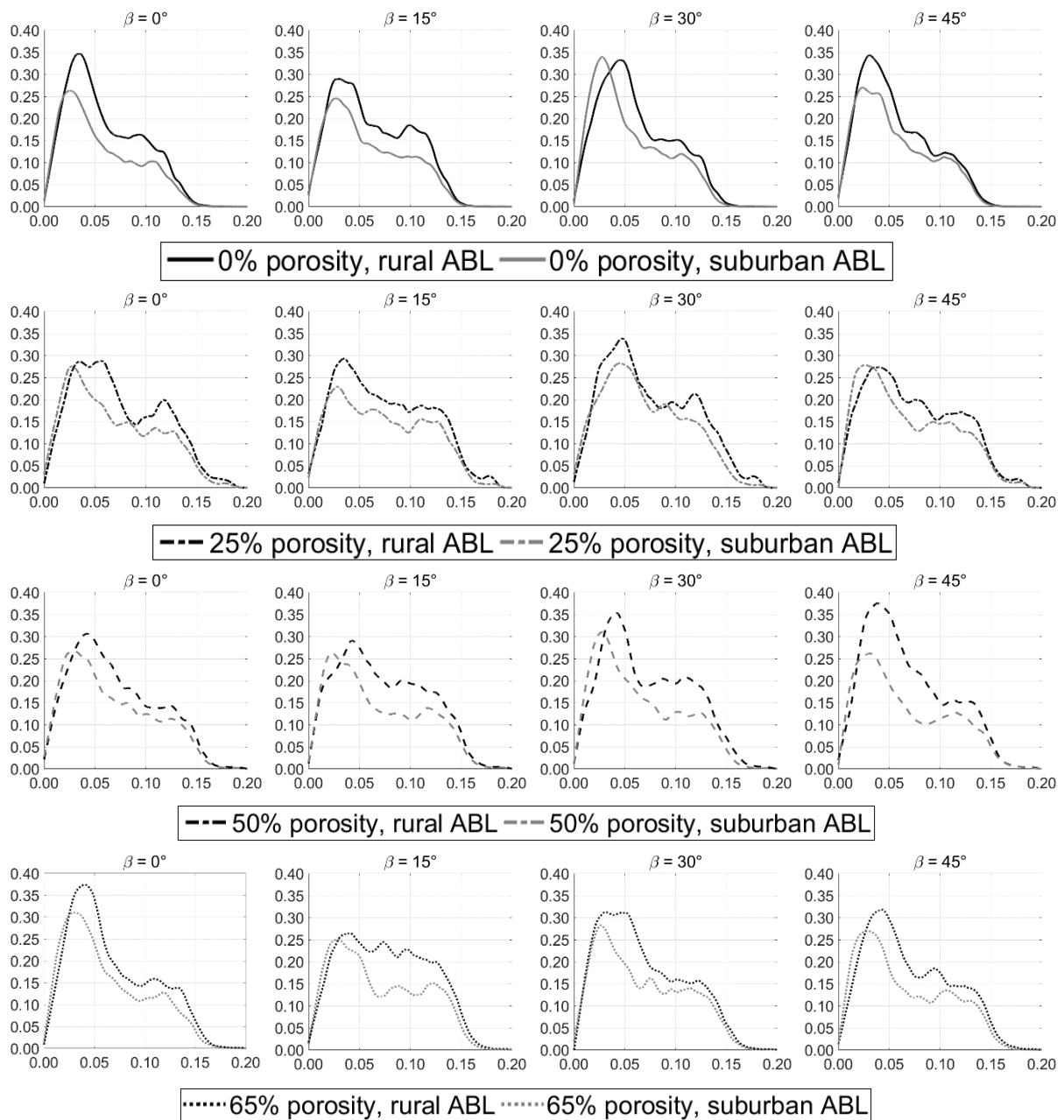


Figure 48. Integral along-wind moment power spectra for  $\beta = 0^\circ, 15^\circ, 30^\circ$  and  $45^\circ$

The spectral energy of the along-wind moment is more distributed across the frequencies compared to the across-wind moment, observed by the less exhibited peaks. The peak of the



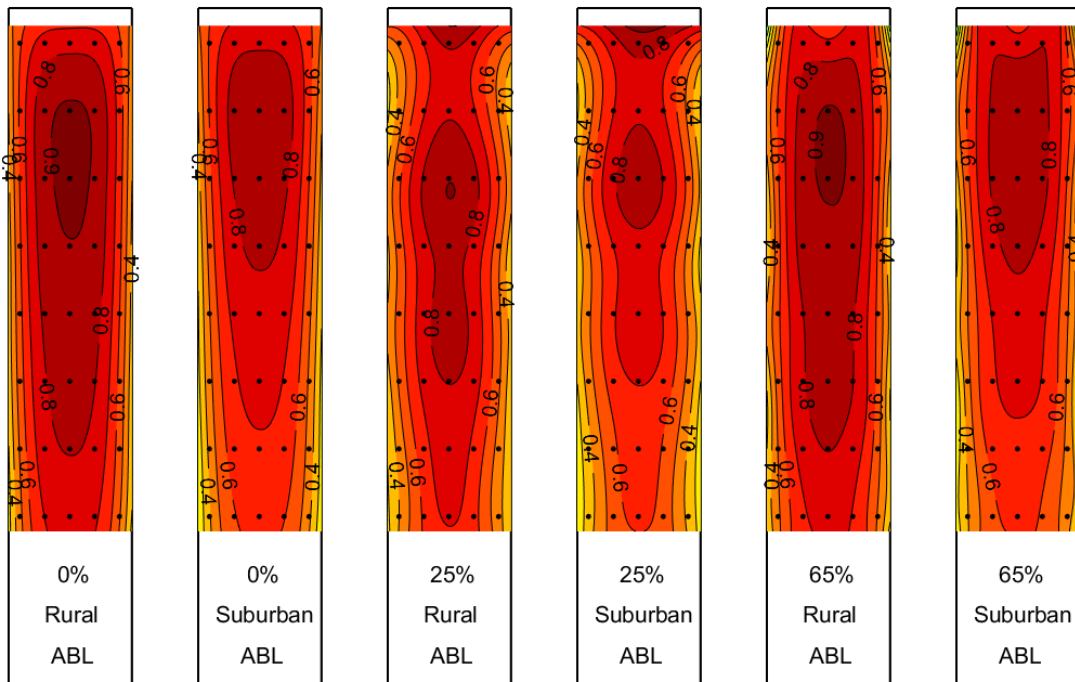
along-wind moment power spectra is at  $\sim 0.36$  reduced frequency, observed for the building model in the rural ABL simulation. The low-frequency peak at  $\sim 0.04$  reduced frequency is most likely a consequence of the inflow characteristics, while the second, smaller peak at  $\sim 0.12$  reduced frequency is due to vortex shedding. The along-wind power spectra in the rural ABL simulation have consistently higher values than in the suburban ABL simulation.

### 7.3.3 Surface pressure

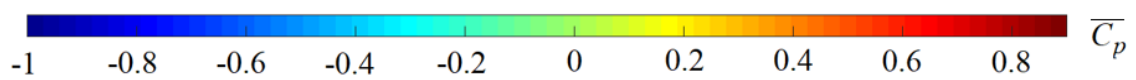
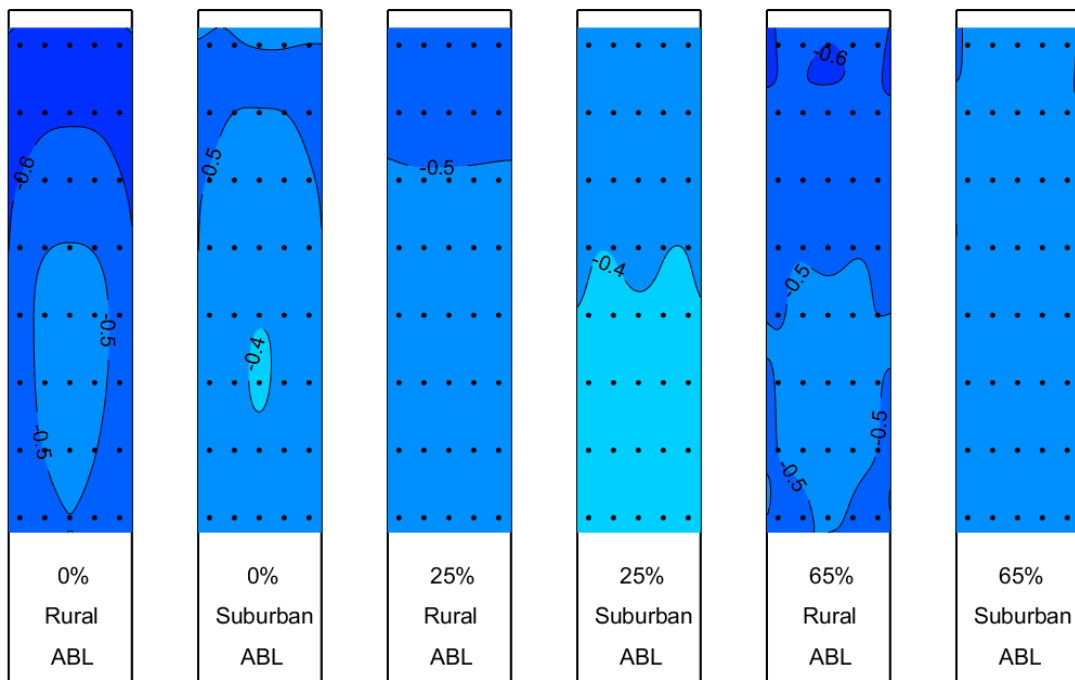
Figure 49 shows the  $\overline{C_p}$  distribution on all four inner façades of the building model at  $\beta = 0^\circ, 15^\circ, 30^\circ$  and  $45^\circ$ . It compares the effect of the rural and suburban ABL models on the building models with varying PDSF systems (0% - reference case (single-skin), 25% and 65% PDSF systems).

$\overline{C_p}$  for  $\beta = 0^\circ$

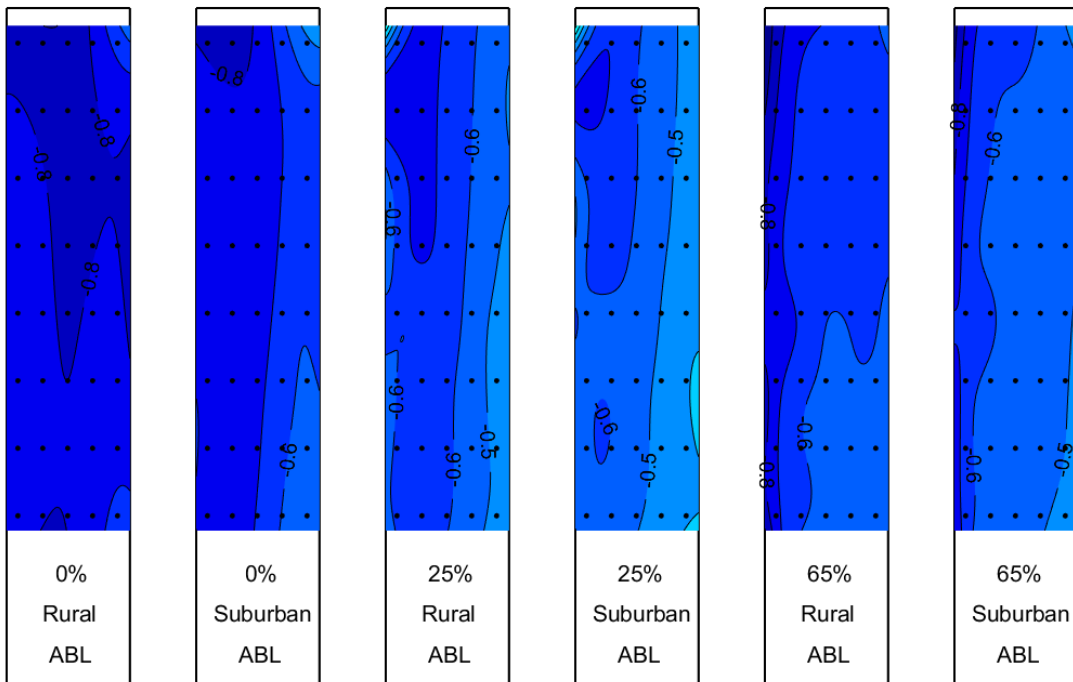
SURFACE 1



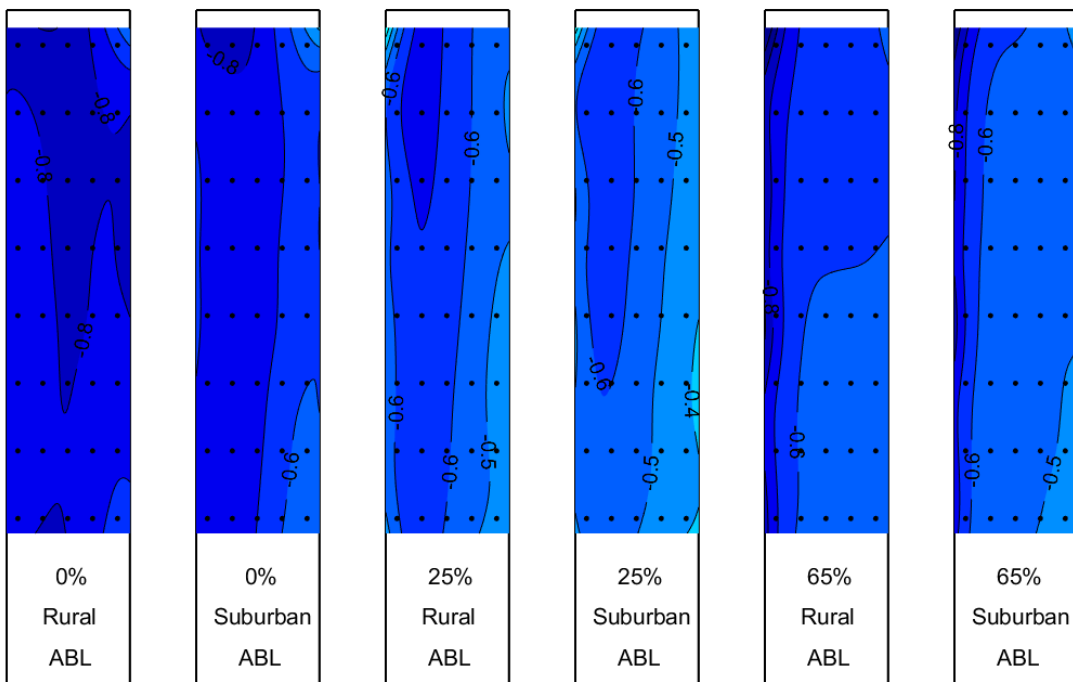
SURFACE 2



SURFACE 3

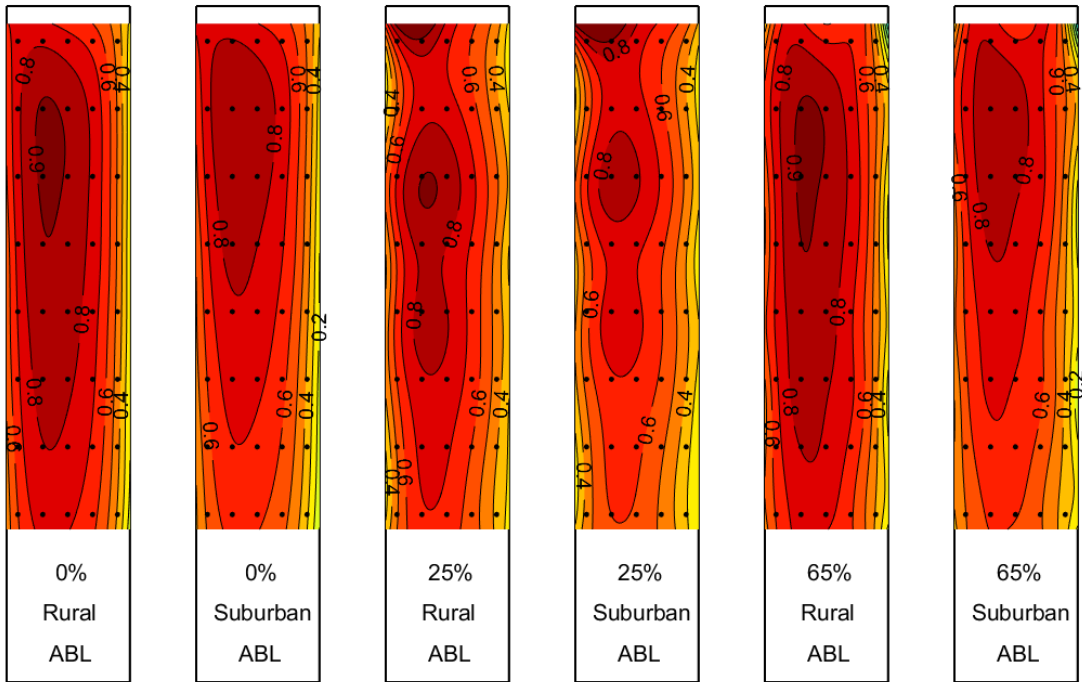


SURFACE 4

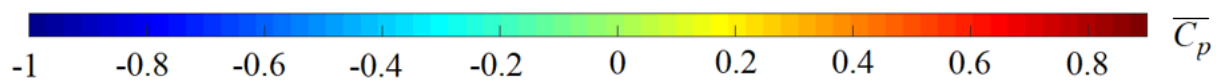
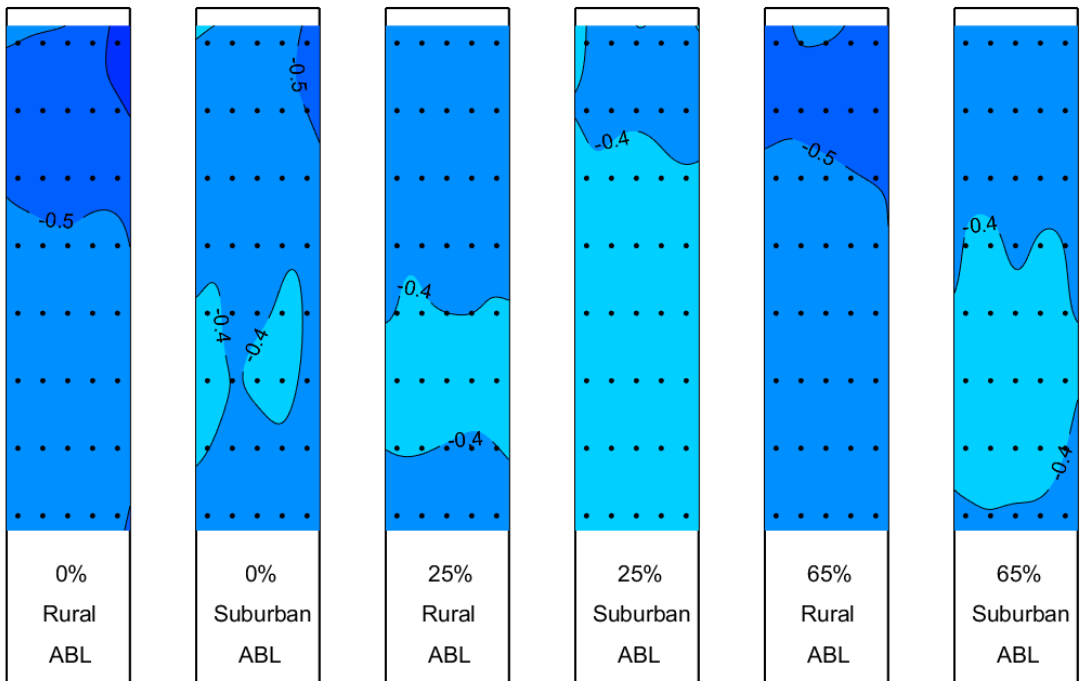


$\overline{C_p}$  for  $\beta = 15^\circ$

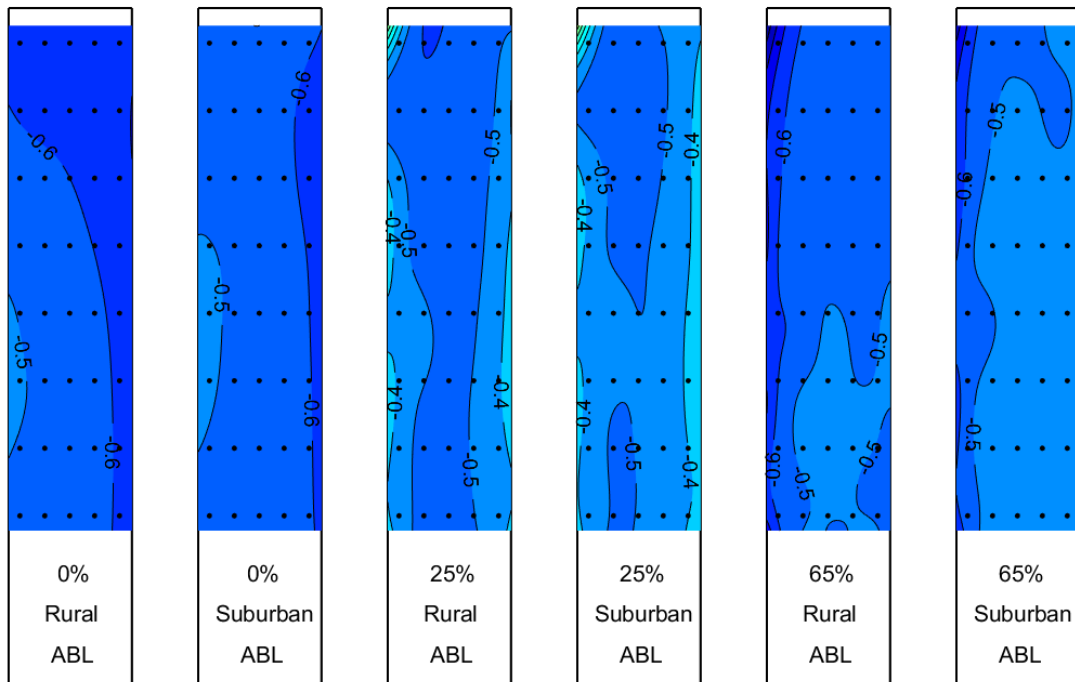
SURFACE 1



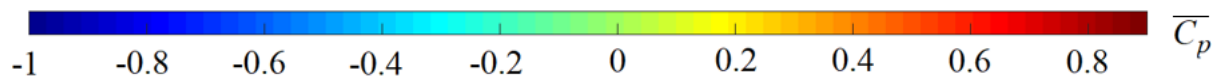
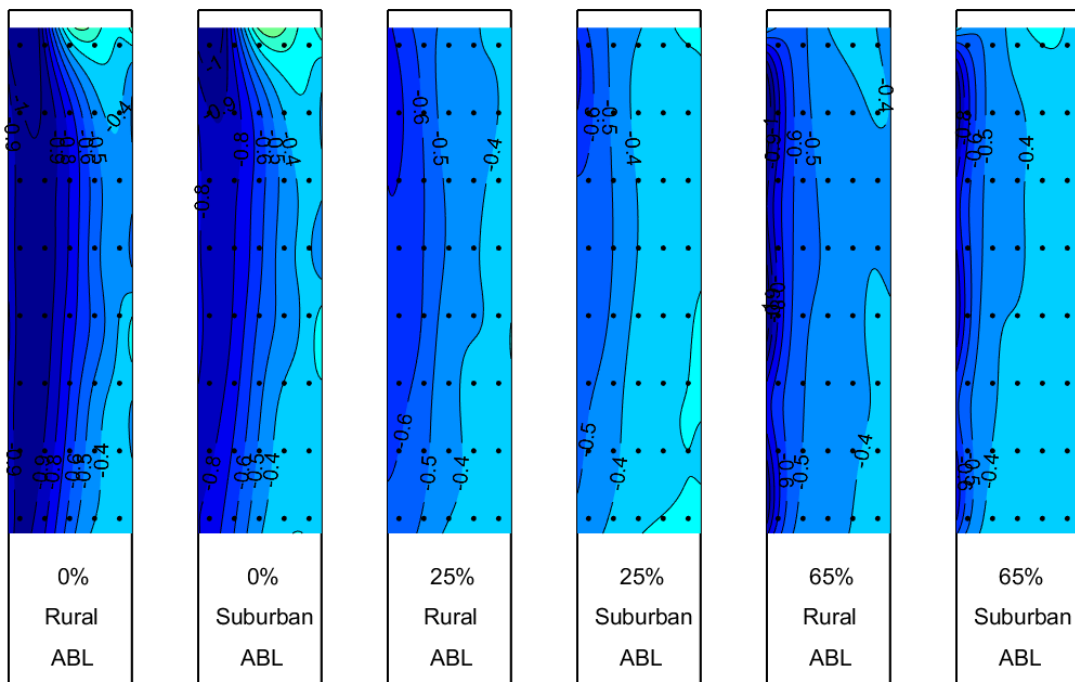
SURFACE 2



SURFACE 3

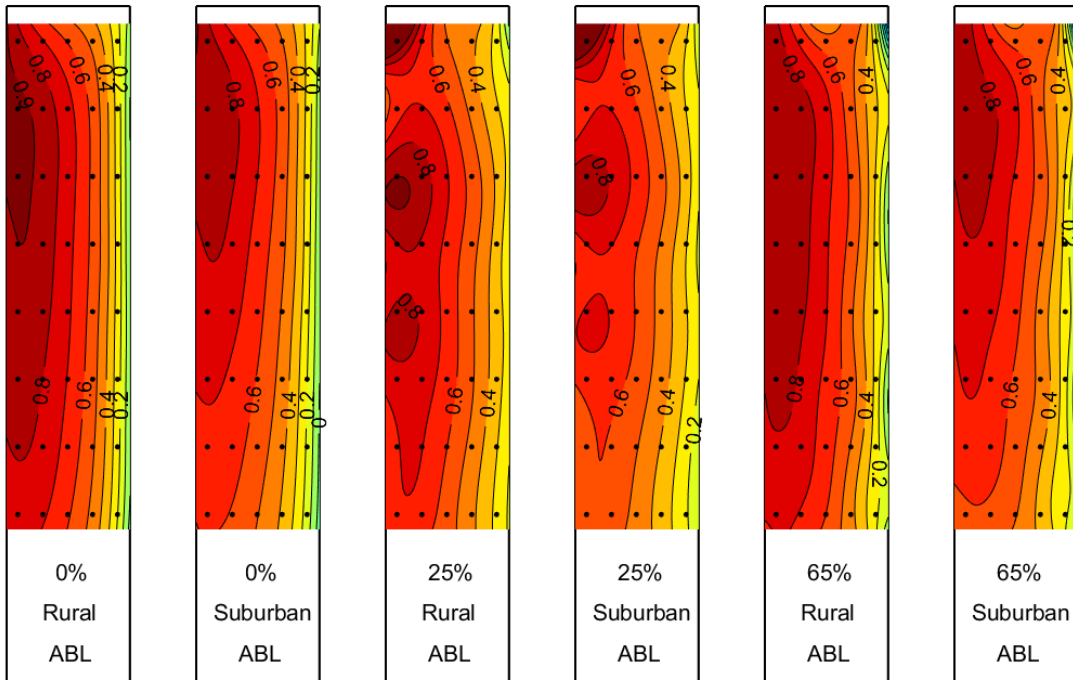


SURFACE 4

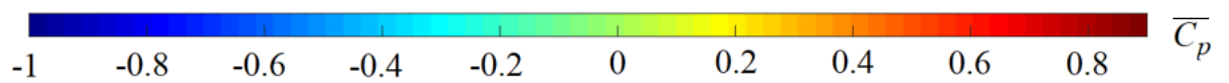
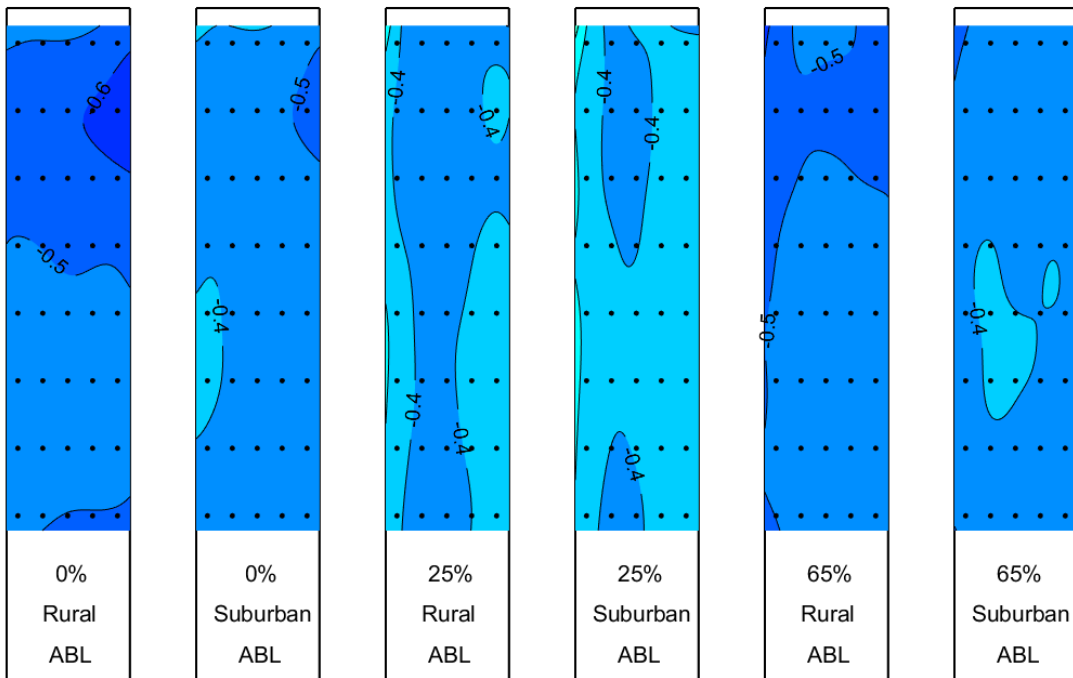


$\overline{C_p}$  for  $\beta = 30^\circ$

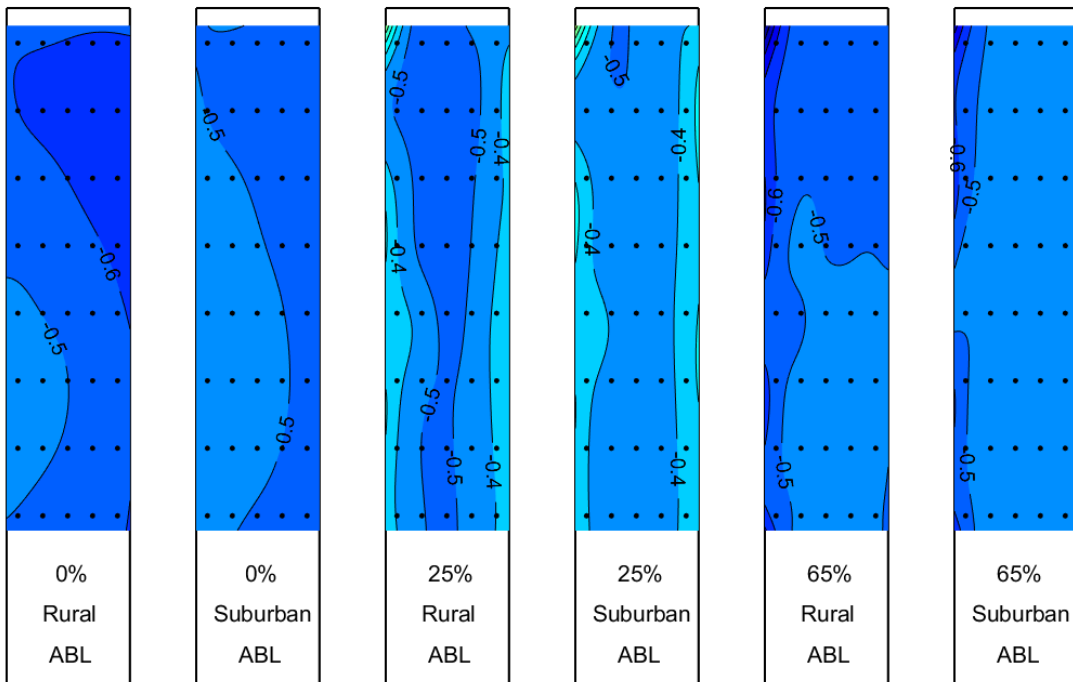
SURFACE 1



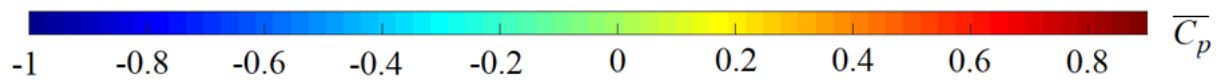
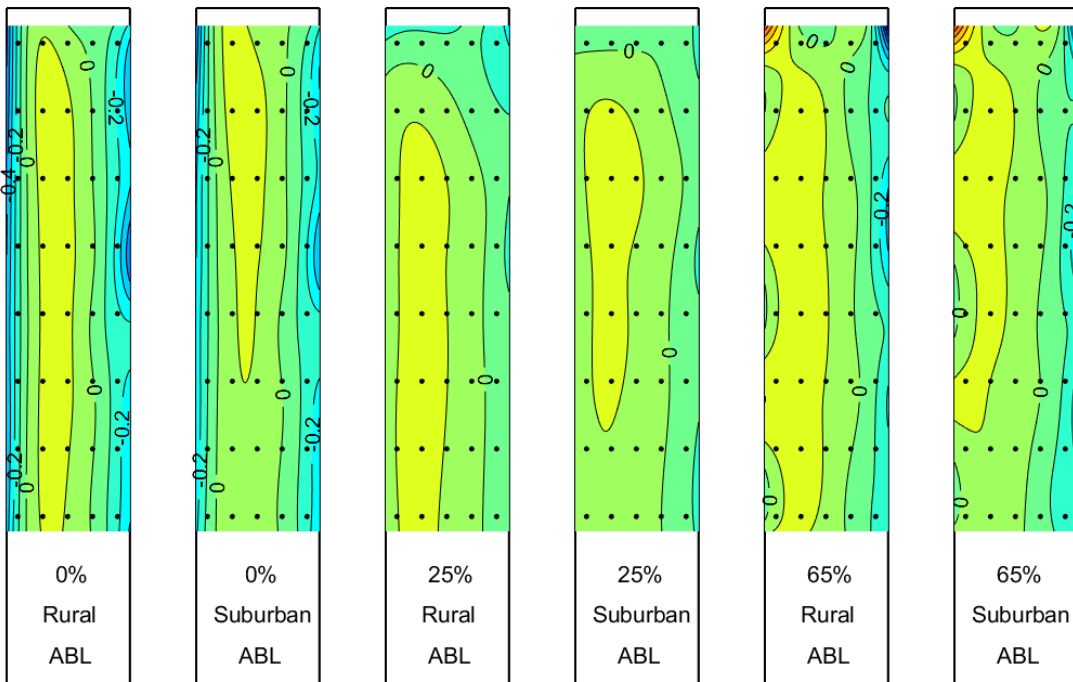
SURFACE 2



SURFACE 3

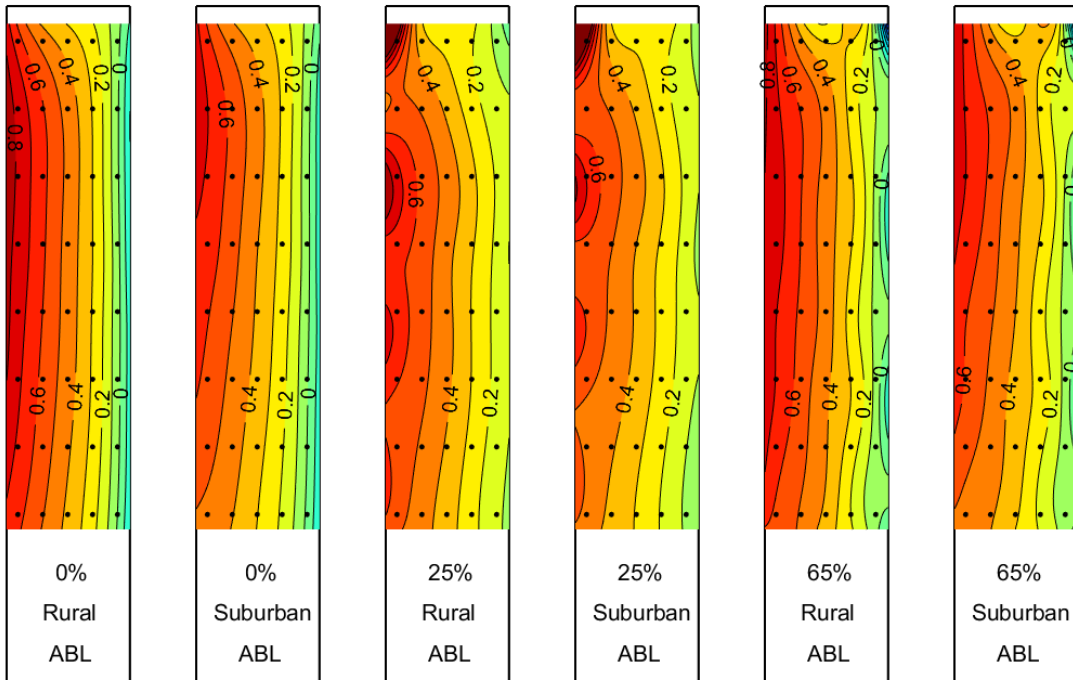


SURFACE 4

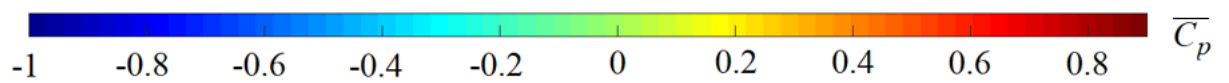
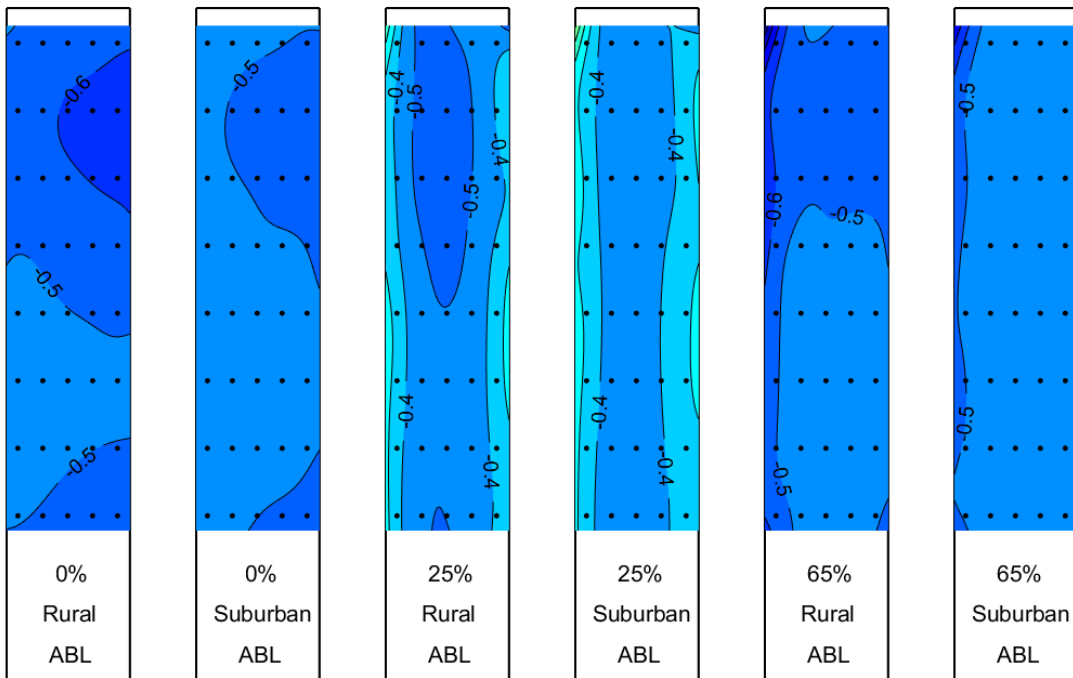


$\overline{C_p}$  for  $\beta = 45^\circ$

SURFACE 1

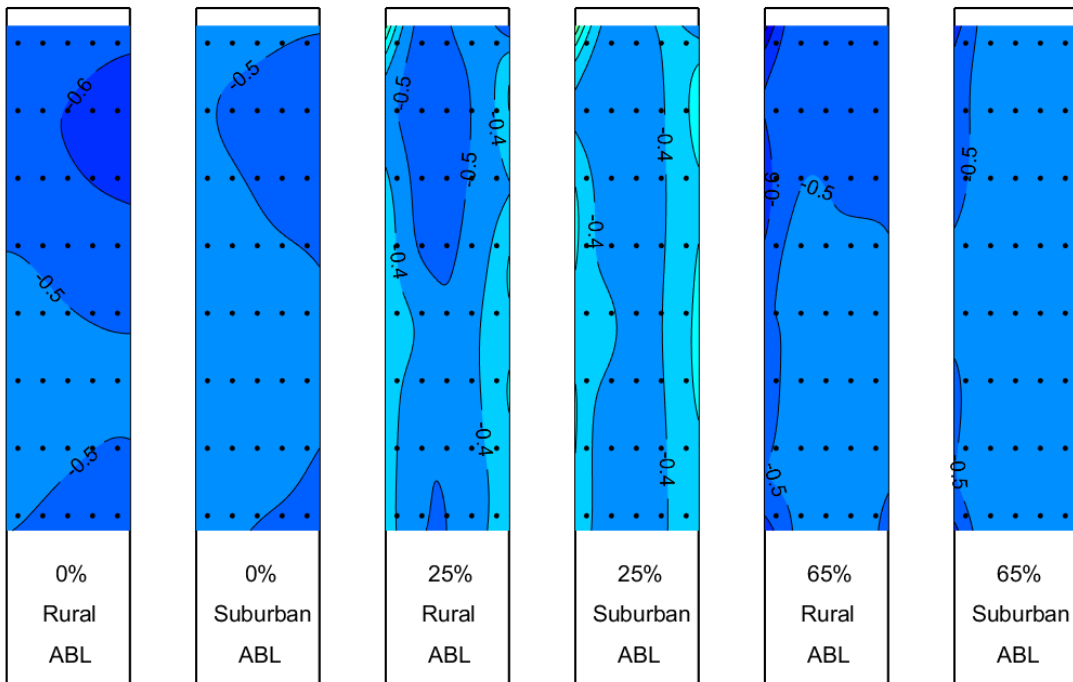


SURFACE 2





SURFACE 3



SURFACE 4

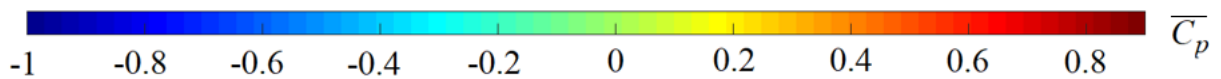
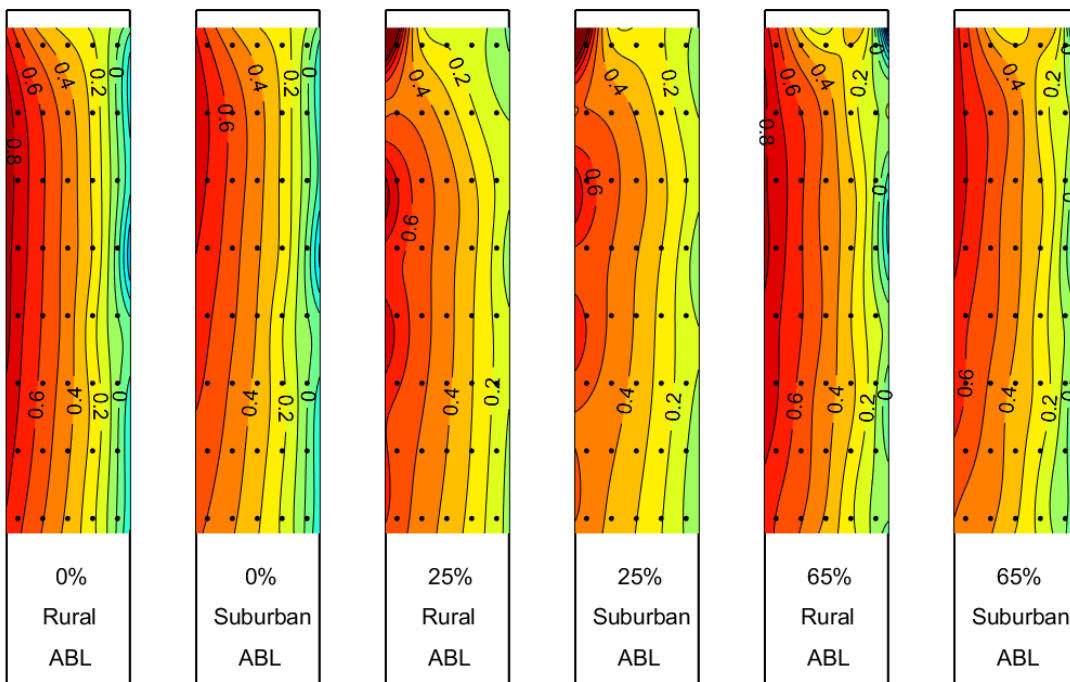


Figure 49.  $\overline{C_p}$  distribution on the building model subjected at  $\beta = 0^\circ, 15^\circ, 30^\circ$  and  $45^\circ$  to the rural and suburban ABL simulations; the building model is characterized by the smooth single-skin surface (0%), and the 25% and 65% PDSF systems

A comparison of the  $\overline{C_p}$  distribution between the single-skin building model Surface 1 at  $\beta = 0^\circ$  (windward surface) shows a decrease in the maximum pressure occurring at the stagnation point from  $\overline{C_p} = 0.9$  in the rural ABL simulation to  $\overline{C_p} = 0.8$  in the suburban ABL case. This is caused by the higher velocity at this height in the rural (less turbulent) ABL simulation. The 25% porosity PDSF system yields a change in the  $\overline{C_p}$  distribution to a pattern which reflects the locations of the openings on the outer façade. The maximum  $\overline{C_p}$  is consistently slightly larger in the rural ABL simulation. The 65% PDSF has little effect on the  $\overline{C_p}$  distribution on Surface 1 compared to the single-skin building model. This is likely due to the very high porosity of the outer façade, which basically provides negligible sheltering of the inner building model surface.

The rural (less turbulent) ABL simulation yields larger suction on the single-skin building model Surface 2 (leeward surface) at  $\beta = 0^\circ$  relative to the more turbulent (suburban) ABL case. Larger suction is near the top of the building model, most likely caused by the downward flow in the lee of the roof. The suction is consistently higher on the surface of the building model in the rural ABL simulation, exhibited by an absolute value of  $\sim 0.1$  compared to the building in the suburban ABL case. The 25% PDSF system yields a decrease in the absolute value of suction on the entire building model surface in both ABL simulations, probably due to the pressure equalization in the gap between the inner and outer façades. The 25% PDSF system affects the  $\overline{C_p}$  distribution on Surface 2 by changing the shape from ellipsoid to horizontal lines. This is due to the main flow detaching from the leeward corners of the outer façade for the building model equipped with a PDSF system, while for the single-skin building model, the detachment occurs on the corners of the inner surfaces, thus yielding lower pressure close to the corners. The effect of the ABL is similar, i.e., the (absolute) suction is consistently  $\sim 0.1$  lower for the more turbulent, ABL category III simulation. The 65% PDSF has little effect on the leeward surface  $\overline{C_p}$  distribution compared to the single-skin building model.

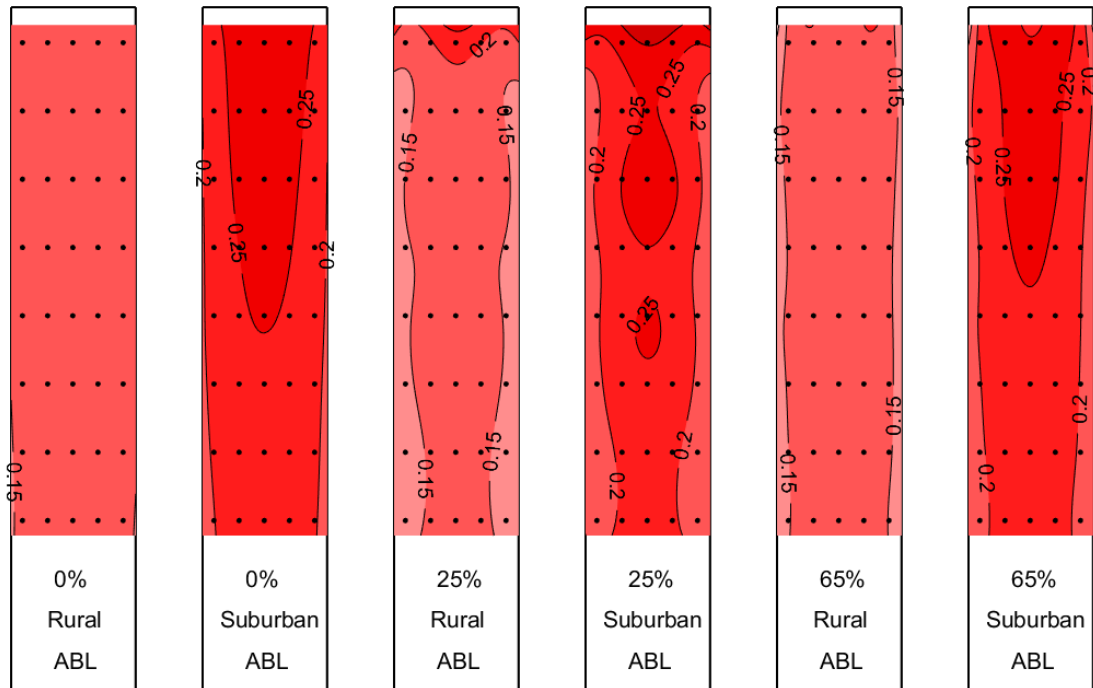
On Surfaces 3 and 4 (lateral surfaces) of the building model at  $\beta = 0^\circ$ , the absolute  $\overline{C_p}$  is  $\sim 0.8$  larger close to the windward edges compared to the leeward edges, where the absolute  $\overline{C_p}$  decreases to  $\sim -0.7$  in the rural ABL simulation and to  $\sim -0.6$  in the suburban ABL experiment. This is due to the flow separating at the windward edge, causing large suction at the corners of the lateral surfaces, which gradually lessens toward the leeward edges as the flow partially reattaches to the lateral surfaces. The (absolute) suction is consistently lower in the suburban (more turbulent) ABL simulation. There is a clear sheltering effect in the 25% PDSF system, with the absolute value of the suction reduced by  $\sim 0.2$ . Here, the difference in the inflow characteristics is less evident, particularly near the windward edge, where the  $\overline{C_p}$  in both ABL simulations is  $\sim -0.6$ . The difference in the mean flow velocity and turbulence intensity has a minor effect on the sheltered inner surface perpendicular to the mean flow direction. The same trend is observed for the 65% PDSF system, i.e., various inflow characteristics have negligible effect on the  $\overline{C_p}$  distribution. However, the sheltering effect is evident for the lateral surfaces even in the case of high PDSF porosity.

The trends in the  $\overline{C_p}$  distribution on the inner surface of the single-skin building model at  $\beta = 0^\circ$  are consistent for the increasing  $\beta$ , i.e., a more turbulent ABL yields a decrease in the absolute  $\overline{C_p}$ . This was also reported by Tamura [148], where the  $\overline{C_p}$  distribution on a single-skin building in two different ABL simulations were studied. For the building models equipped with PDSF systems, the suburban (more turbulent) ABL simulation yields a  $\sim 0.1$  decrease in the absolute  $\overline{C_p}$  distribution at a low  $\beta$ . For the surfaces at a large  $\beta$ , the sheltering effect of the PDSF systems is considerable, even for high porosity (65%), while the difference in the characteristics of the ABL simulations have a negligible effect on  $\overline{C_p}$ .

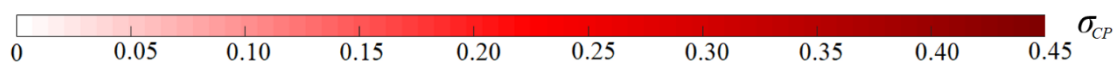
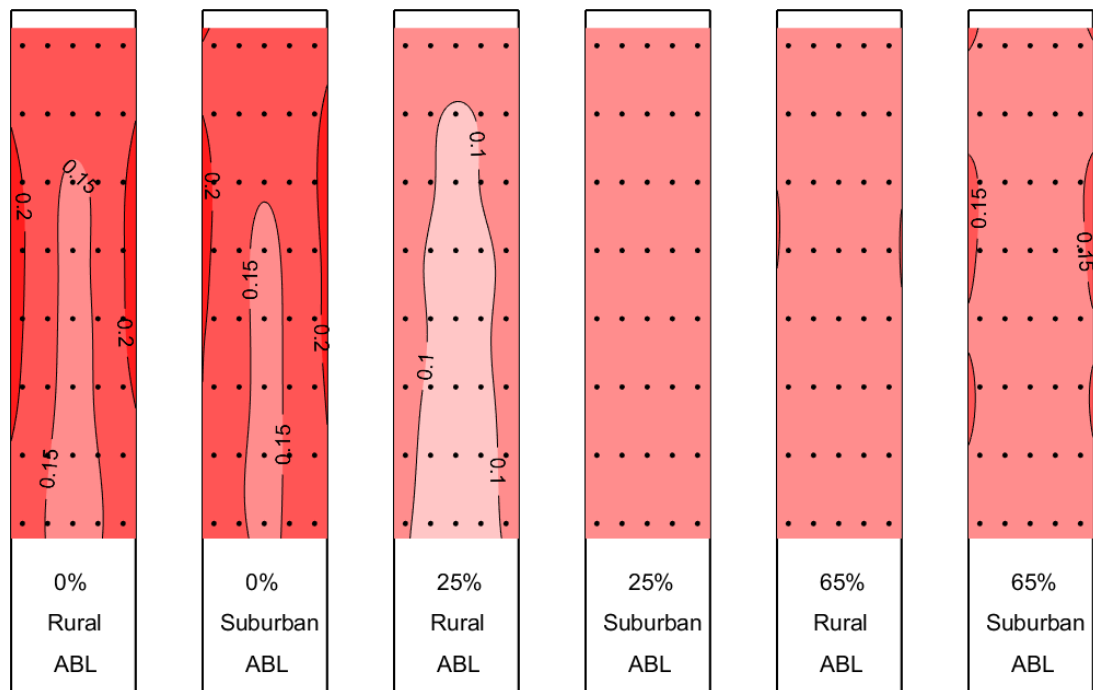
Figure 50 shows the  $\sigma_{C_p}$  distribution on the inner surface of the building model at  $\beta = 0^\circ$ . The experiments were conducted for  $\beta = 15^\circ, 30^\circ$  and  $45^\circ$  as well, but are not shown here since the trends are fully represented for  $\beta = 0^\circ$ . A comparison is made between two ABL simulations on the single-skin building model and the building model equipped with the 25% and 65% PDSF systems.

$\sigma_{cp}$  for  $\beta = 0^\circ$

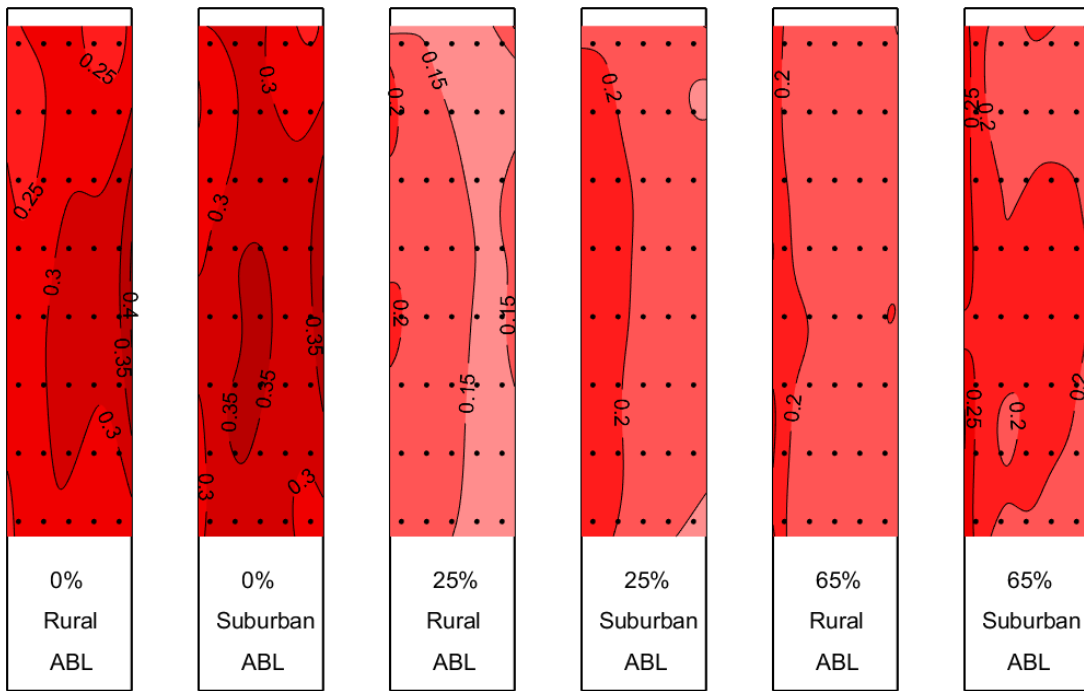
SURFACE 1



SURFACE 2



SURFACE 3



SURFACE 4

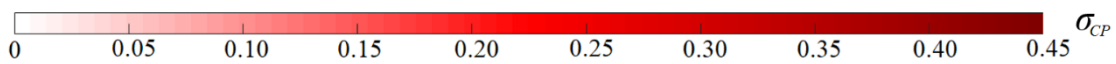
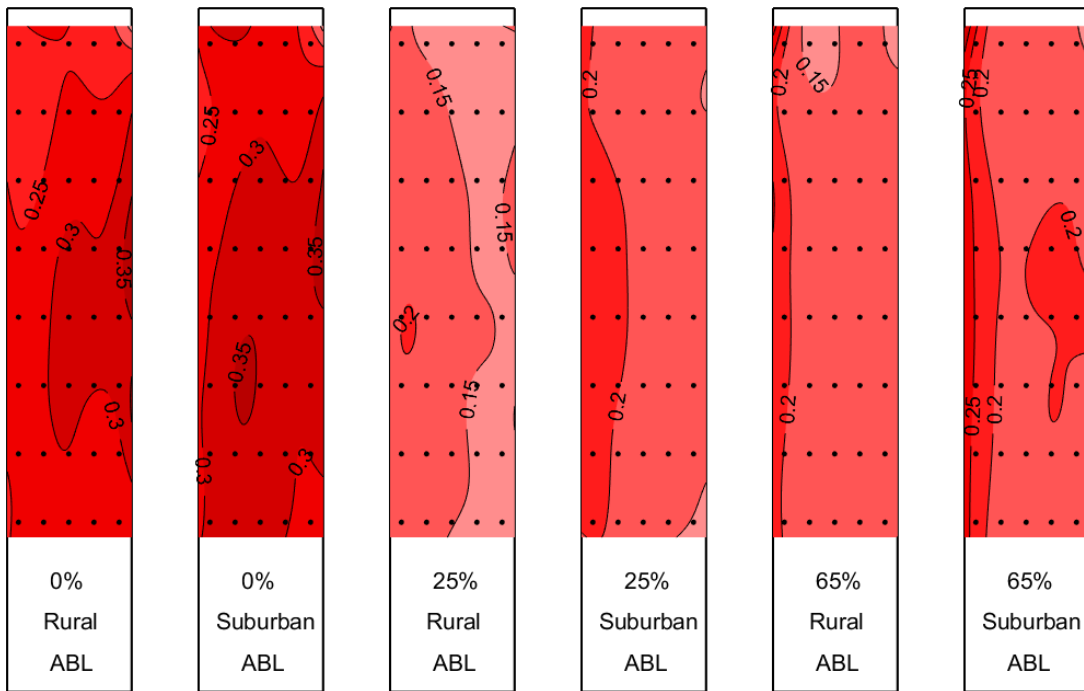


Figure 50.  $\sigma_{cp}$  distribution on the building model subjected at  $\beta = 0^\circ$  to the rural and suburban ABL simulations; the building model is characterized by the smooth single-skin surface (0%), and the 25% and 65% PDSF systems

On the windward surface (Surface 1) of the single-skin building at  $\beta = 0^\circ$ ,  $\sigma_{Cp}$  is almost completely uniform in the rural ABL simulation with  $\sigma_{Cp} = \sim 0.15$  on the entire surface. The same surface in the suburban ABL simulation exhibits a significantly higher  $\sigma_{Cp} = \sim 0.25$  as the maximum, with a decrease to  $\sigma_{Cp} = \sim 0.20$  near the corners. This is indicative of the higher turbulence intensity in the suburban ABL simulation relative to the rural ABL case. The 25% PDSF system yields a small  $\sigma_{Cp}$  decrease near the corners of Surface 1, while a slight increase occurs near the top of the building model. The decrease near the corners is due to the sheltering effect caused by the effectively closed corners of the outer façade, while the increase near the top is most likely due to the interaction of the gap flow and the flow separation on the leading edge on the top of the building model. The 65% PDSF system causes a negligible effect on the  $\sigma_{Cp}$  distribution relative to the single-skin building model.

The  $\sigma_{Cp}$  distribution on the leeward surface (Surface 2) of the single-skin building model at  $\beta = 0^\circ$  is very similar in both ABL simulations. This is likely due to the increased turbulence in the wake of the building model, which effectively diminishes the differences in the characteristic ABL profiles, in this case mainly the turbulence intensity profile. The highest value of  $\sigma_{Cp} = \sim 0.20$  is near the corners of the building model, as this is the location of the flow separation. The  $\sigma_{Cp}$  decreases to a minimum of  $\sim 0.15$  in the center of the surface since this is the most sheltered area. The 25% PDSF system reduces the minimum  $\sigma_{Cp}$  to  $\sim 0.1$  in the rural ABL simulation. The decrease is less exhibited in the suburban (more turbulent) ABL experiment, where  $\sigma_{Cp} = \sim 0.15$  on the entire surface, which can be expected considering the increased turbulence in the suburban ABL simulation. The 65% PDSF system yields slightly less sheltering for the leeward surface, with a uniform  $\sigma_{Cp} \sim 0.15$  distribution on the entire surface in both ABL simulations.

The lateral surfaces (Surfaces 3 and 4) on the single-skin building model show a similar  $\sigma_{Cp}$  distribution, with the values at the leeward corners higher than at the windward corners. This is likely due to the partial flow reattachment near the leeward corners. The  $\sigma_{Cp}$  are consistently slightly higher for the building model in the more turbulent (suburban) ABL model. The presence of the 25% PDSF system causes a slight decrease of  $\sim 0.05$  near the windward corners. However, the decrease is substantial near the leeward corners in both ABL categories up to 50% (from  $\sim 0.3$  to  $\sim 0.10$  in the rural ABL model, and from  $\sim 0.35$  to  $\sim 0.15$  in the suburban ABL model). This is most likely due to the partial flow reattachment now occurring on the outer façade, which reduces the pressure pulsations on the inner surfaces, where the pressure is recorded. A similar trend is observed for the 65% porosity PDSF system, but with a slightly lower decrease in  $\sigma_{Cp}$ .

## 7.4 The effect of the building aspect ratio

Four building models were studied to address the effect of the aspect ratio of the building model on its aerodynamic loads. The aspect ratios of the building models are 1:1:3, 1:1:4, 1:2:5 and 1:3:5. Each of them was tested in two different configurations regarding the PDSF systems, i.e., the single-skin building model as a reference case and the building model equipped with the 65% PDSF system. In these experiments, the building model was subjected to the suburban ABL simulation at  $0^\circ < \beta < 90^\circ$  with a  $5^\circ$  increment. For  $\beta = 0^\circ$ , the wider surface of the building model is perpendicular to the flow direction, Figure 51.

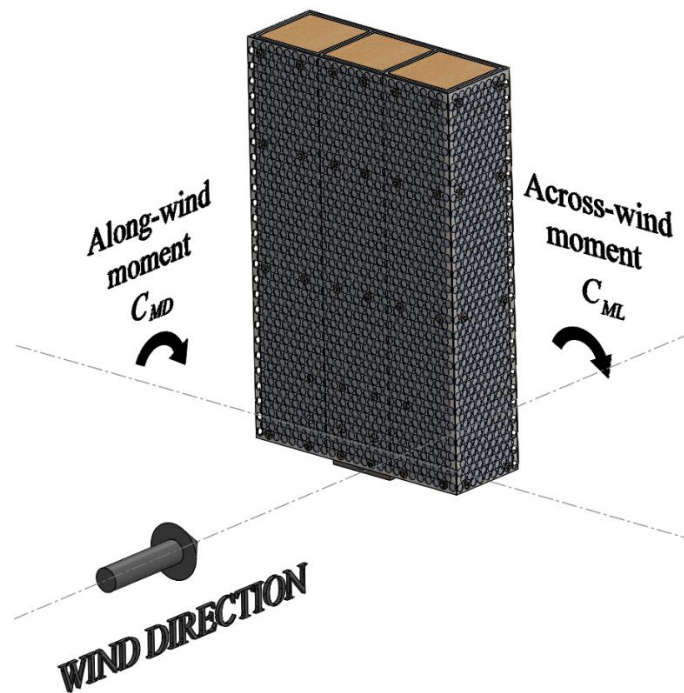


Figure 51. Orientation of the 1:3:5 building model to the flow direction

### 7.4.1 Square cross-section building model

Figure 52 shows  $\overline{C_{ML}}$  and  $\overline{C_{MD}}$  and their respective standard deviations  $\sigma_{CML}$  and  $\sigma_{CMD}$  of the building models with a square cross-section with and without the PDSF systems.

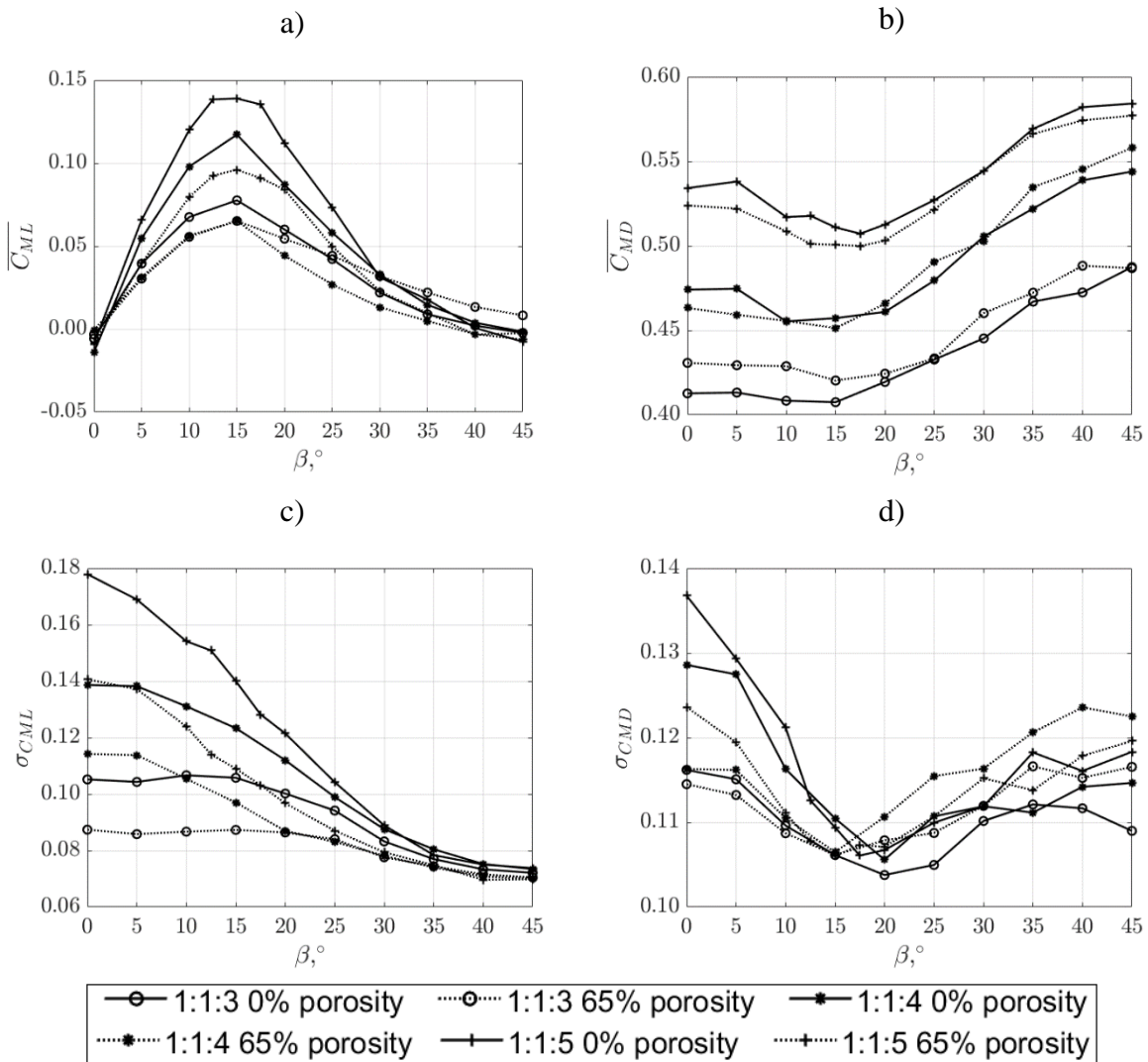


Figure 52.  $\overline{C_{ML}}$ ,  $\overline{C_{MD}}$  and  $\sigma_{CML}$ ,  $\sigma_{CMD}$  for the 1:1:3, 1:1:4 and 1:1:5 single-skin building models and 65% PDSF systems

$\overline{C_{ML}}$  is largest at  $\beta = 15^\circ$ , which is consistent in all experiments. For the 1:1:5 building model, which is the tallest of the three building models,  $\overline{C_{ML}}$  is the largest at its peak at  $\beta = 15^\circ$ , which can be expected due to the height of this building model. With a decrease in the height of the building model, the largest  $\overline{C_{ML}}$  decreases. This is most likely the consequence of the decreased height of the building model which also reduces the surface area of the building model. A smaller surface area yields less total surface pressure on the façades of the building model, which in turn reduces the integral moment. Furthermore, since the ABL simulation is the same, lower models are effectively subjected to lower mean flow velocity due to the characteristics of the ABL simulation. The smaller surface area and concurrently the lower mean flow velocity of the flow impinging on the surfaces of the building model are most likely the cause of the lower  $\overline{C_{ML}}$ . The 65% PDSF system yields a further decrease in  $\overline{C_{ML}}$  for the 1:1:4



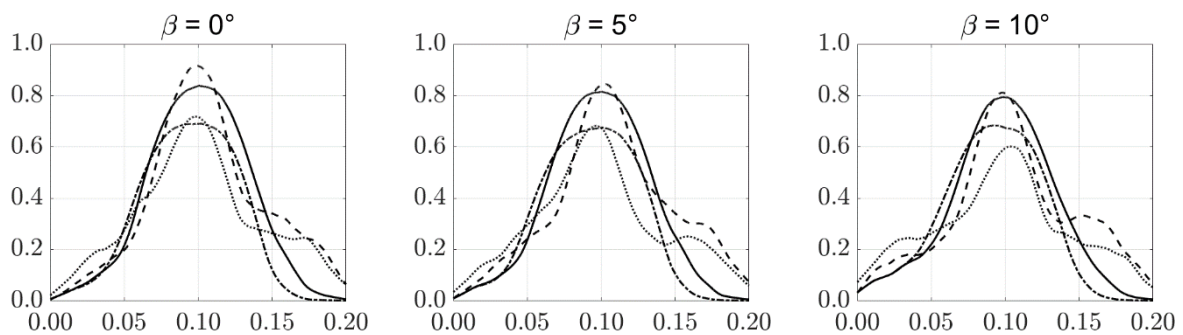
and 1:1:5 building models, probably due to the larger surface roughness on account of the openings in the outer façade. For the 1:1:3 building model, however, this decrease in  $\overline{C_{ML}}$  does not occur. In fact, the application of the 65% PDSF system on the 1:1:3 building model yields a slight increase in  $\overline{C_{ML}}$ , particularly at  $\beta > 25^\circ$ . Based on the HFFB recordings alone, it is difficult to precisely elucidate why this slight increase occurs, and is thus an important topic for future study.

A similar trend is observed for  $\overline{C_{MD}}$ , i.e.,  $\overline{C_{MD}}$  decreases when the building model is lower. The 65% PDSF system causes a further decrease in  $\overline{C_{MD}}$  for the 1:1:5 and 1:1:4 building models, while it slightly increases  $\overline{C_{MD}}$  for the 1:1:3 building model, Figure 52b.

Figure 52c shows  $\sigma_{CML}$ . The largest  $\sigma_{CML}$  is at  $\beta = 0^\circ$  due to the most pronounced vortex-induced vibration at this  $\beta$ . It gradually decreases to its minimum at  $\beta = 45^\circ$ , where the orientation of the building model is streamlined. At  $\beta = 0^\circ$ ,  $\sigma_{CML}$  is at a maximum for the tallest building model (1:1:5), and lowest for the shortest model (1:1:3), a decrease of more than 50%. The 65% PDSF system on all building models also yields a large drop in  $\sigma_{CML}$  of up to 25%.

Regarding  $\sigma_{CMD}$  in Figure 52d, the highest  $\sigma_{CMD}$  is observed for the 1:1:5 building model and lowest for the 1:1:3 building model. The trends are consistent, as observed in the previous experiments, i.e., the largest value at  $\beta = 0^\circ$ , the lowest at  $\beta = 20^\circ$ . No clear effect of the PDSF system is observed for  $\beta > 20^\circ$ .

Figure 53 shows the integral across-wind moment power spectra for the 1:1:3 and 1:1:4 building models with the single skin and the 65% PDSF system. The  $x$ -axis is the dimensionless frequency  $f \cdot d/v_\infty$ , the  $y$ -axis is the dimensionless moment power spectra  $S_M \cdot f/\sigma^2$ , where  $f$  is the frequency in Hz,  $d$  is the width of the building model in m,  $v_\infty$  is the freestream velocity at the location of the building model in m/s,  $S_M$  is the integral moment power spectrum in  $N^2m^2s$ , and  $\sigma^2$  is the integral moment variance in  $N^2m^2$ .



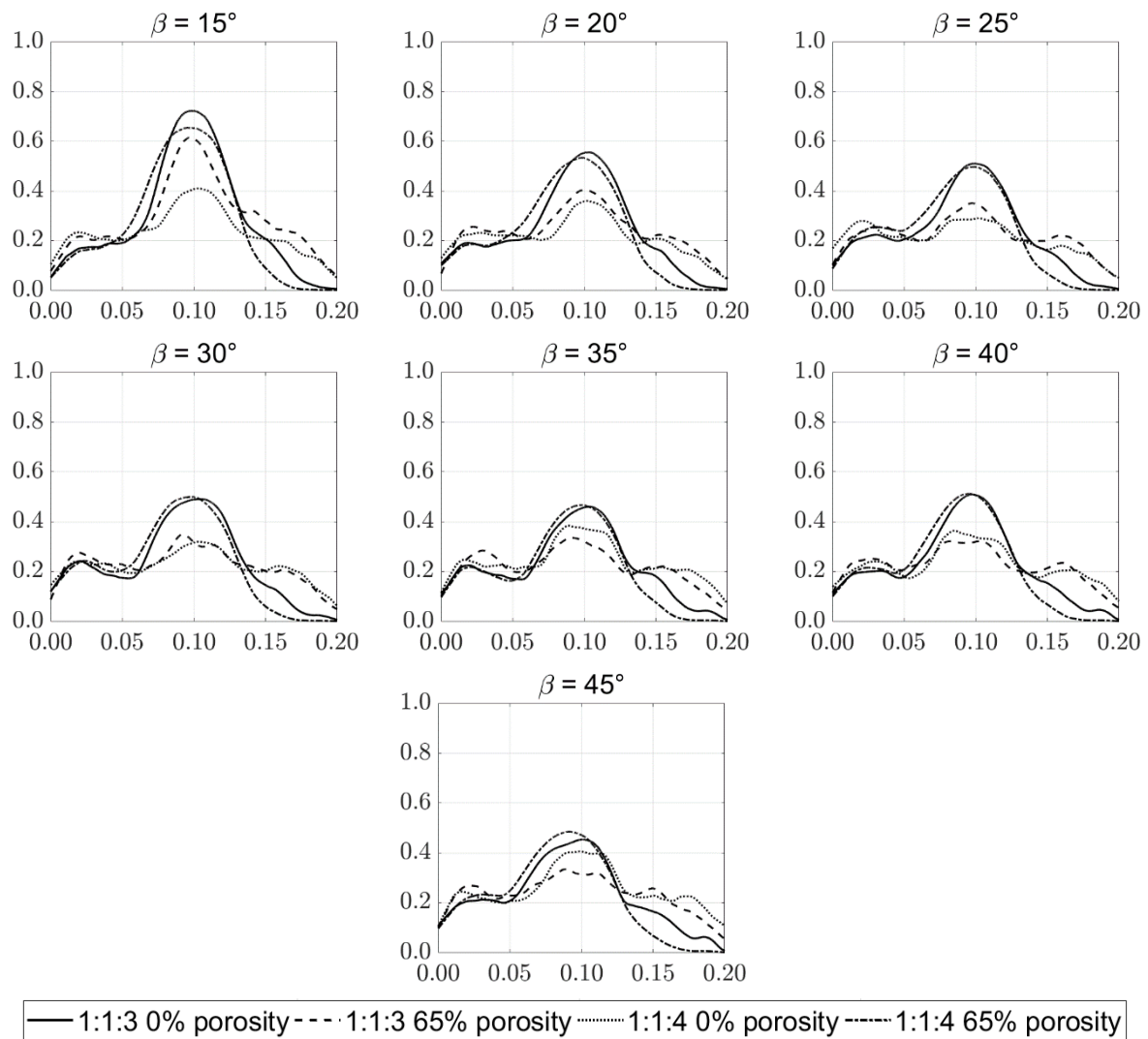


Figure 53. Integral across-wind moment power spectra for the 1:1:3 and 1:1:4 aspect ratio building models with the single-skin and the 65% PDSF system

A peak at  $\sim 0.1$  occurs in all spectra, which corresponds to the vortex-shedding (Strouhal) frequency, also observed for the 1:1:5 building model. With the increase in  $\beta$ , the peak decreases from  $\sim 0.9$  to  $\sim 0.4$  at  $\beta = 45^\circ$ . The difference in the aspect ratio seems to have the largest effect at a low  $\beta$ , with the 1:1:4 building model peak smaller by  $\sim 0.2$  compared to the 1:1:3 building model. For  $\beta < 15^\circ$ , the PDSF system does not have an effect on the across-wind moment power spectra, while for  $\beta > 15^\circ$ , the 65% PDSF system on the 1:1:4 building model yields an increase in the peak by 0.1 to 0.2. This trend of a slight increase of the peak was also observed for the 1:1:5 building model. In general, with the increase of the slenderness of the building model, the PDSF system adversely affects the across-wind moment power spectra. However, it is worth pointing out that this increase is observed for a large  $\beta$  where the spectral peak is  $\sim 50\%$  of the peak at  $\beta = 0^\circ$ , which is the critical case. Therefore, the increase of the peak caused by the PDSF system should not adversely affect the aerodynamic response of the building.

Figure 54 shows the integral along-wind moment power spectra for the 1:1:3 and 1:1:4 building models equipped with the single skin and the 65% PDSF system. The  $x$ -axis is the dimensionless frequency  $f \cdot d/v_\infty$ , the  $y$ -axis is the dimensionless moment power spectra  $S_M \cdot f/\sigma^2$ , where  $f$  is the frequency in Hz,  $d$  is the width of the building model in m,  $v_\infty$  is the freestream velocity at the location of the building model in m/s,  $S_M$  is the integral moment power spectrum in  $N^2m^2s$ , and  $\sigma^2$  is the integral moment variance in  $N^2m^2$ .

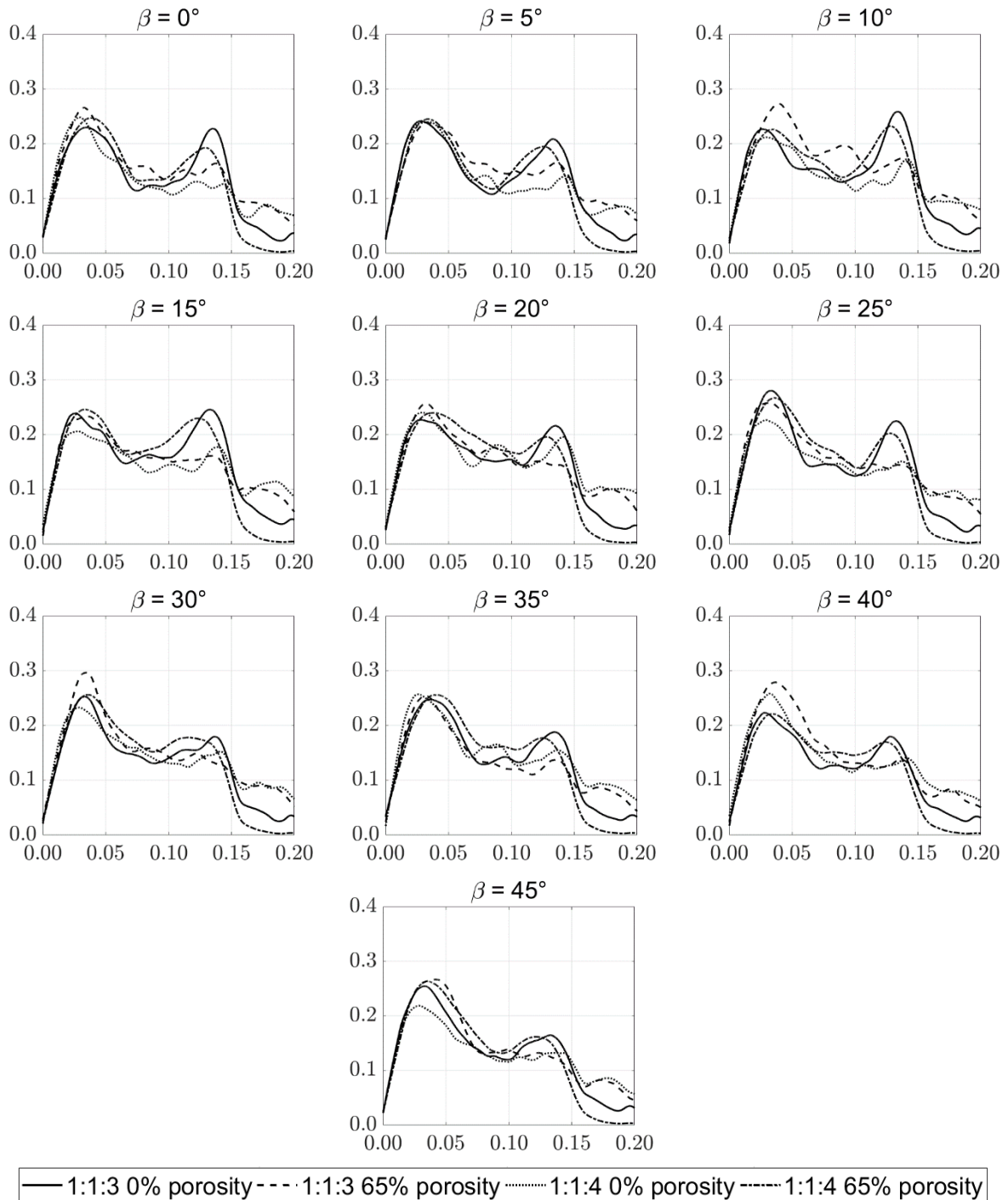


Figure 54. Integral along-wind moment power spectra for the 1:1:3 and 1:1:4 building models with the single-skin and the 65% PDSF system

The along-wind moment power spectra exhibit a significantly lower peak compared to the across-wind spectra. There are two peaks at  $\beta < 25^\circ$  at  $\sim 0.04$  and  $\sim 0.14$ . The peak at  $\sim 0.04$  is most likely the consequence of the inflow characteristics, while the peak at  $\sim 0.14$  may be a result of the natural frequency of the building model. Both the 1:1:4 and 1:1:3 building models with and without the PDSF system significantly overlap over the entire spectra at all  $\beta$ .

### 7.4.2 Rectangular cross-section building model

Figure 55 shows the  $\overline{C_{ML}}$ ,  $\overline{C_{MD}}$  and  $\sigma_{CML}$ ,  $\sigma_{CMD}$  for the 1:2:5 and 1:3:5 single-skin building models and 65% PDSF systems.

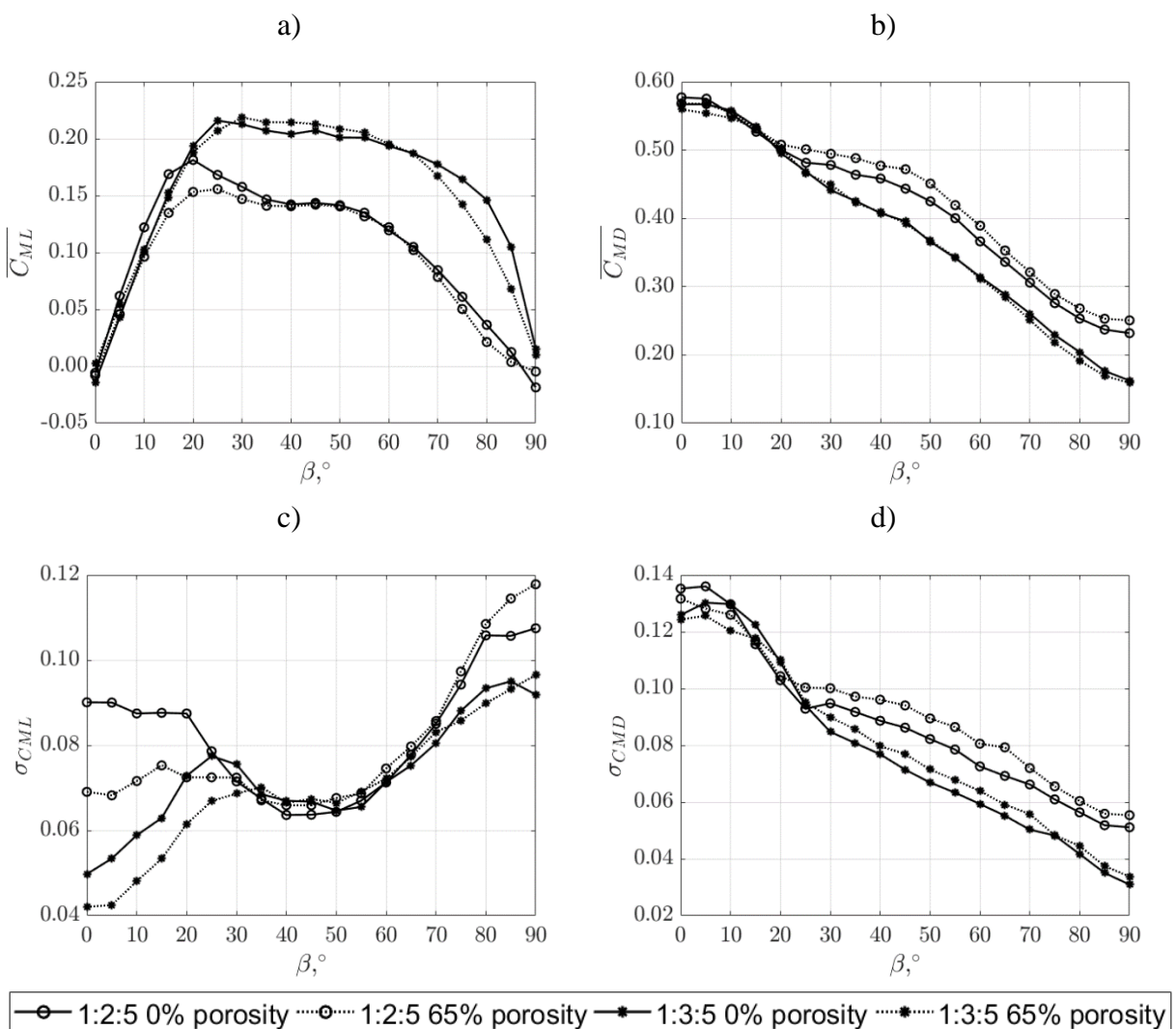


Figure 55.  $\overline{C_{ML}}$ ,  $\overline{C_{MD}}$  and  $\sigma_{CML}$ ,  $\sigma_{CMD}$  for the 1:2:5 and 1:3:5 single-skin building models and 65% PDSF systems

It is important to mention that for the measurements of the 1:2:5 and 1:3:5 building models, the characteristic length used for the calculation of moment coefficients is  $d = 0.2$  and  $d = 0.3$ ,

respectively. Unlike the experiments performed for the building models with the square cross-section, the integral aerodynamic loads on the 1:2:5 and 1:3:5 building models were assessed at  $0^\circ < \beta < 90^\circ$ .  $\overline{C_{ML}}$  (Figure 55a) exhibits a characteristic shape with  $\overline{C_{ML}} \sim 0$  for  $\beta = 0^\circ$  and  $90^\circ$ .  $\overline{C_{ML}}$  is at its maximum for  $25^\circ < \beta < 50^\circ$ , and slowly decreases to  $\sim 0$  at  $\beta = 90^\circ$ . The maximum  $\overline{C_{ML}}$  is  $\sim 25\%$  lower for the 1:2:5 building model, which can be attributed to the shorter width  $d$  of this model compared to the 1:3:5 building model. The 65% PDSF system on both building models does not affect  $\overline{C_{ML}}$ .

$\sigma_{CML}$  is shown in Figure 53b. For  $\beta = 0^\circ$ , the 1:3:5 building model exhibits substantially lower  $\sigma_{CML}$  ( $\sim 50\%$ ) than the 1:2:5 model. This is most likely due to the shorter width  $d$  of the windward surface at  $\beta = 0^\circ$ . The shorter width  $d$  increases the interaction of the flow in the lee of the building model, which yields an increase in  $\sigma_{CML}$ . This is further emphasized by comparing the 1:2:5 and 1:3:5 building models with the 1:1:5 model where  $\sigma_{CML} = 0.19$  at  $\beta = 0^\circ$ .  $\sigma_{CML}$  overlaps for both building models at  $30^\circ < \beta < 70^\circ$ , while the 1:3:5 building model exhibits lower  $\sigma_{CML}$  at  $\beta = 90^\circ$ . The 65% PDSF system yields a significant decrease in  $\sigma_{CML}$  at  $\beta = 0^\circ$ , which indicates that the highly porous PDSF systems yield less intense pressure fluctuations on the building models.

$\overline{C_{MD}}$  is shown in Figure 55b. It reaches a maximum at  $\beta = 0^\circ$ , which is expected since in this orientation the longer surface is perpendicular to the flow.  $\overline{C_{MD}}$  decreases to a minimum at  $\beta = 90^\circ$ , where the shorter surface is perpendicular to the flow.  $\overline{C_{MD}}$  overlaps for both building models in the range of  $0^\circ < \beta < 20^\circ$ . At  $\beta > 20^\circ$ ,  $\overline{C_{MD}}$  for the 1:2:5 building model is slightly lower compared to the 1:3:5 model. Larger  $\overline{C_{MD}}$  observed for the 1:3:5 building model is likely due to larger suction on the leeward surface of the building model due to the stronger flow reattachment, while this still needs to be proven. The 65% PDSF system does not have a significant effect, except for the slight increase in  $\overline{C_{MD}}$  for the 1:2:5 building model.

$\sigma_{CMD}$  exhibits similar trends to  $\overline{C_{MD}}$  regarding  $\beta$ . The maximum  $\sigma_{CMD}$  at  $\beta = 0^\circ$  is a consequence of the orientation of the building model relative to the flow direction. In this experiment, the larger surface is perpendicular to the flow, thus causing large fluctuations on the entire windward surface. There is a significant overlap in the results at  $\beta < 20^\circ$  regardless of the PDSF systems. For  $\beta > 30^\circ$ , the 1:2:5 building model exhibits larger  $\sigma_{CMD}$  compared to the 1:3:5 model, most likely caused by the larger dimension of the 1:3:5 building model in the flow direction. The application of the 65% PDSF system yields a slight increase in  $\sigma_{CMD}$  for both building models.

Figure 56 shows the integral across-wind moment power spectra for the 1:2:5 and 1:3:5 building models with the single skin and the 65% PDSF system. The  $x$ -axis is the dimensionless frequency  $f \cdot d / v_\infty$ , the  $y$ -axis is the dimensionless moment power spectra  $S_M \cdot f / \sigma^2$ , where  $f$  is the frequency in Hz,  $d$  is the width of the building model in m,  $v_\infty$  is the freestream velocity

at the location of the building model in m/s,  $S_M$  is the integral moment power spectrum in  $N^2m^2s$ , and  $\sigma^2$  is the integral moment variance in  $N^2m^2$ .

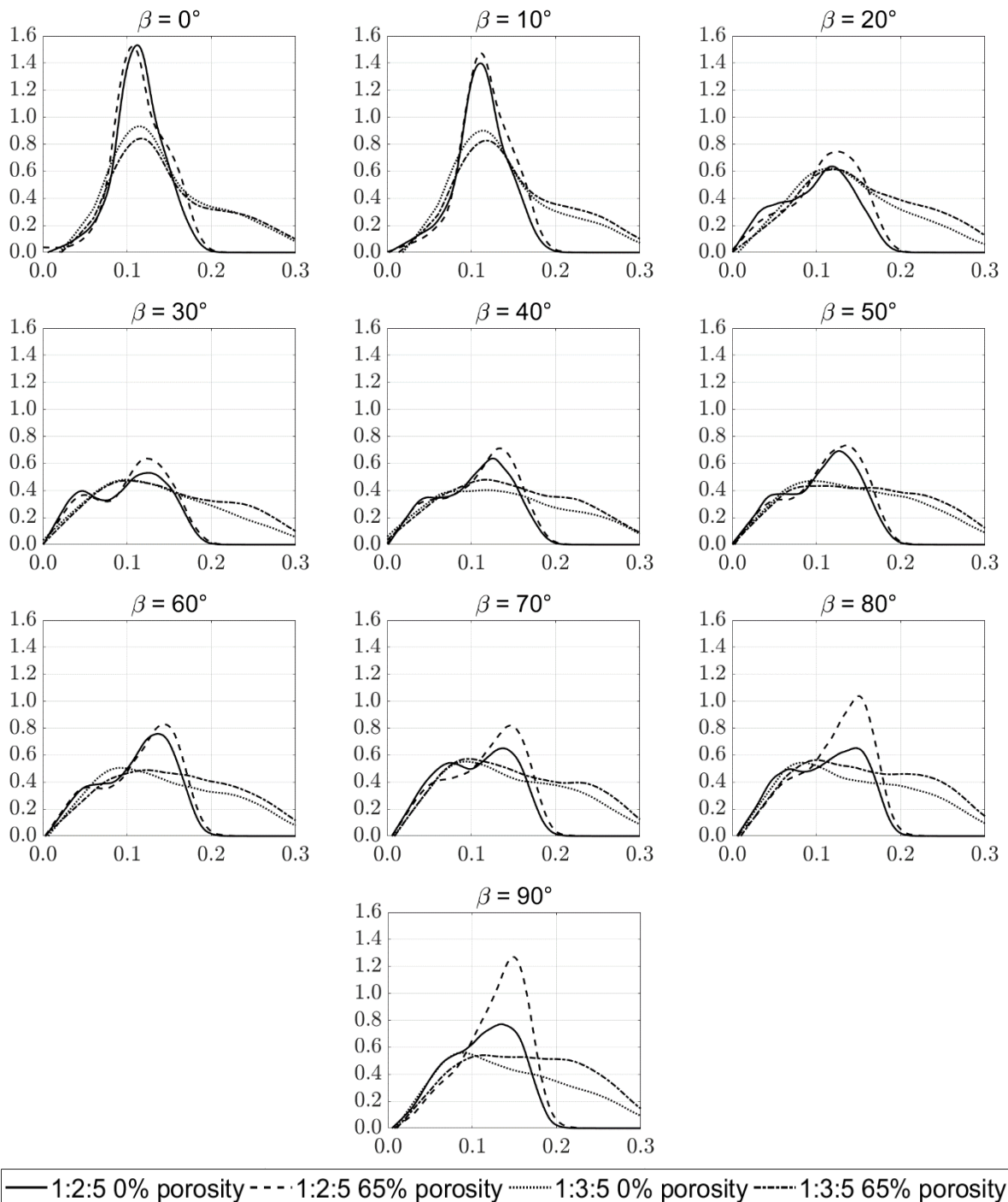
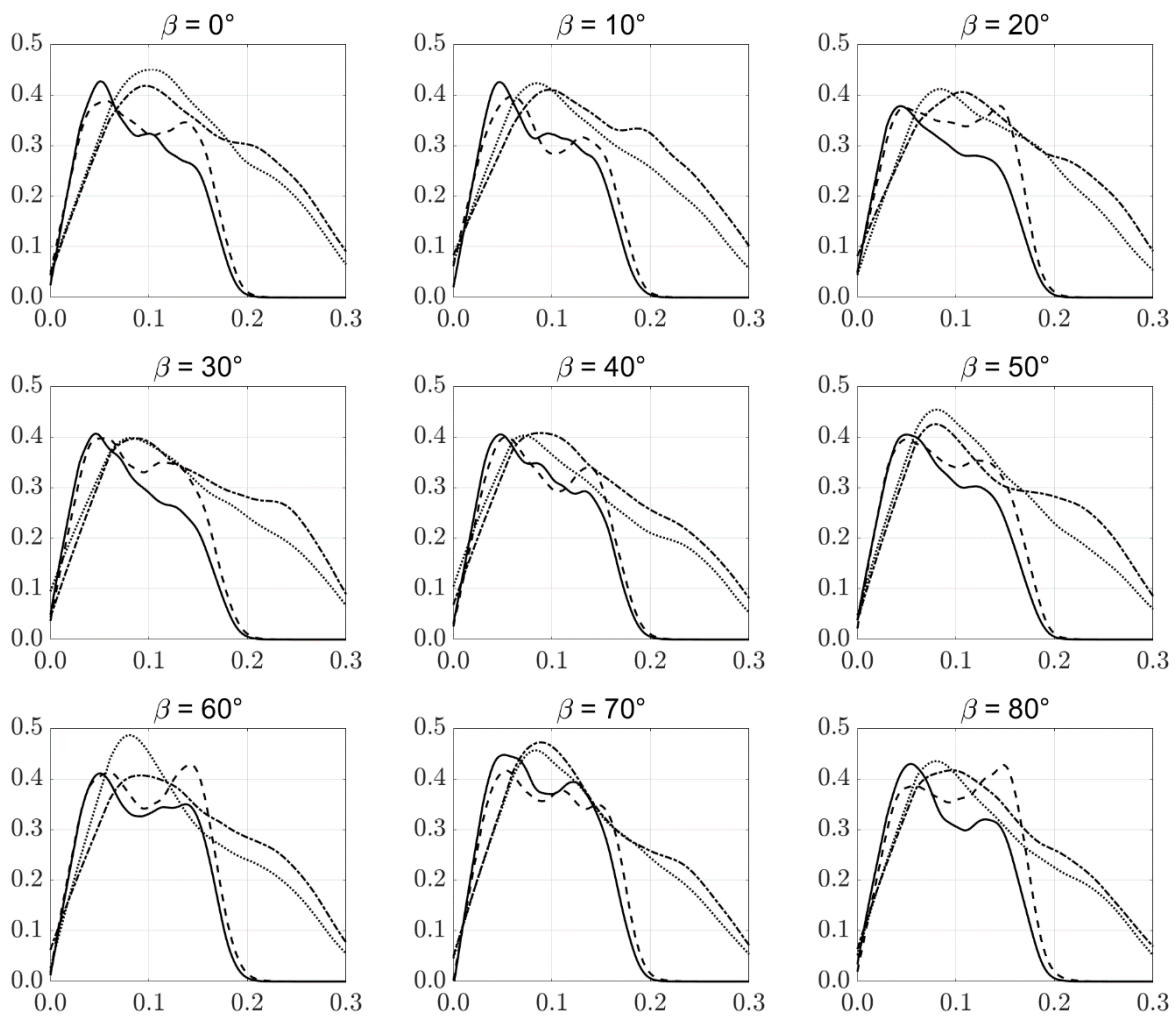


Figure 56. Integral across-wind moment power spectra for the 1:2:5 and 1:3:5 building models with the single skin and the 65% PDSF system

At  $\beta = 0^\circ$ , the peak spectra at 0.1 reduced frequency are much larger for the 1:2:5 building model than for the 1:3:5 building model. On the other hand, the spectrum for the 1:3:5 building model has a lower peak, but a much broader distribution of the spectrum in a range from  $\sim 0.02$

to  $\sim 0.3$  reduced frequency, compared to the 1:2:5 building model at  $\sim 0.2$ . The Strouhal frequency increases when  $\beta = 0^\circ$  changes to  $\beta = 90^\circ$ , observed by the shift of the peak towards a higher reduced frequency. The peak is lower at  $\beta = 90^\circ$  than at  $\beta = 0^\circ$ . The 65% PDSF system yields an increase in the across-wind moment power spectra for the 1:2:5 building model at a large  $\beta$ .

The integral along-wind moment power spectra are shown in Figure 57. The  $x$ -axis is the dimensionless frequency  $f \cdot d/v_\infty$ , the  $y$ -axis is the dimensionless moment power spectra  $S_M \cdot f/\sigma^2$ , where  $f$  is the frequency in Hz,  $d$  is the width of the building model in m,  $v_\infty$  is the freestream velocity at the location of the building model in m/s,  $S_M$  is the integral moment power spectrum in  $N^2m^2s$ , and  $\sigma^2$  is the integral moment variance in  $N^2m^2$ .



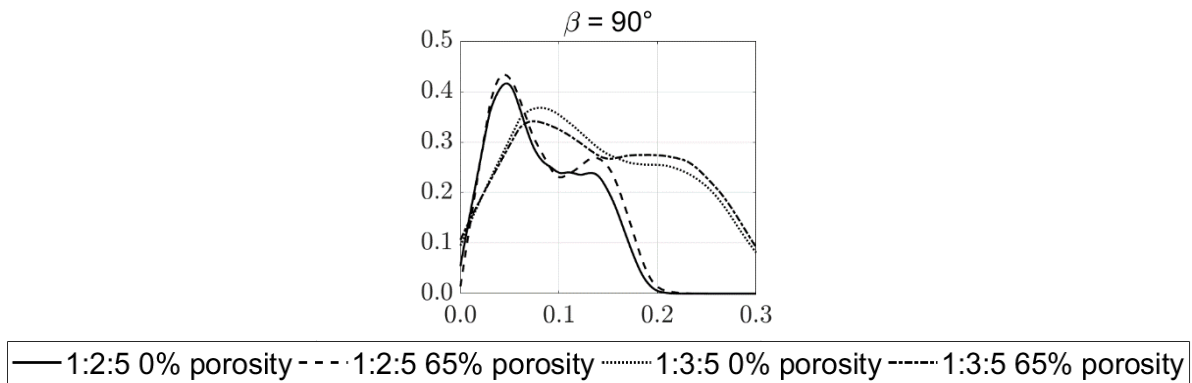


Figure 57. Integral along-wind moment power spectra for the 1:2:5 and 1:3:5 building models with the single-skin and the 65% PDSF system

The spectra for the 1:3:5 building model are much broader, in the range from  $\sim 0.02$  to  $\sim 0.3$  reduced frequency. The maximum is similar for both building models, thus exhibiting that the along-wind load is comparable for both cases. The 65% PDSF system has a negligible effect on the along-wind moment power spectra.

## 7.5 Aerodynamic interference of tall buildings with porous façades

The interference of multiple buildings of equal dimensions was studied regarding aerodynamic loads on the principal 1:1:5 building model subjected to the suburban ABL simulation. The single-skin building model was used as a reference case. Eight 1:1:5 dummy building models were arranged in an in-line pattern surrounding the principal building model used for aerodynamic load measurements.

There were two focus points in this work segment: a) the effect of  $\beta$ , and b) the effect of spacing between the building models. For a), the spacing between the building models was  $D = 5d$ , where  $d$  is the width of the building model ( $d = 100$  mm).  $\beta$  was studied in the  $0^\circ < \beta < 45^\circ$  range with a  $5^\circ$  increment. While the distance between the building models was the same, the principal building model was studied for various PDSF systems:

- 1) Building model without a PDSF system (single-skin non-porous façade);
- 2) Building model with the 25% PDSF system;
- 3) Building model with the 50% PDSF system.

The urban environment model was rotated around the principal building model to achieve various  $\beta$ , Figure 58.



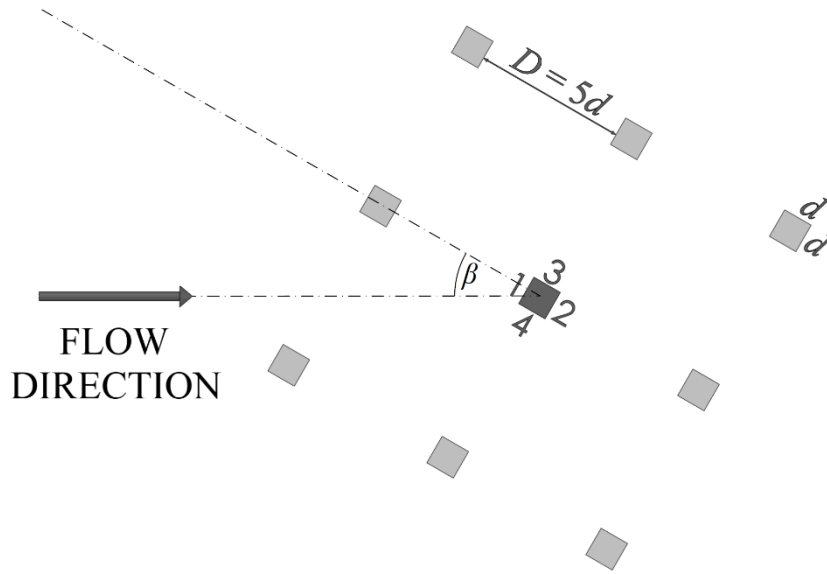


Figure 58. Urban environment model

### 7.5.1 The effect of the flow incidence angle

Figure 59 shows  $\overline{C_{MD}}$  at various  $\beta$  for the principal building model situated in the model urban environment at  $D = 5d$ .

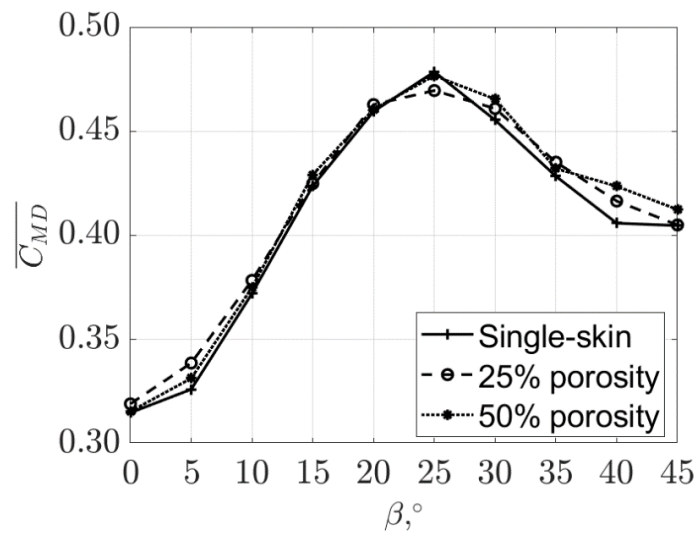


Figure 59.  $\overline{C_{MD}}$  for the building model situated in the urban environment model at  $D = 5d$

The  $\overline{C_{MD}}$  of the single-skin building model is similar to the respective results obtained using the 25% and 50% PDSF systems at all  $\beta$ . The peak is present at  $\beta = 25^\circ$  because of the

characteristic flow phenomena. In particular, the studied building model at  $\beta = 0^\circ$  is in the wake of the upstream dummy building model, while the flow at  $\beta = 25^\circ$  directly impinges on the principal building model. At other  $\beta$ , the building model is entirely or partially sheltered by the upstream dummy building model, a phenomenon that influences the  $\overline{C_{MD}}$  of the principal building model.

$\overline{C_{MD}}$  is larger for  $\beta = 45^\circ$  compared to  $\beta = 0^\circ$  most likely because a) the principal building model at  $\beta = 45^\circ$  is in a more streamlined position, and b) the dummy building directly downstream of the principal building model is in a more streamlined position and closer to the principal building model.

Figure 60 shows the  $\overline{C_{ML}}$  of the building model situated in the urban environment model at various  $\beta$ .

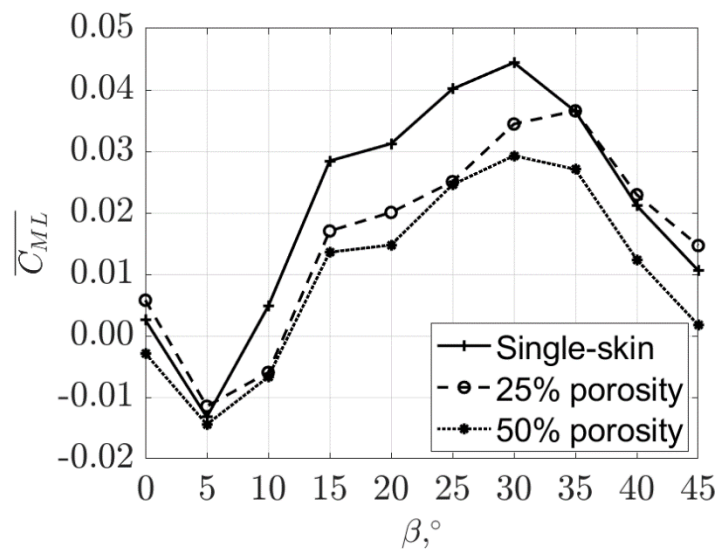


Figure 60.  $\overline{C_{ML}}$  of the building model situated in the urban environment model at  $D = 5d$

Due to the symmetry of the experimental setup,  $\overline{C_{ML}}$  at  $\beta = 0^\circ$  and  $45^\circ$  was expected to be zero. However, even the slightest asymmetry in the setup may lead to some discrepancies in  $\overline{C_{ML}}$ . Therefore, in the studied setup of nine building models, perfect symmetry of the setup was unfortunately not achieved. The reason why the results for  $\beta = 45^\circ$  are higher than for  $\beta = 0^\circ$  is because  $\beta = 45^\circ$  is the most streamlined configuration and an asymmetry has a more pronounced effect on the results than at  $\beta = 0^\circ$ .

The maximum  $\overline{C_{ML}}$  is present at  $\beta = 30^\circ$  for the single-skin building model, while for the 25% and 50% PDSF systems, the maximum  $\overline{C_{ML}}$  is at  $30 < \beta < 35^\circ$ . This slight discrepancy in the maximum  $\overline{C_{ML}}$  is likely due to the combined effect of  $\beta$  and PDSF porosity, where the flow

is mainly unaffected among the dummy building models for  $20^\circ < \beta < 30^\circ$ , thus allowing for higher flow velocity impinging on the principal building model.

There is a clear effect of lower  $\overline{C_{ML}}$  in more porous PDSF systems. The largest difference is observed in the  $20^\circ < \beta < 30^\circ$  range, thus in the flow not largely affected by the dummy building models, where the surface pressure on the principal building model influencing  $\overline{C_{ML}}$  is for the most part dictated by the flow separation and reattachment phenomena on the building model surfaces characterized by a variety of surface roughness.

Figure 61 shows the power spectra of the integral along-wind moment. The  $x$ -axis is the dimensionless frequency  $f \cdot d/v_\infty$ , the  $y$ -axis is the dimensionless moment power spectra  $S_M \cdot f/\sigma^2$ , where  $f$  is the frequency in Hz,  $d$  is the width of the building model in m,  $v_\infty$  is the freestream velocity at the location of the building model in m/s,  $S_M$  is the integral moment power spectrum in  $N^2m^2s$ , and  $\sigma^2$  is the integral moment variance in  $N^2m^2$ .

For a reduced frequency less than 0.1, for all  $\beta$  except  $\beta = 0^\circ$ , there is good agreement in the along-wind moment power spectra regardless of the outer façade porosity. The application of the PDSF system at  $\beta = 0^\circ$  is in fact beneficial, as the along-wind moment power spectra are lower for any PDSF porosity compared to the single-skin building. This indicates that the PDSF system characteristics have either a positive or a negligible effect on the along-wind vibration of the building at low reduced frequencies.

A significant peak in the along-wind moment power spectra appears in the  $10^\circ < \beta < 35^\circ$  range at  $\sim 0.1$  reduced frequency, which is most likely caused by vortex shedding from the building model at the characteristic Strouhal frequency. It should be noted for the  $10^\circ < \beta < 40^\circ$  range that the freestream flow for the most part impinges on the studied building model, as shown in Figure 61, which probably enhances vortex shedding and along-wind moment fluctuations. The application of the PDSF yields a peak at 0.1 reduced frequency at a lower  $\beta$  than for the single-skin building model, e.g., at  $\beta = 10^\circ$  the peak for the single-skin building model is not present.

For a reduced frequency larger than 0.15, the building model with the PDSF systems is consistently characterized by higher along-wind moment fluctuations, which is likely due to the surface roughness because of the openings of the PDSF systems. The openings cause high-frequency fluctuations due to the flow entering and exiting the gap between two building façades through the small openings. The small diameter of the openings limits the size of the vortices around the building model, causing larger fluctuations at high frequencies. In Figure 61, the  $x$ -axis is the dimensionless frequency  $f \cdot d/v_\infty$ , the  $y$ -axis is the dimensionless moment power spectra  $S_M \cdot f/\sigma^2$ , where  $f$  is the frequency in Hz,  $d$  is the width of the building model in m,  $v_\infty$  is the freestream velocity at the location of the building model in m/s,  $S_M$  is the integral moment power spectrum in  $N^2m^2s$ , and  $\sigma^2$  is the integral moment variance in  $N^2m^2$ .

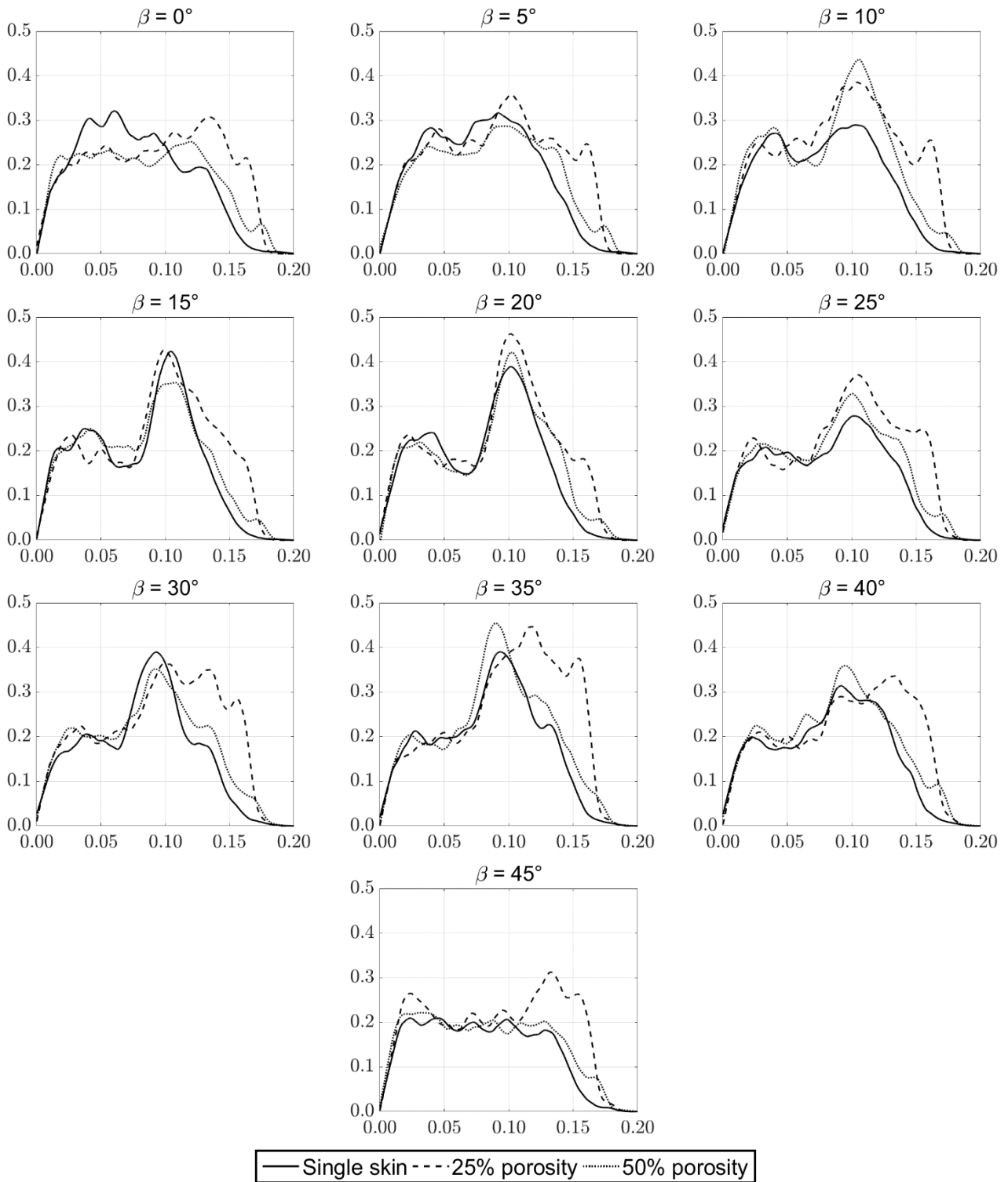


Figure 61. Integral along-wind moment power spectra for the principal building model situated in the urban environment model at  $D = 5d$

The across-wind moment power spectra are shown in Figure 62. The  $x$ -axis is the dimensionless frequency  $f \cdot d/v_\infty$ , the  $y$ -axis is the dimensionless moment power spectra  $S_M$ .

$f/\sigma^2$ , where  $f$  is the frequency in Hz,  $d$  is the width of the building model in m,  $v_\infty$  is the freestream velocity at the location of the building model in m/s,  $S_M$  is the integral moment power spectrum in  $N^2m^2s$ , and  $\sigma^2$  is the integral moment variance in  $N^2m^2$ .

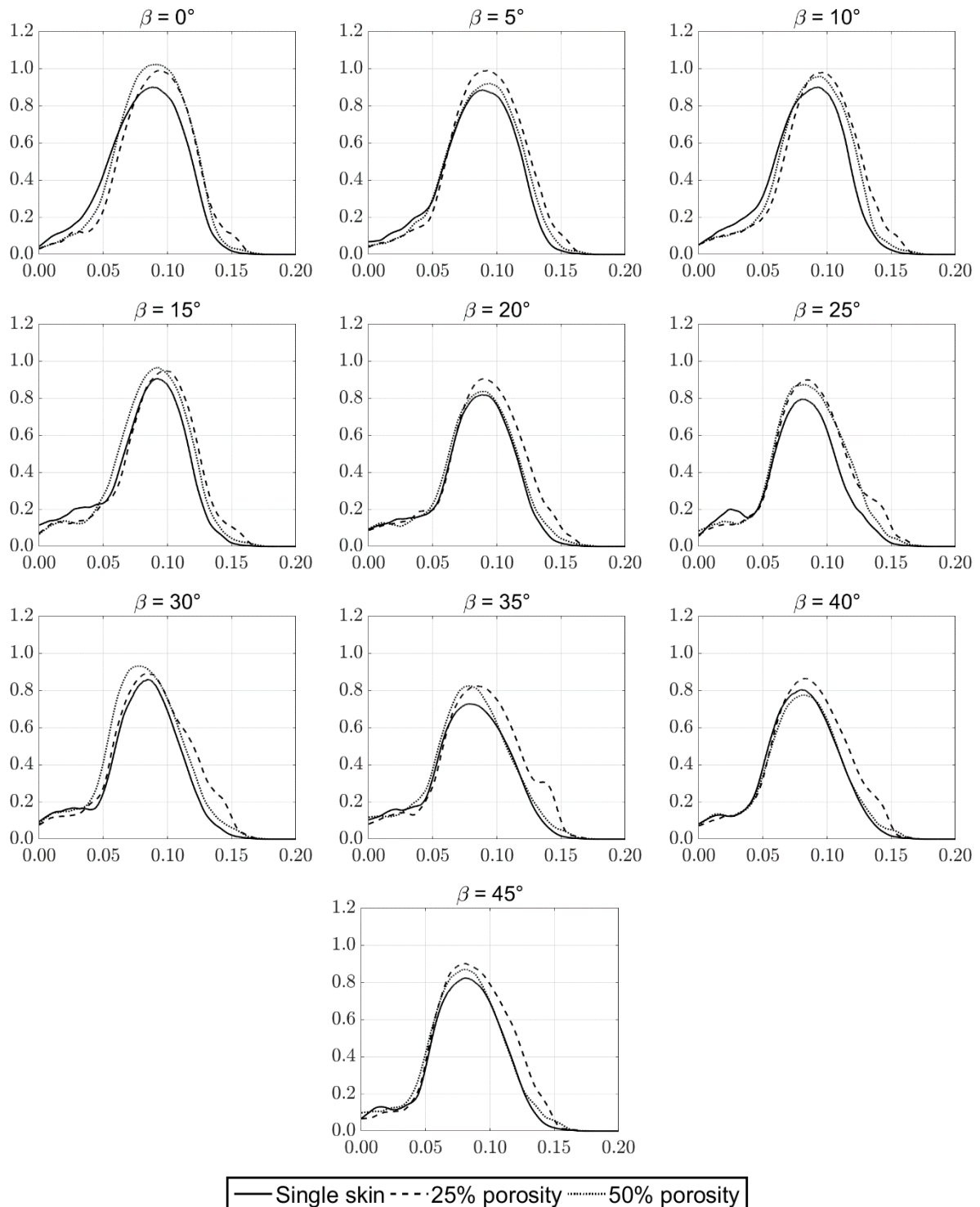


Figure 62. Integral cross-wind moment power spectra for the principal building model situated in the urban environment model at  $D = 5d$

There are several important findings to note regarding the power spectra of the across-wind moment fluctuations: a) there is a clearly exhibited peak at the reduced frequency of 0.1, b) the effect of  $\beta$  is rather negligible, c) the PDSF systems cause shifts in the peak magnitude and its respective frequency.

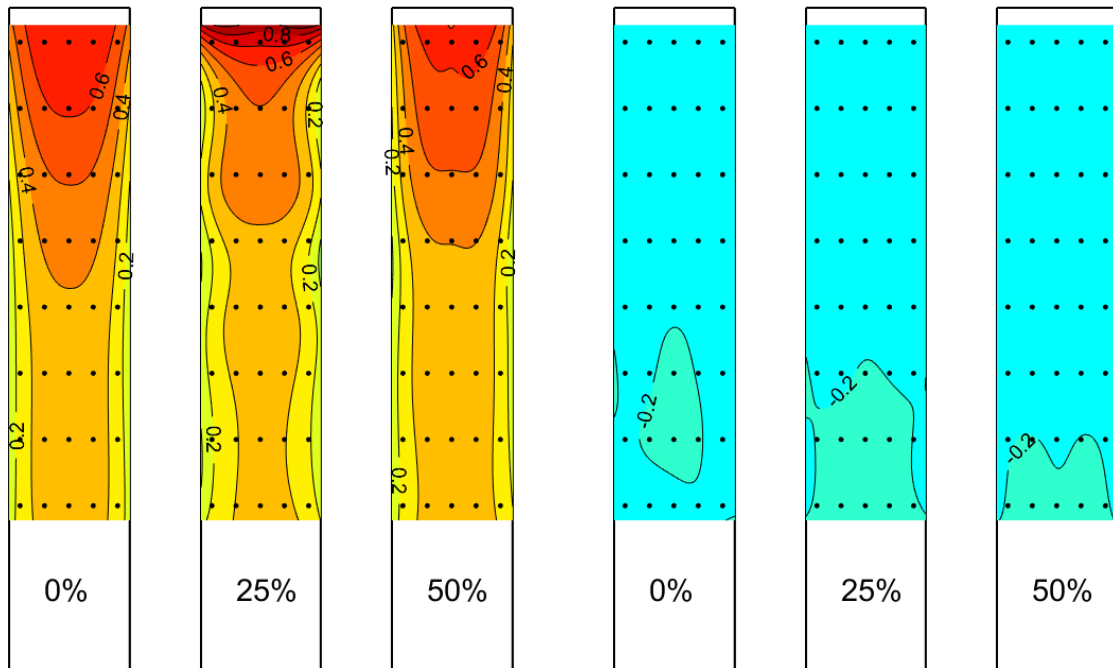
The across-wind moment fluctuations at a low  $\beta$  are slightly higher compared to the results obtained at a larger  $\beta$ . The reason is the vortex shedding from the building model that is more evident at a low  $\beta$ . This phenomenon is attributed to the dummy building models situated upstream of the principal building model, a setup that causes an increase in turbulence impinging on the principal building model. Thus, the principal building model is in the wake of the dummy building models, a flow range characterized by strong vortices causing lateral vibration. Higher peak magnitudes are observed for the principal building model equipped with PDSF systems, a trend observed at almost all  $\beta$ . The cause of this phenomenon may be the complex, highly turbulent flow created by many openings in the porous façade. Based on this analysis, it can be stated that the use of PDSF systems in an urban environment yields slightly greater vibration in the lateral direction of the principal building model.

The  $\overline{C_p}$  distribution for various  $\beta$  is shown in Figure 63. The configuration without the porous façade is on the left-hand side of each row. In the middle of each row is the configuration with the 25% PDSF system, and on the right-hand side is the configuration with the 50% PDSF system.

$\beta = 0^\circ$

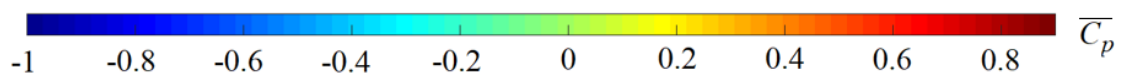
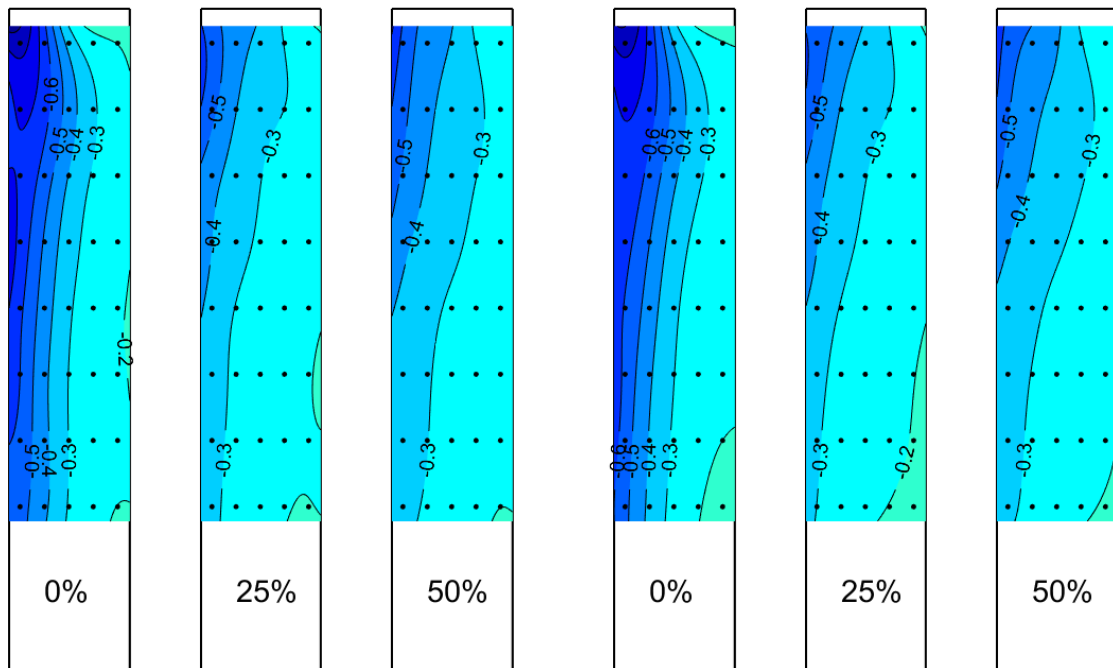
SURFACE 1

SURFACE 2

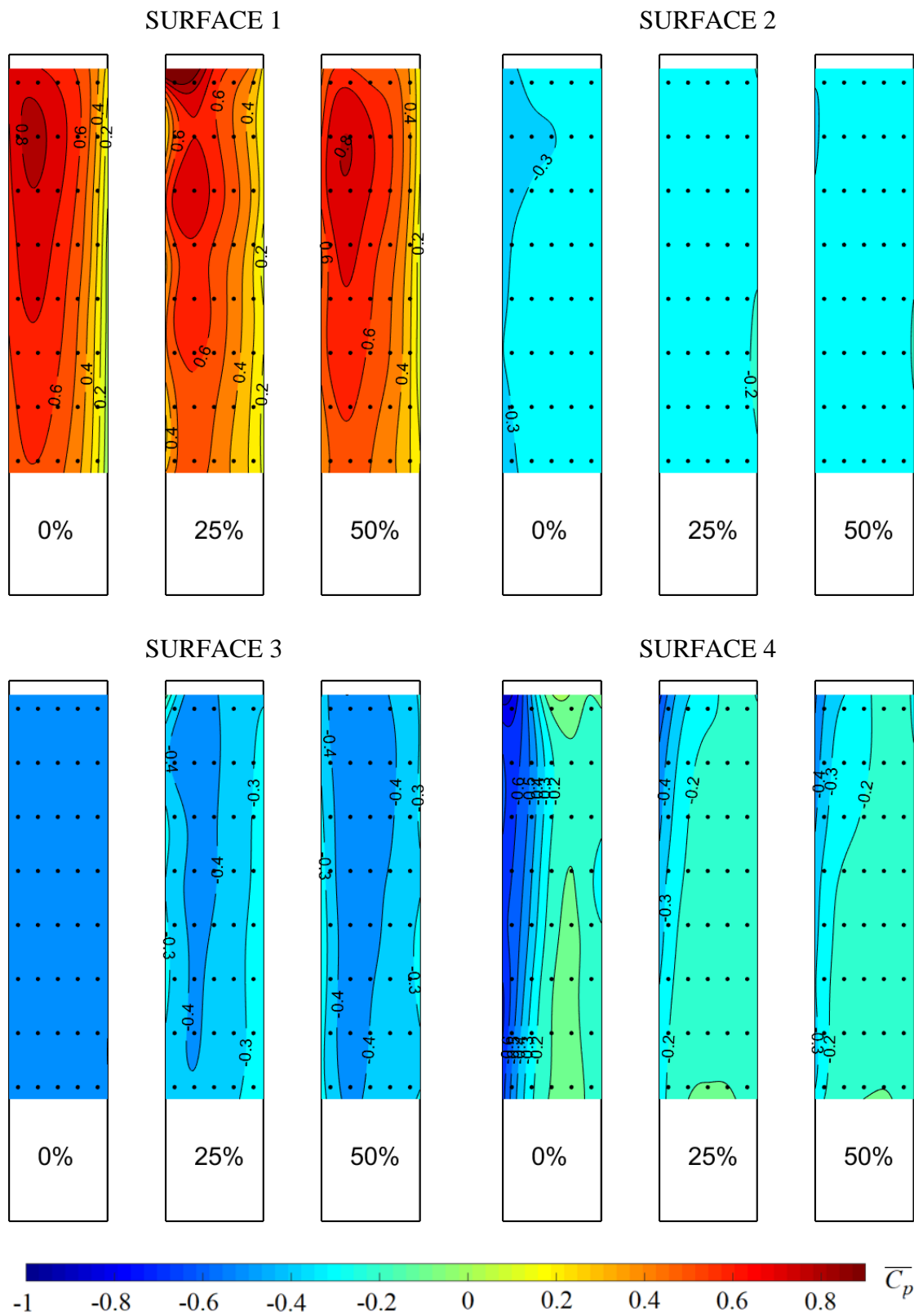


SURFACE 3

SURFACE 4



$\beta = 15^\circ$

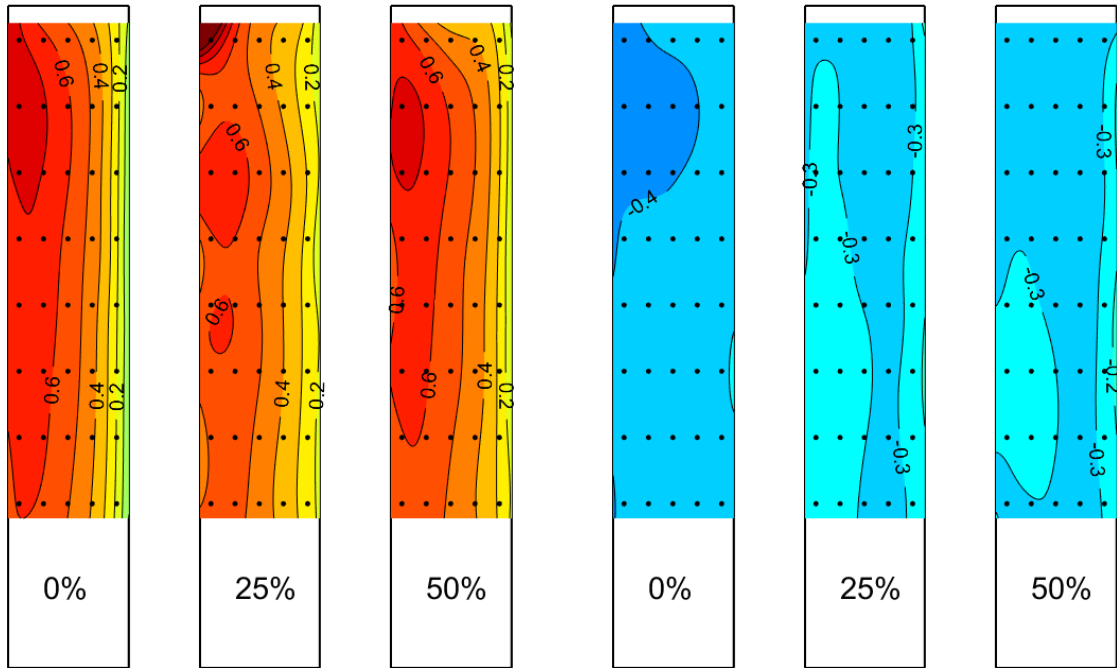




$\beta = 30^\circ$

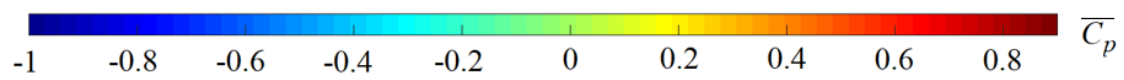
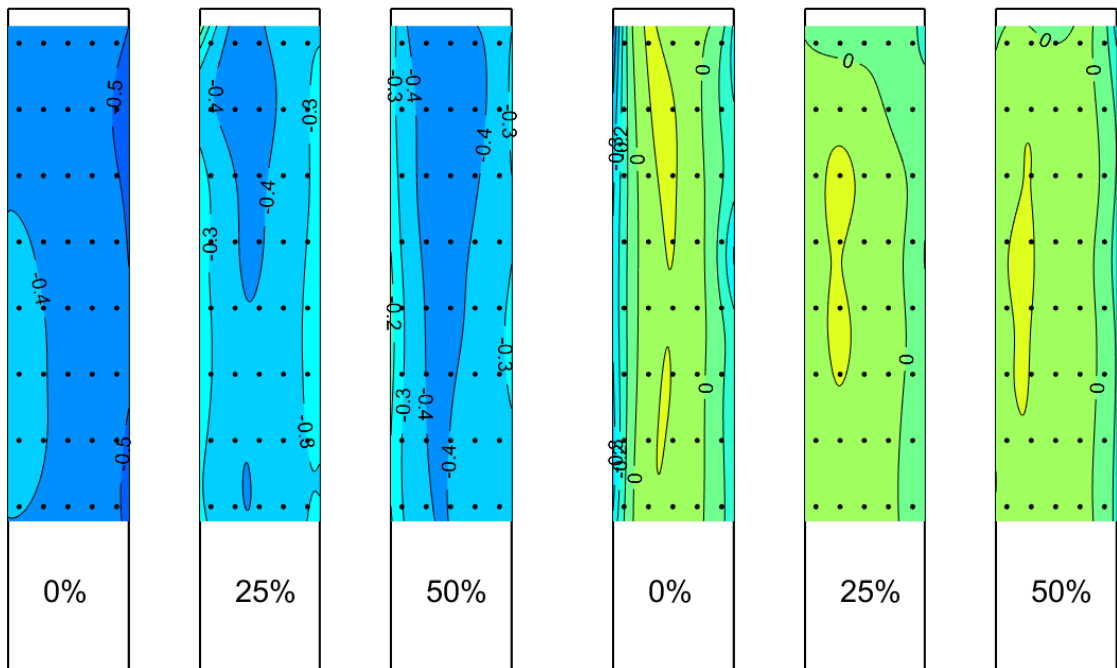
SURFACE 1

SURFACE 2



SURFACE 3

SURFACE 4



$\beta = 45^\circ$

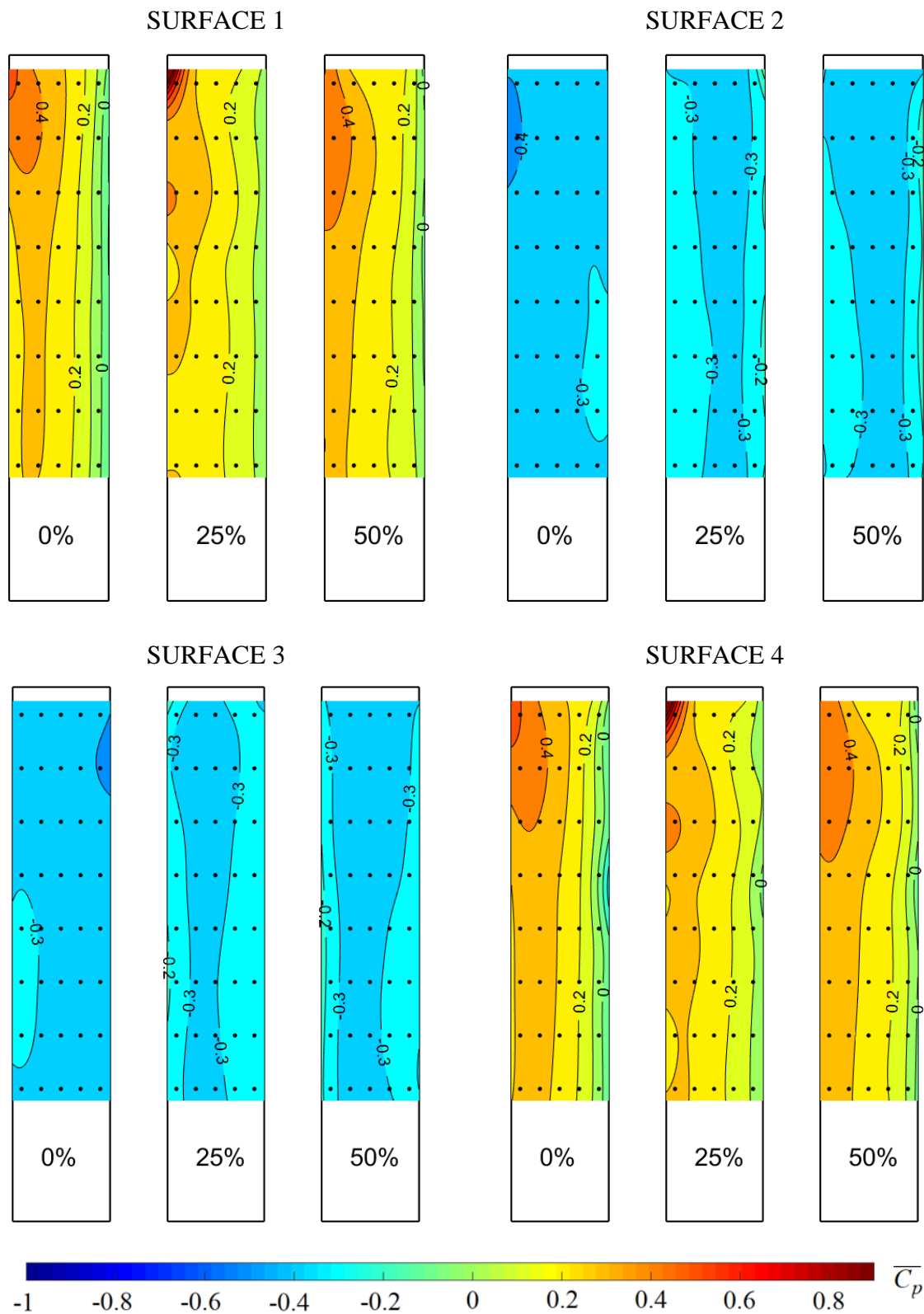


Figure 63.  $\overline{C_p}$  distribution for various  $\beta$

For  $\beta = 0^\circ$ , the maximum  $\overline{C_p}$  in the stagnation zone on Surface 1 is  $\sim 0.6$ , which is  $\sim 30\%$  lower than the maximum  $\overline{C_p}$  of  $\sim 0.9$  previously observed on the building model situated in the undisturbed boundary layer, i.e., not in the wake of the upstream building model. As expected,  $\overline{C_p}$  is positive on Surface 1, there is uniform suction on Surface 2, while the negative and symmetric  $\overline{C_p}$  distribution on Surfaces 3 and 4 is dictated by the flow separation and the respective suction underlying the shed vortices. Earlier reattachment in more turbulent flow closer to the ground surface can be clearly observed, as the flow previously proved to reattach closer to the leading edge in more turbulent flow.

The PDSF system yields a change in the shape of the  $\overline{C_p}$  distribution, while the extreme values remain nearly the same. The change is most apparent on Surface 1 where the contours for each façade type have a different shape corresponding to the openings on the porous façade.  $\overline{C_p}$  is 10% to 20% lower depending on the PDSF type and  $\beta$ , thus showing the clear sheltering effect of the outer façade.

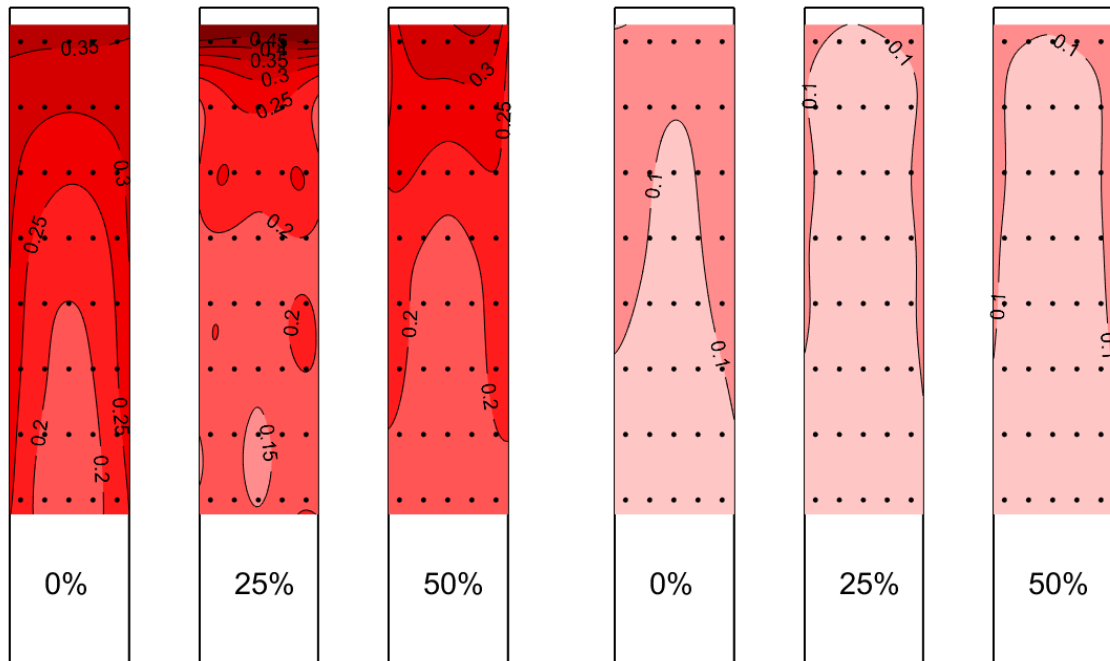
The trends at  $\beta = 0^\circ$  may be generally observed also at  $\beta = 15^\circ$ ,  $30^\circ$ , and  $45^\circ$ . This fact clearly indicates that  $\overline{C_p}$  on the entire building model surface decreases when a PDSF system is used.

$\sigma_{C_p}$  for various  $\beta$  and the spacing of building models  $D = 5d$  are shown in Figure 64 to allow for an analysis of the fluctuating pressure on the inner surface of the principal building model.

$\beta = 0^\circ$

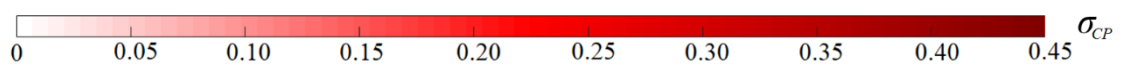
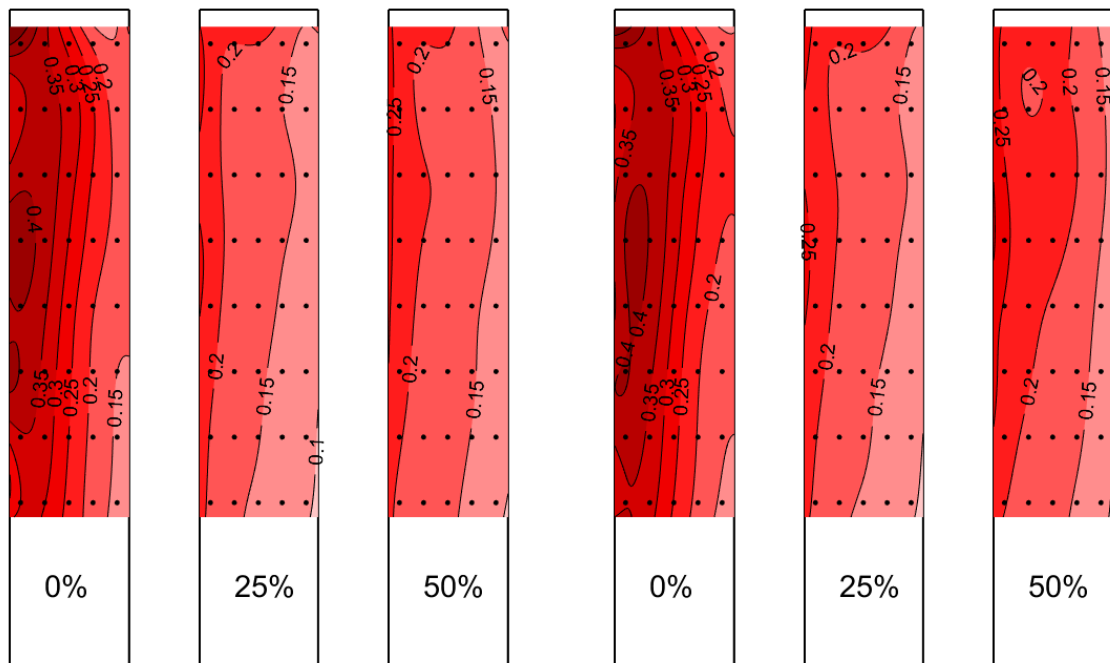
SURFACE 1

SURFACE 2



SURFACE 3

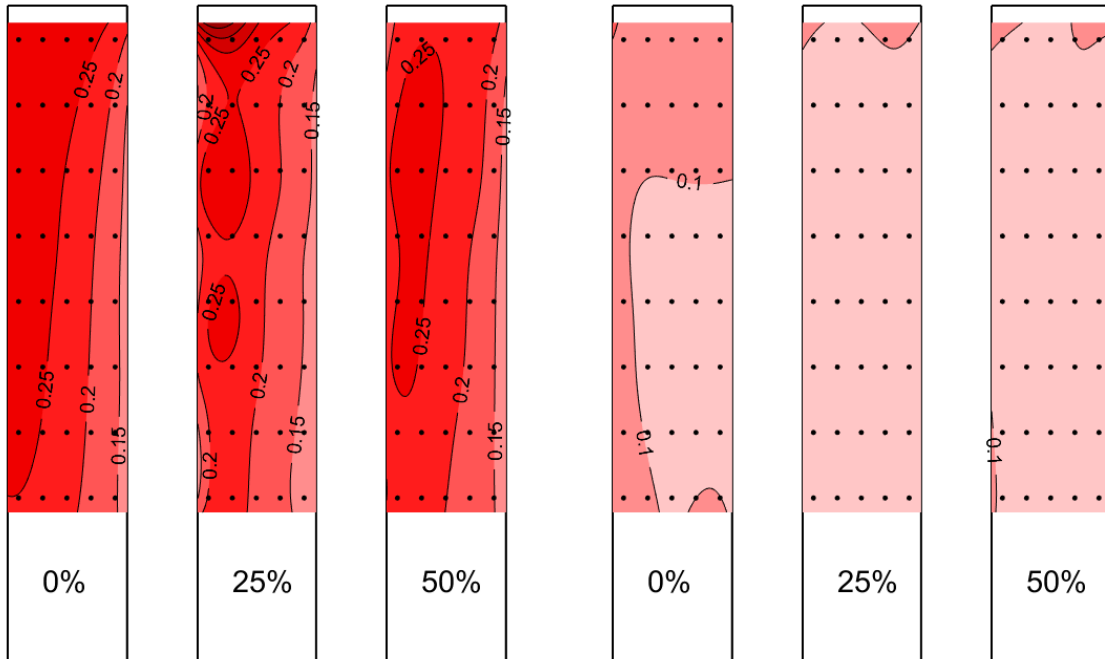
SURFACE 4



$\beta = 15^\circ$

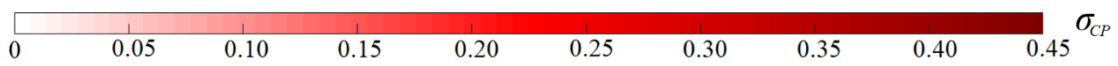
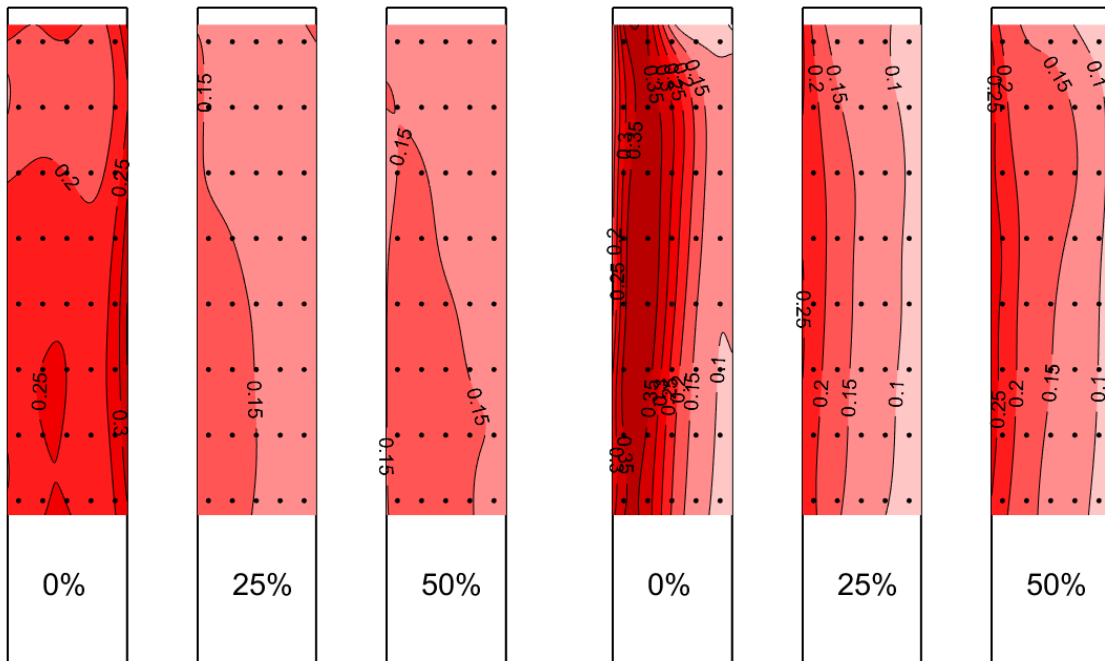
SURFACE 1

SURFACE 2



SURFACE 3

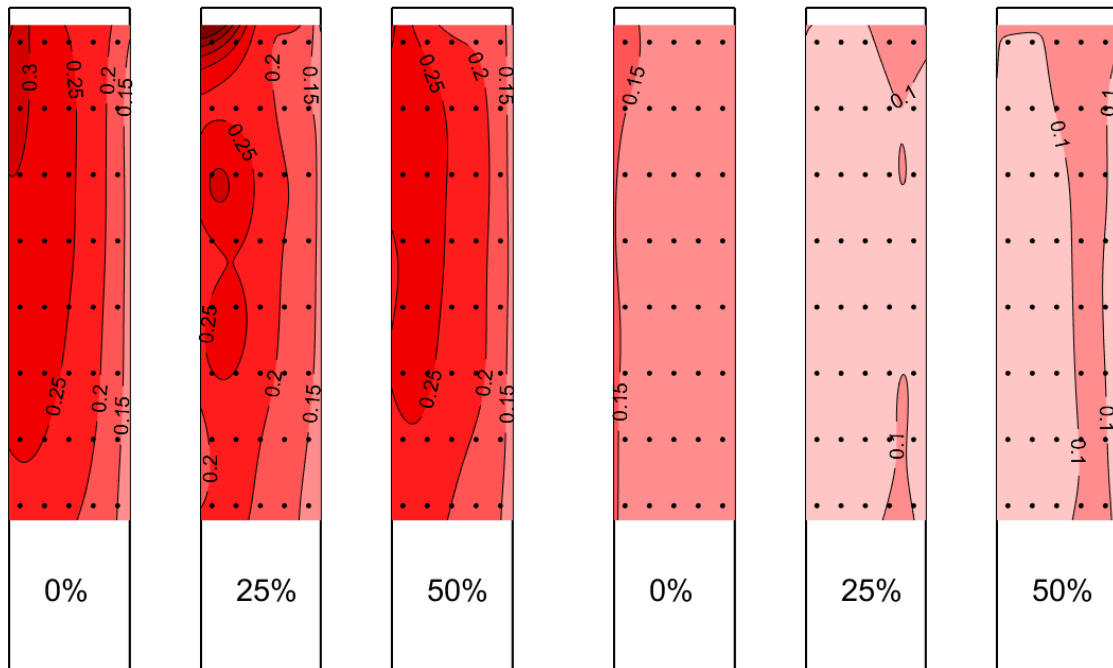
SURFACE 4



$\beta = 30^\circ$

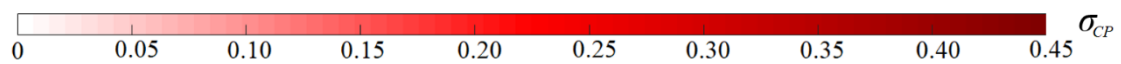
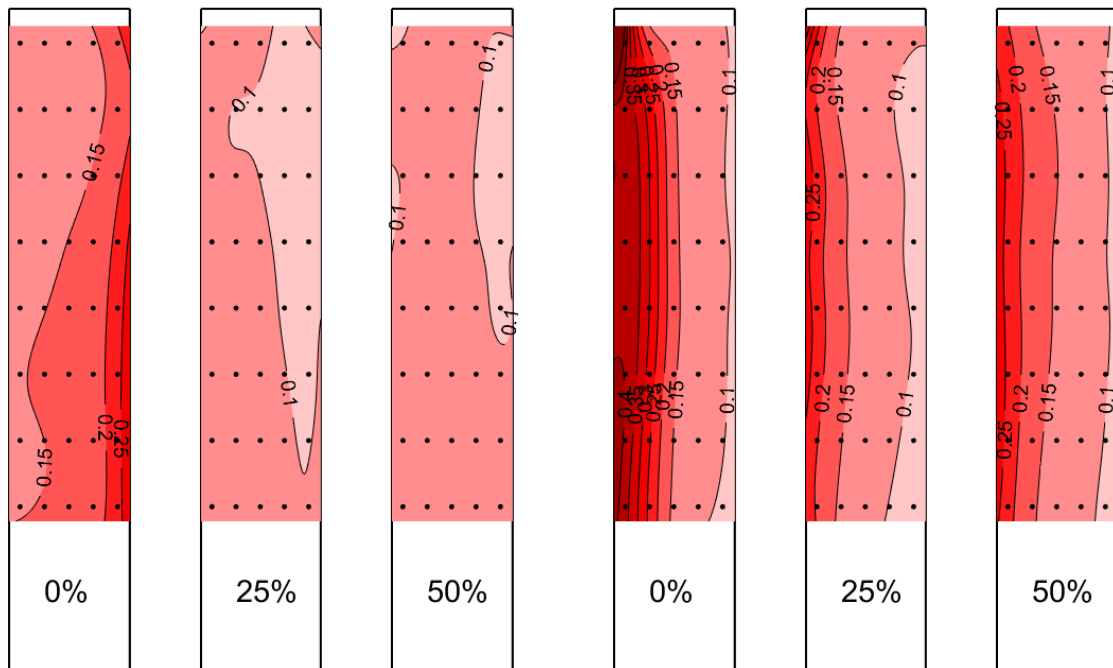
SURFACE 1

SURFACE 2



SURFACE 3

SURFACE 4



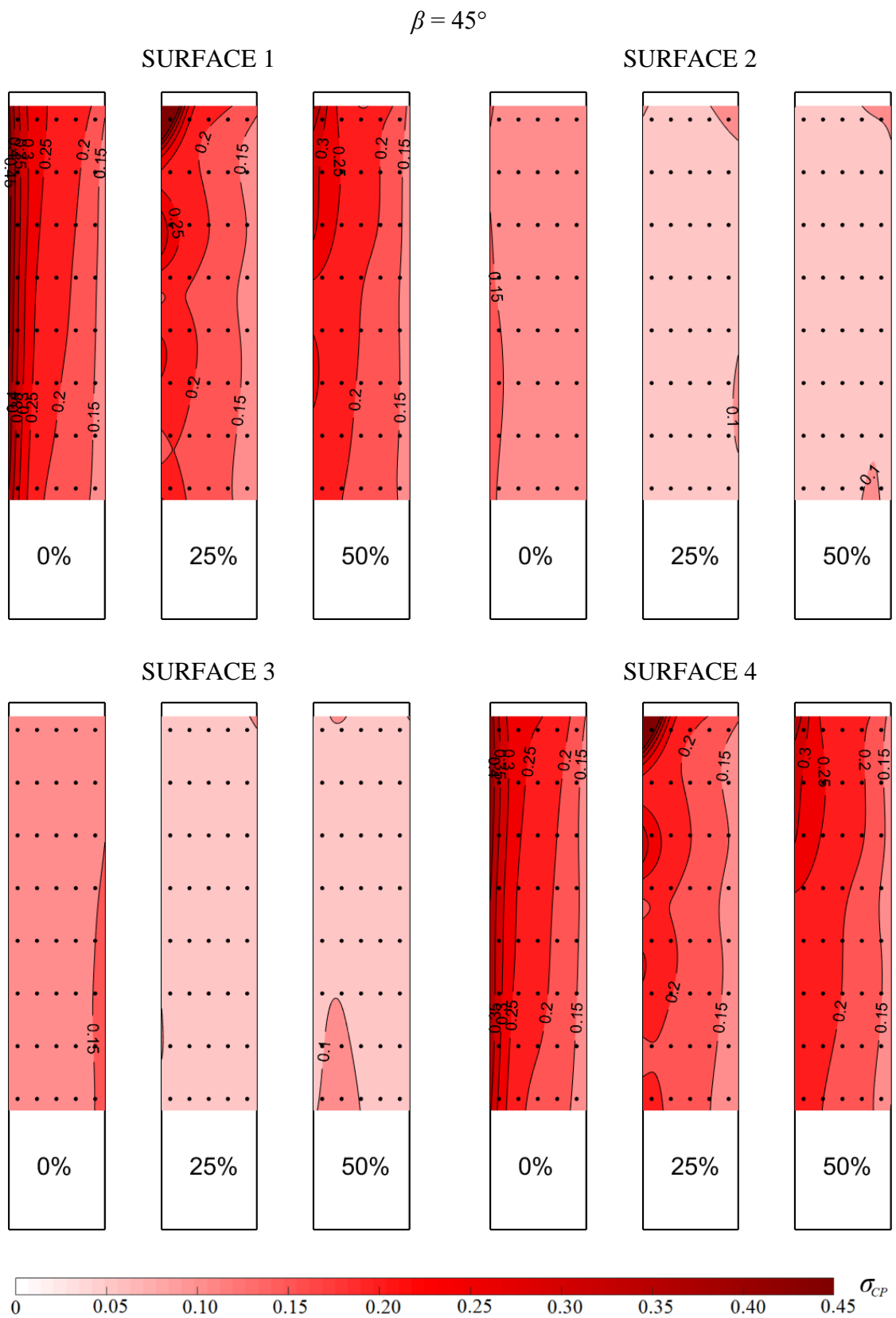


Figure 64.  $\sigma_{CP}$  for various  $\beta$

$\sigma_{Cp}$  is predominantly influenced by the turbulence in the flow. In particular, at  $\beta = 0^\circ$ , on the lower 70% of Surface 1,  $\sigma_{Cp}$  remains nearly constant. With the increasing height from  $z = 0.7H$ ,  $\sigma_{Cp}$  increases towards the upper edge of the building model surface. An increase in  $\sigma_{Cp}$  in the upper part of Surface 1 is due to the buffeting vortices impinging on the windward building Surface 1. The 25% PDSF yields a slight decrease in  $\sigma_{Cp}$  and the alteration of the shape of its respective distribution related to the openings on the porous outer façade.  $\sigma_{Cp}$  for the 25% and 50% PDSF systems is nearly the same.

The effect of the PDSF system on  $\sigma_{Cp}$  on Surfaces 3 and 4 is substantial. The inner flow is sheltered from the outer, highly turbulent flow. Thus,  $\sigma_{Cp}$  on the inner façade is considerably reduced when the PDSF systems are employed. A particularly important area on Surfaces 3 and 4 is near the vertical edge close to Surface 1. In that surface area, the flow separates, thus creating a recirculation bubble, which is reflected in the  $\sigma_{Cp}$  on the single-skin façade configuration. In contrast,  $\sigma_{Cp}$  is substantially lower on the configurations equipped with the PDSF systems due to the sheltered inner flow.

Surface 2 is entirely in the wake, thus characterized by low and nearly constant  $\sigma_{Cp}$  over the entire building model surface. In general, the PDSF system yields a low-turbulent flow between the outer and inner building model surfaces. The inner façade is sheltered from the highly turbulent freestream flow. The trend of lower  $\sigma_{Cp}$  may be observed at all  $\beta$  when PDSF systems are in place.

### 7.5.2 The effect of the spacing between buildings

The effect of spacing between building models in an urban environment model was studied for three spacings, Figure 65:

- 1) Small spacing between building models, i.e.,  $D = d = 100$  mm;
- 2) Medium spacing between building models, i.e.,  $D = 3d = 300$  mm;
- 3) Large spacing between building models, i.e.,  $D = 5d = 500$  mm.



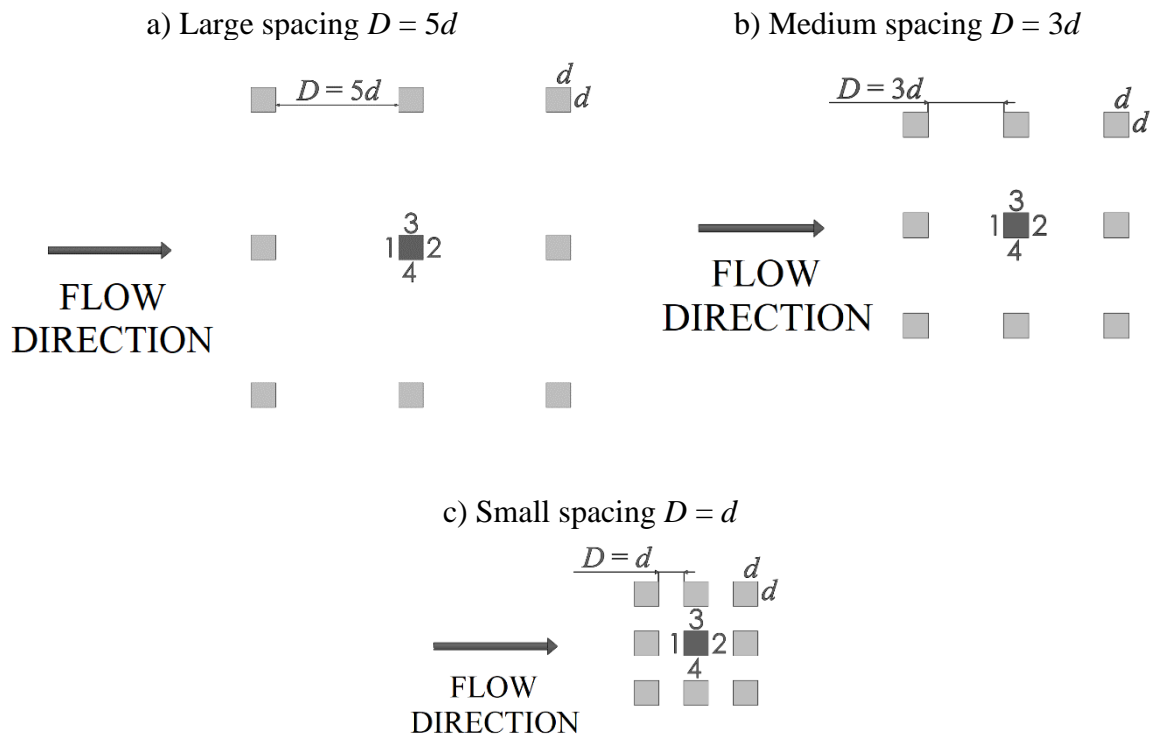


Figure 65. Studied spacing between building models

Two configurations of the principal building model were analyzed: a) a single-skin façade building model and b) a double-skin façade building model equipped with the 25% PDSF system. For the small spacing of building models  $D = d$ , the effect of the PDSF system was not assessed because it was observed in the preliminary experiments that the principal building model was entirely sheltered. Flow in such densely built-up areas is the skimming flow, e.g., Britter and Hanna [149], and is characterized by limited direct penetration into the spaces between the buildings. In this  $D = d$  arrangement, the PDSF systems proved to have marginal effect, as the results for the building models equipped with the PDSF systems and the smooth single-skin building model are basically the same.

Figure 66 shows the  $\overline{C_{MD}}$  for various  $\beta$  for the principal building model situated in the urban environment model.

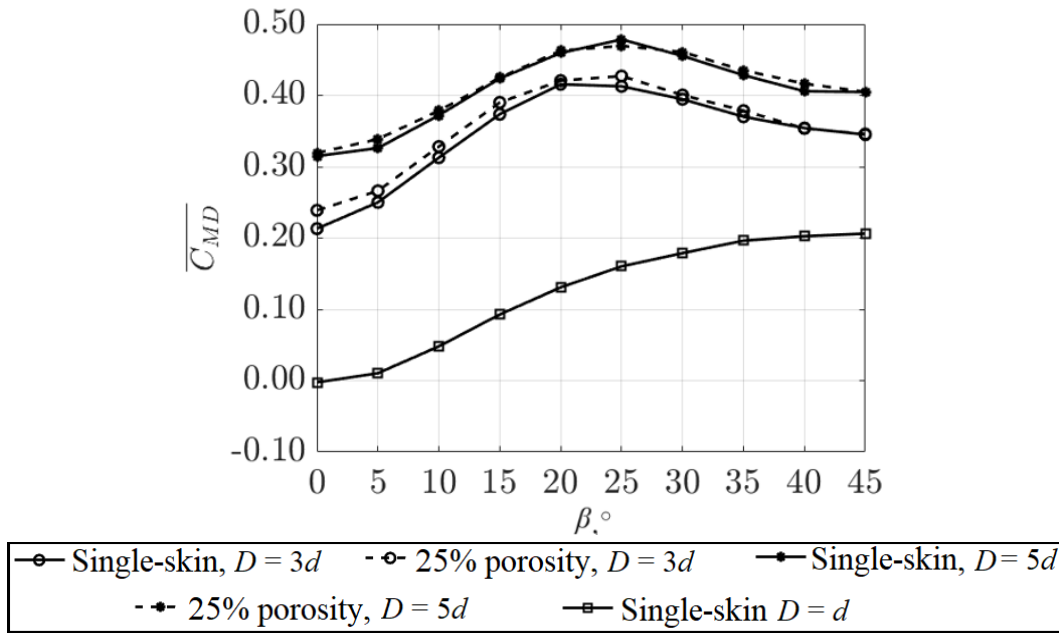


Figure 66.  $\overline{C_{MD}}$  for the principal building model situated in the urban environment model at  $D = d, D = 3d$  and  $D = 5d$

In general,  $\overline{C_{MD}}$  is substantially lower on the smooth single-skin building model in the minimum spacing  $D = d$  compared to the larger spacings  $D = 3d$  and  $D = 5d$ , i.e., for the same PDSF system,  $\overline{C_{MD}}$  is greater in larger spacing between the building models. There is a negligible discrepancy in the  $\overline{C_{MD}}$  for the PDSF system and a single-skin building model when both are situated in the urban environment model of the same spacing. For the small spacing ( $D = d$ ) at  $\beta = 0^\circ$ ,  $\overline{C_{MD}} \sim 0$  indicates that the principal building model was entirely sheltered. For the medium ( $D = 3d$ ) and large ( $D = 5d$ ) spacing, the maximum  $\overline{C_{MD}}$  was at  $\beta = 25^\circ$ , which is due to the characteristic flow between building models, Figure 11.

The  $\overline{C_{ML}}$  of the principal building model situated in various models of the urban environment are shown in Figure 67.

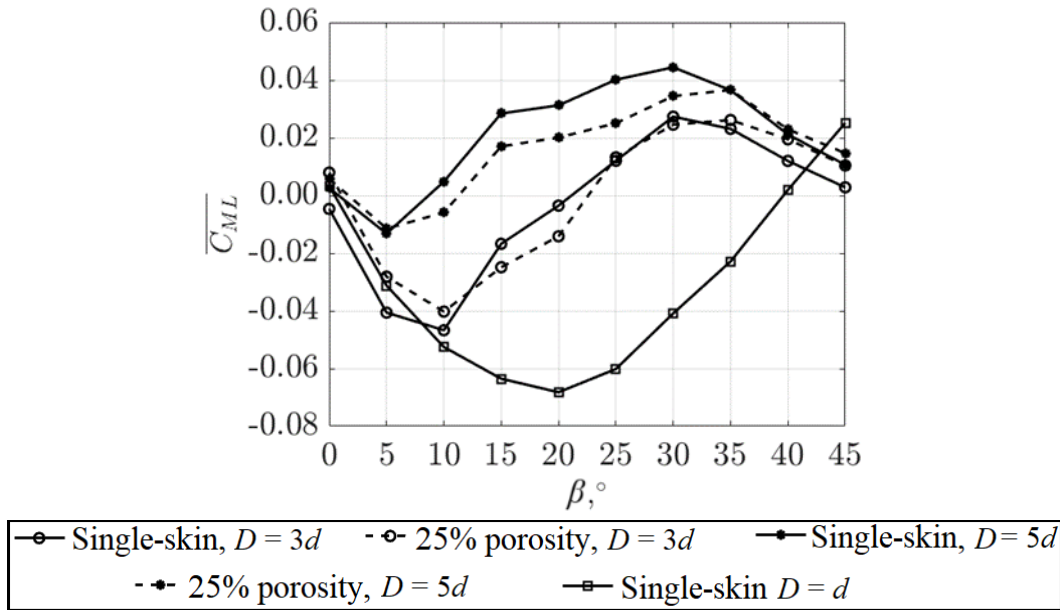
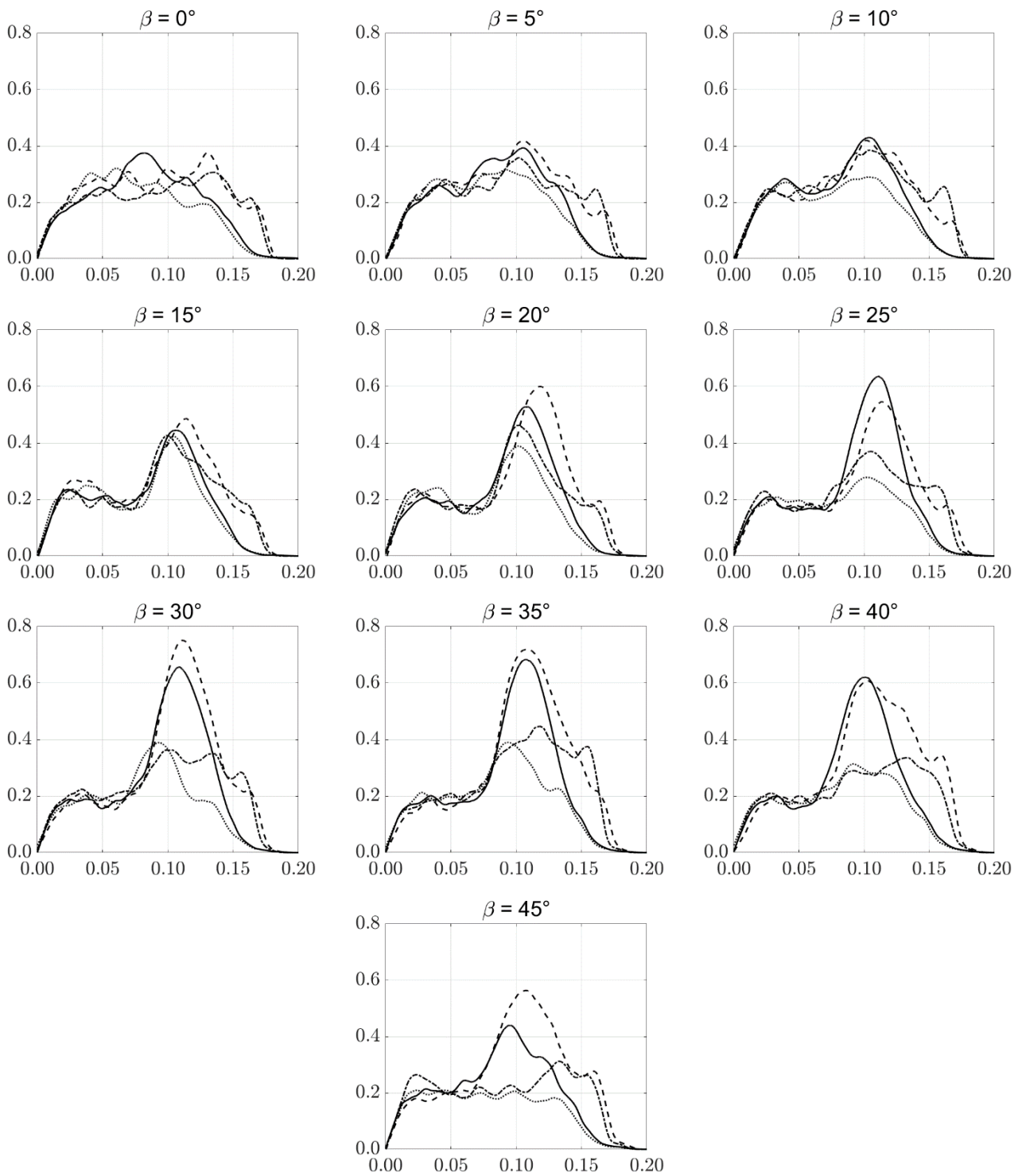


Figure 67.  $\overline{C_{ML}}$  for the principal building model situated in the urban environment model at  $D = d, D = 3d$  and  $D = 5d$

The maximum absolute  $\overline{C_{ML}}$  is observed in the small spacing ( $D = d$ ) at  $\beta = 20^\circ$ , while the second largest value is in the large spacing ( $D = 5d$ ) at  $\beta = 20^\circ$ , which indicates that the spacing between the building models has a negligible effect on  $\overline{C_{ML}}$ . There is no clear trend in the  $\overline{C_{ML}}$  for various PDSF systems in the medium spacing ( $D = 3d$ ). Given these results, there is no improvement in the aerodynamics of the principal building model when using PDSFs on buildings in urban environments, but there are also no adverse effects.

Figure 68 shows the along-wind moment power spectra of the principal building model with a single-skin façade system as well as that equipped with the 25% PDSF system situated in the urban environment model for the spacing of  $D = 3d$  and  $D = 5d$ . The  $x$ -axis is the dimensionless frequency  $f \cdot d/v_\infty$ , the  $y$ -axis is the dimensionless moment power spectra  $S_M \cdot f/\sigma^2$ , where  $f$  is the frequency in Hz,  $d$  is the width of the building model in m,  $v_\infty$  is the freestream velocity at the location of the building model in m/s,  $S_M$  is the integral moment power spectrum in  $N^2m^2s$ , and  $\sigma^2$  is the integral moment variance in  $N^2m^2$ .



— Single-skin,  $D = 3d$     - - - 25% porosity,  $D = 3d$     ..... Single-skin,  $D = 5d$     - · - · 25% porosity,  $D = 5d$

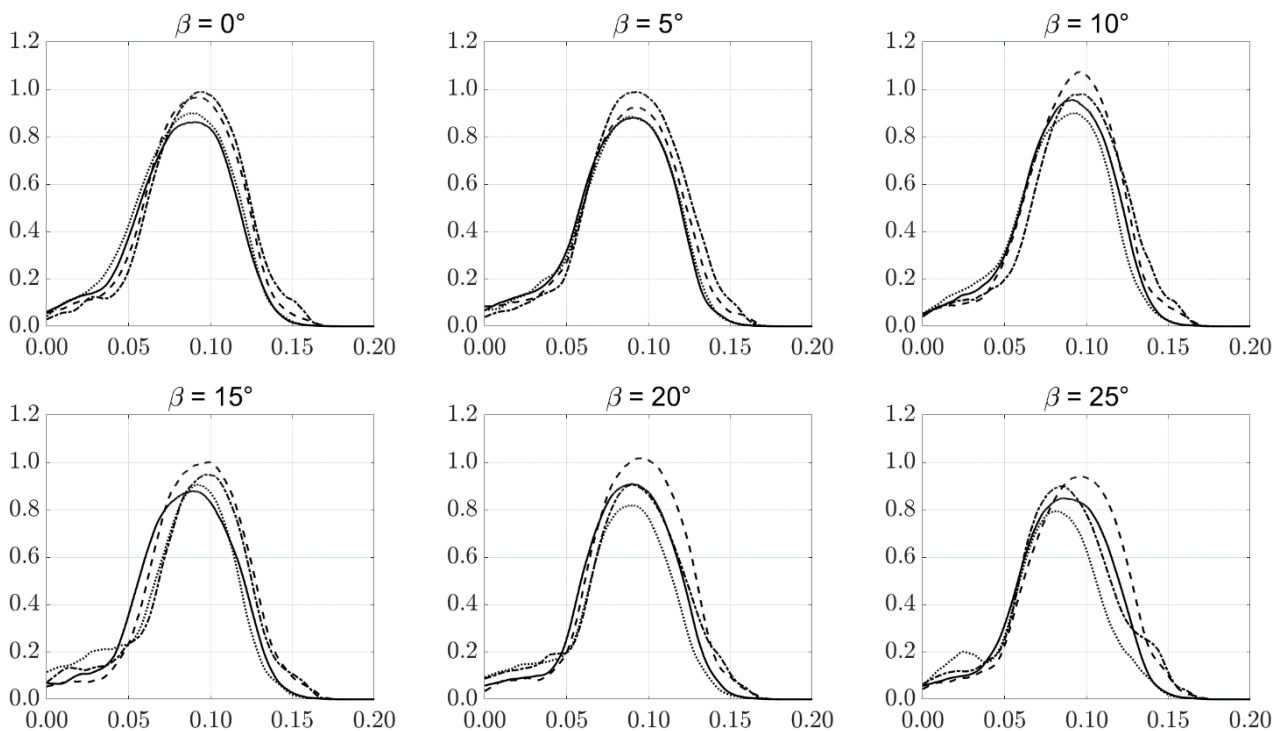
Figure 68. Integral along-wind moment power spectra for the principal building model situated in the urban environment model at  $D = 3d$  and  $D = 5d$

The power spectral density of the along-wind moment does not exceed 0.4 for  $\beta < 10^\circ$ , while its maximum value of  $\sim 0.7$  is at  $\beta < 30^\circ$ . This is most likely the consequence of the dummy building model relative to the flow direction, where the principal building model is

sheltered from the flow to a large extent for  $\beta < 10^\circ$ , which yields lower power spectral density of the along-wind moment. The largest power spectral density of the along-wind moment coincides with the most open configuration of the dummy building models, where the principal building model is exposed to the incoming flow.

There is a clear trend in the  $25^\circ < \beta < 40^\circ$  range, where there is a peak at the reduced frequency of  $\sim 0.11$  for the building model in the environment with the  $D = 3d$  spacing. This peak is not there for the  $D = 5d$  spacing, which indicates there is a flow speed-up in the space between the dummy building models in this configuration.

The power spectral density of the across-wind moment fluctuations of the principal building model is shown in Figure 69. The  $x$ -axis is the dimensionless frequency  $f \cdot d/v_\infty$ , the  $y$ -axis is the dimensionless moment power spectra  $S_M \cdot f/\sigma^2$ , where  $f$  is the frequency in Hz,  $d$  is the width of the building model in m,  $v_\infty$  is the freestream velocity at the location of the building model in m/s,  $S_M$  is the integral moment power spectrum in  $\text{N}^2\text{m}^2\text{s}$ , and  $\sigma^2$  is the integral moment variance in  $\text{N}^2\text{m}^2$ .



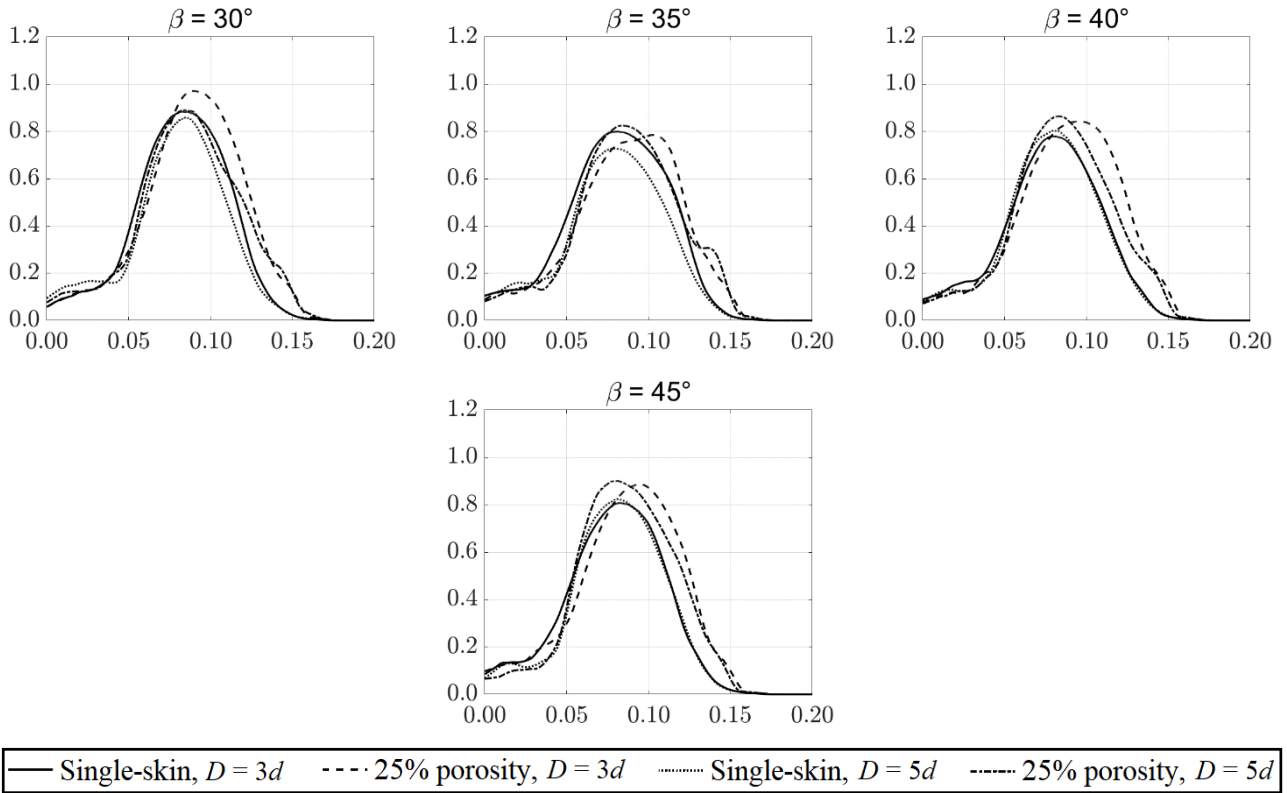


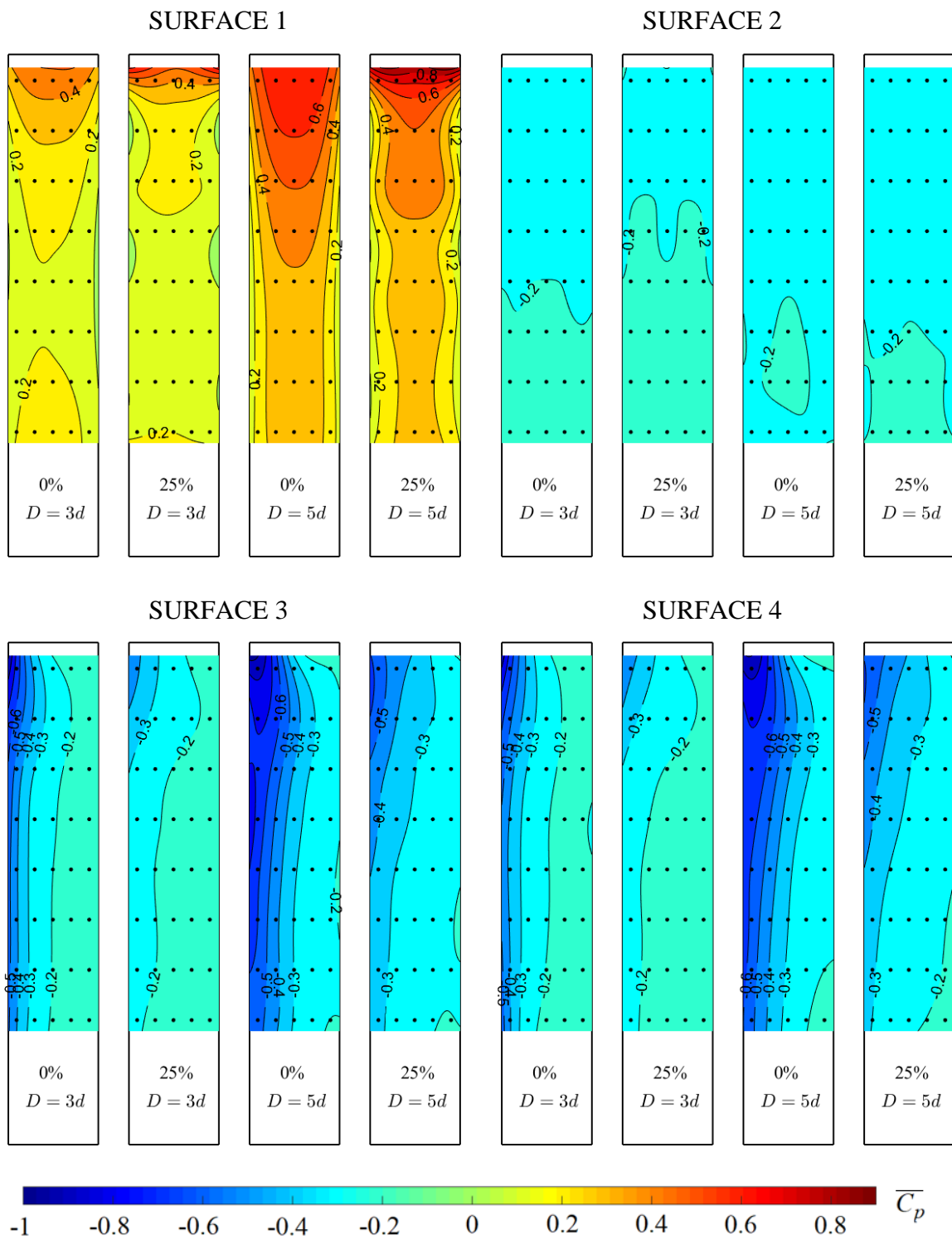
Figure 69. Integral across-wind moment power spectra for the principal building model situated in the urban environment model at  $D = 3d$  and  $D = 5d$

The peak is observed in all spectra at the reduced frequency of 0.1 at  $\beta = 0^\circ$  which coincides with the vortex shedding (Strouhal) frequency. With the increase in  $\beta$  to  $\beta = 30^\circ$ , the peak decreases by  $\sim 15\%$  to 0.8. This is in contrast with the findings of Škvorc and Kozmar [150], where the peak power spectral density is 0.5 at  $\beta = 30^\circ$ . This could be a consequence of larger turbulence in the space among the building models, which causes the increased vibration of the principal building model.

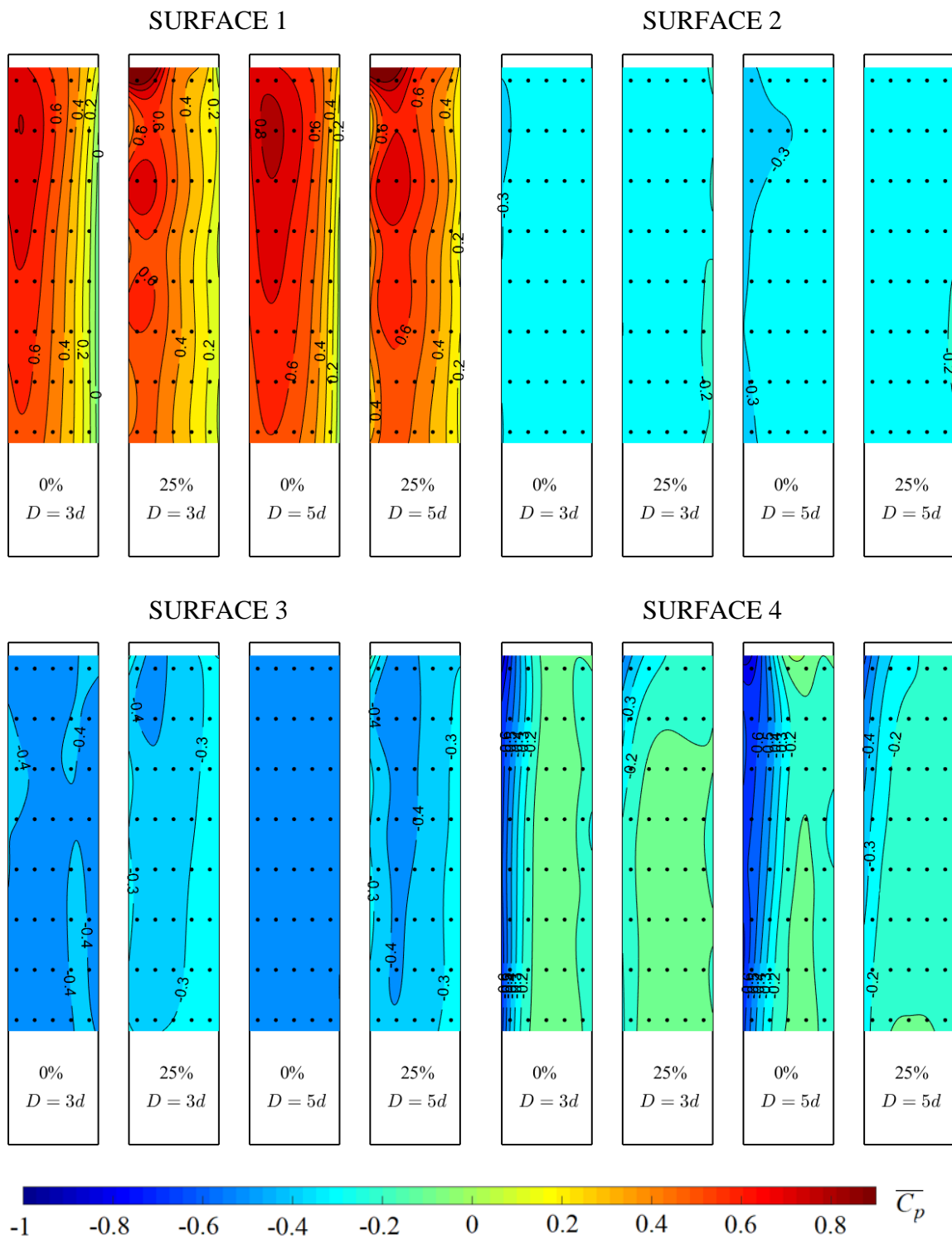
There is negligible change in the across-wind moment power spectra in Figure 69 with a difference in spacing between the building models. The reason for this trend is possibly the large turbulence in the wake of the dummy building models impinging on the principal building model. The principal building model is in a highly turbulent flow regardless of the spacing. Therefore, the across-wind moment power spectra exhibit marginal effects of the spacing between building models.

Figure 70 shows  $\overline{C_p}$  distribution on the surfaces of the principal building model with the single skin and 25% PDSF system in two arrangements of the urban environment model, i.e., at  $D = 3d$  and  $D = 5d$ .

$\beta = 0^\circ$

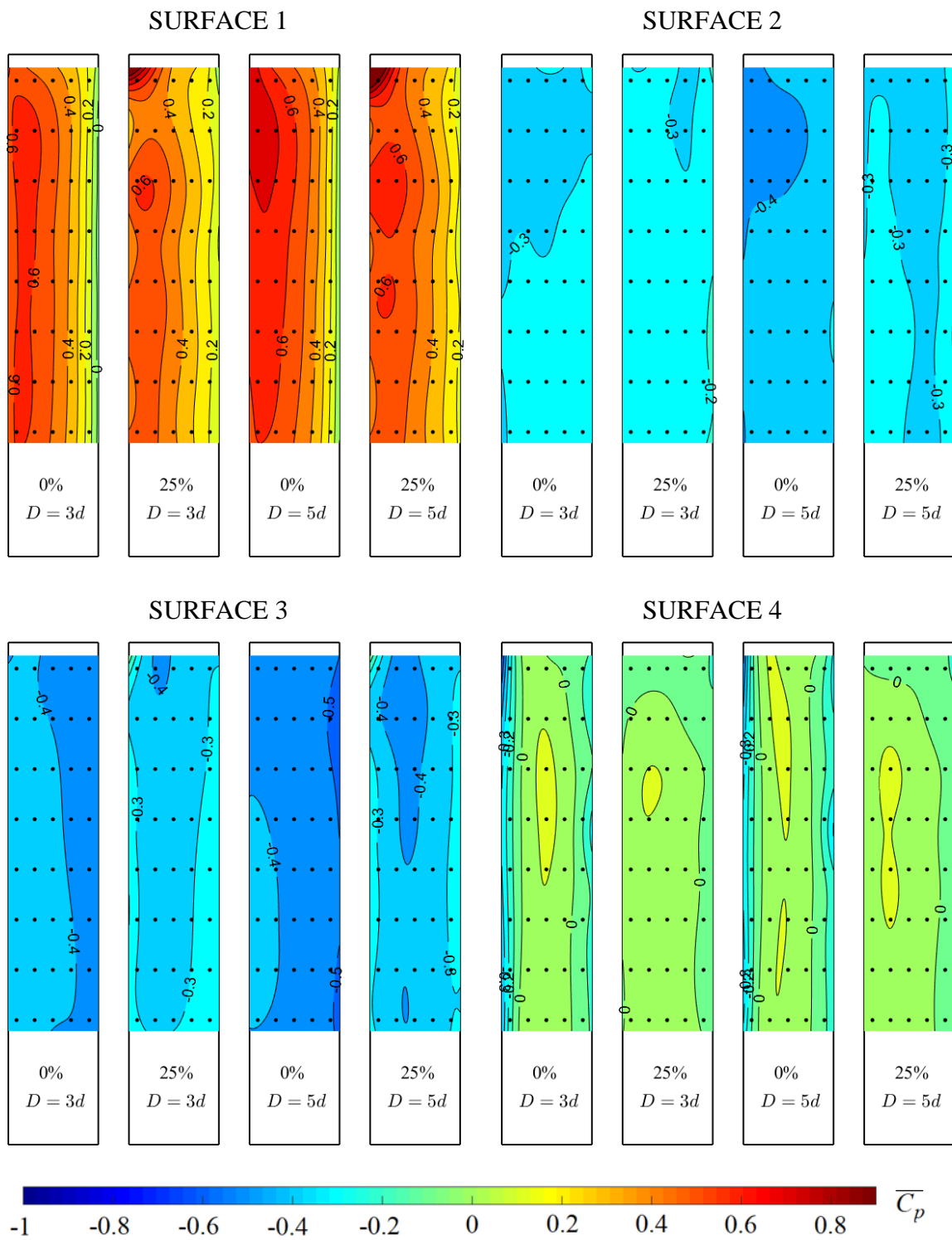


$\beta = 15^\circ$





$\beta = 30^\circ$



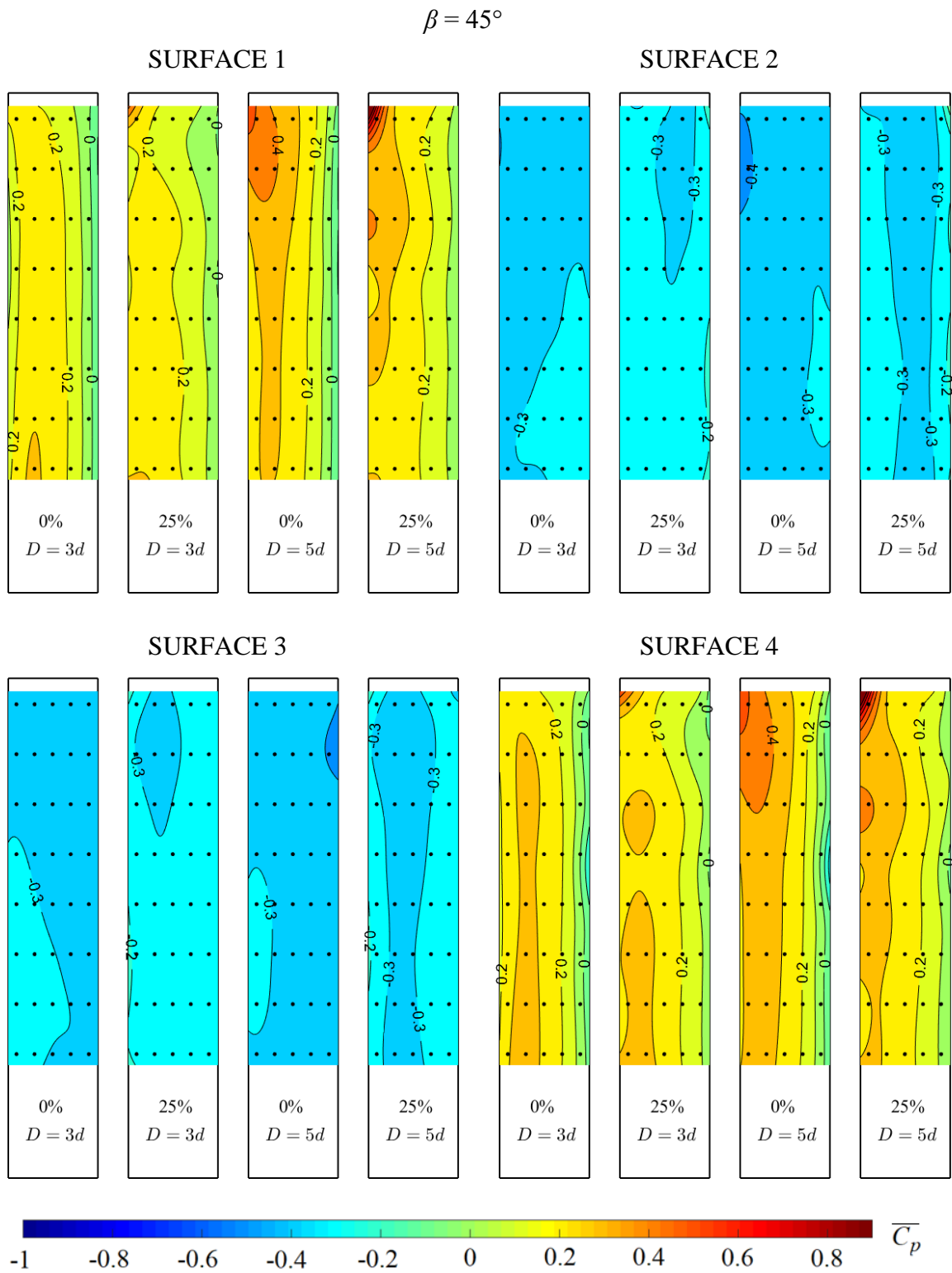


Figure 70.  $\overline{C_p}$  distribution on the principal building model at  $D = 3d$  and  $D = 5d$

The principal building model is in the wake of the windward dummy building model at  $\beta = 0^\circ$ . At  $\beta = 15^\circ$ , a narrow gap (passage) is present, which causes flow channeling, thus the respective  $\overline{C_p}$  distribution on the left-hand side of Surface 1 at  $\beta = 15^\circ$  and  $30^\circ$ . At  $\beta = 45^\circ$ , the

dummy building model entirely shelters the principal building model. However, at  $\beta = 45^\circ$ , the building models are in the most streamlined configuration, so the windward vertical edge between Surfaces 1 and 4 is characterized by the positive  $\overline{C_p}$ . In the case of small spacing between building models, all surfaces on the principal building model are sheltered in the entire range of  $\beta$  and are thus not analyzed at this point.

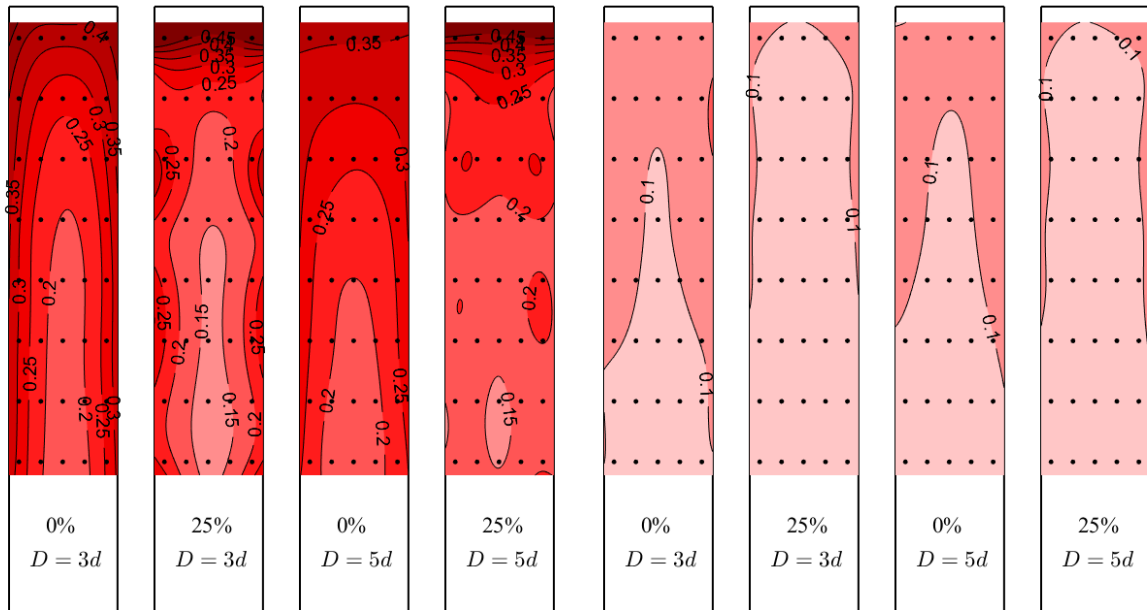
By increasing the spacing between the building models, there is more space for the flow between the dummy building models, thus resulting in a  $\sim 10\%$  larger  $\overline{C_p}$  on the windward surface of the principal building model. This difference is less exhibited on other building model surfaces, i.e., the absolute peak of the  $\overline{C_p}$  at  $D = 5d$  is  $5\% - 10\%$  larger than at  $D = 3d$ . The PDSF system yields a decrease in  $\overline{C_p}$  of  $\sim 20\%$  on the windward surface and on surfaces characterized by large suction, e.g., Surfaces 3 and 4 at  $\beta = 0^\circ$ , for both these spacings. On surfaces where  $\overline{C_p}$  is low, e.g., Surface 2 at  $\beta = 0^\circ$  and  $15^\circ$ , the PDSF system does not yield any obvious effect.

Figure 71 shows the  $\sigma_{C_p}$  on the surfaces of the principal building model with the single skin and the 25% PDSF system at  $D = 3d$  and  $D = 5d$ .

$$\beta = 0^\circ$$

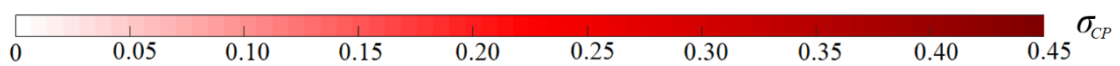
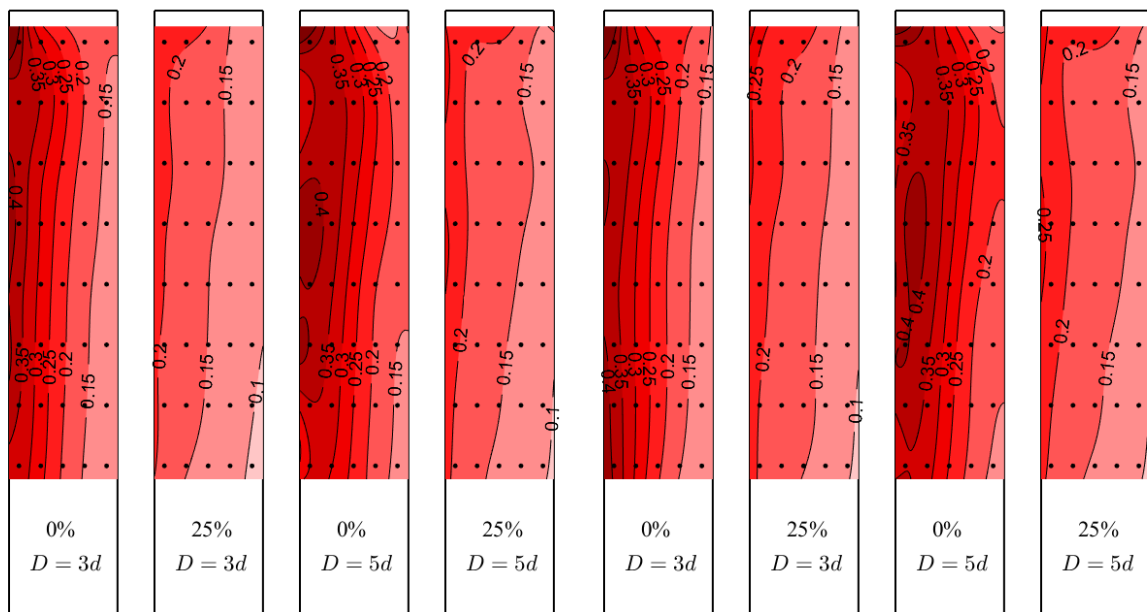
SURFACE 1

SURFACE 2



SURFACE 3

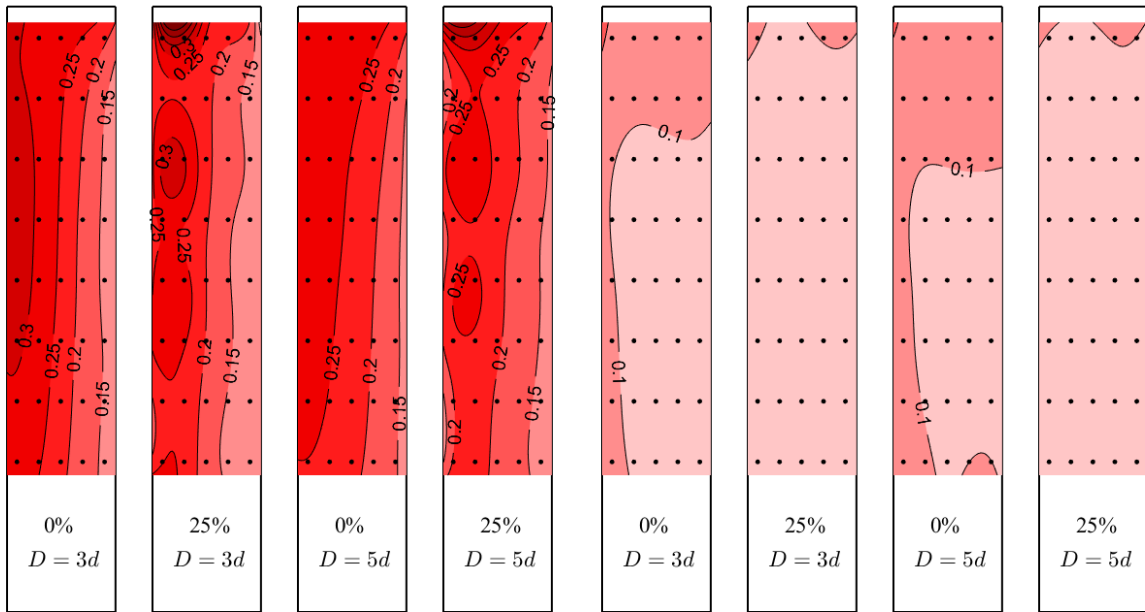
SURFACE 4



$\beta = 15^\circ$

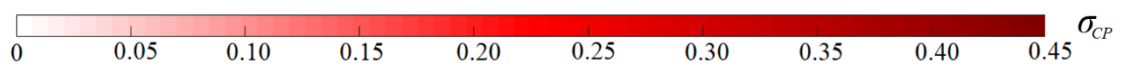
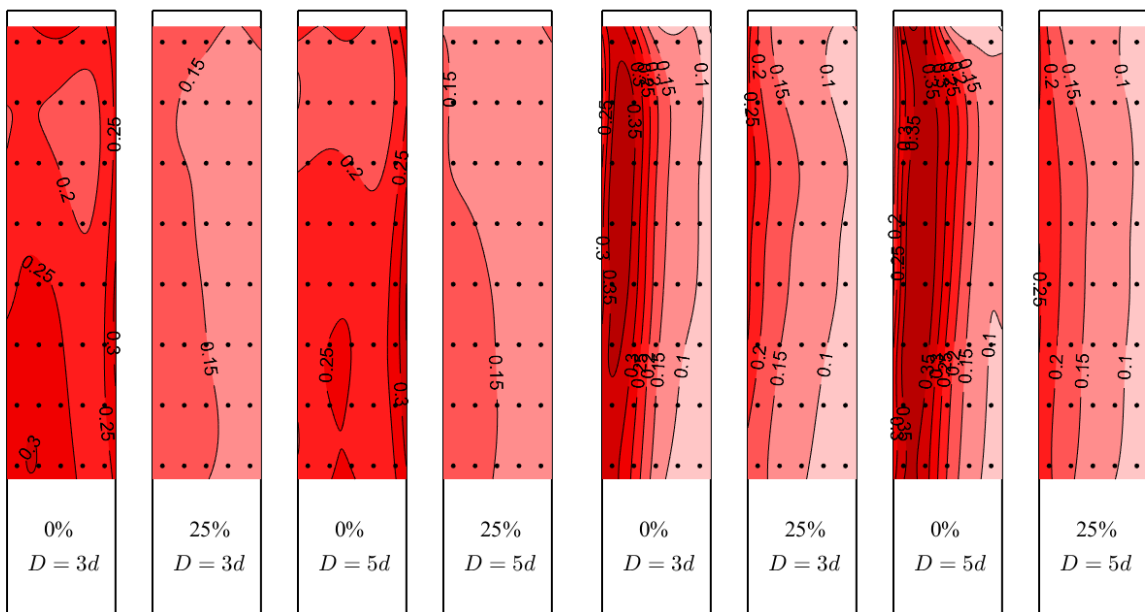
SURFACE 1

SURFACE 2



SURFACE 3

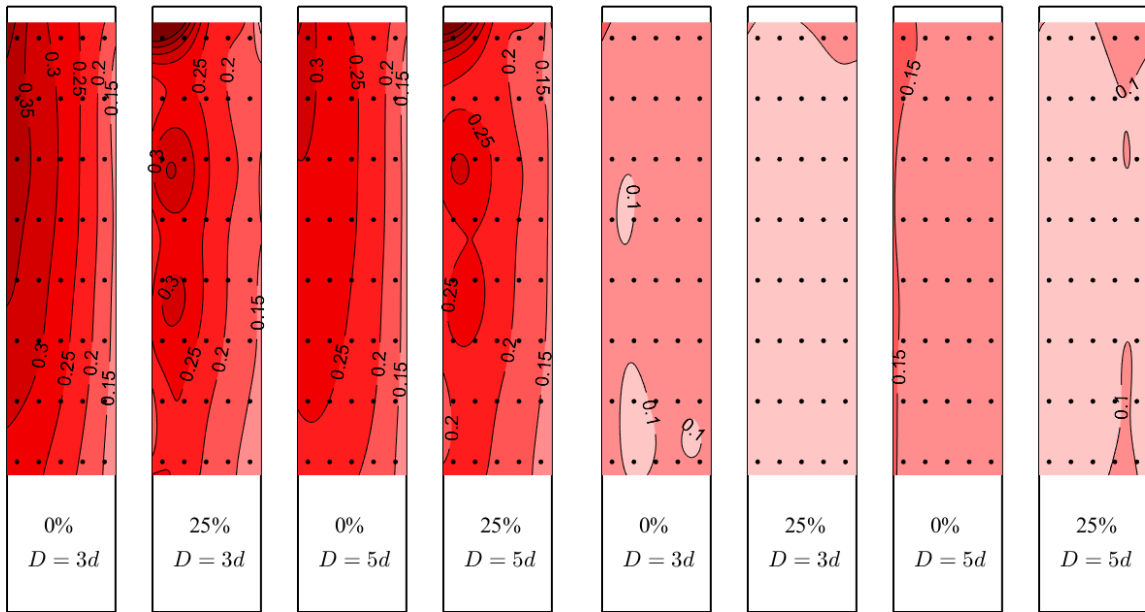
SURFACE 4



$\beta = 30^\circ$

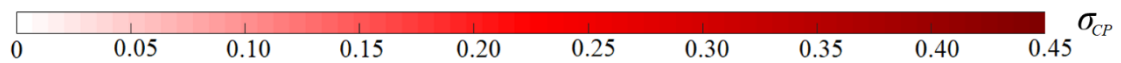
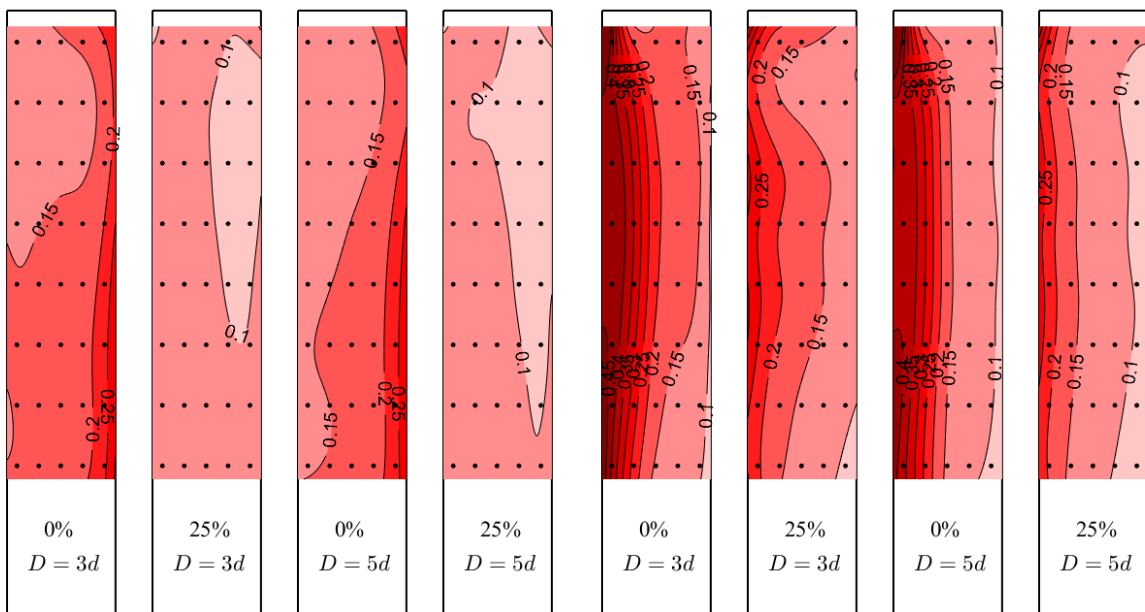
SURFACE 1

SURFACE 2



SURFACE 3

SURFACE 4



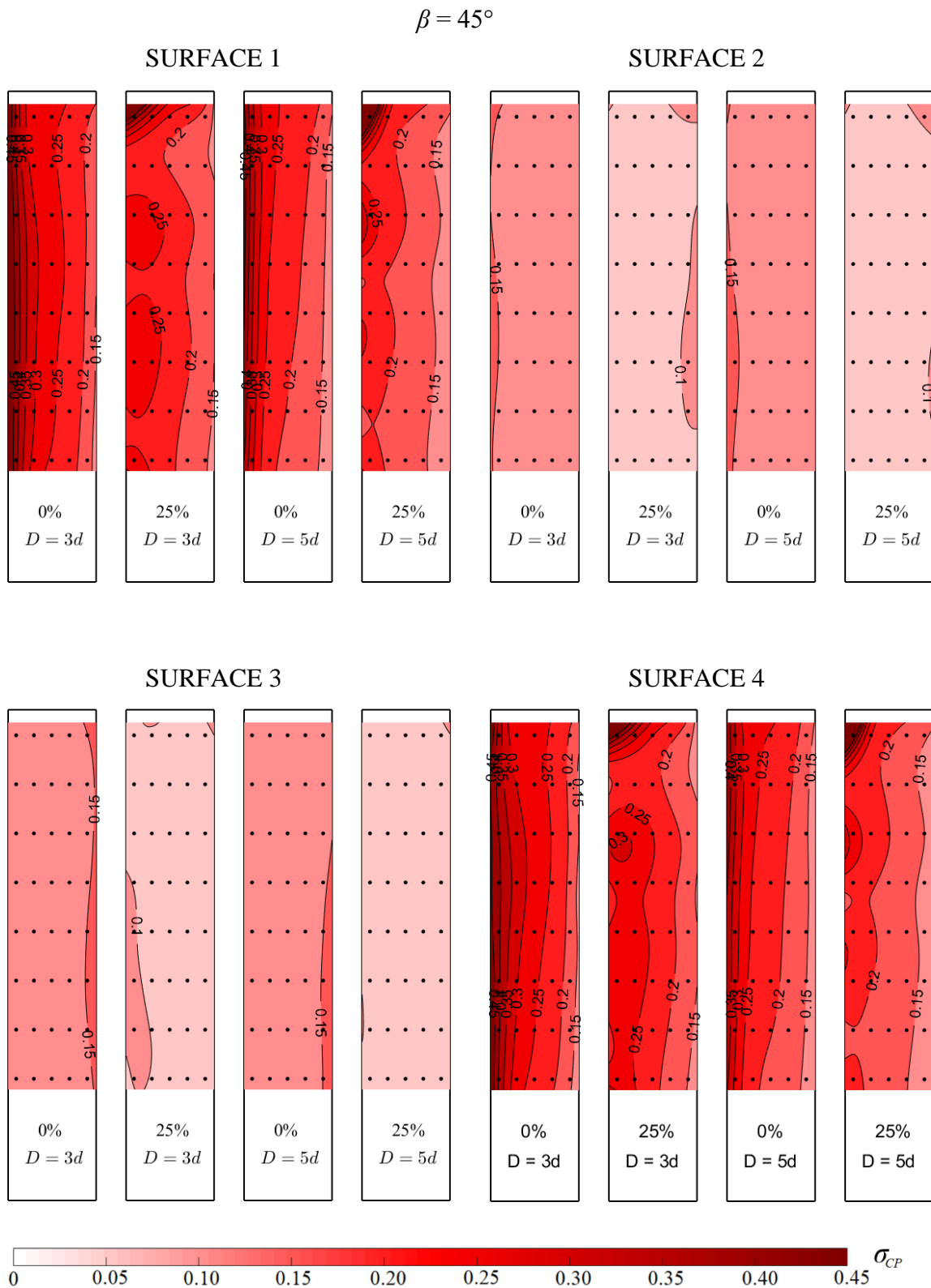


Figure 71.  $\sigma_{CP}$  on the principal building model at  $D = 3d$  and  $D = 5d$

By increasing the spacing between the dummy building models, the area with high  $\sigma_{CP}$  concurrently increases in size. For example, on Surface 4 at  $\beta = 15^\circ$ , the area of high  $\sigma_{CP}$  is

much smaller at  $D = 3d$  than is the case at  $D = 5d$ . The same phenomenon may also be observed at  $\beta = 0^\circ$ ,  $\beta = 30^\circ$ , and  $\beta = 45^\circ$ . On the other hand, the effect of the spacing between building models on the peak magnitude of  $\sigma_{Cp}$  is negligible.

The PDSF system in the case of both spacings yields lower  $\sigma_{Cp}$ . For example, on Surfaces 3 and 4 at  $\beta = 0^\circ$  and  $15^\circ$ , which are in the separation zone (wake), where  $\sigma_{Cp}$  is high, the PDSF system may cause a  $\sim 40\%$  decrease in the  $\sigma_{Cp}$  peak magnitude. On other surfaces characterized by high  $\sigma_{Cp}$ , the effectiveness of the PDSF system is slightly smaller but is still present.



## 8 Conclusions

The present thesis focuses on the aerodynamic characteristics of tall buildings with porous double-skin façade systems. This work was conducted experimentally on small-scale building models in a boundary layer wind tunnel at the University of Florence, Italy.

Four sets of experiments were performed to study the aspects of tall building aerodynamics:

- Aerodynamic loads on a tall building equipped with PDSF systems of various porosity;
- Aerodynamic loads on a tall building equipped with PDSF systems for various wind conditions;
- Aerodynamic loads on buildings equipped with PDSF systems for various building aspect ratios;
- Aerodynamic interference of tall buildings equipped with PDSF systems in urban environments.

Two ABL simulations impinging on building models were created using surface roughness elements and sawtooth barriers. Characteristic profiles of mean flow velocity, turbulence intensity and integral turbulence length scales were validated using the Eurocode EN1991-1-4:2005 recommendations for rural and suburban terrains.

The principal model of a 200 m high rectangular building characterized by a 1:1:5 length to width to height ratio was manufactured on a 1:400 length scale. It is equipped with an array of pressure sensors on all vertical façades for the purpose of surface pressure measurements. High-frequency force balance (HFFB) was used for the integral forces and moment measurements on the building model. The flow incidence angle  $\beta$  was adjusted using a turntable.

Three different porous skins of a PDSF system were manufactured with 25%, 50% and 65% porosities. Circular openings 10 mm in diameter were designed on the outer skins. Various porosities were achieved by increasing the number of openings. This allowed for a total of four configurations of the PDSF systems used in the experiments, i.e., three PDSF systems and a single-skin building model as a reference case.

Four additional building models were designed to study the effect of the building aspect ratio on its aerodynamic loads. The aspect ratios of additional building models are 1:1:3, 1:1:4, 1:2:5 and 1:3:5. These building models were studied with a single skin, as a reference case, and equipped with the 65% PDSF system.

Eight 1:1:5 dummy building models were used to study the effects of the aerodynamic interference of tall buildings in an urban environment. Two sets of experiments were performed. The first set observed the effects of various porosities (single-skin, 25%, 50%) on the outer

façade of the building model. The building model was situated in an urban environment model that consisted of nine building models aligned in 3x3 in-line patterns with a distance between them of  $D = 5d$ , where  $d$  is the width of the building model. The second set of experiments analyzed the effects of various spacing, i.e.,  $D = 3d$ ,  $D = 5d$ , between dummy building models in an urban environment. The experiments were performed in a range of  $0^\circ < \beta < 45^\circ$  with an increment of  $\beta = 5^\circ$  for the HFFB measurements and  $\beta = 15^\circ$  for the surface pressure measurements.

There are several general findings of this work, which occur in all the configurations of the PDSF systems studied:

- PDSF systems lead to reduced across-wind vibration of tall buildings;
- The effect of PDSF systems on the along-wind vibration of tall buildings is negligible;
- The porosity of the outer PDSF façade substantially affects the surface pressure on the inner façade of tall buildings;
- There is extreme local pressure on the inner façade downstream of the PDSF openings on tall buildings;
- For buildings in urban environments, the position of upstream buildings relative to the principal building is a major cause of aerodynamic loads on the principal building, i.e., not the PDSF systems;
- Higher buildings are characterized by larger across- and along-wind vibration.

The effect of the PDSF porosity proved to be substantial:

- The mean across-wind moment coefficient  $C_{ML}$  is lower for all studied PDSF systems compared to the single-skin building model. This effect is most evident at  $\beta = 12.5^\circ$ , where the decrease caused by the PDSF system is  $\sim 30\%$  for all of them. All PDSF systems yield a  $\sim 27\%$  decrease in the maximum  $\sigma_{CML}$ , a phenomenon observed at  $\beta = 0^\circ$ . The effect of the studied PDSF systems on  $C_{MD}$  is generally negligible at all  $\beta$ . Only at  $\beta = 0^\circ$  is a lower ( $\sim 10\%$ )  $\sigma_{CMD}$  observed for all PDSF systems.
- Pressure measurements on the inner surface of the building model generally corroborate the integral load trends. The absolute value of the mean pressure coefficient  $\overline{C_p}$  on the inner building façade model is lower when the PDSF system is in place. The effects on the windward surface are more exhibited for less porous (more solid) PDSF systems. A substantial decrease in mean suction occurs on the lateral surfaces. In particular, at  $\beta = 15^\circ$ , a decrease caused by the PDSF system is in certain points of the order of 30%.
- The aerodynamic sheltering effect of the PDSF systems generally causes pressure equalization in the gap between the outer and inner building model façades. This phenomenon yields lower pressure fluctuations on all building model surfaces, which

can be clearly observed at  $\beta = 0^\circ$  due to the strongly exhibited vortex-shedding phenomena.

The main findings regarding the effects of inflow characteristics are outlined in several key points:

- The rural ABL simulation yields larger absolute  $\overline{C_p}$  on all surfaces of the building model regardless of the PDSF system. The effect of the ABL simulation on the standard deviation of the pressure coefficient  $\sigma_{C_p}$  is complex and depends highly on  $\beta$ . For the  $\beta = 0^\circ$ ,  $\sigma_{C_p}$  is significantly larger for the windward surface in the suburban ABL simulation, while the effect of the ABL simulation is negligible on the leeward surface.  $\sigma_{C_p}$  in the suburban ABL simulation is slightly higher on the lateral surfaces of the building model.
- The suburban ABL simulation yields significantly lower  $C_{ML}$  at all  $\beta$ . The effect of the ABL simulation on  $\sigma_{C_{ML}}$  is negligible at  $\beta = 0^\circ$ , while  $\sigma_{C_{ML}}$  is  $\sim 20\%$  lower at  $\beta = 45^\circ$  in the rural ABL simulation.
- $C_{MD}$  in the suburban ABL simulation is  $\sim 20\%$  smaller at all  $\beta$ , while  $\sigma_{C_{MD}}$  is  $\sim 25\%$  larger. The power spectral density of the across-wind moment  $M_L$  is higher in the rural ABL simulation.

There are several important contributions regarding the effect of the building aspect ratio:

- Taller buildings exhibit larger mean across- and along-wind moment coefficients,  $C_{ML}$  and  $C_{MD}$ , respectively. With a decrease in the height of the building model, the maximum  $C_{ML}$  decreases. This is most likely the consequence of the reduced surface area of the building model. A smaller surface area yields lower surface pressure on the façades of the building model, which in turn lowers the integral moment. The 65% PDSF system yields a further decrease in both integral moments.
- With an increase in the slenderness of the building model, the PDSF system adversely affects the  $M_L$  power spectra with a  $\sim 15\%$  increase of their maximum. This increase is observed for large  $\beta$  where the spectral peak is  $\sim 50\%$  of the peak at  $\beta = 0^\circ$ , which is the critical case.
- The mean  $M_L$  is  $\sim 25\%$  lower for the 1:2:5 building model compared to the 1:3:5 building model, which can be attributed to the shorter width  $d$  of the 1:2:5 building model. The 65% PDSF system on both building models does not affect the mean integral moments.

The interference between buildings proved to be important:

- The PDSF systems on the studied building in the urban environment model do not affect either  $C_{ML}$  or  $C_{MD}$  for any spacing of the building models and the single-skin façade arrangement. At higher spacing between the building models,  $C_{MD}$  increased, while  $C_{ML}$  was nearly the same.

- The PDSF system has a slightly negative effect on the  $M_L$  power spectra exhibited in increased peak magnitudes, while the effect on the along-wind moment  $M_D$  power spectra is negligible. There is no clear effect of the spacing between the building models on the moment power spectra.
- The PDSF system yields a decrease in maximum  $\overline{C_p}$  and a decrease of 10% to 20% in  $\overline{C_p}$  on the entire building model surface. As the spacing between the building models increases, the studied building model is less sheltered by the dummy building models, which causes an increase in  $\overline{C_p}$ .
- The PDSF system proved to reduce the maximum of  $\sigma_{C_p}$  by up to ~40%. Spacing between the building models did not affect the maximum  $\sigma_{C_p}$  but increasing the spacing between the building models yielded larger areas of high  $\sigma_{C_p}$ .

The aerodynamic characteristics of tall buildings with PDSF systems are complex and general conclusions do not necessarily apply in all cases. Any design of such structures should be subjected to detailed wind-tunnel testing and computational modeling. Further work is still required on synoptic and non-synoptic wind effects on tall buildings with PDSF systems, the surface pressure on the inner building façade, building design, urban architecture, and the interference of buildings in built environments.

## Bibliography

- [1] X. W. Zheng, H. N. Li, Y.B. Yang, G. Li, L.S. Huo, Y. Liu, “Damage risk assessment of a high-rise building against multihazard of earthquake and strong wind with recorded data,” *Engineering Structures*, vol. 200, 109697, 2019.
- [2] Y. Tamura, S. Cao, “International group for wind-related disaster risk reduction,” *Journal of Wind Engineering and Industrial Aerodynamics*, vol. 104-106, pp. 3-11, 2012.
- [3] Insurance Information Institute, <https://www.iii.org>. Accessed: January 2023.
- [4] D. W. Olson, S. F. Wolf, J. M. Hook, “The Tacoma Narrows Bridge collapse,” *Physics Today*, vol. 68, pp. 64-65, 2015.
- [5] G. Arioli, F. Gazzola, “Torsional instability in suspension bridges: The Tacoma Narrows Bridge case,” *Communications in Nonlinear Science and Numerical Simulation*, vol. 42, pp. 342-357, 2017.
- [6] M. Burton, K. C. S. Kwok, A. Abdelrazaq, “Wind-induced motion of tall buildings: Designing for occupant comfort,” *International Journal of High-Rise Buildings*, vol. 4, no. 1, pp. 1-8, 2015.
- [7] E. Bernardini, S. M. J. Spence, D. K. Kwon, A. Kareem, “Performance-based design of high-rise buildings for occupant comfort,” *Journal of Structural Engineering*, vol. 141, 04014244, 2015.
- [8] M. D. Burton, K. C. S. Kwok, P. A. Hitchcock, R. O. Denoon, “Frequency dependence of human response to wind-induced building motion,” *Journal of Structural Engineering*, vol. 132, pp. 296-303, 2006.
- [9] N. Isyumov, “Criteria for acceptable wind-induced motions of tall buildings,” *Council on Tall Buildings and Urban Habitat*, Chicago, pp. 411–423, 1993.
- [10] S. Lamb, K. C. S. Kwok, D. Walton, “Occupant comfort in wind-excited tall buildings: Motion sickness, compensatory behaviours and complaint,” *Journal of Wind Engineering and Industrial Aerodynamics*, vol. 119, pp. 1-12, 2013.
- [11] R. McNamara, A. Kareem, T. Kijewski, “Ask the experts...perception of motion criteria for tall buildings subjected to wind: a panel discussion,” *Structures Congress*, 2002.
- [12] F. A. Johann, “Impact of structural design criteria on the comfort assessment of tall buildings author names and affiliations,” *Journal of Wind Engineering and Industrial Aerodynamics*, vol. 180, pp. 231-248, 2018.

- [13] A. Beghini, D. Shook, A. Mazurek, “Material optimization for tall buildings,” *Architectural Engineering Proceedings*, pp. 567-580, 2015.
- [14] F. Petrini, A. Giaralis, Z. Wang, “Optimal tuned mass-damper-inerter (TMDI) design in wind-excited tall buildings for occupants’ comfort, serviceability, performance and energy harvesting”, *Engineering structures*, vol. 204, 109904, 2019.
- [15] Y. Tamura, X. Xu, H. Tanaka, Y. C. Kim, A. Yoshida, Q. Yang, “Aerodynamic and pedestrian-level wind characteristics of super-tall buildings with various configurations,” *Procedia Engineering*, vol. 199, pp. 28-37. 2017.
- [16] X. Xu, Q. Yang, A. Yoshida, Y. Tamura, “Characteristics of pedestrian-level wind around super-tall buildings with various configurations,” *Journal of Wind Engineering and Industrial Aerodynamics*, vol. 166, pp. 61-73, 2017.
- [17] N. Serteser, I. Karadag, “Design for improving pedestrian wind comfort: a case study on a courtyard around a tall building,” *Architectural science review*, vol. 61, pp. 492-499, 2018.
- [18] W. Lou, M. Huang, M. Zhang, M. Lin. “Experimental and zonal modeling for wind pressures on double-skin facades of a tall building,” *Energy and Buildings*, vol. 54. pp. 179-191, 2012.
- [19] G. Pomaranzi, N. Daniotti, P. Schito, L. Rosa, A. Zasso. “Experimental assessment of the effects of a porous double skin façade system on cladding loads,” *Journal of Wind Engineering and Industrial Aerodynamics*, vol. 196, 104019, 2020.
- [20] P. Kosiński, R. Wójcik, B. Semen. “Experimental study on the deterioration of thermal insulation performance due to wind washing of the cavity insulation in leaky walls,” *Science and Technology for the Built Environment*, vol. 0, pp. 1-14, 2019.
- [21] G. Baldinelli. “Double skin façades for warm climate regions: Analysis of a solution with an integrated movable shading system,” *Building and Environment*, vol. 44(6), pp. 1107–1118, 2009.
- [22] J. D. Holmes, “Wind Loading of Structures,” *Taylor & Francis*, 2015.
- [23] H. J. Gerhardt, F. Janser, “Wind loads on wind permeable facades,” *Journal of Wind Engineering and Industrial Aerodynamics*, vol. 53(1–2), pp. 37–48, 1994.
- [24] F. H. Kemper, M. Feldmann, “Wind load assumptions for permeable cladding elements considering the installation context,” *Journal of Wind Engineering and Industrial Aerodynamics*, vol. 184, pp. 277–288, 2019.

- [25] S. Cammelli, D. Azagra, V. Buttgereit, C. Fussell, M. Grey, Y. Kaneko, G. Knapp, R. Marshall, A. Scotti, “Adventures in architectural aerodynamics,” *Proceedings of the Institution of Civil Engineers: Structures and Buildings*, vol. 163(2), pp. 119–127, 2010.
- [26] M. Belloli, D. Rocchi, L. Rosa, A. Zasso, “Wind tunnel studies on the effects of porous elements on the aerodynamic behavior of civil structures,” *7<sup>th</sup> International Colloquium on Bluff Body Aerodynamics and Applications (BBAA7)*, pp. 1132–1141, 2012.
- [27] M. Belloli, L. Rosa, A. Zasso, “Wind loads and vortex shedding analysis on the effects of the porosity on a high slender tower,” *Journal of Wind Engineering and Industrial Aerodynamics*, vol. 126, pp. 75–86, 2014.
- [28] G. Hu, S. Hassanli, K. C. S. Kwok, K. T. Tse, “Wind-induced responses of a tall building with a double-skin façade system,” *Journal of Wind Engineering and Industrial Aerodynamics*, vol. 168, pp. 91–100, 2017.
- [29] G. Hu, J. Song, S. Hassanli, R. Ong, K. C. S. Kwok, “The effects of a double-skin façade on the cladding pressure around a tall building,” *Journal of Wind Engineering and Industrial Aerodynamics*, vol. 191, pp. 239–251, 2019.
- [30] A. Giachetti, Wind effects on permeable building envelopes: A two dimensional exploratory study, *Ph.D. Dissertation*, University of Braunschweig – Institute of Technology; Germany and University of Florence, Italy, 2018.
- [31] A. Giachetti, G. Bartoli, C. Mannini, “Two-dimensional study of a rectangular cylinder with a forebody airtight screen at a small distance,” *Journal of Wind Engineering and Industrial Aerodynamics*, vol. 189, pp. 11–21, 2019.
- [32] A. Giachetti, G. Bartoli, C. Mannini, “Wind effects on permeable tall building envelopes: issues and potentialities,” *Council on Tall Building and Urban Habitat, CTBUH Journal*, vol. 3, pp. 20-27, 2019.
- [33] A. Giachetti, G. Bartoli, C. Mannini, “Aerodynamics of a tall building equipped with a solid screen close to the façade,” *Journal of Wind Engineering and Industrial Aerodynamics*, vol. 225, 104999, 2022.
- [34] M. Jafari, A. Alipour, “Aerodynamic shape optimization of rectangular and elliptical double-skin façades to mitigate wind-induced effects on tall buildings,” *Journal of Wind Engineering and Industrial Aerodynamics*, vol. 213, 104586, 2021.
- [35] R. B. Stull, “An Introduction to Boundary Layer Meteorology,” Kluwer Academic, Dordrecht, Netherlands, 2003.

- [36] J. R. Garratt, *The Atmospheric Boundary Layer*, University Press, Cambridge, 1992.
- [37] M. Cindori, I. Džijan, F. Juretić, H. Kozmar, “The Atmospheric Boundary Layer Above Generic Hills: Computational Model of a Unidirectional Body Force-Driven Flow,” *Boundary-Layer Meteorology*, vol. 176, pp. 159–196, 2020.
- [38] H. Oertel, *Prandtl: Führer durch die Strömungslehre*, Vieweg & Sohn, Braunschweig/Wiesbaden, 2002.
- [39] R. H. Thuillier, U. O. Lappe, “Wind and temperature profile characteristic from a 1400ft tower,” *Journal of Applied Meteorology*, vol. 3, pp. 299–306, 1964.
- [40] G. Hellman, “Über die Bewegung der Luft in den untersten Schichten der Atmosphäre,” *Königlich Preussischen Akademie der Wissenschaften*, 1917.
- [41] J. Counihan, “Adiabatic atmospheric boundary layers: A review and analysis of data from the period 1880-1972,” *Atmospheric Environment*, vol. 9, pp. 871-905, 1975.
- [42] G. I. Taylor, “The spectrum of turbulence,” *Proceedings of the Royal Society of London*, vol. 164, pp. 476-490, 1938.
- [43] T. Von Karman, “Progress in the statistical theory of turbulence,” *Proceedings of the Natural Academy of Sciences*, Washington, DC, pp. 530-539, 1948.
- [44] EN1991-1-4:2005, (2005), Eurocode 1: Actions on structures – General actions, Part 1-4: Wind actions. CEN.
- [45] A. N. Kolmogorov, “The local structure of turbulence in incompressible viscous fluid for very large Reynolds numbers,” *Proceedings of the Academy of Sciences of the USSR*, vol. 30 pp. 299-303, 1941.
- [46] Y. Nakayama, *Introduction to fluid mechanics*, Butterworth-Heinemann, 2018.
- [47] C. H. Ho, J. J. Baik, J. H. Kim, D. Y. Gong, C. H. Sui, “Interdecadal changes in summertime typhoon tracks,” *Journal of Climate*, vol. 17(9), pp. 1767–1776, 2004.
- [48] M. T. Montgomery, R. K. Smith, “Recent Developments in the Fluid Dynamics of Tropical Cyclones,” *Annual Review of Fluid Mechanics*, vol. 49, 541–574, 2017.
- [49] K. A. Emanuel, “The theory of hurricanes,” *Annual Review of Fluid Mechanics*, vol. 23(1), pp. 179–196, 1991.
- [50] E., Simiu, P. Vickery, A. Kareem, “Relation between Saffir–Simpson Hurricane Scale Wind Speeds and Peak 3-s Gust Speeds over Open Terrain,” *Journal of Structural Engineering*, vol. 133(7), pp. 1043–1045, 2007.



- [51] S. P. Leatherman, "Hurricane Wind Damage Mitigation: Research and Outlook," *Natural Hazards Review*, vol. 12(4), pp. 202–206, 2011.
- [52] J. C. L. Chan, "The physics of tropical cyclone motion," *Annual Review of Fluid Mechanics*, vol. 37, pp. 99–128, 2005.
- [53] T. T. Fujita, "Tornadoes and downbursts in the context of generalized planetary scales," *Journal of the Atmospheric Sciences*, vol. 38(8), pp. 1511–1534, 1981.
- [54] S. A. Changnon, "Tornado Losses in the United States," *Natural Hazards Review*, vol. 10(4), pp. 145–150, 2009.
- [55] H. Kikitsu, P. P. Sarkar, "Building Damage, Wind Speed Estimation, and Post Disaster Recovery in an EF5 Tornado," *Natural Hazards Review*, vol. 16(2), 04014019, 2015.
- [56] T. T. Fujita, "The downburst: Microburst and macroburst," *SMRP Research Paper 210*, 1985.
- [57] J. D. Holmes, S. E. Oliver, "An empirical model of a downburst," *Engineering Structures*, vol. 22(9), pp. 1167–1172, 2000.
- [58] M. Hughes, A. Hall, "Local and synoptic mechanisms causing Southern California's Santa Ana winds," *Climate Dynamics*, vol. 34(6), pp. 847–857, 2010.
- [59] W. T. Sommers, "LFM Dorecast Variables Related to Santa Ana Wind Occurrences," *Monthly Weather Review*, vol. 106, pp. 1307–1316, 1978.
- [60] R. G. Fovell, Y. Cao, "The santa ana winds of southern California: Winds, gusts, and the 2007 witch fire," *Wind and Structures, An International Journal*, vol. 24(6), pp. 529–564, 2017.
- [61] J. Guzman-Morales, A. Gershunov, J. Theiss, H. Li, D. Cayan, "Santa Ana Winds of Southern California: Their climatology, extremes, and behavior spanning six and a half decades," *Geophysical Research Letters*, vol. 43(6), pp. 2827–2834, 2016.
- [62] P. Lepri, H. Kozmar, Ž. Večenaj, B. Grisogono, "A summertime near-ground velocity profile of the Bora wind," *Wind and Structures*, vol. 19(5), pp. 505–522, 2014.
- [63] P. Lepri, H. Kozmar, Ž. Večenaj, B. Grisogono, "Near-ground turbulence of the Bora wind in summertime," *Journal of Wind Engineering and Industrial Aerodynamics*, vol. 147, pp. 345–357, 2015.
- [64] P. Lepri, H. Kozmar, Ž. Večenaj, B. Grisogono, "Bora wind characteristics for engineering applications," *Wind and Structures*, vol. 24(6), pp. 579–611, 2017.

- [65] B. Grisogono, D. Belušić, “A review of recent advances in understanding the meso- and microscale properties of the severe Bora wind,” *Tellus, Series A: Dynamic Meteorology and Oceanography*, vol. 61, pp. 1–16, 2009.
- [66] H. Kozmar, K. Butler, A. Kareem, “Transient cross-wind aerodynamic loads on a generic vehicle due to bora gusts,” *Journal of Wind Engineering and Industrial Aerodynamics*, vol. 111, pp. 73–84, 2012.
- [67] H. Kozmar, D. Allori, G. Bartoli, C. Borri, “Complex terrain effects on wake characteristics of a parked wind turbine,” *Engineering Structures*, vol. 110, pp. 363–374, 2016.
- [68] A. M. Loredou-Souza, A. R. Wittwer, M. M. Rohcha, M. E. De Bortoli, M. G. K. Oliveira, J. O. Marighetti, “Brazil and Argentina Joint Program in Wind Engineering,” *Wind Engineers JAWES*, vol. 41(4), pp. 331–335, 2016.
- [69] P. L. Antico, S. C. Chou, C. Mourão, “Zonda downslope winds in the central Andes of South America in a 20-year climate simulation with the Eta model,” *Theoretical and Applied Climatology*, vol. 128(1–2), pp. 291–299, 2017.
- [70] D. E. Puliafito, Allende, C. Mulena, P. Cremades, S. Lakkis, “Evaluation of the WRF model configuration for Zonda wind events in a complex terrain,” *Proceedings of the 12th German Wind Energy Conference – DEWEK*, November 7–8, Bremen, Germany, 2015.
- [71] K. P. Hoinka, “Observation of the airflow over the alps during a foehn event,” *The Quarterly Journal of the Royal Meteorological Society*, vol. 111(463), pp. 199–224, 1985.
- [72] M. Burlando, M. Tizzi, G. Solari, “Characteristics of downslope winds in the Liguria Region,” *Wind and Structures*, vol. 24(6), pp. 613–635, 2017.
- [73] J. C. Speirs, D. F. Steinhoff, H. A. McGowan, D. H. Bromwich, A. J. Monaghan, “Foehn winds in the McMurdo Dry Valleys, Antarctica: The origin of extreme warming events,” *Journal of Climate*, vol. 23(13), pp. 3577–3598, 2010.
- [74] M. R. Cape, M. Vernet, P. Skvarca, S. Marinsek, T. Scambos, E. Domack, “Foehn winds link climate-driven warming to ice shelf evolution in Antarctica,” *Journal of Geophysical Research*, vol. 120(21), pp. 11037–11057, 2015.
- [75] W. D. Baines, “Effects of velocity distribution on wind loads and flow patterns on buildings,” *Proceedings of the Conference on Wind Effects on Buildings and Structures*, Teddington, England, pp. 198–225, 1965.

- [76] A. G. Davenport, "The buffeting of large superficial structures by atmospheric turbulence," *Annals of the New York Academy of Sciences*, vol. 116, pp. 135-160, 1964.
- [77] W. A. Dalglish, 1971. "Statistical treatment of peak gusts on cladding," *ASCE Journal of the Structural Division*, vol. 97. pp. 2173-2187, 1971.
- [78] J. A. Peterka, J. E. Cermak, "Wind pressures on buildings – probability densities," *ASCE Journal of the Structural Division*. vol. 101, pp. 1255-1267, 1975.
- [79] A. Kareem, "Mitigation of wind induced motion of tall buildings," *Journal of Wind Engineering and Industrial Aerodynamics*, vol. 11, pp. 273–284, 1983.
- [80] H. Kawai, "Effect of corner modifications on aeroelastic instabilities of tall buildings," *Journal of Wind Engineering and Industrial Aerodynamics*, vol. 74-76, 719–729, 1998.
- [81] Y. C. Kim, E. K. Bandi, A. Yoshida, Y. Tamura, "Response characteristics of super-tall buildings - Effects of number of sides and helical angle," *Journal of Wind Engineering and Industrial Aerodynamics*, vol. 145, pp. 252–262, 2015.
- [82] M. Gu, Y. Quan, "Across-wind loads of typical tall buildings," *Journal of Wind Engineering and Industrial Aerodynamics*, vol. 92, pp. 1147–1165, 2004.
- [83] H. Tanaka, Y. Tamura, K. Ohtake, M. Nakai, Y. Chul Kim, "Experimental investigation of aerodynamic forces and wind pressures acting on tall buildings with various unconventional configurations," *Journal of Wind Engineering and Industrial Aerodynamics*, vol. 107–108, pp. 179–191, 2012.
- [84] K. C. S. Kwok, "Effect of building shape on wind-induced response of tall building," *Journal of Wind Engineering and Industrial Aerodynamics*, vol. 28, pp. 381–390, 1988.
- [85] K. C. S. Kwok, P. A. Wilhelm, B. G. Wilkie, "Effect of edge configuration on wind-induced response of tall buildings," *Engineering Structures*, vol. 10, pp. 135–140, 1988.
- [86] T. Tamura, T. Miyagi, T. Kitagishi, "Numerical prediction of unsteady pressures on a square cylinder with various corner shapes," *Journal of Wind Engineering and Industrial Aerodynamics*, vol. 74–76, 531–542, 1998.
- [87] H. Hayashida, Y. Iwasa, "Aerodynamic shape effects of tall building for vortex induced vibration," *Journal of Wind Engineering and Industrial Aerodynamics*, vol. 33(1–2), pp. 237–242, 1990.

- [88] Z. Zhang, Y. Quan, M. Gu, Y. Xiong, “Effects of corner chamfering and rounding modification on aerodynamic coefficients of square tall buildings,” *Tumu Gongcheng Xuebao/China Civil Engineering Journal*, vol. 46(9), pp.12–20, 2013.
- [89] K. T. Tse, P. A. Hitchcock, K. C. S. Kwok, S. Thepmongkorn, C. M. Chan, “Economic perspectives of aerodynamic treatments of square tall buildings,” *Journal of Wind Engineering and Industrial Aerodynamics*, vol. 97(9–10), pp. 455–467, 2009.
- [90] Y. M. Kim, K. P. You, “Dynamic responses of a tapered tall building to wind loads,” *Journal of Wind Engineering and Industrial Aerodynamics*, vol. 90(12–15), pp. 1771–1782, 2002.
- [91] Y. M. Kim, K. P. You, N. H. Ko, “Across-wind responses of an aeroelastic tapered tall building,” *Journal of Wind Engineering and Industrial Aerodynamics*, vol. 96(8–9), pp. 1307–1319, 2008.
- [92] Y. C. Kim, J. Kanda, Y. Tamura, “Wind-induced coupled motion of tall buildings with varying square plan with height,” *Journal of Wind Engineering and Industrial Aerodynamics*, vol. 99(5), pp. 638–650, 2011.
- [93] Y. M. Kim, J. Kanda, “Characteristics of aerodynamic forces and pressures on square plan buildings with height variations,” *Journal of Wind Engineering and Industrial Aerodynamics*, vol. 98(8–9), pp. 449–465, 2010.
- [94] Q. Wang, Qiao, H., Li, W., You, Y., Fan, Z., Tiwari, N., 2020. “Parametric optimization of an inerter-based vibration absorber for wind-induced vibration mitigation of a tall building,” *Wind and Structures*, vol. 31 pp. 241-253, 2020.
- [95] P. A. Irwin, “Bluff body aerodynamics in wind engineering,” *Journal of Wind Engineering and Industrial Aerodynamics*, vol. 96(6–7), pp. 701–712, 2008.
- [96] Q. Li, S., L. H. Zhi, A. Y. Tuan, C. S. Kao, S. C. Su, C. F. Wu, “Dynamic Behavior of Taipei 101 Tower: Field Measurement and Numerical Analysis,” *Journal of Structural Engineering*, vol. 137(1), pp. 143–155, 2011.
- [97] X. Chen, A. Li, Z. Zhang, L. Hu, P. Sun, Z. Fan, X. Liu, “Improving the wind-induced human comfort of the Beijing Olympic Tower by a double-stage pendulum tuned mass damper,” *Structural Design of Tall and Special Buildings*, vol. 29(4), pp. 1–17, 2020.
- [98] Y. G. Li, M. Y. Zhang, Y. Li, Q. S. Li, S. J. Liu, “Experimental study on wind characteristics of high-rise buildings with opening,” *Structural Design of Tall and Special Buildings*, e1734, pp. 1-15. 2020.

- [99] R. Dutton, N. Isyumov, “Reduction of tall building motion by aerodynamic treatments,” *Journal of Wind Engineering and Industrial Aerodynamics*, vol. 36, pp. 739–747, 1990.
- [100] K. Miyashita, J. Katagiri, O. Nakamura, T. Ohkuma, Y. Tamura, M. Itoh, T. Mimachi, “Wind-induced response of high-rise buildings Effects of corner cuts or openings in square buildings,” *Journal of Wind Engineering and Industrial Aerodynamics*, vol. 50(C), pp. 319–328, 1993.
- [101] H. Okada, L. Kong, “The Effects of Open Passage on Reducing Wind Response of Tall Building,” *29th Technical Report, Public Works Research institute, Japan*, pp. 561-566, 1999.
- [102] N. Isyumov, A. A. Fediw, J. Colaco, P. V. Banavalkar, “Performance of a tall building under wind action,” *Journal of Wind Engineering and Industrial Aerodynamics*, vol. 42(1–3), pp. 1053–1064, 1992.
- [103] X. Li, Q. S. Li, “Wind-induced interference effects between twin tapered skyscrapers,” *Structural Design of Tall and Special Buildings*, vol. 28(6), pp. 1–14, 2019.
- [104] Y. Quan, J. Chen, M. Gu, “Aerodynamic interference effects of a proposed taller high-rise building on wind pressures on existing tall buildings,” *Structural Design of Tall and Special Buildings*, vol. 29(4), pp. 1–17, 2020.
- [105] S. K. Nagar, Raj, R., Dev, N, “Experimental study of wind-induced pressures on tall buildings of different shapes,” *Wind and Structures*, vol. 31 pp. 431-443, 2020.
- [106] J. Xie, X. Y. Yang, “Exploratory study on wind-adaptable design for super-tall buildings,” *Wind and Structures*, vol. 29, pp. 489-497, 2019.
- [107] A. Erdal, “A numerical investigation of different parameters that affect the performance of a flow conditioner,” *Flow Measurement and Instrumentation*, vol. 8, pp. 93–102. 1998.
- [108] A. K. Ouazzane, R. Benhadj, “Flow conditioners design and their effects in reducing flow metering errors,” *Sensor review*, vol. 22, pp. 223-231, 2002.
- [109] R. Liu, D. S. K. Ting, “Turbulent flow downstream of a perforated plate: Sharp-edged orifice versus finite-thickness holes,” *Journal of Fluids Engineering, Transactions of the ASME*, vol. 129, 1164–1171, 2007.
- [110] N. Mazellier, L. Danaila, B. Renou, “Multi-scale energy injection: A new tool to generate intense homogeneous and isotropic turbulence for premixed combustion,” *Journal of Turbulence*, vol. 11, pp. 1-30 2010.

- [111] E. P. Spearman, J. A. Sattary, M. J. Reader-Harris, "Comparison of velocity and turbulence profiles downstream of perforated plate flow conditioners," *Flow Measurement and Instrumentation*, vol. 7, pp. 181–199, 1996.
- [112] B. Şahin, A. J. Ward-Smith, "The use of perforated plates to control the flow emerging from a wide-angle diffuser, with application to electrostatic precipitator design," *International Journal of Heat and Fluid Flow*, vol. 8, pp. 124–131, 1987.
- [113] B. Şahin, "Pressure losses in an isolated perforated plate and jets emerging from the perforated plate," *International Journal of Mechanical Sciences*, vol. 31, pp. 51–61, 1989.
- [114] I. P. Castro, "Wake characteristics of two-dimensional perforated plates normal to an air-stream," *Journal of Fluid Mechanics*, vol. 46, pp. 599–609, 1971.
- [115] G. Gan, S. B. Riffat, "Pressure loss characteristics of orifice and perforated plates," *Experimental Thermal and Fluid Science*, vol. 14, pp. 160–165, 1997.
- [116] R. Liu, D. S. K. Ting, G. W. Rankin, "On the generation of turbulence with a perforated plate," *Experimental Thermal and Fluid Science*, vol. 28, pp. 307–316, 2004.
- [117] E. Özahi, "An analysis on the pressure loss through perforated plates at moderate Reynolds numbers in turbulent flow regime," *Flow Measurement and Instrumentation*, vol. 43, pp. 6–13, 2015.
- [118] S. Malavasi, G. Messa, U. Fratino, A. Pagano, "On the pressure losses through perforated plates," *Flow Measurement and Instrumentation* vol. 28, pp. 57–66, 2012.
- [119] W. Jeon, B.H. Lee, H. Yun, J. Kim, S. Kang, Y. Seo, "Characterization of pressure drop through two-stage particulate air filters," *Science and Technology for the Built Environment*, vol. 26, pp. 835-843, 2020.
- [120] M.D.A.E.S. Perera, "Shelter behind two-dimensional solid and porous fences," *Journal of Wind Engineering and Industrial Aerodynamics*, vol. 8, pp. 93-104, 1981.
- [121] I. Seginer, R. Sagi, "Drag on a windbreak in two-dimensional flow," *Agricultural Meteorology*, vol. 9, pp. 323–333, 1971.
- [122] K. G. Ranga Raju, R. J. Garde, S. K. Singh, N. Singh, "Experimental study on characteristics of flow past porous fences," *Journal of Wind Engineering and Industrial Aerodynamics*, vol. 29(1–3), pp. 155–163, 1988.
- [123] S. C. Yaragal, H. S. Govinda Ram, K. Keshava Murthy, "An experimental investigation of flow fields downstream of solid and porous fences," *Journal of Wind Engineering and Industrial Aerodynamics*, vol. 66, pp. 127–140, 1997.

- [124] Kozmar H, Procino L, Borsani A, Bartoli G (2012) Sheltering efficiency of wind barriers on bridges, *Journal of Wind Engineering and Industrial Aerodynamics* 107-108, 274-284.
- [125] Kozmar H, Procino L, Borsani A, Bartoli G (2014) Optimizing height and porosity of roadway wind barriers for viaduct and bridges, *Engineering Structures* 81, 49-61.
- [126] M. Telenta, J. Duhovnik, F. Kosel, V. Šajn, “Numerical and experimental study of the flow through a geometrically accurate porous wind barrier model,” *Journal of Wind Engineering and Industrial Aerodynamics*, vol. 124, pp. 99–108, 2014.
- [127] J. K. Raine, D. C. Stevenson, “Wind protection by model fences in a simulated atmospheric boundary layer,” *Journal of Wind Engineering and Industrial Aerodynamics*, vol. 2, pp. 159–180, 1977.
- [128] A. Buljac, H. Kozmar, S. Pospíšil, M. Macháček, “Aerodynamic and aeroelastic characteristics of typical bridge decks equipped with wind barriers at the windward bridge-deck edge,” *Engineering Structures*, vol. 137, pp. 310–322, 2017.
- [129] A. Buljac, H. Kozmar, S. Pospíšil, M. Macháček, “Flutter and galloping of cable-supported bridges with porous wind barriers,” *Journal of Wind Engineering and Industrial Aerodynamics*, vol. 171, pp. 304–318, 2017.
- [130] A. Buljac, Aerodynamic and Aeroelastic Characteristics of Cable-Supported Bridges with Roadway Wind Barriers, *Ph.D. Dissertation*, University of Zagreb, Croatia, 2019.
- [131] D. Allori, Mitigation of cross wind effects on road vehicles by porous screens, *Ph.D. Dissertation*, University of Braunschweig, Germany, and University of Florence, Italy, 2012.
- [132] D. Allori, G. Bartoli, C. Mannini, “Wind tunnel tests on macro-porous structural elements: A scaling procedure,” *Journal of Wind Engineering and Industrial Aerodynamics*, vol. 123, pp. 291–299, 2013.
- [133] S. J. Lee, H. B. Kim, “Laboratory measurements of velocity and turbulence field behind porous fences,” *Journal of Wind Engineering and Industrial Aerodynamics*, vol. 80, pp. 311–326, 1999.
- [134] Y. Bayazit, E. M. Sparrow, D. D. Joseph, “Perforated plates for fluid management: Plate geometry effects and flow regimes,” *International Journal of Thermal Sciences*, vol. 85, pp. 104–111, 2014.
- [135] M. Jensen, “The model law phenomena in natural wind,” *Ingenioren* vol. 2(4), pp. 121–128, 1958.

- [136] K. Költzsch, H. Ihlenfeld, J. Brechling, “Einfluss des Modellierungsmaßstabes bei der Ermittlung von Windlastannahmen in Grenzschichtwindkanälen,” *Baukonstruktionen unter Windeinwirkung, WTG-Berichte*, vol. 18, 1997.
- [137] H. W. Tieleman, “Wind tunnel simulation of wind loading on low-rise structures: a review,” *Journal of Wind Engineering and Industrial Aerodynamics*, vol. 91, pp. 1627-1649, 2003.
- [138] P. W. Bearman, “On vortex shedding from a circular cylinder in the critical Reynolds number regime,” *Journal of Fluid Mechanics*, vol. 37, pp. 577-585, 1969.
- [139] C. H. K. Williamson, R. Govardhan, “Vortex-induced vibrations,” *Annual Review of Fluid Mechanics*, vol. 36, pp. 413-455, 2004.
- [140] C. C. Feng, “The measurement of vortex induced effects in flow past stationary and oscillating circular and D-section cylinders,” *Ms.C, Univ. BC, Vancouver, Canada*, 1968.
- [141] M. M. Zdravkovich, “Review and classification of various aerodynamic and hydrodynamic means for suppressing vortex shedding,” *Journal of Wind Engineering and Industrial Aerodynamics*, vol. 7, pp. 145–189, 1981.
- [142] F. E. Jorgensen, “How to measure turbulence with hot-wire anemometers - a practical guide,” *Dantec Dynamics*, 2002.
- [143] E. Simiu, R. H. Scanlan, “Wind Effects on Structures,” *John Wiley & Sons*, 1996.
- [144] H. Kozmar, “Scale effects in wind tunnel modeling of an urban atmospheric boundary layer,” *Theoretical and Applied Climatology*, vol. 100, pp. 153–162, 2010.
- [145] D. Golubić, W. Meile, G. Brenn, H. Kozmar, “Wind-tunnel analysis of natural ventilation in a generic building in sheltered and unsheltered conditions : Impact of Reynolds number and wind direction,” *Journal of Wind Engineering and Industrial Aerodynamics*, vol. 207, 104388, 2020.
- [146] T. von Kármán, “Progress in the statistical theory of turbulence,” *Proceedings of the National Academy of Sciences, USA*, vol. 34 (11), pp. 530–539, 1948.
- [147] A. N. Kolmogorov, “The local structure of turbulence in incompressible viscous fluid for very large Reynolds numbers,” *Proceedings of the National Academy of Sciences. USSR*, vol. 30, pp. 299–303, 1941.
- [148] Y. Tamura, “New frontier of education and research in wind engineering,” *6th International Symposium on Wind Effects on Buildings and Urban Environment (ISWE6)*, Tokyo, Japan, pp. 1-38, 2013.



- [149] R. E. Britter, S. R. Hanna, “Flow and dispersion in urban areas,” *Annual Review of Fluid Mechanics*, vol. 35, pp. 469–496, 2003.
- [150] P. Škvorc, H. Kozmar, “The effect of wind characteristics on tall buildings with porous double-skin façades,” *Journal of Building Engineering*, vol. 69, 106135, 2023.

## Curriculum vitae

Petar Škvorc was born on January 20, 1995, in Čakovec, Croatia. He completed primary and secondary school in Varaždin, Croatia, in 2013, and that same year he enrolled in the Faculty of Mechanical Engineering and Naval Architecture, University of Zagreb, Croatia. He completed the Design Engineering undergraduate program in 2018 with a BSc thesis on the design of a regulatory valve. He graduated *magna cum laude* in 2019 in the Engineering Modelling and Computer Simulations graduate program with an MSc thesis on the computational modeling of fatigue delamination damage in carbon composite structures. He started his PhD studies in 2019. In 2023, he was appointed Head of the Hydrodynamics and Hydraulic Machinery Laboratory at the Faculty of Mechanical Engineering and Naval Architecture, University of Zagreb. He has published three peer-reviewed journal articles and four conference contributions.

## Declaration

Parts of the work presented in this thesis have been published in scientific journals.